POLITECNICO DI TORINO

SCUOLA DI DOTTORATO
Dottorato in Ingegneria Aerospaziale – XXIV ciclo

Tesi di Dottorato

Low-order models and numerical techniques for the analysis of rotorcraft flight mechanics

Alberto Torasso

Tutore
Prof. Giulio Avanzini

Coordinatore del corso di dottorato
Prof. Fulvia Quagliotti

Maggio 2012

Summary

The dissertation describes (i) a mathematically rigorous approach for the derivation and validation of low–order helicopter mathematical models from first principles and (ii) the development or improvement of a set of numerical techniques that provide computationally efficient and reliable tools for the analysis of rotorcraft flight mechanics, and in particular evaluation of maximum performance and assessment of handling qualities. Simplified models are expected to provide results at a fraction of the computational cost required for performing the same analysis on the basis of higher order models, but, at the same time, the reliability of these results needs to be carefully assessed, which is one of the objectives of the present work. The techniques developed are tested on various single main rotor rotorcraft configurations, with a focus on articulated, teetering, and two–bladed–gimballed rotors.

In particular, the model of a single main rotor helicopter with individual blade flap, lag, and dynamic twist degrees of freedom was used as a reference for the analysis. Simplified models based on tip–path–plane dynamics, uniform inflow, linear blade aerodynamic and parasite drag area were developed for the same helicopter configuration. An ordering scheme based on a symbolic math–manipulation toolbox was developed, in order to automatically generate the equations of motions for the simplified model up to a given user–defined accuracy. The results obtained for a simplified helicopter models are validated against those derived for the most complete one, used as a reference. The latter in turn is validated against available flight test data. The effects of both helicopter model complexity and trim technique on the accuracy of performance estimate were analysed.

Two themes were developed in the framework of helicopter handling quality assessment. A stability analysis in the presence of severe gusts is carried out first for a two–bladed gimballed rotor with coning hinges and pitch–coning coupling, based on a time–periodic linearized model. The behaviour of the system is thus related to system parameters and features peculiar to this original configuration and compared with that obtained for a more conventional equivalent teetering rotor. A second contribution is then proposed for the determination of the agility potential of a given rotorcraft on prescribed manoeuvres. An inverse simulation algorithm was implemented and improved for the determination of the necessary command travel for performing the considered task. The effects of different modelling approaches on the control action were then studied in order to (i) analyse the origin of the discrepancies between inverse solutions obtained from different models and (ii) quantify the reliability of simplified models, while evaluating an uncertainty interval associated to the control time–histories derived for a certain vehicle model.

Provided that rotorcraft dynamics often results into computationally demanding numerical techniques for performing a given (set of) analysis task(s), a further contribution is represented by two novel and numerically efficient techniques that solve the trim and inverse simulation problems, respectively, for individual blade rotorcraft models. In the first case, a nested trim algorithm is proposed, based on decoupling rotor and fuselage dynamics. As for the inverse simulation problem, a Model Predictive Control architecture is developed, that allows for the solution of the inverse problem formulated for a complex rotorcraft model by evaluating the control action that successfully tracks a prescribed trajectory on the basis of a low–order simplified one. Both these algorithms were demonstrated to provide reliable results at a fraction of the computational burden required by more conventional shooting algorithms.

to Alessandra

Contents

List of Tables

List of Figures

Nomenclature

$\boldsymbol{A}$	State matrix
A_{1_S}, B_{1_S}	Lateral and longitudinal cyclic pitch commands
$\boldsymbol{a}$	Acceleration vector
a_0	Tip Path Plane coning angle
a_1,b_1	Tip Path Plane longitudinal and lateral tilt angles
a_y	Lateral airframe acceleration
$\boldsymbol{B}$	Control matrix
B	Tip loss correction factor
c	Rotor chord
C_D	Profile drag coefficient
C_L	Profile lift coefficient
C_{L_α}	Lift-curve slope
C_P	Rotor power coefficient
C_Q	Rotor torque coefficient
c	Rotor chord
e	Hinge offset of main rotor blade
$\mathcal{F}_B$	Body reference frame
g	Gravity acceleration
$\boldsymbol{h}$	Angular momentum
$\dot{h}$	Rate of climb (ROC)
h_C	Vertical position of coning hinge
i_θ,i_ϕ	Longitudinal and lateral shaft tilt angles
$\boldsymbol{i}_B$,$\boldsymbol{j}_B$,$\boldsymbol{k}_B$	Unit vectors of body–fixed reference frame
$\boldsymbol{i}_S$,$\boldsymbol{j}_S$,$\boldsymbol{k}_S$	Unit vectors of non–rotating shaft reference frame
$\boldsymbol{i}_R$,$\boldsymbol{j}_R$,$\boldsymbol{k}_R$	Unit vectors of rotating shaft reference frame
$\boldsymbol{i}_b$,$\boldsymbol{j}_b$,$\boldsymbol{k}_b$	Unit vectors of blade reference frame
$\boldsymbol{I}$	Inertia tensor
I_{xx},I_{yy},I_{zz}	Moment of inertia around body axes
I_{xy},I_{xz},I_{yz}	Products of inertia around body axes
I_b	Blade inertia around flap/coning hinge
J_{fb}	Fly–bar inertia
J_{H_i}	Hub moments of inertia around feathering (F), polar (P) and teetering (T) axes
K	Guidance gain
$K_{H/T}$	Stiffness of spherical gimbal (H) or feathering hinge (T)

K_{PC}	pitch–flap/coning coupling
K_{β}	Stiffness in flap hinges
k_{fr}	Dry friction in coning hinge
ℓ_{ref}	Reference length
$\mathbb{M}$	Inertial coupling matrix
M	Mach number
m	Fuselage mass
m_b	Blade mass
n	Rotor rpm
N_b	Number of blades
N_s	Number of blade elements
p, q, r	Angular speed components
$\boldsymbol{P}$	Permutation matrix
R	Rotor radius
R_{fb}	fly–bar mean radius
r	Radial position along blade span
r_C	Radial position of coning hinge
S_b	blade static inertia around flap/coning hinge
S_{fb}	paddle area
s	Rotor solidity ($=N_b c/\pi R$)
T	$= N\Delta t$, Receding time horizon
t	Time
t_k	Time at the beginning of the k–th IS step
u, v, w	Speed components in body frame
$\boldsymbol{u}$	Control vector
$\boldsymbol{v}$	Velocity vector
$\boldsymbol{y}$	Output vector
$\boldsymbol{y}_{des}$	Desired output vector
$\boldsymbol{x}$	State vector
V	Speed norm

Greek Symbols

α	Angle of attack (AoA)
α_g	Blade AoA variation caused by a gust
β	Angle of sideslip (AoS)
β	Blade flap/coning angle
β_0, γ	Hub flapping and feathering angles
β_p	Blade precone angle
β_c, β_{lng}, β_{lat}, β_{dif}	coning, longitudinal, lateral, and differential flapping multiblade coordinates
$\tilde{\beta}_0$, $\tilde{\beta}_{1c}$, $\tilde{\beta}_{1s}$	first order harmonic flapping coefficients for low–order rotor models
Δt	forward simulation step
$\Delta\boldsymbol{u}$, $\Delta\boldsymbol{x}$, $\Delta\boldsymbol{y}$	increments for control, state and output variables w.r.t. values at trim
$\Delta\boldsymbol{y}^{\star}$	desired increment for the tracked outputs
Γ	Tail rotor cant angle

γ	Flight path angle
γ	Lock number $= 2\rho C_{L_\alpha} c R^4 / I_{bl}$
ϵ	Rotor eccentricity
ζ	Blade lead/lag angle
θ_0	Main rotor collective pitch command
$\theta_{0_{tr}}$	Tail rotor collective pitch command
θ_{cyc}	Cyclic pitch command
θ_{tw}	Built-in blade twist
θ_{tw_x}	Built-in twist coefficient
θ_H, ϕ_H	longitudinal and lateral hub tilt angles
θ_{SW}, ϕ_{SW}	longitudinal and lateral swashplate rotations
λ	Inflow ratio
λ_0,λ_c,λ_s	Uniform, cosine and sine components of rotor inflow velocity
λ_{tr}	Tail rotor inflow
μ	Advance ratio
ν_0,ν_c,ν_s	Uniform, cosine and sine components of nondimensional rotor inflow velocity
ρ	air density
ϕ, θ, ψ	Fuselage attitude angles
φ	Blade dynamic twist angle
χ	Wake skew angles
ψ	Reference blade anomaly angle
$\dot{\psi}$	Rate of turn (ROT)
$\boldsymbol{\omega}$	Angular rate vector
Ω	Rotor angular speed

Subscripts

$_0$	Trim conditions
$_A$	Aerodynamic
$_B$	Body–fixed reference frame
$_b$	Blade, blade reference frame
$_c$	Inertially coupled
$_{CM}$	Center of Mass
$_{dt}$	Dynamic twist
$_F$	At final time
$_{fb}$	Flybar
$_f$	Fuselage
$_H$	Hub
$_h$	hover
$_{ht}$	Horizontal tail
$_g$	Gust
$_k$	Elastic
$_I$	Inertial reference frame
$_I$	at initial time
$_{In}$	Inertial

ld	Lag Damper
R	Rotating shaft reference frame
r	Main rotor
S	Non–Rotating shaft reference frame
T	Tail rotor reference frame
TPP	Tip Path Plane
tr	Tail rotor
uc	Inertially uncoupled
vt	Vertical tail
W	Wind reference frame
w	Hub wind reference frame
λ	Inflow

Chapter 1

Introduction

1.1 Low order models in rotorcraft flight mechanics

The analysis of rotorcraft flight mechanics is an important task in the development of new vehicles. Helicopter aeromechanics, according to [1], is *the branch of aeronautical engineering and science dealing with equilibrium, motion, and control of elastic rotorcraft in air.* For these purposes the development of mathematical models capable of describing the most relevant features of rotorcraft behaviour represents a fundamental need since the onset of helicopter engineering. When properly linked with suitable numerical techniques, these models allow for the evaluation of rotorcraft performance, agility potential and handling qualities with various degrees of reliability, depending on model complexity and availability of vehicle's data.

From a historical perspective, the development of helicopter models has been based on relatively simple analytical methods until the development of computers. A great deal of engineering judgment, rules of thumbs, and flight testing characterized the development of early rotary–wing vehicles. Reference [1] describes the historical milestones of aeromechanics until the onset of CFD/CSD loose coupling in the mid-80s. As the computational power of computers increased, numerical techniques of increasing complexity have been proposed for the description of flexible blade dynamics and aerodynamic loads (including rotor–fuselage interaction) on the other. Recent developments have led to full coupling of CFD and CSD method for the analysis of blade operating conditions, vibrations, aeroacoustic. Leishman [2] overviews the open problems in rotorcraft aeromechanics research, with particular attention to the development of new approaches for the representation of aerodynamic phenomena which are typical of rotorcrafts, such as dynamic stall, blade–vortex interaction, wake representation.

Models which include CFD representation can provide an accurate description of many aerodynamic features, but they are not well suited for flight mechanics analysis, especially during a preliminary design phase. Their complexity does not allow (at present) fast solutions required for performance evaluation and their use in direct dynamic simulation is ruled out by their computational cost. At present, the use of high complexity, fully coupled CFD/CSD models is limited to the representation of complex phenomena (e.g. blade aeroelasticity, vibrations, aeroacustics). Furthermore these model can be used to validate lower order models when flight or wind tunnel data is not available. As underlined in Ref. [3], despite the improvement that high–order models will make as computers become more powerful, simplified tools for rotorcraft analysis will not become obsolete early in the future for several reasons. First, even if computers are becoming more powerful, in the near future this computational advantage does not allow the use of high–order models for extensive analysis as in performance evaluation or multidisciplinary optimization. Second, the need for real-time simulation requires simplified models that can execute in reasonable CPU times. Third and most important, simple models provide direct relations between system parameters and simplifying assumptions at the basis of the mathematical model, on one side, and the resulting vehicle behaviour on the other. Thus, they play a crucial role in gaining physical insight into rotorcraft behaviour. Finally the development of rotorcraft control laws, even with advanced techniques such as robust and adaptive control, is based on linear or very simple models (see [4] among many possible examples). As a consequence, reliable simplified models are required not only for analysis or simulation purposes, but for the development of Flight control System (FCS) as well. While acknowledging the importance of improvements of high order models, the development of simple or simplified model is still needed for many engineering tasks.

Two different strategies are possible in the development of low–order rotorcraft mathematical models: building the models from first–principles (i.e. from physical laws), or identifying the model from flight–data. The identification approach is possible only when the system to be modeled is available or require the development of large databases based on the design experience of a particular company or group. Limited exception to these problems are subsystem models (e.g. engine model) or blade profile or fuselage aerodynamic models. In this cases data may be available provided that tests were performed for previous use of these components.

On the converse modelling from first principles is available at any point in the helicopter life–cycle, including the design and development phases. In these latter cases, the full set of helicopter configuration data may not be available, thus precluding the possibility of using higher order models. At the same time, the high order models may simply be too costly (from an implementation or computational cost point of view) for the particular flight mechanics analysis task. Lower order models are thus the only viable option either because of the lack of the data needed for generating a high–order rotorcraft model, or because of their better efficiency in generating the results required from the analysis.

Although the development of suitable mathematical models is a fundamental task in aeromechanics, the evaluation of the effects of simplifying assumptions at the basis of each model on performance, loads, and handling qualities evaluation needs to be carefully assessed. Such an analysis can provide an estimation of the reliability of the results obtained from each model and it allows for the identification of the minimum complexity level that correctly represents each feature or task. For this reason models which are developed need to be validated against flight or wind tunnel data, when available, or at least compared to the results of higher order models in order to identify their range of validity and possible areas of improvement.

This study is aimed at developing low order mathematical models and numerical techniques for the evaluation of rotorcraft performance and handling qualities. Furthermore an assessment of the effects of model simplifying assumptions on the relevant results is performed in order to identify minimum complexity level required to correctly represent each flight mechanics task. Several rotorcraft configuration are considered in the analysis, including an unconventional two–bladed gimballed rotor, which requires the development of ad hoc analysis techniques as its dynamic behaviour is different from conventional articulated and teetering rotors. As a consequence standard simplifying assumption can not be used and original models for its analysis are required. In order to discuss in greater detail the objectives and the original contribution of this work, the state of the art in the fields of mathematical modelling, performance and handling qualities evaluation of rotary-wing aircraft is reviewed in the following section.

1.2 State of the art

1.2.1 Helicopter mathematical modelling

Helicopter mathematical modelling is a fundamental step in the analysis of performance, stability, dynamic behaviour and handling qualities. For this reason, starting from the very beginning of rotorcraft engineering, mathematical models of increasing complexity have been proposed in order to provide a better estimation of helicopter behaviour. A more detailed analysis of modelling technique and classical simplification assumption is discussed in Chapter 2.

Many helicopter textbooks describe mathematical modelling approaches and numerical techniques for the analysis of performance, dynamic behaviour and handling qualities. Bramwell [5] proposes a very simple static model (i.e. based on the equilibrium of forces and moments, with no dynamic equations) based on momentum theory and decoupled longitudinal and lateral equilibria. Padfield [6] develops a more detailed static model, introducing an equivalent hinge stiffness located at the rotor centre, that results in a unified modelling approach valid for both articulated and hingeless rotors. Johnson [7], Prouty [8], Arra [9], and Leishman [10] introduce models based on a more extensive use of blade element theory. In particular their attention is focused on the description of tip-path-plane (TPP) dynamics and rotor loads transmitted to the fuselage. All these textbooks describe empirical corrections with the aim of providing a more realistic estimate of helicopter performance. Correction factors for induced, parasite, and profile power losses are introduced in this framework.

Heffley and Minch [11] propose a minimum complexity mathematical model for a conventional helicopter configuration to be used in flight simulation. Rotor motion is described by first order dynamics for longitudinal and lateral TPP tilt angles, whereas coning is assumed constant. A uniform static inflow is used and rotor inplane forces are determined by thrust tilt only. Such model has been developed with the aim of minimizing the number of parameters required to tune the model to represent the desired helicopter for pilot training purposes.

In a series of reports Chen et al. [12, 13, 14] propose a mathematical model for both articulated and teetering rotors. The rotor is described by second order Tip–Path–Plane dynamics where rotor states are the Fourier coefficients of the blade flapping truncated at the first harmonic terms (i.e. coning, longitudinal and lateral tilt). Linear aerodynamics is used to evaluate blade loads, so that average rotor force and moment coefficients can be evaluated analytically by integrating aerodynamic and inertial loads along blade span and over one rotor revolution. Static uniform inflow is used. Effects of main rotor downwash on tail surfaces are included. The tail rotor is described similarly to the main rotor but the 2^{nd} order dynamic description of the tip–path–plane is replaced by a quasi–static approach and cyclic pitch is not represented.

Howlett [15, 16] presents an individual blade model of the UH-60A helicopter. This model, described in detail also in [17], features a full nonlinear description of fuselage aerodynamics, constant rotor angular speed, rigid articulated blades with an accurate representation of the lag damper, a dynamic model of main rotor triangular inflow, and a simple tail–rotor model with dynamic uniform inflow [18]. Effects of blade torsional deformation are also accounted for, but the model neglects blade bending in the flap and lead-lag planes, shaft and fuselage elastic modes, and important aerodynamic effects, such as circulation hysteresis and rotor wake distortion.

In recent years the development of mathematical models for flight mechanics have been focused on the description of blade flexibility, rotor wake and its interaction with fuselage, tail surfaces, tail rotor, and main rotor itself. Blade flexibility is often modeled by one-dimensional finite elements using bending in flap and lag directions, torsion around blade span and elongation along blade span due to centrifugal forces as degrees of freedom. In this framework models with fully flexible rotor blades are presented for an articulated configuration in [19], while in [20] a teetering rotor is considered together with a flexible fuselage. Aerodynamic models are even more complex. Fixed wake models have been superseded by prescribed wake models first, free wake models later on, and eventually advanced CFD calculation (such as direct Navier-Stokes simulations). Since such CFD simulations are extremely demanding from the computational point of view, simpler inflow and wake models are used for flight mechanics studies. This justifies the interest for simpler but effective approaches such as low order dynamic inflow models [3].

In spite of the extensive literature dealing with rotor dynamic behaviour (in particular articulated and hingeless rotors), two–bladed teetering rotors received a marginal attention from the researchers. Two–balded gimballed rotors have attracted even less studies. Teetering rotors were adopted in the past for relatively large military rotorcraft, such as the Bell models 205 [21] and 212. Nowadays they are still popular for light helicopters, such as the Robinson R–22, and remotely piloted vehicles (RPV) like the Yamaha R–Max. Teetering rotor dynamic characteristics are often improved by means of additional devices, such as a stabilizing Bell bar, as on the AB–47 helicopter, or the Bell–Hiller bar, featuring aerodynamic paddles, such as in the Yamaha R–Max RPV [22]. These devices are effective in improving the dynamic characteristics of the rotor, especially during manoeuver transients, yet they are designed on grounds of some reasonable engineering practice, previous experience and flight testing.

A two–bladed gimballed rotor was considered in the 60's as a possible configuration for heavy lift helicopters with tip jets and no pitch hinge [23]. The spherical hinge, allowing for feathering motion, and a blade circulation control based on small jets distributed along the blade span should have allowed for full rotor control.

1.2.2 Trim

An extensive literature on rotorcraft trim is available, where different techniques are proposed, ranging from relatively simple analytical or algebraic [5, 6] techniques, to methods based on direct numerical simulation [24], including the more sophisticated autopilot method [25], up to computationally more demanding techniques which include the determination of periodic rotor states by means of shooting techniques [26] or harmonic balance [27].

A comprehensive review of rotorcraft trim techniques was proposed by Peters [28], where the paper is focused on the formal mathematical description of the trim problem and on implementation aspects rather than on performance of the different methods. Starting from the mathematical definition of a trim problem for a rotorcraft (i.e. the fact that periodicity needs to be included in the trim approach to take into due account rotor behaviour and its coupling with rigid body states), the authors define the most general equations to describe rotorcraft trim. The mathematical formulation requires a state space approach, the periodicity constraint can be enforced by means of a permutation matrix (which may degenerate to the identity matrix for rigid body states) between states as in [26]. The equations include Lagrangian multipliers for internal forces in case of a multibody system formulation. To solve the trim problem, two different class of constraints need to be enforced: periodicity constraints and trim constraints. The latter ones depend on the states, their derivatives and control variables, but cannot be a linear combination of periodicity constraints (i.e. no sum of forces or moments on the system can be used). A mathematical approach to the solution of optimal trim is proposed, i.e. when the number of controls is higher than the number of constraints. To solve a trim problem, four different sets of equations are thus required: (i) differential equations, (ii) implicit equations, (iii) quasi-periodicity conditions and (iv) trim constraints. To enforce periodicity an approach based on either enforced periodicity or on transfer-matrix methods is required.

Schank [29] in his PhD dissertation proposes an analysis of trim as an optimization problem, in particular when variable rotor speed and several aerodynamic surfaces are present. The optimal trim is based on a nonlinear programming method for the generalized reduced gradient and it is integrated with a multi–body, comprehensive rotorcraft aeroelastic code.

1.2.3 Performance

The analysis of helicopter performance requires a rotorcraft mathematical model and a trimming algorithm. Classical performance tasks are the evaluation of flight envelopes, maximum rate of climb, ceiling in and out of ground effect, maximum rate of turn.

Several comprehensive helicopter analysis tools are now available. They have been developed by government agencies (2GCHAS [30], RCAS [31]), helicopter industry (TECH02, COPTER, CRFM, HOST [32]), academia (UMARC [33], DYMORE [34], MBDyn [35]), or commercial companies (FLIGHTLAB [36], CHARM [37], CAMRAD II [38]). All these tools allow for the evaluation of rotorcraft performance. Harris [39] compares the results obtained by some of the comprehensive codes at high advancing speed with flight test or full rotor wind tunnel tests in order to highlight the reliability, field of applicability of present rotor modelling techniques and their improvements in the last years.

Despite the ongoing development of more complex models, reasonable performance evaluation can be achieved also with lower order models. Johnson [40] describe the use of low order models for the development of a conceptual design tool for rotorcraft performance analysis, while in [41] the performance results obtained with the simplified models used in NDARC are compared with those obtained with CAMRAD and other high order models.

Bousman and Norman [42] describe techniques for the analysis of predictive capabilities of aeromechanics numerical techniques, in particular hover and forward flight performance, blade aerodynamic and structural loads, vibratory forces, and aeroelastic/aeromechanical stability. The main objective of the study is the identification of the accuracy level of current techniques in the previous areas and to identify the research areas in which improvement is required. The accuracy of the mathematical model and numerical technique is determined by the slope of the regression line which relates measured and calculated behaviour (a perfect agreement is represented by a slope of 1). The standard error of estimate of the linear regression is a measure of scatter or dispersion, and in some cases may provide a better assessment of accuracy than the regression line slope.

1.2.4 Inverse simulation

Inverse simulation has been considered in the past as a useful and versatile tool for investigating several aspects of fixed– and rotary–wing vehicle dynamics [43], from early works aimed at the evaluation of manoeuvring performance [44, 45, 46], including agility [47, 48], up to more recent developments in the framework of support to design [49], model validation [50] and handling quality evaluation [51]. Bagiev and Thomson [52] provide a technique for a preliminary assessment of handling qualities for an autogyro by means of inverse simulation demonstrating that an approach based on inverse simulation of mission task elements can be used for various rotorcraft configurations, including nonconventional ones. The results of the numerical analysis were compared to Cooper Harper grading of the same manoeuvres executed in flight tests. A fairly good agreement was obtained, thus validating the technique.

A wide plethora of methods for solving inverse simulation problems in flight mechanics has been considered, which can be grouped into three major categories: (i) differential methods [44], suitable for nominal problems only, where the number of control inputs matches that of the tracked variables; (ii) integration methods [53, 46], where the required control action is evaluated over a discrete time interval, a method that can handle also redundant problems, where the number of control variables exceeds that of tracked outputs (e.g. by means of a local optimization approach [54]); and (iii) global methods, where the time-history of control variables is determined over the whole duration of the tracked manoeuvre by means of a variational approach [55] or optimization method [56].

As underlined in Ref. [43], the solution of the inverse problem is a task significantly more challenging for the rotorcraft case than for a conventional airplane, especially when individual blade dynamics is incorporated in the model [57]. On the other hand, one of the advantages of integration methods is represented by their capability of dealing with complex, high order mathematical models of the vehicle. In this respect, the same baseline inverse solution scheme can easily accommodate models of various levels of complexity without substantial changes to the architecture of the algorithm. This allows for a fair comparison among different inverse solutions obtained on the basis of different vehicle models, provided that the issue of unconstrained states is properly addressed. This often results in numerically demanding algorithms [54, 57].

It is evident that by keeping helicopter model complexity down to a minimum level, the computational effort necessary for a systematic analysis of the agility potential can be substantially reduced. Computation efficiency can be increased by application of a two–time–scale approach [58].

Rutheford and Thomson compared the results obtained for a helicopter model where rotor was represented either as a disk or by means of individual rotor blade dynamics [57], but their paper was more focused on the extension of the inverse simulation approach to the individual blade model and the comparison was carried out mainly with a validation purpose.

A detailed description of inverse simulation peculiarities for the rotorcraft case is reported in Lu's PhD dissertation [59]. Lu describes two different approaches for the solution of inverse problems in helicopter and ship control including systems having nonminimum–phase characteristics. The first technique, based on sensitivity-analysis theory, allows the Jacobian matrix to be calculated by solving a sensitivity equation and overcome to some extent the problem of high–frequency oscillations. The second one, based on a Nelder–Mead search–based optimization algorithm, is completely derivative–free and overcome problems often encountered in control applications when discontinuous features such as actuator amplitude or rate limits are introduced.

Bagiev et al. [60] showed that a modified inverse simulation scheme that includes a predictive step can provide more realistic solutions to the inverse simulation problem, especially when dealing with aggressive manoeuvres. A baseline IS algorithm may predict values which exceed the physical limits of the real vehicle, such as mechanical limitations on control travel or control rates (based on hydraulic actuator stroke and other characteristics), limits on main and tail rotor torque, total required power or even structural limits of critical components. A predictive step is thus introduced in order to identify in advance if and when such limits are approached during a manoeuvre, so that the control task can be modified and turned into a feasible one.

Together with inverse simulation, other numerical techniques are available for the evaluation of performance and handling quality over prescribed, possibly optimal, manoeuvres. Among other examples, Bottasso et al. [61] propose two different techniques for the solution of rotorcraft trajectory optimization problem in this framework. A direct transcription is used to solve an optimization problem by introducing a function of system states in the cost function at every time interval. Conversely, direct multiple shooting allows for the definition of a cost function only at discrete points along the trajectory. The first technique suits well lower order model, whereas the direct multiple shooting can be coupled also to medium complexity models.

1.2.5 Handling qualities

In the rotorcraft field, handling qualities (HQ) are regulated by ADS 33 standards [62]. These standard require rotorcraft to comply with handling qualities requirements which are stated either in the frequency domain or as Mission Task Elements (MTE). The requirements in the frequency domain are formulated in terms of acceptable range for frequency and damping of rotorcraft characteristic modes and can thus be evaluated by means of linearization or Fourier analysis of helicopter models or real flight data, when available. Mission Task Elements are elementary manoeuvres which must be accomplished while fulfilling requirements on speed, position tolerance with respect to the prescribed trajectory, maximum time to complete the manouevre, minimum Cooper–Harper grades in performing the manoeuvre in nominal/degraded environments. Other requirements are set for the dynamic behaviour in hover, low speed, and advancing flight. In particular threshold values are set for rotorcraft mode frequency and damping while control response type are analyzed in detail.

During the whole design phase, compliance of rotorcraft with handling quality requirements is based on the development of mathematical models. All comprehensive rotorcraft analysis tools include techniques for linearization and model dynamic evaluation for the analysis of handling qualities. Linearization is easily performed on helicopter models which do not include individual blade dynamics. The introduction of individual blade dynamics leads to time variant models. The stability analysis of such models require different techniques and in particular Poincaré maps and Floquet analysis. Floquet theory for the analysis of handling qualities was introduced by Peters and Hohenemser [63], and refined by Peters [64] and McVicar and Bradley [65] together with a faster technique for the evaluation of rotorcraft trim. In a recent paper, Peters et al. [66] describe a technique to solve the the integer-multiple arbitrariness in the imaginary part of the characteristic exponents of the system which determine the frequency of the mode in the Floquet analysis. Bauchau and Wang [67] present two methodologies for the stability analysis that are applicable to generic nonlinear rotorcraft models, which do not rely on linearization of the system but exploit the behaviour of some of the system states when perturbations from an equilibrium condition are introduced. The technique of singular value decomposition is used to generate either a partial Floquet or an autoregressive approach, depending on the base of functions used to describe system dynamics, in order to assess system stability. Guglieri [68] describe the effects of modelling assumptions on drive train and fuel control design on the evaluation of handling qualities.

As described above, inverse simulation allows for the evaluation of helicopter behaviour in performing Mission Task Elements and therefore provides valuable data on handling qualities. The trajectory of a mission task element can be used as the objective function in an inverse problem and therefore command, attitude and more in general whole rotorcraft state time–histories can be derived in order to provide information on command action, command travel, frequencies excited in the manoeuvre, dominant modes, etc.

1.3 Objectives of the study

During the whole design cycle, and in particular when developing novel or nonconventional configurations, a mathematical model which can reliably assess system behaviour at a small computational cost represents a valuable tool. In particular during early phases of the design (feasibility, conceptual design or preliminary design), key configuration choices are taken. The possibility of performing preliminary flight mechanic analysis, evaluating the impact of design choices on performance and handling qualities with only a limited set of data, and with a known confidence in the results, allows a formidable advantage in the development of better rotorcraft platform.

The objective of this dissertation is to propose an approach for the derivation of low order helicopter mathematical models from first principles and for the development of numerical techniques that provide computationally efficient and reliable tools for rotorcraft flight mechanic analysis. These approaches are tested on a wide range of single main rotor rotorcraft configurations with special attention to articulated and teetering rotors, and including innovative designs such as an unconventional two–bladed–gimballed rotor. The effects of model detail are analyzed for both steady–state flight performance and handling quality evaluation. For these tasks numerical techniques for trim, linearization, and inverse simulation have been implemented. In this framework a contribution is provided by improving existing techniques (e.g. inverse simulation) and developing new analysis tools (e.g. metrics for comparing the reliability of inverse solutions command time histories) in order to develop faster techniques that provide reliable information based on low–order, simplified helicopter models. As the choice of model complexity is a tradeoff between computational cost and accuracy of the results, for each analysis task the minimum level of model complexity that correctly represents helicopter behaviour is assessed.

As stated above, the analysis is focused on the development of models from first principles. This approach is followed for two main reasons. First of all the purpose of this work is to propose a modelling approach able to represent any rotorcraft configuration, including innovative ones at the design stage, whereas the approach based on system identification requires the availability of a flying vehicle. Furthermore modeling from first principles allows for a direct assessment of the relation between system parameters and the resulting rotorcraft behaviour, with a thorough analysis of the effect of configuration changes.

The attention will be focused on performance and handling quality evaluation. These fields were chosen because they cover some of the most important tasks in flight mechanics and also as they require a thorough test of mathematical models in many conditions, including the most demanding ones.

The most widespread use of flight mechanic models is for performance evaluation (including those modelling techniques where only steady–state conditions are evaluated and no dynamic simulation is required). With respect to steady state performance, the objective is to investigate the trade–off between the computation effort necessary for obtaining a set of trimmed flight conditions and the accuracy of the results. Both helicopter model complexity and trimming technique are considered in this analysis and their effects on rotorcraft equilibrium is studied in detail. An estimate of the accuracy of low–order models and the relevant simplifying assumptions in predicting vehicle characteristics is useful in order to assess their reliability with respect to the same set of results obtained from more accurate models or flight tests. The relevance of the study becomes evident if one acknowledges the mathematical complexity, numerical difficulties, and computational cost of determining the trimmed flight conditions for a high–order individual blade helicopter model. In such a case the periodic nature of helicopter steady states must be taken into account, so that trim conditions on flight path variables (velocity, flight–path angle and turn–rate) must be enforced in an average sense. For preliminary design purposes and/or vehicle comparison, simpler model may suit the scopes of the analysis. The requirement for a simplified analysis may be dictated by the availability of a limited set of vehicle parameters and configuration data or by the necessity for a fast evaluation of global characteristics in terms of performance.

In this framework, one goal of the research activity is to develop an ordering scheme based on a symbolic math–manipulation toolbox, in order to automatically generate the equations of motions for the simplified model up to a given user–defined accuracy. Using this tool, the generation of helicopter models with different level of details becomes a straightforward activity and analysis of performance and handling qualities can rely on more models.

In the framework of handling qualities (HQ) analysis, the evaluation of a minimum level of complexity required to provide reliable information on stability and characteristic modes as well as vehicle capability in performing a given (set of) flight task(s) allows for the preliminary assessment of its HQ potential as soon as a sufficient amount of information is available during the design process. Depending on rotorcraft configuration, the task of determining characteristic modes and stability margins for handling qualities analysis may not be trivial. In particular, when time-varying periodic models are used a Floquet analysis is required to evaluate stability and (indirectly) frequency. Furthermore, innovative configurations such as the two–bladed gimballed rotor discussed in Chapter 3.6, may introduce rotor degrees of freedom which lead to modes not even present in conventional rotor, and hardly discussed in the literature. For this reason complete and simplified models are compared to analyze whether low–order ones can represent the most relevant features of vehicle's dynamics.

It is clear that the assessment of the ability of a rotorcraft platform to comply with handling qualities requirements [62] already in the early design phases allows a sound selection of rotorcraft configuration and relevant parameters when design changes are more easily implemented and less expensive. Furthermore, an early definition of the bare airframe flying qualities allows the definition of flight–control system requirements in the early phases of the design, allowing more time for their development and more reliable models to be used as reference. As an example, the evaluation of the total required power allows one to determine the feasibility of a given manoeuvre prescribed by handling quality requirements, if the required power remains within acceptable limits (zero to maximum) during the whole manoeuvre. At the same time the manoeuvre can be made more demanding (*e.g.* increasing the required displacement or turn rate), in order to identify vehicle performance limits for a particular configuration. Furthermore vehicle dynamics in the presence of large command travel can be analyzed without the need for including stability augmentation systems in the model, as long as the IS scheme easily compensates for mild instabilities. This allows for the analysis of pure baseline helicopter model performance.

Given the important information that inverse simulation can provide on handling qualities, the analysis of the effects of different approaches in deriving a helicopter model on the results obtained from inverse simulation algorithms (command action, command travel, etc.) is performed. The objectives are (i) to analyze the origin of the discrepancies between inverse solutions obtained from different models of the same vehicle, while performing a given task, and (ii) to evaluate the uncertainty on command laws necessary to realize a specified flight task associated to a certain vehicle model. The first objective requires the identification of those critical situations in which a given model fails to provide a reliable inverse solution for the considered task. The definition of an uncertainty interval is a parameter of paramount importance for the development of robust control laws (*e.g.* stability and command augmentation systems that equip modern rotorcraft). Both tasks are then focused towards the identification of the minimum level of detail required in the model in order to provide reliable information on vehicle's agility potential.

Provided that the inverse solution of helicopter equations of motion becomes computationally more demanding and numerically more difficult, a novel tool was developed for solving the inverse simulation problem for rotorcraft motion. The solution proposed is based on the evaluation of the control action that successfully tracks a prescribed trajectory on the basis of a low–order simplified model and its implementation on a high order, more accurate one. The algorithm proposed uses a Model Predictive Control (MPC) scheme for the solution of the inverse simulation problem for rotorcraft dynamics. The complex model which needs to be analyzed is substituted in the inverse simulation step by a simplified lower–order one that requires a significantly shorter CPU time to solve the inverse problem. The control action evaluated for the low–order model is then propagated forward in time on the most complex, high–order one. The architecture of the system requires a continuous exchange of data on control activity and (a possibly selected subset of) state variables between the two models. This limits the drift of system output from the desired one during unsteady manoeuvres and allows for asymptotically recovering the correct airspeed during steady–state flight phases.

Finally, helicopter flight mechanics studies are often focused on the impact of main rotor level of detail on the evaluation of performance, trim conditions and dynamic behaviour. Limited attention is devoted to the fuselage aerodynamic description and its impact on flight mechanic analysis, as the main rotor is usually the major subject of these studies. This is due to the lack of data on fuselage aerodynamics caused mainly by cost constrains. With respect to fuselage models, two goals are pursued in this work. The first one is the description of the impact of fuselage aerodynamic models on the most important helicopter flight mechanic analysis tasks, and for this reason both performance and handling qualities analysis are carried out. The second objective is the description of an approach that provides a satisfactory fuselage aerodynamic characterization when a limited set of data is available. A technique which enables extension of available data based on a limited range of angles of attack and sideslip to a full database in spherical coordinates to allow realistic simulation of forward, backward and sideward flight is developed. The approach is based on empirical techniques such as drag area and shape evaluation and on published reference data on fuselage aerodynamic characterization.

1.4 Outline of the dissertation

In what follows, chapters 2 and 3 are dedicated to the description of rotorcraft mathematical modelling. Chapter 2 provides an overview of helicopter model levels of complexity, and it is then focused on common features shared by helicopter models, with a special attention to fuselage models and the assembly of helicopter equations of motion. The last task is not trivial, as main rotor and fuselage states are strongly inertially coupled. A detailed description of the mathematical approach used is thus proposed.

Chapter 3 is dedicated to the description of main rotor models, taking into consideration different configurations (in particular articulated and gimballed rotors) and individual blades vs tip–path–plane models. The derivation of low–order models and possible improvements are presented.

The results for performance and handling quality analysis are reported in the following chapters. Chapter 4 describes the evaluation of helicopter steady–state performance. Attention is devoted to the effects of simplifying assumptions and model complexity on maximum performance evaluation for a UH–60A helicopter. Performance analysis is presented for an articulated configuration only.

The results on handling qualities are collected in Chapter 5 for both gimballed, teetering and articulated configurations. The first part is dedicated to the evaluation of handling qualities by means of low–order models for gimballed rotor focusing the attention on stability analysis and identification of fuselage and rotor characteristic modes. The second part is focused on inverse simulation as a tool to analyze handling qualities and in particular the effects of model complexity on command time histories determined by means of inverse simulation algorithm. After an extensive qualitative and quantitative analysis of the results, the chapter presents an original technique for solving the inverse simulation problem for a high order model derived from a model predictive control scheme.

A chapter of conclusions ends the dissertation.

Chapter 2

Mathematical model of the helicopter

The mathematical description of the helicopter is a complex task and different strategies may be adopted, depending on the purpose for which the model is developed. The equations of motion of the vehicle are written by combining the contributions of all elements. Each element (and in particular the main rotor) can be described by means of models characterized by various levels of complexity. More detailed models are expected to be more accurate, but at the same time they require longer development time for implementing the model, more configuration data and higher computational power for running the desired analysis.

This chapter is devoted to the description of the features which are common for all helicopter models, in particular fuselage, empennage, tail rotor and rigid–body equation of motions. Before going into deeper detail, the coordinate systems used in helicopter modelling are introduced. A self standing chapter (Chapter 3) is dedicated to the main rotor model, which plays a major role in the development of a helicopter model.

In spite of considerable differences in terms of model complexity and level of details, all rotorcraft models share a similar structure. They are based on a modular approach involving a rotor, fuselage, empennage and tail rotor model as clearly described in [6]. Forces and moments generated in each element of the helicopter are then summed to evaluate the rotorcraft rigid body dynamics.

2.1 Levels of helicopter modelling

The complexity of an helicopter simulation model is characterized mainly by two aspects:

- the description of rotor dynamics (depending on how the blade is connected to the hub: articulated vs. rigid blade);
- the aerodynamic interaction between the main rotor and the surrounding air; this can be described by a variety of models for rotor/blade aerodynamics, as well as inflow, downwash, and rotor wake models;

Table 2.1. Levels of rotor modelling*.

Level 0	*Aerodynamics*	linear airfoil aerodynamics static uniform inflow with momentum theory analytically averaged aerodynamic loads
	Dynamics	rigid blades featuring steady-state flapping motion possibly described in terms of multi–blade coordinates
Level 1	*Aerodynamics*	linear airfoil aerodynamics dynamic inflow with momentum theory analytically integrated aerodynamic loads
	Dynamics	rigid blades featuring 1.1) quasi-steady motion 1.2) flap dynamics 1.3) flap+lag dynamics 1.4) flap+lag dynamics and quasi steady torsion
Level 2	*Aerodynamics*	nonlinear airfoil aerodynamics with (limited) 3-D effects dynamic inflow with momentum theory local effects of blade–vortex interaction 2-D unsteady aerodynamics and compressibility effects numerically integrated aerodynamic loads
	Dynamics	2.1) rigid blades featuring flap+lag dynamics 2.2) low–order elastic bending and torsional blade models
Level 3	*Aerodynamics*	nonlinear 3-D aerodynamics with full wake analysis unsteady aerodynamics and compressibility effects numerically integrated aerodynamic loads
	Dynamics	detailed structural representation in terms of either elastic modes or finite elements

*Note: the definitions of Levels 1 to 3 are taken from [6].

- rotor-fuselage interaction.

In this framework, Padfield [6] proposes a classification of rotor models for simulation divided into three levels of increasing complexity (Tab. 2.1, Levels 1 to 3). Level 1 models can be used for performance studies and “evaluation of parametric trends for flying qualities”, only in the framework of low–bandwidth control tasks and “well within operational flight envelope”. Level 2 models permit to extend the study to the whole operational flight envelope, with medium–bandwidth control tasks. Level 3 models are necessary for describing vehicle dynamics in extreme conditions, such as at the bounds of the safe flight envelope, including “rotor limit loads predictions, vibration analysis, rotor stability analysis”.

This classification, developed for the analysis of helicopter dynamic response to controls, suits also studies aimed at performance evaluation. For preliminary design purposes and/or vehicle comparison, simpler models may suit the goals of the analysis. The requirement for a simplified analysis may be dictated by the availability of just a limited set of vehicle parameters and configuration or by the necessity for a fast evaluation of global characteristics in terms of performance. A Level 0 rotor modelling is thus introduced which considers blade motion at steady state and the average force and moment exchanged by rotor and fuselage in the framework of the trim problem. Such a model is unsuitable for simulation, but it provides a useful physical insight into the relation between design parameters, vehicle characteristics and expected performance. As one of the goals of this work is to provide an evaluation of the reliability of these simplified approaches, Level 0 models are introduced in the analysis when possible and their results are compared with respect to data obtained from higher complexity models.

2.2 Coordinate Systems

For the development of the helicopter equations of motion, the following reference frames are used:

- inertial coordinate system $\mathcal{F}_I$
- body coordinate system $\mathcal{F}_B$
- wind coordinate system $\mathcal{F}_W$
- nonrotating shaft coordinate system $\mathcal{F}_S$
- rotating shaft coordinate system $\mathcal{F}_R$
- hub–wind coordinate system $\mathcal{F}_w$
- rotating hub coordinate system $\mathcal{F}_H$
- blade span coordinate systems $\mathcal{F}_{b_i}$ with $i = 1, \cdots, N_b$
- tail rotor coordinate system $\mathcal{F}_T$

Coordinate transformation matrices between different frames are defined through suitable sets of Euler angles. Most of the coordinate systems are used in all helicopter models. Only the hub–wind coordinate system $\mathcal{F}_w$ is used in models where rotor dynamics is described by Tip–Path Plane model whereas a rotating hub coordinate system $\mathcal{F}_H$ is used with gimballed models or other configurations where rotor hub is free to move with respect to the shaft.

2.2.1 Inertial reference frame

The inertial frame is assumed fixed to a flat, non rotating Earth, $\mathcal{F}_I$ $\{N, E, D\}$ (North-East-Down). The coordinates of the centre of mass of the aircraft are defined in terms of latitude, longitude, and altitude $h = -D$.

2.2.2 Body axes

The body fixed reference frame $\mathcal{F}_B$ has its origin at the fuselage centre of mass and moves with it. The x_B axis lies in the longitudinal plane towards the nose of the aircraft, the z_B axis lies in the longitudinal plane towards the bottom, and the y_B axis directed towards the right side of the aircraft completes a right-hand triad. Aircraft equations of motion are written in body reference frame. The attitude of the body fixed reference frame with respect to the inertial one can be described by means of roll ϕ, pitch θ, ad yaw ψ angles. The transformation between the two reference frames is given by the matrix

$$\boldsymbol{L}_{BI} = \begin{bmatrix} \cos\theta\cos\psi & \sin\psi\cos\theta & -\sin\theta \\ \sin\phi\sin\theta\cos\psi - \cos\phi\sin\psi & \sin\phi\sin\theta\sin\psi + \cos\phi\cos\psi & \sin\phi\cos\theta \\ \cos\phi\sin\theta\cos\psi + \sin\phi\sin\psi & \cos\phi\sin\theta\sin\psi - \cos\phi\cos\psi & \cos\phi\cos\theta \end{bmatrix} \tag{2.1}$$

In order to prevent singularities, Euler angles are limited in the following range

$$\begin{array}{rcl} -\pi \leq & \psi & \leq \pi \\ -\pi/2 < & \theta & < \pi/2 \\ -\pi \leq & \phi & \leq \pi \end{array} \tag{2.2}$$

2.2.3 Wind axes

The origin of the wind reference frame, $\mathcal{F}_W$, lies on the fuselage centre of mass. The x_W axis points in the direction of the velocity, z_W towards the bottom and y_W completes a right–handed coordinate system, as shown in Fig. 2.1. The transformation between the body and wind reference frames is given by

$$\boldsymbol{L}_{BW} = \begin{bmatrix} \cos\alpha_f\cos\beta_f & -\cos\alpha_f\sin\beta_f & -\sin\alpha_f \\ \sin\beta_f & \cos\beta_f & 0 \\ \sin\alpha_f\cos\beta_f & -\sin\alpha_f\sin\beta_f & \cos\alpha_f \end{bmatrix} \tag{2.3}$$

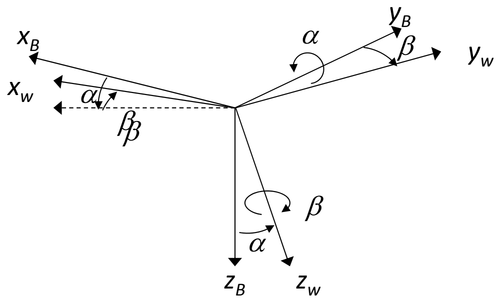

Figure 2.1. Wind axes reference frame.

where α_f is the fuselage angle of attack, whereas β_f is the fuselage angle of sideslip. The velocity vector in wind axis is written as $\boldsymbol{v}_W = (V,\ 0,\ 0)^T$. In body reference frame it becomes

$$\boldsymbol{v}_B = \boldsymbol{L}_{BW}\boldsymbol{v}_W = \begin{pmatrix} V\cos\alpha_f\cos\beta_f \\ V\sin\beta_f \\ V\sin\alpha_f\cos\beta_f \end{pmatrix} \tag{2.4}$$

2.2.4 Rotor reference frames

Nonrotating and Rotating shaft

Both nonrotating and rotating shaft coordinate systems, $\mathcal{F}_S$ and $\mathcal{F}_R$, have their origin at the rotor hub centre, in position $\boldsymbol{r}_B^H$ with respect to the aircraft centre of mass. The orientation depends on shaft longitudinal i_θ and lateral i_ϕ tilt as shown in Fig. 2.2. The transformation between body and nonrotating shaft reference frames is given by

$$\boldsymbol{L}_{SB} = \begin{bmatrix} \cos(i_\theta) & 0 & -\sin(i_\theta) \\ \sin(i_\theta)\sin(i_\phi) & \cos(i_\phi) & \cos(i_\theta)\sin(i_\phi) \\ \sin(i_\theta)\cos(i_\phi) & -\sin(i_\theta) & \cos(i_\theta)\cos(i_\phi) \end{bmatrix} \tag{2.5}$$

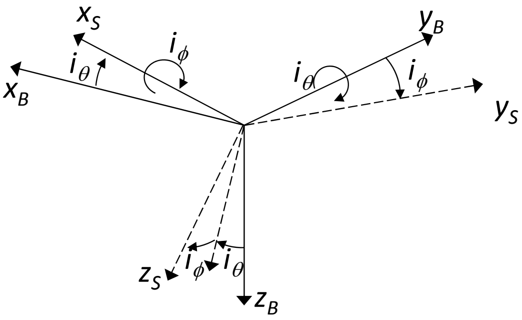

Figure 2.2. Nonrotating shaft reference frame.

The y_R axis of $\mathcal{F}_R$ is aligned with the reference blade, x_R axis is aligned with the reference blade advancing direction, while $z_R = z_S$ is alighed with the z axis of the nonrotating shaft frame, so that its orientation depends on the shaft longitudinal i_θ and lateral i_ϕ tilt. The rotation angle between the nonrotating and rotating shaft coordinate systems is given by the reference blade azimuth position ψ counted from the $-x_S$ axis and positive in the direction of rotation of the rotor, as described in figure 2.3. The transformation between nonrotating and rotating shaft reference frames is given by, when the rotor turns in anticlockwise direction when seen from above,

$$\boldsymbol{L}_{RS} = \begin{bmatrix} \sin(\psi) & \cos(\psi) & 0 \\ -\cos(\psi) & \sin(\psi) & 0 \\ 0 & 0 & 1 \end{bmatrix} \tag{2.6}$$

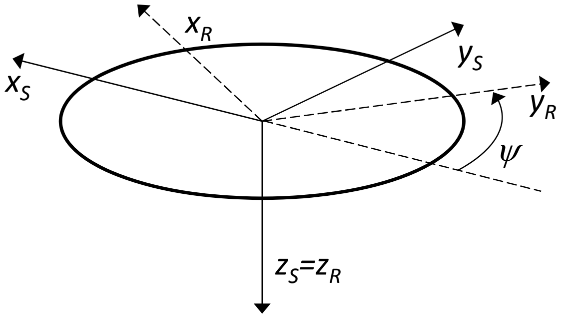

Figure 2.3. Rotating shaft reference frame.

Hub wind reference frame

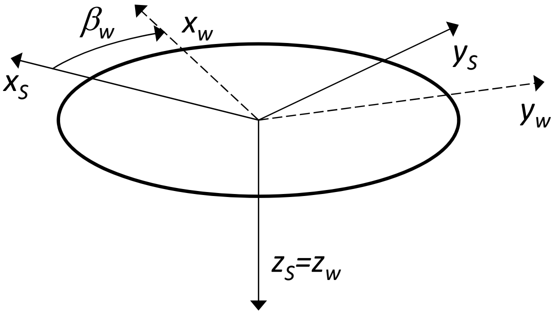

Figure 2.4. Hub wind reference frame.

In models based on tip–path–plane (TPP) dynamics, the aerodynamic loads are more easily written in a hub wind reference frame. As shown in Fig 2.4, the hub wind reference frame $\mathcal{F}_w$ shares the same origin with the nonrotating shaft reference frame (i.e. the hub centre) as well as the same z axis ($z_S = z_w$). The x_w axis points towards the direction of the inplane airflow velocity at the rotor hub centre. The rotation angle β_w between the nonrotating shaft and hub wind reference frames is

$$\beta_w = \sin^{-1}\left(v_S/\sqrt{u_S^2 + v_S^2}\right) \tag{2.7}$$

Finally the rotation matrix $\boldsymbol{L}_{wS}$ between the reference frames is evaluated as

$$\boldsymbol{L}_{wS} = \begin{bmatrix} \cos\beta_w & \sin\beta_w & 0 \\ -\sin\beta_w & \cos\beta_w & 0 \\ 0 & 0 & 1 \end{bmatrix} \tag{2.8}$$

In hub wind axis the components of the airstream speed along the y_w axis is always equal to zero. The velocity along x_w and z_w axes is often written in nondimensional form as

$$\boldsymbol{v}_w^H = \Omega R\,(\mu,\ 0,\ \lambda)^T$$

where μ is the advance ratio, whereas λ is the rotor inflow ratio, which takes into account the uniform inflow speed and the vertical component of the rotor hub speed, $\lambda = w_S/(\Omega R) - \nu$. The nondimensional inflow is $\nu = \nu_0 + (r+e)/R(\nu_c \cos\psi + \nu_s \sin\psi)$. As the velocity is evaluated at the rotor centre the sine and cosine components can be dropped so that $\lambda = w_S/(\Omega R) - \nu_0$. Note that in normal operating conditions the inflow ratio λ is negative and the nondimensional uniform inflow coefficients ν_0 is positive.

Nonrotating and Rotating hub reference frame

In the gimballed rotor, the nonrotating hub (NRH) coordinate system $\mathcal{F}_{NRH}$ $\{x', y'', z_H\}$ has the same origin of the nonrotating shaft system (the hub gimbal centre), but it is tilted with respect to the nonrotating shaft by two rotations: a first rotation of an angle θ_H about the y_S axis, that brings x_S in x' and z_S in z', then a rotation about the x' axis of an angle ϕ_H that brings the y_S axis in y'' and z' in z_H. Finally the rotating hub coordinate system $\mathcal{F}_H$ $\{x_H, y_H, z_H\}$ is rotated from the NRH about z_H of an angle $\psi = \pi/2 - \tilde{\psi}_H$. At $\psi = 0$ the reference blade is in the aft position (similarly to the rotating shaft reference frame), and ψ increases with time in the direction of the rotation.

Blade span

The blade span coordinate system $\mathcal{F}_{b_i}$ with $i = 1, \cdots, N_b$, is centered at the i^{th} blade hinge, in a position $\boldsymbol{r}_R^{R,e} = (0, e, 0)$ in the rotating shaft reference frame with respect to the rotor hub centre, when an articulated rotor is considered, or $\boldsymbol{r}_H^{H,r_c} = (0, r_c, \delta)$ in rotating hub reference frame for a gimballed rotor. The y_b axis is aligned with the blade, the x_b axis is aligned with the blade advancing direction, and z_b completes a right–handed coordinate system. The transformation between the rotating shaft (or rotating hub) and blade span reference frames depends on flap (or coning) β and lag (if present) ζ angles and on the hinge system geometry. For the UH–60A helicopter the lag and flap hinges are assumed as coincident but the lag degree of freedom anticipates the flap one. The transformation matrix is thus given by

$$\boldsymbol{L}_{bR} = \begin{bmatrix} \cos(\zeta) & -\sin(\zeta)\cos(\beta) & \sin(\zeta)\sin(\beta) \\ \sin(\zeta) & \cos(\zeta)\cos(\beta) & -\cos(\zeta)\sin(\beta) \\ 0 & \sin(\beta) & \cos(\beta) \end{bmatrix} \tag{2.9}$$

2.2.5 Tail rotor reference frame

Tail rotor coordinate system is fixed to the vehicle. The origin is placed at the tail rotor centre. The x_T axis is parallel to the x_B axis, z_T axis is aligned with the tail rotor shaft. The tail rotor is canted with respect to the fuselage around the x_T axis. The tail rotor cant angle Γ correspond to the main rotor lateral can angle i_ϕ. The transformation matrix between body and tail reference frame is given by

$$\boldsymbol{L}_{TB} = \begin{bmatrix} 1 & 0 & 0 \\ 0 & \cos(\Gamma) & \sin(\Gamma) \\ 0 & -\sin(\Gamma) & \cos(\Gamma) \end{bmatrix} \tag{2.10}$$

2.3 Equations of motion

The equations of motion of the fuselage are formulated in the body fixed coordinate system, using a Newtonian approach. Assuming a rigid fuselage, the governing equations are

$$m(\dot{\boldsymbol{v}}_B + \boldsymbol{\omega}_B \times \boldsymbol{v}_B) = \boldsymbol{F}_B \tag{2.11}$$

$$\boldsymbol{I}\dot{\boldsymbol{\omega}}_B + \boldsymbol{\omega}_B \times (\boldsymbol{I}\boldsymbol{\omega}_B) = \boldsymbol{M}_B \tag{2.12}$$

with

$$\boldsymbol{v}_B = (u\ v\ w)^T \tag{2.13}$$

$$\boldsymbol{\omega}_B = (p\ q\ r)^T \tag{2.14}$$

$$\boldsymbol{I} = \begin{bmatrix} I_{xx} & 0 & -I_{xz} \\ 0 & I_{yy} & 0 \\ -I_{xz} & 0 & I_{zz} \end{bmatrix} \tag{2.15}$$

$$\boldsymbol{F}_B = (F_x\ F_y\ F_z)^T \tag{2.16}$$

$$\boldsymbol{M}_B = (L\ M\ N)^T \tag{2.17}$$

External forces $\boldsymbol{F}_B$ and moments $\boldsymbol{M}_B$ acting on the fuselage can be divided into the following contributions

- main rotor inertial, elastic and aerodynamic loads, $\boldsymbol{F}_r$ and $\boldsymbol{M}_r$
- fuselage aerodynamic loads, $\boldsymbol{F}_f$ and $\boldsymbol{M}_f$
- horizontal and vertical tail aerodynamic loads, $\boldsymbol{F}_{ht,vt}$ and $\boldsymbol{M}_{ht,vt}$
- tail rotor thrust and moment, $\boldsymbol{F}_{tr}$ and $\boldsymbol{M}_{tr}$
- weight, $\boldsymbol{W}$

so that

$$\boldsymbol{F}_B = \boldsymbol{F}_r + \boldsymbol{F}_f + \boldsymbol{F}_{ht} + \boldsymbol{F}_{vt} + \boldsymbol{F}_{tr} + \boldsymbol{W} \tag{2.18}$$

$$\boldsymbol{M}_B = \boldsymbol{M}_r + \boldsymbol{M}_f + \boldsymbol{M}_{ht} + \boldsymbol{M}_{vt} + \boldsymbol{M}_{tr} \tag{2.19}$$

Note that all the contributions of the helicopter main components $\boldsymbol{F}_x$ and $\boldsymbol{M}_x$ are written without subscript when referred to the body–fixed reference frame. The following paragraphs describe how fuselage, rotor, tail rotor and empennage forces and moments can be evaluated. Some of the models (in particular rotor ones) add states (e.g. blade flap and lag degrees of freedom, and inflow states) to the fuselage rigid body states, $\boldsymbol{x}_f = (u, v, w, p, q, r, \phi, \theta, \psi)^T$.

2.3.1 Fuselage

Until recently, fuselage aerodynamic forces and moments were usually determined by means of wind tunnel testing, with full scale models [69, 70] when possible or with scaled ones [71]. In recent year the developments of computational fluid dynamics (CFD) methods allowed the reduction of wind tunnel testing campaigns by generating most of the data by means of computer simulations. In particular Direct Navier Stokes (DNS) solvers provide good results even including the complex aerodynamic behaviour generated by the rotor [72]. This comes at a very high computational cost which largely exceeds the limits imposed by flight mechanic studies. Therefore the applicability of these techniques is restricted to other areas of study such as fuselage design and helicopter configuration.

As a consequence simpler approaches are used in flight mechanics literature. The simplest ones [5, 11, 73] are based on the description of fuselage drag only by means of equivalent parasite area. This approach is followed even in models where the rotor model is very complex [73]. The fuselage forces are referred to the fuselage aerodynamic centre which is placed in a position $\boldsymbol{r}_B^f$ with respect to the aircraft centre of mass. In this case let u_f,v_f, and w_f be the components of the flow in body reference frame where w_f includes the effect of rotor inflow, so that $w_f = w_B - k_\lambda \lambda_0$ where $k_\lambda = k_\lambda(\boldsymbol{x}_B^H)$ depends on the vertical position of the rotor with respect to the fuselage. Fuselage aerodynamic forces are evaluated as

$$\boldsymbol{F}_f = \begin{bmatrix} -\frac{1}{2}\rho u_f \left|u_f\right| S_x C_{D_x} \\ -\frac{1}{2}\rho v_f \left|v_f\right| S_y C_{D_y} \\ -\frac{1}{2}\rho w_f \left|w_f\right| S_z C_{D_z} \end{bmatrix} \tag{2.20}$$

where S_x, S_y, S_z are the projections of the fuselage area on the frontal, lateral and vertical plane while C_{D_i} with $i = x,\ y,\ z$ is the drag coefficient of the section. The product of $S_i C_{D_i}$ is called the effective flat plate drag. An estimate of these terms can be obtained by a methodology described in Prouty (p. 280) [8], not recalled here. The simple model of Eq. (2.20) takes into account the aerodynamic drag in forward flight, in non symmetrical flight and the main rotor downwash on the fuselage. Fuselage aerodynamic moments can be evaluated as $\boldsymbol{M}_f = \boldsymbol{r}_B^f \times \boldsymbol{F}_f$. In the first phases of the design process, when the final shape of the fuselage and the aerodynamic centre position are unknown, the aerodynamic forces can be evaluated directly at the fuselage centre of mass.

A more complex approach involves the description of the variation of aerodynamic forces (not only drag but also lift and sideforce) and moments as a function of the direction of the impinging flux. This is achieved using the aerodynamic angles $\alpha_f = \arctan\left(w_f/u_f\right)$ and $\beta_f = \arctan\left(v_f/\sqrt{u_f^2 + w_f^2}\right)$, which describe the direction of the flow in body axes. Force and moment coefficients are provided in body or wind reference frame, but depend only on the direct variable (α_f for longitudinal parameters, β_f for lateral-directional ones). The relationship can be described by means of interpolating polynomials [74, 14, 6] or tables [75, 76, 15, 77] accessed trough lookup table functions. The polynomial description is faster but less accurate and cannot describe some local behaviour which conversely can be well represented in tables.

In most of the previous references the longitudinal values (drag, lift and pitch moment) are corrected for small variation of the β_f angle. Large variations of β_f are assumed either unlikely at high speed or possible at low speeds only, when they have a limited impact due to the small dynamic pressure. This assumption is correct for forward flight which is the main objective of most of the studies cited above. A further confirmation of this is given by the fact that aerodynamic coefficients are usually provided for an interval $-90^\circ < \alpha_f < 90^\circ$ and $-30^\circ < \beta_f < 30^\circ$, as in [15], with the notable exception of [6], where data at high angles of attack and sideslip is provided for a generic fuselage shape, and coefficients for normal operating condition are provided for each helicopter studied.

The limited availability of data at high angles of sideslip has a detrimental effect on the ability to represent some important flight conditions. As an example in hover $\alpha_f \approx -90^\circ$ and β_f may vary due to small perturbations from perfectly stationary flight. The results of lateral and rearwards flight are even more biased when a limited set of data is used or data available on narrow ranges are extrapolated.

For this reason for this thesis a complete map of aerodynamic coefficients based on the full α_F and β_f envelope has been developed. When data is not available (i.e. in rearward flight) the database was built on the bases of both empirical considerations [8] and available data of rearward flight [71, 6]. Even when the database is complete for all α_f and β_f values, particular attention needs to be paid for ensuring that the boundary conditions of the database are consistent (e.g. when $\beta_f = \pm 90^\circ$, α_f is not defined but forces and moments in body reference frame have to be close to constant for small perturbations around that particular condition).

This method allows for the evaluation at any time step of fuselage forces and moments in body reference frame as a function of the dynamic pressure and aerodynamic angles. This approach was used to model a UH-60A fuselage based on data published in Refs. [15] and [77].

The final force and moment coefficients are written in the fuselage reference frame (with axes parallel to the body–fixed ones, but centered in the aerodynamic centre) to avoid at any time step the coordinate transformation between wind and fuselage (body) reference frames, where aerodynamic coefficients are evaluated as in [17]. Forces are thus evaluated in the form

$$\boldsymbol{F}_f = \frac{\rho}{2} V_f^2 S_{ref} \begin{bmatrix} C_{A,x_f}(\alpha_f, \beta_f) \\ C_{A,y_f}(\alpha_f, \beta_f) \\ C_{A,x_f}(\alpha_f, \beta_f) \end{bmatrix} \tag{2.21}$$

where S_{ref} is a reference area which is used to scale force coefficients and $V_f = u_f^2 + v_f^2 + w_f^2$. By taking into account the displacement between fuselage aerodynamic centre and CoG, the fuselage aerodynamic moments are evaluated according to the following formula,

$$\boldsymbol{M}_f = \frac{\rho}{2} V_f^2 S_{ref} \ell_{ref} \begin{bmatrix} C_{A,l_f}(\alpha_f, \beta_f) \\ C_{A,m_f}(\alpha_f, \beta_f) \\ C_{A,n_f}(\alpha_f, \beta_f) \end{bmatrix} + \boldsymbol{r}_B^f \times \boldsymbol{F}_f \tag{2.22}$$

where ℓ_{ref} is a reference length (e.g. $\ell_{ref} = R$).

2.3.2 Main rotor

The rotor is the most important element of the helicopter and, as a consequence, its model plays a fundamental role in the description of helicopter flight mechanics. As described in detail is section 2.1, the level of detail introduced in rotor dynamic and aerodynamic description defines the mathematical model complexity and accuracy and therefore its possible fields of use. Provided that the aim of this dissertation is to identify which level of detail is required for particular tasks in rotorcraft flight mechanics analysis (e.g. performance in level flight, handling qualities, etc.), a wide set of rotor models are developed and coupled with the same fuselage aerodynamic model. To allow a modular approach in the development of full rotorcraft simulators, a standard interface was developed between fuselage and rotor models. Furthermore, since the evaluation of inflow speed is strictly related to the rotor operating condition, the inflow model is included in the main rotor model. This is a reasonable choice when a dynamic inflow model is selected, and it becomes mandatory when a static inflow is used, as its evaluation requires an iterative scheme with main rotor thrust.

Chapter 3 describes in great details rotor models including different configurations such as articulated and gimballed rotors. Rotor states dynamic equations as well as force and moment equations are derived for both individual blade and low–order models. In particular the rotor of the UH-60A helicopter is used as a reference for the derivation of the equations of motion of an articulated rotor. If the rotor is described by means of individual blade dynamics with flap, lag, and dynamic twist degrees of freedom, the rotor state is described by

$$\boldsymbol{x}_r = \left(\beta_i, \cdots, \beta_{N_b}, \dot{\beta}_i, \cdots, \dot{\beta}_{N_b}, \zeta_i, \cdots, \zeta_{N_b}, \dot{\zeta}_i, \cdots, \dot{\zeta}_{N_b}, \varphi_i, \cdots, \varphi_{N_b}, \dot{\varphi}_i, \cdots, \dot{\varphi}_{N_b}\right)^T$$

where β_i, ζ_i, and φ_i are the flap, lag, and dynamic twist angles of the i^{th} blade, respectively. Conversely, if the rotor is described by 2^{nd} order TPP dynamics, the rotor state is

$$\boldsymbol{x}_r = \left(a_0, \dot{a}_0, a_1, \dot{a}_1, b_1, \dot{b}_1\right)^T$$

where a_0, a_1, and b_1 are rotor coning, longitudinal and lateral TPP tilt respectively.

2.3.3 Tail rotor

The tail rotor can be modeled as the main rotor, but usually such a level of detail is not necessary as the most important features are rotor thrust and its inflow speed, whereas inplane forces and tail rotor hub moments are often neglected. Simpler models are usually sufficient, such as those based on Bailey coefficients [18], adopted in Refs. [15] and [17], or tip–path–plane models like that proposed by Talbot et al. [14]. The tail rotor model described in [15] and used in this work for the UH–60A model is described later in this section.

In other cases, the tail rotor model is identified from wind tunnel data. One example is represented by K4A-2H tail rotor, which presents a peculiar configuration where the thrust delivered by a ducted fan, or fenestron, is controlled varying rotor rpm rather than blade pitch. Furthermore, the tail rotor is driven by a hydraulic motor. Due to these innovative features, a wind tunnel test campaign was conducted and the results used to identify a mathematical model [78]. Thrust is evaluated as

$$T_{tr} = T_{tr}(n_{tr}, V, \beta_{tr})$$

where n_{tr} represents rotor rpm, V and β_{tr} are speed and angle of sideslip at the tail rotor hub centre, respectively.

The most difficult part in the development of a tail rotor model is often represented by the reliable evaluation of main rotor and fuselage downwash effect on the air impinging on the tail rotor itself. Due to the complex shape of main rotor and fuselage downwash and the fact that the tail rotor enters the downwash region only in a limited speed range, the interaction is usually described by a lookup table as a function of advance ratio μ, rotor skew angle χ and tip–path–plane tilt.

Tail rotor aerodynamic model

Tail rotor forces and moments are evaluated by means of momentum theory, as described in [7]. This technique is computationally far less demanding than individual blade models used for the main rotor. The smaller size and a (relatively) limited impact on vehicle dynamics allow for the employment of such a technique even in high–order models. Tail rotor thrust T_{tr} and inflow intensity ν_{tr} are thus reasonably estimated as a function of collective command $\theta_{0_{tr}}$ at a modest computational cost.

Tail rotor forces and moments are evaluated in tail rotor reference frame, described in section 2.2.5. The velocity of the tail rotor centre $\boldsymbol{v}_{tr} = (u_{tr},\ v_{tr},\ w_{tr})^T$ is given by

$$\boldsymbol{v}_{tr} = \boldsymbol{L}_{TB}\left(\boldsymbol{v}_B^{tr} + \boldsymbol{v}_{\lambda_r} + \boldsymbol{v}_{\lambda_f}\right) = \boldsymbol{L}_{TB}\left(\boldsymbol{v}_B - \boldsymbol{r}_B^{tr} \times \boldsymbol{\omega}_B + \boldsymbol{v}_{\lambda_r} + \boldsymbol{v}_{\lambda_f}\right) \tag{2.23}$$

where $\boldsymbol{r}_B^{tr}$ is the vector which connects fuselage centre of mass with tail rotor hub centre and $\boldsymbol{v}_{\lambda_r}$ and $\boldsymbol{v}_{\lambda_f}$ are the induced velocities due to interaction with main rotor and fuselage, respectively. Given the tail rotor radius R_{tr} and its angular speed Ω_{tr}, the tail rotor advance ratio μ_{tr} is given by

$$\mu_{tr} = \frac{\sqrt{u_{tr}^2 + v_{tr}^2}}{\Omega_{tr} R_{tr}} \tag{2.24}$$

The inflow coefficient is

$$\lambda_{tr} = \frac{w_{tr}}{\Omega_{tr} R_{tr}} - \nu_{tr} \tag{2.25}$$

Tail rotor thrust T_{tr} is evaluated as

$$T_{tr} = 2\rho\pi R_{tr}^4 \nu_{tr} \Omega_{tr}^2 v_{T_{tr}} \tag{2.26}$$

where

$$v_{T_{tr}} = \sqrt{\mu_{tr}^2 + \lambda_{tr}^2} \tag{2.27}$$

Tail rotor blade pitch is given by

$$\Theta'_{tr} = \theta_{0_{tr}} - T_{tr}\frac{\partial a_0}{\partial T_{tr}} \tan \delta_{3_{tr}} + \Theta_{bias} \tag{2.28}$$

where $\theta_{0_{tr}}$ is the collective command, a_0 is the tail rotor coning angle, $\delta_{3_{tr}}$ is the tail rotor flapping hinge offset angle, and Θ_{bias} is the blade pitch correction due to linear twist.

The inflow dynamics is derived with the same approach used for main rotor inflow and described in Section 2.4. Only the uniform nondimensional term ν_{tr} is considered for the tail rotor, which evolves according to the first-order dynamics

$$\frac{1}{\Omega_{tr} v_{T_{tr}}} \frac{4}{3\pi} \dot{\nu}_{tr} + \nu_{tr} = \frac{1}{2 v_{T_{tr}}} C_{T_{tr}} \tag{2.29}$$

where $C_{T_{tr}}$ is the tail rotor thrust coefficient. To evaluate rotor thrust, Bailey coefficients [18] are introduced

$$\begin{aligned} t_{3.1} &= \tfrac{1}{2} B_{tr}^2 + \tfrac{1}{4} \mu_{tr}^2 \\ t_{3.2} &= \tfrac{1}{3} B_{tr}^3 + \tfrac{1}{2} B_{tr} \mu_{tr}^2 \\ t_{3.3} &= \tfrac{1}{4} B_{tr}^4 + \tfrac{1}{4} B_{tr}^2 \mu_{tr}^2 \end{aligned} \tag{2.30}$$

where B_{tr} is the blade tip loss factor. According to Bailey, the thrust coefficient can be expressed as

$$C_{T_{tr}} = v_{T_{tr}} \sigma_{tr} a_{tr} \frac{\mu_{tr} t_{3.1} + \Theta'_{tr} t_{3.2} + \theta_{1t} t_{3.3}}{2 v_{T_{tr}} + \frac{\sigma_{tr} a_{tr}}{2} t_{3.1}} \tag{2.31}$$

where σ_{tr} is tail rotor solidity, a_{tr} is the tail rotor airfoil linear lift coefficient, whereas θ_{1t} represents blade twist.

Taking into account only the aerodynamic contribution, tail rotor forces and moments in body axes are evaluated as

$$\begin{aligned} X_{tr} &= 0 \\ Y_{tr} &= T_{tr} \sin \Gamma_{tr} \\ Z_{tr} &= -T_{tr} \cos \Gamma_{tr} \end{aligned} \tag{2.32}$$

$$\begin{bmatrix} L_{tr} \\ M_{tr} \\ N_{tr} \end{bmatrix} = \begin{bmatrix} x_{tr} \\ y_{tr} \\ z_{tr} \end{bmatrix} \times \begin{bmatrix} X_{tr} \\ Y_{tr} \\ Z_{tr} \end{bmatrix} \tag{2.33}$$

2.3.4 Empennage

Helicopters with a conventional configuration (single main and tail rotors) usually include a vertical tail to lessen the yaw moment balancing effort required to the tail rotor at higher speed, thus saving power as the tail rotor requires less thrust. Furthermore a horizontal stabilizer is often introduced to improve longitudinal stability in forward flight. Sometimes the horizontal stabilizer can be tilted at low speed to decrease the drag of the downwash impinging on the stabilizer.

Horizontal tail aerodynamics

The horizontal tail is modeled as a low aspect ratio finite wing. Lift and drag are given by the classic expressions

$$L_{ht} = \frac{\rho}{2} V_{ht}^2 S_{ht} C_L(\alpha_{ht}) \tag{2.34}$$

$$D_{ht} = \frac{\rho}{2} V_{ht}^2 S_{ht} C_D(\alpha_{ht}) \tag{2.35}$$

where $V_{ht} = \sqrt{u_{ht}^2 + v_{ht}^2 + w_{ht}^2}$ is the wind velocity on the surface, and α_{ht} is the angle of attack of the horizontal tail. $C_L(\alpha_{ht})$ and $C_D(\alpha_{ht})$ are evaluated from lookup tables based on wind tunnel tests or high fidelity CFD simulations of the airfoil used or wing configuration.

The main rotor wake and fuselage downwash affect the tailplane aerodynamics in a complex way. To model this influence accurately an extensive analysis of the wake would be required. This can be accomplished by wind tunnel testing or CFD simulation. If data is available (as in the case of UH–60A) the airspeed V_{ht} at the horizontal tail can be evaluated as

$$\boldsymbol{v}_{ht} = (u_{ht},\ v_{ht},\ w_{ht})^T = (\boldsymbol{v}_B + \boldsymbol{\omega}_B \times \boldsymbol{r}_B^{ht}) k_{ht} + \boldsymbol{v}_{ht_\lambda} \tag{2.36}$$

where $\boldsymbol{r}_B^{ht}$ is the position of the horizontal tail aerodynamic centre with respect to the aircraft centre of mass, $\boldsymbol{v}_{ht_\lambda}$ collects the influence of the rotor and fuselage wake onto the horizontal tail, and k_{ht} is a factor accounting for the loss of dynamic pressure.

When the detailed data on the effects of wakes on the tailplane is not available, some simplifying assumptions can be used to derive an approximate solution: the wake has constant radius and the induced flow has uniform speed; no circulation effects are considered, and the inflow is considered parallel to the rotor shaft. Under these simplifying assumptions, the main rotor wake affects the aerodynamic characteristics on the horizontal tail only in a limited range of flying conditions: under or above some forward flight velocities, the wake does not impinges on the tail. This effect is modeled with a inflow velocity intensity factor k_i [79, 6] for the inflow velocity $\lambda_0 = \nu_0 \Omega R$ in the expression of $\boldsymbol{v}_{ht_\lambda} = (0,\ 0,\ k_i \lambda_0)^T$.

The coefficient k_i is equal to 1 when the tail is completely immersed in the wake, it is equal to zero when the tail plane is outside of the wake. These values are interpolated at intermediate values when there is only a partial interaction. As shown in the sketch of Fig. 2.5 the wake angle is

$$\tan \chi_u = \frac{u}{v_i - w} \tag{2.37}$$

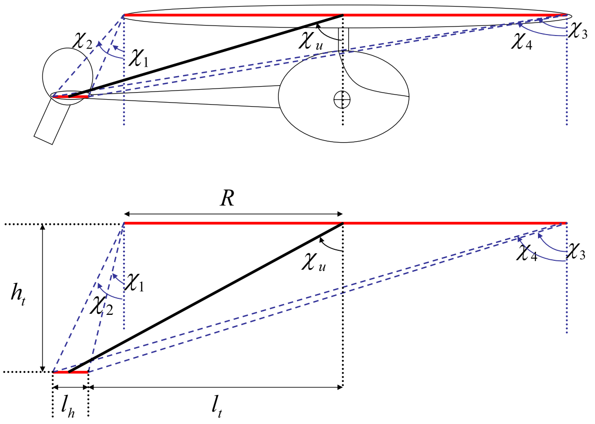

Figure 2.5. Interference of the main rotor wake with the horizontal stabilizer at different skew angles.

Let

$$\tan\chi_1 = \frac{l_t - R}{h_t} \tag{2.38}$$

$$\tan\chi_2 = \frac{l_t - R + l_h}{h_t} \tag{2.39}$$

$$\tan\chi_3 = \frac{l_t + R}{h_t} \tag{2.40}$$

$$\tan\chi_4 = \frac{l_t + R + l_h}{h_t} \tag{2.41}$$

If the wake angle is lower that χ_1, or larger than χ_4, the wake does not impinge on the horizontal tail and $k_i = 0$. If χ_u is between χ_2 and χ_3 than $k_i = 1$, if χ_u is between χ_1 and χ_2 or χ_3 e χ_4 then $k_i = (\chi_u - \chi_1)/(\chi_2 - \chi_1)$ in the first case, and $k_i = (\chi_u - \chi_4)/(\chi_3 - \chi_4)$ in the second one.

Lift and drag are then projected onto the body frame so that

$$\boldsymbol{F}_{ht} = \begin{bmatrix} \cos\alpha_{ht}\cos\beta_{ht} & -\cos\alpha_{ht}\sin\beta_{ht} & -\sin\alpha_{ht} \\ \sin\beta_{ht} & \cos\beta_{ht} & 0 \\ \sin\alpha_{ht}\cos\beta_{ht} & -\sin\alpha_{ht}\sin\beta_{ht} & \cos\alpha_{ht} \end{bmatrix} \begin{bmatrix} -D_{ht} \\ 0 \\ -L_{ht} \end{bmatrix} \tag{2.42}$$

where

$$\begin{aligned} \alpha_{ht} = & \tan^{-1}\left(w_{ht}/\left|u_{ht}\right|\right) \\ \beta_{ht} = & \tan^{-1}\left(v_{ht}/\sqrt{u_{ht}^2 + w_{ht}^2}\right) \end{aligned} \tag{2.43}$$

Finally horizontal tail moment in body reference frame can be evaluated as $\boldsymbol{M}_{ht} = \boldsymbol{r}_B^{ht} \times \boldsymbol{F}_{ht}$.

Vertical tail aerodynamics

A similar approach can be used for the vertical tail even if in this case the rotor wake effect is less important and the fuselage sidewash plays a more significant role. Vertical lift and drag are modeled as

$$\begin{aligned} L_{vt} &= \frac{\rho}{2} V_{vt}^2 S_{vt} C_L(\beta_{vt}) && (2.44) \\ D_{vt} &= \frac{\rho}{2} V_{vt}^2 S_{vt} C_D(\beta_{vt}) && (2.45) \end{aligned}$$

where β_{vt} is the angle of sideslip and is evaluated as

$$\begin{aligned} \alpha_{vt} = &\ \tan^{-1}\left(w_{vt}/\left|u_{vt}\right|\right) \\ \beta_{vt} = &\ \tan^{-1}\left(v_{vt}/\sqrt{u_{vt}^2 + w_{vt}^2}\right) \end{aligned} \qquad (2.46)$$

and $V_{vt} = \sqrt{u_{vt}^2 + v_{vt}^2 + w_{vt}^2}$ is the wind velocity on the surface. Its components are evaluated as

$$\boldsymbol{v}_{vt} = (u_{vt},\ v_{vt},\ w_{vt})^T = (\boldsymbol{v}_B + \boldsymbol{\omega}_B \times \boldsymbol{r}_B^{vt}) k_{vt} + \boldsymbol{v}_{vt_\lambda} \qquad (2.47)$$

where, as in the horizontal tail case, $\boldsymbol{v}_{vt_\lambda}$ collects the influence of rotor and fuselage wakes onto the vertical tail while k_{vt} is a factor accounting for the loss of dynamic pressure. Vertical tail forces in body axes are evaluated as

$$\boldsymbol{F}_{vt} = \begin{bmatrix} \cos\alpha_{vt}\cos\beta_{vt} & -\cos\alpha_{vt}\sin\beta_{vt} & -\sin\alpha_{vt} \\ \sin\beta_{vt} & \cos\beta_{vt} & 0 \\ \sin\alpha_{vt}\cos\beta_{vt} & -\sin\alpha_{vt}\sin\beta_{vt} & \cos\alpha_{vt} \end{bmatrix} \begin{bmatrix} -D_{vt} \\ L_{vt} \\ 0 \end{bmatrix} \qquad (2.48)$$

while moment in body reference frame can be evaluated as $\boldsymbol{M}_{vt} = \boldsymbol{r}_B^{vt} \times \boldsymbol{F}_{vt}$.

2.4 Inflow

The frequencies of inflow dynamic modes are of the same order of magnitude as those of rotor blade flapping modes. It is therefore important to use a dynamic model for rotor inflow to analyse the stability characteristics of the helicopter. There are many possible inflow models for the representation of induced velocities at and near a lifting rotor: uniform or nonuniform, static or dynamic, finite-state or distribute parameters models. A survey of nonuniform inflow models can be found in Ref. [80].

The Peters-Ha [81] inflow model adopted here is a three-state unsteady inflow model that treats the inflow variables as dynamic states. It is widely used in flight dynamics applications. A more detailed modelling approach could have been achieved considering higher order inflow harmonics [82], but the added complexity was considered not necessary for the analysis of performance and handling qualities carried out in this study.

The inflow velocity field is modeled with a three-state model, and the flow is considered orthogonal to the tip–path–plane. The three states represent the uniform component of induced velocity on the rotor disk ν_0 and the first harmonic terms, namely, the longitudinal and the lateral components of a triangular velocity distribution, ν_c and ν_s, respectively.

The velocity field is therefore described as

$$v_i(x,\psi) = \Omega R\left[\nu_0 + x\nu_s \sin\psi + x\nu_c \cos\psi\right] \tag{2.49}$$

where $x = (e+r)/R$ is the nondimensional position along blade span in articulated rotors, whereas it is $x = (r_c + r)/R$ for gimballed ones.

The equations of motion are first order, linear, time-variant ordinary differential equations, which are written in hub wind axes in the form [81]

$$\frac{1}{\Omega}\boldsymbol{M}_\lambda \begin{bmatrix} \dot{\nu}_0 \\ \dot{\nu}'_s \\ \dot{\nu}'_c \end{bmatrix} + \boldsymbol{L}_\lambda^{-1} \begin{bmatrix} \nu_0 \\ \nu'_s \\ \nu'_c \end{bmatrix} = \begin{bmatrix} C_T \\ C'_l \\ C'_m \end{bmatrix}_{aero} \tag{2.50}$$

where the apparent mass matrix $\boldsymbol{M}_\lambda$ is given by

$$\boldsymbol{M}_\lambda = \begin{bmatrix} \frac{8}{3\pi} & 0 & 0 \\ 0 & -\frac{16}{45\pi} & 0 \\ 0 & 0 & -\frac{16}{45\pi} \end{bmatrix} \tag{2.51}$$

The static gain matrix $\boldsymbol{L}_\lambda$ is

$$\boldsymbol{L}_\lambda = \begin{bmatrix} \frac{1}{2v_T} & 0 & \frac{15\pi}{64 v_M}\tan\frac{\chi}{2} \\ 0 & -\frac{4}{v_M(1+\cos\chi)} & 0 \\ \frac{15\pi}{64 v_T}\tan\frac{\chi}{2} & 0 & -\frac{4 cos\chi}{v_M(1+\cos\chi)} \end{bmatrix} \tag{2.52}$$

where

$\mu = \sqrt{u_S^2 + v_S^2}/(\Omega R)$ is the advance ratio in wind axes

$\lambda = -w_S/(\Omega R) + \nu_0$ represents total inflow through the rotor

$v_T = \sqrt{\lambda^2 + \mu^2}$ is the resultant flow through the rotor

$\chi = \arctan\frac{\mu}{\lambda}$ provides the wake skew angle and

$v_M = \frac{\mu^2 + \lambda(\lambda + \nu_0)}{v_T}$ represents the mass-flow parameter due to cyclic disturbances

The model is expressed in hub wind axes. It is thus necessary to transform the longitudinal and lateral inflow terms into the nonrotating shaft frame, with a rotation β_w described by the coordinate transformation matrix $\tilde{\boldsymbol{L}}_{wS}$ (see section 2.2.4).

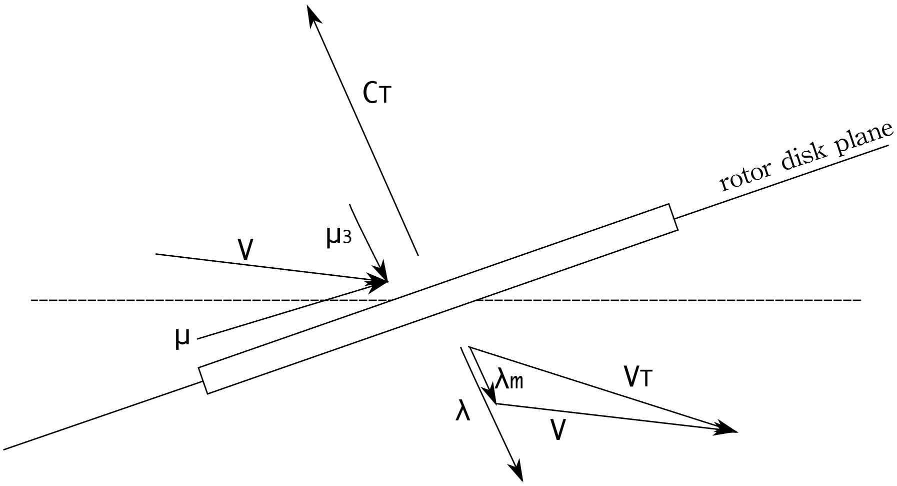

Figure 2.6. Inflow diagram in wind axes.

$$\tilde{\boldsymbol{L}}_{wS} = \begin{bmatrix} 1 & 0 & 0 \\ 0 & \cos\beta_w & \sin\beta_w \\ 0 & -\sin\beta_w & \cos\beta_w \end{bmatrix} \tag{2.53}$$

with $\beta_w = \sin^{-1}\left(v_S/\sqrt{u_S^2 + v_S^2}\right)$. The following formulation is thus obtained

$$\frac{1}{\Omega}\boldsymbol{M}_\lambda \tilde{\boldsymbol{L}}_{wS} \begin{bmatrix} \dot{\nu}_0 \\ \dot{\nu}_s \\ \dot{\nu}_c \end{bmatrix} + \boldsymbol{L}^{-1}\tilde{\boldsymbol{L}}_{wS} \begin{bmatrix} \nu_0 \\ \nu_s \\ \nu_c \end{bmatrix} = \tilde{\boldsymbol{L}}_{wS} \begin{bmatrix} C_T \\ C_l \\ C_m \end{bmatrix}_A \tag{2.54}$$

with thrust, pitch and roll moments coefficients defined as

$$C_T = \frac{T}{\rho\pi R^2(\Omega R)^2} \tag{2.55}$$

$$C_l = \frac{L_A}{\rho\pi R^3(\Omega R)^2} \tag{2.56}$$

$$C_m = \frac{M_A}{\rho\pi R^3(\Omega R)^2} \tag{2.57}$$

$$\tag{2.58}$$

in the nonrotating shaft frame. The evaluation of rotor thrust and aerodynamic moments is described in detail in Chapter 3.

2.5 Assembly of equations of motion

The system of nonlinear differential equations of motion presented in this chapter together with rotor equations described in detail in chapter 3 is not explicitly written in first–order state variable form. In fact when the rotor is described by 2nd order dynamics, some rotor states are inertially coupled with fuselage ones. As a consequence derivatives of velocity variables appear both on the left and on the right hand side in some equations. In the most general form, the model can be written in 1st order form as

$$\dot{\boldsymbol{x}} = \tilde{\boldsymbol{f}}\left(\dot{\boldsymbol{x}},\ \boldsymbol{x},\ \boldsymbol{u},\ t\right) = \boldsymbol{f}^*\left(\boldsymbol{x},\ \boldsymbol{u},\ t\right) - \tilde{\mathbb{M}}\left(\boldsymbol{x},\ \boldsymbol{u},\ t\right)\dot{\boldsymbol{x}} \tag{2.59}$$

where $\boldsymbol{x}$ collects all rotorcraft states as

$$\boldsymbol{x} = (\boldsymbol{x}_f^T, \boldsymbol{x}_r^T, \boldsymbol{x}_\lambda^T, \boldsymbol{x}_{tr}^T)^T \tag{2.60}$$

assuming that $\boldsymbol{x}_f$, $\boldsymbol{x}_r$, $\boldsymbol{x}_\lambda$, and $\boldsymbol{x}_{tr}$ are fuselage, main rotor, inflow and tail rotor states, respectively, and $\boldsymbol{u} = (\theta_0,\ A_{1_s},\ B_{1_s},\ \theta_{0_{tr}})^T$ is the command vector. The matrix $\tilde{\mathbb{M}}$ collects all the coefficients of derivatives of velocity variables in the right hand side of $\tilde{\boldsymbol{f}}$ set of equations. Conversely $\boldsymbol{f}^*$ collects all the terms which do not depend on state derivatives. To integrate in time, the system is rewritten in first–order form as

$$\mathbb{M}\left(\boldsymbol{x},\ \boldsymbol{u},\ t\right)\dot{\boldsymbol{x}} = \boldsymbol{f}\left(\boldsymbol{x},\ \boldsymbol{u},\ t\right) \tag{2.61}$$

so that it can be solved as

$$\dot{\boldsymbol{x}} = \mathbb{M}^{-1}\boldsymbol{f}\left(\boldsymbol{x},\ \boldsymbol{u},\ t\right) \tag{2.62}$$

The inertial coupling matrix $\mathbb{M} = \mathbb{I} + \tilde{\mathbb{M}}$ is divided for practical reasons into two diagonal blocks

$$\mathbb{M} = \begin{bmatrix} \mathbb{M}_c & \mathbf{0} \\ \mathbf{0} & \mathbb{M}_{uc} \end{bmatrix} \tag{2.63}$$

where the block $\mathbb{M}_c$ is relative to the inertially coupled states ($\boldsymbol{x}_c$), and the block $\mathbb{M}_{uc}$ which contains uncoupled states ($\boldsymbol{x}_{uc}$). The latter block $\mathbb{M}_{uc}$ is diagonal and does not need to be inverted for the solution of the system, while $\mathbb{M}_c$ is a full–order matrix which needs to be inverted at every time step in order to evaluate state derivatives. When second order dynamics is used to describe the rotor, rotor state accelerations (either flap,lag, TPP tilt or hub tilt) are inertially coupled with rigid body velocity derivatives. The coupled states vector can be assembled as

$$\boldsymbol{x}_c = \left(u_B, v_B, w_B, p_B, q_B, r_B,\ \boldsymbol{x}_{r_c}^T\right)^T \tag{2.64}$$

where $\boldsymbol{x}_{r_c}$ contains the inertially coupled states of the rotor which depend both on the rotor configuration (articulated, teetering, gimballed, etc.) and on modelling approach (individual blade, TPP dynamics, etc.). As an example, in an articulated rotor with flap and lag degrees of freedom described by means of individual blade dynamics, the coupled states are $\boldsymbol{x}_{r_c} = \left(\dot{\beta}_i, \cdots, \dot{\beta}_{N_b}, \dot{\zeta}_i, \cdots, \dot{\zeta}_{N_b}\right)^T$. For a 4-bladed rotor ($N_b = 4$) the $\boldsymbol{x}_c$ vector of coupled states counts 14 elements (6 for the fuselage and 8 for the rotor) and as a consequence $\mathbb{M}_c$ is a 14x14 matrix (which needs to be inverted at every time step). If the same rotor configuration is described by means of 2nd order TPP dynamics (see Sect. 3.2), the vector of rotor coupled states is $\boldsymbol{x}_{r_c} = \left(\dot{a}_0, \dot{a}_1, \dot{b}_1\right)^T$ and $\boldsymbol{x}_c$ counts only 9 elements.

The vector of uncoupled states $\boldsymbol{x}_{uc}$ includes fuselage attitude angles as well as all the rotor and inflow states which are not inertially coupled. As an example, for the articulated rotor with flap and lag degrees of freedom described by individual blade dynamics the uncoupled state vector is given by

$$\boldsymbol{x}_{uc} = (\phi_B, \theta_B, \psi_B, \beta_i, \cdots, \beta_{N_b}, \zeta_i, \cdots, \zeta_{N_b}, \nu_0, \nu_s, \nu_c, \nu_{tr}) \tag{2.65}$$

The matrix $\mathbb{M}_c$ is the results of the contributions of rigid-body fuselage equations of motion and of rotor equations, and is given by

$$\mathbb{M}_c = \mathbb{M}_{f_c} + \mathbb{M}_{r_c} \tag{2.66}$$

The contribution of the fuselage equations of motion is limited to rigid body states $\boldsymbol{x}_{f_c} = (u_B, v_B, w_B, p_B, q_B, r_B)^T$ and is given by

$$\mathbb{M}_{f_c} = \begin{bmatrix} m\mathbb{I}_3 & \mathbf{0} \\ \mathbf{0} & \boldsymbol{I} \end{bmatrix} \tag{2.67}$$

where m is the fuselage mass, $\mathbb{I}_3$ is a 3x3 identity matrix, and $\boldsymbol{I}$ is the helicopter inertia tensor. All the terms in the $\mathbb{M}_{r_c}$ matrix are derived in Chapter 3 for both individual blade and TPP dynamics model for an articulated rotor configuration. A similar description of a two–bladed gimballed rotor is presented in [78].

Chapter 3

Rotor models

As already discussed in Section 2.3.2, the rotor is the most important element of the helicopter and, as a consequence, its model plays a fundamental role in the description of helicopter flight mechanics. The present chapter is aimed at presenting the development of mathematical models for the description of different rotor configuration. First an articulated rotor is considered and both individual blade dynamics and tip–path–plane lower order models are developed for the UH-60A main rotor. In the sequel a similar approach is followed for the description of a teetering rotor. At the end of the chapter, the development of low order models for a two–bladed gimballed rotor is discussed in detail, whereas a high order model for this configuration is discussed in detail in [78].

In order to develop an approach to helicopter modelling as modular as possible, the rotor models developed for this analysis share the same inputs and outputs. The same fuselage model can thus be interfaced with rotor models with different levels of complexity. Standard inputs for the rotor models are

- linear $\boldsymbol{v}_B^H$ and angular $\boldsymbol{\omega}_B^H$ speed at rotor hub centre in body reference frame;
- rotor states $\boldsymbol{x}_r$;
- inflow states $\boldsymbol{x}_\lambda$;
- main rotor commands $\boldsymbol{\Theta} = (\theta_0,\ A_{1_S},\ B_{1_S})^T$;
- rotor configuration data (including lag damper, if required);
- air density and temperature.

Standard outputs for the rotor models are:

- rotor forces $\boldsymbol{F}_{r_S}$ and moments $\boldsymbol{M}_{r_S}$ in nonrotating shaft reference frame.
- rotor states derivatives $\dot{\boldsymbol{x}}_r$ or right hand side of the equation $\mathbb{M}_r \dot{\boldsymbol{x}}_r = \boldsymbol{f}(\boldsymbol{x}_r)$ in case of dynamic coupling between rotor and fuselage states;
- mass matrix of coupled states derivatives $\mathbb{M}_r$ if needed;

- inflow states derivatives $\dot{\boldsymbol{x}}_\lambda$;
- wake skew angle χ;
- coning β_c, longitudinal β_{lng}, and lateral β_{lat} flapping multiblade coordinates, in case individual blade models are considered.

One of the helicopters whose details and configuration data are more easily available, as well as the baseline of many studies in rotorcraft aeromechanics (including the present one) is the UH–60A [15]. It features a single main rotor with articulated blades. The availability of a rather complete set of data, and a considerable amount of publicly available studies, including flight tests, made it the ideal choice for the present analysis. Both individual blade and tip–path–plane models were developed for this vehicle. The following sections describe in details the derivation of these models.

3.1 Individual blade models

This chapter describes the procedure for the evaluation of blade dynamics together with forces and moments transmitted by the rotor to the fuselage for an individual blade model. The procedure is then implemented for the UH-60A rotor, a fully articulated rotor with coincident flap and lag hinge axes. The same set of equations can be used (with minor variations) to describe an articulated rotor with a different hinge sequence or a teetering rotor. An equivalent flap hinge with elastic restraint can be used for representing, with a coarser accuracy, the dynamic response of a rigid (hingeless) rotor.

A Newtonian approach is adopted, based on the description of a generic blade element motion, where the blade element speed in blade span reference frame determines the relative velocity of the airfoil on which the blade element is fixed and as a consequence the aerodynamic loads. Equations of motion for both blade flap and lag degrees of freedom are thus derived, together with rotor inertial loads from the acceleration of the generic blade element.

3.1.1 Assumptions

In the development of the individual blade model for an articulated rotor, the most important simplifying assumptions are:

1. rotor blades are assumed rigid in the flap and lag direction;
2. blade mass is assumed to be concentrated along the blade span axes;
3. blade torsional degree of freedom is modeled empirically as a dynamic twist affecting independently each blade;
4. aerodynamic moments developed by the airfoil around the blade pitch axis are neglected;

5. flap and lag hinges are assumed to be coincident, with the flap rotation following the lag rotation in the sequence;

6. No pitch–flap coupling K_{PC} is included in the model. Nonetheless the introduction of pitch–flap coupling has no direct effect on the inertial coupling of rotor and fuselage equations of motion (its effect is mainly aerodynamic and given by the reduction of the blade geometric pitch θ_G when flap is increased);

7. The weight of the blade is assumed negligible and it is thus not included in the flap and lag equations of motion;

8. Aerodynamic loads on the blade are evaluated by means of blade element theory;

9. The calculation of aerodynamic loads on each blade section is based on quasi–steady aerodynamics; the only unsteady aerodynamic effect is represented by the dynamic inflow (see Section 2.4);

10. Compressibility effects on rotor blades are accounted for, when data are available from wind tunnel testing (e.g. for the UH–60A airfoil a complete database is found in Ref. [15] for airfoil lift and drag coefficients for $-180\,\mathrm{deg} < \alpha < 180\,\mathrm{deg}$ and Mach number ranging from 0 to 1); if experimental data are not available, Prandtl-Glauert correction can be used;

11. Dynamic stall effects are not included; static stall is accounted for in the lift and drag coefficients.

3.1.2 Blade element kinematics

To describe the motion of a generic blade element, the motion of rotor hub is related to the motion of the helicopter centre of mass first, then the motion of the blade element with respect to the rotor centre is added. In this process the selection of the correct reference frames is fundamental in achieving a formulation as compact as possible. The equations are derived only in vector form. The components are presented only for the most important variables. The starting points in the description of blade element motion are the linear ($\boldsymbol{v}_B$) and angular ($\boldsymbol{\omega}_B$) velocities of the helicopter in body–fixed reference frame, where

$$\boldsymbol{v}_B = (u \quad v \quad w)^T \tag{3.1}$$

$$\boldsymbol{\omega}_B = (p \quad q \quad r)^T \tag{3.2}$$

To evaluate the linear and angular speed of the hub centre in nonrotating frame, the position vector $\boldsymbol{r}_B^H$ of the hub centre in body frame is required,

$$\boldsymbol{r}_B^H = (x_H \quad y_H \quad z_H)^T \tag{3.3}$$

Using the transformation matrix $\boldsymbol{L}_{SB}$ from body to nonrotating shaft reference frames (see section 2.2.4) the linear and angular speed in nonrotating shaft are evaluated as

$$\boldsymbol{v}_S = (u_S, v_S, w_S)^T = \boldsymbol{L}_{SB}\boldsymbol{v}_B^S = \boldsymbol{L}_{SB}\left(\boldsymbol{v}_B + \boldsymbol{\omega}_B \times \boldsymbol{r}_B^H\right) \tag{3.4}$$

$$\boldsymbol{\omega}_S = (p_S, q_S, r_S)^T = \boldsymbol{L}_{SB}\boldsymbol{\omega}_B^S = \boldsymbol{L}_{SB}\boldsymbol{\omega}_B \tag{3.5}$$

The body frame and the nonrotating frame are both fixed to the fuselage. The only difference lies in the shaft tilt angles i_θ and i_ϕ in the longitudinal and lateral plane respectively. The relative rotation speed $\boldsymbol{\omega}_B^{S/B}$ between the two reference frames is equal to zero and the transformation matrix $\boldsymbol{L}_{SB}$ is constant in time. In the description of blade motion and rotor force and moments the components of linear and angular motion in the nonrotating frame are used in place of the components in body frame to save the overhead of the rotation matrix and radius between centre of gravity and hub centre.

The rotating shaft reference frame shares the same origin with the nonrotating one, but the relative angular speed between the two frames $\boldsymbol{\omega}_R^{R/S}$ is determined by the rotor angular speed Ω. For an anticlockwise rotation of the rotor when seen from above, $\boldsymbol{\omega}_R^{R/S} = (0{,}0, -\Omega)^T$. Linear and angular speed in rotating frame are

$$\boldsymbol{v}_R = \boldsymbol{L}_{RS}\boldsymbol{v}_S \tag{3.6}$$

$$\boldsymbol{\omega}_R = \boldsymbol{L}_{RS}\boldsymbol{\omega}_S^S + \boldsymbol{\omega}_R^{R/S} = \boldsymbol{L}_{RS}\boldsymbol{\omega}_S^S + (0{,}0, -\Omega)^T \tag{3.7}$$

To evaluate the speed of a generic blade element, the position vector $\boldsymbol{r}_R^{R,b}$ with respect to the origin of the rotating shaft reference frame is defined for a generic blade element. This vector is characterized by two parts: the first part describes the distance of the flap/lag hinge from the rotor centre along blade span, whereas the second term accounts for the radial distance r of the blade element from the hinge in blade reference frame:

$$\boldsymbol{r}_R^{R,b} = (0, e{,}0) + \boldsymbol{L}_{Rb}\,(0, r, 0)^T \tag{3.8}$$

The speed of the generic blade element in rotating shaft frame is thus given by

$$\boldsymbol{v}_R^b = \boldsymbol{v}_R + \boldsymbol{\omega}_R \times \boldsymbol{r}_R^{R,b} + \dot{\boldsymbol{r}}_R^{R,b} \tag{3.9}$$

Finally, the speed of the blade element in blade span reference frame can be evaluated as:

$$\boldsymbol{v}_b = \mathbf{L}_{bR}\boldsymbol{v}_R^b \tag{3.10}$$

To determine rotor inertial force, blade element acceleration is required. Among the reference frames available, the nonrotating shaft is preferred, as it allows to write the equations in the most compact form. To evaluate the acceleration of the blade element, as a first step the blade element speed is transformed into nonrotating shaft components:

$$\boldsymbol{v}_S^b = \boldsymbol{L}_{SR}\boldsymbol{v}_R^b \tag{3.11}$$

Then the acceleration is evaluated as

$$\boldsymbol{a}_S^b = \dot{\boldsymbol{v}}_S^b + \boldsymbol{\omega}_S \times \boldsymbol{v}_S^b \tag{3.12}$$

The derivation of blade equations of motion requires the blade element accelerations written in blade span reference frame,

$$\boldsymbol{a}_b^b = \boldsymbol{L}_{bR}\boldsymbol{L}_{RS}\boldsymbol{a}_S^b \tag{3.13}$$

3.1.3 Aerodynamic loads

Equation (3.10) can be modified in order to include the speed of the blade element with respect to the surrounding air including the effect of the inflow. In this respect, the usual approach presented in the literature (see for example [17]) is to write the components of $\boldsymbol{v}_b$ in terms of tangential, radial and vertical terms,

$$\boldsymbol{v}_b = U_T\boldsymbol{i}_b + U_R\boldsymbol{j}_b + U_P\boldsymbol{k}_b \tag{3.14}$$

where the components U_T,U_R, and U_P are

$$\begin{aligned}
U_T = \;& [u_S \sin(\psi+\zeta) + v_S\cos(\psi+\zeta)] - e(r_S-\Omega)\cos\zeta \\
& +r\left\{\dot{\zeta}\cos\beta + \sin\beta\left[p_S\cos(\psi+\zeta) - q_S\sin(\psi+\zeta)\right]\right. \\
& \left. -(r_S-\Omega)\cos\beta\right\} \\[1ex]
U_R = \;& -\left[u_S\cos\beta\cos(\psi+\zeta) - v_S\cos\beta\sin(\psi+\zeta) + w_S\sin\beta\right] \\
& -e\left[\sin\beta(q_S\cos\psi + p_S\sin\psi) + (r_S-\Omega)\cos\beta\sin\zeta\right] + U_{R_\lambda} \\[1ex]
U_P = \;& [-u_S\sin\beta\cos(\psi+\zeta) + v_S\sin\beta\sin(\psi+\zeta) + w_S\cos\beta] \\
& +e\left[\cos\beta(q_S\cos\psi + p_S\sin\psi) - (r_S-\Omega)\sin\beta\sin\zeta\right] \\
& +r\left[-\dot{\beta} + q_S\cos(\psi+\zeta) + p_S\sin(\psi+\zeta)\right] + U_{P_\lambda}
\end{aligned} \tag{3.15}$$

The contribution of the inflow to the local velocity components assuming a three–states triangular inflow model (described in section 2.4) are

$$\begin{aligned}
U_{R_\lambda} = \;& \Omega R\sin\beta\,\{-\nu_0 - \epsilon(\nu_c\cos\psi + \nu_s\sin\psi) \\
& -r/R[\nu_c\cos(\psi+\zeta) + \nu_s\sin(\psi+\zeta)]\} \\[1ex]
U_{P_\lambda} = \;& \Omega R\cos\beta\,\{-\nu_0 - \epsilon(\nu_c\cos\psi + \nu_s\sin\psi) \\
& -r/R[\nu_c\cos(\psi+\zeta) + \nu_s\sin(\psi+\zeta)]\}
\end{aligned} \tag{3.16}$$

When the effects of inflow are included in the vertical and radial speed, the angle of attack on the blade element can be evaluated as

$$\alpha = \theta_G + \tan^{-1}\frac{U_P}{U_T}; \tag{3.17}$$

where the geometric pitch θ_G at the desired blade element is given by

$$\theta_G = \theta_0 + A_{1_S} \cos\psi + B_{1_S} \sin\psi + \theta_{tw} + \theta_{dt}; \tag{3.18}$$

In the most general case blade twist is a nonlinear function $\theta_{tw} = \theta_{tw}(r)$ which can be obtained from lookup tables as a function of blade element radial position. The dynamic twist (when included in the model) is a function of radial position through a shape function in the spatial domain and of the generalized coordinate φ_1, which describe the motion in time, $\theta_{dt} = \theta_{dt}(r, \varphi_1)$. The dynamic twist is described in detail in section 3.1.6.

The direction φ of the airstream imping on the blade element in blade span reference frame is given by

$$\varphi = \tan^{-1} \frac{U_P}{U_T} \tag{3.19}$$

The lift and drag coefficient (C_L and C_D respectively) are read from lookup tables as a function of angle of attack α and Mach number. The blade is divided into N_s elements with width Δy_b and area $S_b = c\Delta y_b$, which centre is at a distance r_k from the blade hinges. If the elements are all equal, $\Delta y_b = (R - e)/N_s$. The aerodynamic loads acting on the k^{th} blade elements are

$$\boldsymbol{F}_{A_k} = \begin{pmatrix} \frac{1}{2}\rho V^2 S_b \left(-C_D \cos\varphi - C_L \sin\varphi\right) \\ 0 \\ \frac{1}{2}\rho V^2 S_b \left(C_D \sin\varphi - C_L \cos\varphi\right) \end{pmatrix} \tag{3.20}$$

where $V^2 = U_P^2 + U_T^2$. The aerodynamic load is assumed to act at the midpoint $\boldsymbol{r}_k$ of the blade element. The total aerodynamic shear forces at the hinge and the aerodynamic moments about the hinge in blade span frame for the i^{th} blade are given by

$$\begin{aligned} \boldsymbol{F}_{A,i_b} &= \textstyle\sum_{k=1}^{N_s} \boldsymbol{F}_{A_k} \\ \boldsymbol{M}_{A,i_b} &= \left(M_{\beta_A},\ 0,\ M_{\zeta_A}\right)^T = \textstyle\sum_{k=1}^{N_s} \boldsymbol{r}_k \times \boldsymbol{F}_{A_k} \end{aligned} \tag{3.21}$$

The force and moments of the i^{th} blade in non rotating shaft can be evaluated as

$$\begin{aligned} \boldsymbol{F}_{A,i_S} &= \boldsymbol{L}_S R \boldsymbol{L}_{Rb_i} \boldsymbol{F}_{A,i_b} \\ \boldsymbol{M}_{A,i_S} &= \boldsymbol{L}_S R \left[\boldsymbol{r}_R^e \times \left(\boldsymbol{L}_{Rb_i} \boldsymbol{F}_{A,i_b}\right)\right] \end{aligned} \tag{3.22}$$

3.1.4 Inertial loads

The inertia forces are derived integrating blade accelerations in the nonrotating frame, as described in Eq. (3.12). Shear forces are transmitted to the rotor hub through the hinges. The components of the inertia forces $\boldsymbol{F}_{I_S} = F_{I,x_S} \boldsymbol{i}_S + F_{I,y_S} \boldsymbol{j}_S + F_{I,z_S} \boldsymbol{k}_S$ for each blade can be evaluated as

$$\begin{aligned} F_{I,x_S} &= \textstyle\int_e^R \rho_b \, a_{S,x} \, dr \\ F_{I,y_S} &= \textstyle\int_e^R \rho_b \, a_{S,y} \, dr \\ F_{I,z_S} &= \textstyle\int_e^R \rho_b \, a_{S,z} \, dr \end{aligned} \tag{3.23}$$

After the computation is performed, the components of the rotor inertia force in nonrotating frame for the i^{th} blade are

$$
\begin{aligned}
F_{I,x_S} = \quad & m_b \Big\langle -\dot{u}_S - e \Big\{ \cos\psi_i \Big[(\Omega - r_S)^2 + q_S^2 \Big] - \sin\psi_i \left(\dot{r}_S - q_S p_S \right) \Big\} \Big\rangle \\
& +S_b \Big\langle \sin\beta_i \Big[\dot{q}_S + r_S p_S - \ddot{\beta}_i \cos\left(\psi_i + \zeta_i\right) - 2 \Big(r_S - \Omega - \dot{\zeta}_i \Big) \dot{\beta}_i \sin\left(\psi_i + \zeta_i\right) \Big] \\
& - \cos\beta_i \left\{ \left[\Big(r_S - \Omega - \dot{\zeta}_i \Big)^2 + \dot{\beta}_i^2 + q_S^2 \right] \cos\left(\psi_i + \zeta_i\right) - \Big(\dot{r}_S - \ddot{\zeta}_i - q_S p_S \Big) \sin\left(\psi_i + \zeta_i\right) \right\} \\
& +2\dot{\beta}_i \cos\beta q_S \Big\rangle \\
\\
F_{I,y_S} = \quad & m_b \Big\langle -\dot{v}_S - e \Big\{ -\sin\psi_i \Big[(\Omega - r_S)^2 + p_S^2 \Big] - \cos\psi_i \left(\dot{r}_S + q_S p_S \right) \Big\} \Big\rangle \\
& +S_b \Big\langle \sin\beta_i \Big[-\dot{p}_S + q_S r_S + \ddot{\beta}_i \sin\left(\psi_i + \zeta_i\right) - 2 \Big(r_S - \Omega - \dot{\zeta}_i \Big) \dot{\beta}_i \cos\left(\psi_i + \zeta_i\right) \Big] \\
& \cos\beta_i \left\{ \left[\Big(r_S - \Omega - \dot{\zeta}_i \Big)^2 + \dot{\beta}_i^2 + p_S^2 \right] \sin\left(\psi_i + \zeta_i\right) + \Big(\dot{r}_S - \ddot{\zeta}_i + q_S p_S \Big) \cos\left(\psi_i + \zeta_i\right) \right\} \\
& -2\dot{\beta}_i \cos\beta p_S \Big\rangle ; \\
\\
F_{I,z_S} = \quad & m_b \left\{ -\dot{w}_S - e [\dot{p}_S \sin\psi_i + \dot{q}_S \cos\psi_i + (2\Omega - r_S)(p_S \cos\psi_i - q_S \sin\psi_i)] \right\} \\
& +S_b \Big\langle \cos\beta_i \Big\{ -\dot{p}_S \sin(\psi_i + \zeta_i) - \dot{q}_S \cos(\psi_i + \zeta_i) + \ddot{\beta}_i \\
& +2\dot{\beta}_i \sin\beta_i [p_S \sin(\psi_i + \zeta_i) + q_S \cos(\psi_i + \zeta_i)] - \sin\beta_i (p_S^2 + q_S^2 + \dot{\beta}_i^2) \Big\} \\
& +(r_S - 2\Omega - 2\dot{\zeta}_i)[p_S \cos(\psi_i + \zeta_i) - q_S \sin(\psi_i + \zeta_i)] \Big\rangle
\end{aligned}
\tag{3.24}
$$

The main rotor inertial forces include terms which depend on state highest order derivatives. For this reason these terms need to be grouped in an inertial coupling matrix $\mathbb{M}$ (see Section 2.5). As a consequence, Eq. 3.24 can be rearranged in the form

$$
\begin{aligned}
\mathbb{M}_{FI,x} \dot{\boldsymbol{x}}_c = \quad & f_{FI,x} \\
\mathbb{M}_{FI,y} \dot{\boldsymbol{x}}_c = \quad & f_{FI,y} \\
\mathbb{M}_{FI,z} \dot{\boldsymbol{x}}_c = \quad & f_{FI,z}
\end{aligned}
\tag{3.25}
$$

where $\mathbb{M}_{FI,i}$ with $i = x, y, z$ is the array which contains the term of the inertial forces depending on highest order state derivatives and $\dot{\boldsymbol{x}}_c$ is the vector which contains the derivatives of the velocity variables which are inertially coupled. These states are expressed in body fixed reference frame and the vector of coupled velocity variables for an articulated rotor with N_b blades is given by

$$
\boldsymbol{x}_c = \Big(u_B, v_B, w_B, p_B, q_B, r_B, \dot{\beta}_i, \cdots, \dot{\beta}_{N_b}, \dot{\zeta}_i, \cdots, \dot{\zeta}_{N_b} \Big)^T \tag{3.26}
$$

Equation (3.25) and all the following equations in the present section are referred to the i^{th} blade. No i subscript is included in the formula in order to maintain the notation as simple as possible. The coupling matrices can be reorganized as follows

$$\begin{aligned}
\mathbb{M}_{FI,x} = \;& \Big(\mathbb{M}_{FI,x_V}\boldsymbol{L}_{SB},\ \mathbb{M}_{FI,x_V}\boldsymbol{L}_{SB}\tilde{\boldsymbol{r}}_B^H + \mathbb{M}_{FI,x_\omega}\boldsymbol{L}_{SB},\ \mathbb{M}_{FI,x_\beta},\ \mathbb{M}_{FI,x_\zeta}\Big)\\
\mathbb{M}_{FI,y} = \;& \Big(\mathbb{M}_{FI,y_V}\boldsymbol{L}_{SB},\ \mathbb{M}_{FI,y_V}\boldsymbol{L}_{SB}\tilde{\boldsymbol{r}}_B^H + \mathbb{M}_{FI,y_\omega}\boldsymbol{L}_{SB},\ \mathbb{M}_{FI,y_\beta},\ \mathbb{M}_{FI,y_\zeta}\Big)\\
\mathbb{M}_{FI,z} = \;& \Big(\mathbb{M}_{FI,z_V}\boldsymbol{L}_{SB},\ \mathbb{M}_{FI,z_V}\boldsymbol{L}_{SB}\tilde{\boldsymbol{r}}_B^H + \mathbb{M}_{FI,z_\omega}\boldsymbol{L}_{SB},\ \mathbb{M}_{FI,z_\beta},\ \mathbb{M}_{FI,z_\zeta}\Big)
\end{aligned} \tag{3.27}$$

The right hand side of the inertia forces $f_{FI,i}$ with $i = x, y, z$ is thus given by

$$\begin{aligned}
f_{FI,x} = \;& m_b\left\langle -q_Sw_S + r_Sv_S - e\left\{\cos\psi_i[(\Omega - r_S)^2 + q_S^2] + \sin\psi_i q_Sp_S\right\}\right\rangle\\
& + S_b\Big\langle -\cos\beta_i\Big\{\Big[(r_S - \Omega - \dot{\zeta}_i)^2 + \dot{\beta}_i^2 + q_S^2\Big]\cos(\psi_i + \zeta_i) + q_Sp_S\sin(\psi_i + \zeta_i)\Big\}\\
& + \sin\beta_i\Big[r_Sp_S - 2(r_S - \Omega - \dot{\zeta}_i)\dot{\beta}_i\sin(\psi_i + \zeta_i)\Big] + 2\dot{\beta}_i\cos\beta q_S\Big\rangle\\[2ex]
f_{FI,y} = \;& m_b\left\langle -r_Su_S + p_Sw_S - e\left\{-\sin\psi_i[(\Omega - r_S)^2 + p_S^2] - \cos\psi_i q_Sp_S\right\}\right\rangle\\
& + S_b\Big\langle \cos\beta_i\Big\{\Big[(r_S - \Omega - \dot{\zeta}_i)^2 + \dot{\beta}_i^2 + p_S^2\Big]\sin(\psi_i + \zeta_i) + q_Sp_S\cos(\psi_i + \zeta_i)\Big\}\\
& + \sin\beta_i\Big[q_Sr_S - 2(r_S - \Omega - \dot{\zeta}_i)\dot{\beta}_i\cos(\psi_i + \zeta_i)\Big] - 2\dot{\beta}_i\cos\beta p_S\Big\rangle\\[2ex]
f_{FI,z} = \;& m_b\left[-v_Sp_S + u_Sq_S - e(2\Omega - r_S)(p_S\cos\psi_i - q_S\sin\psi_i)\right]\\
& + S_b\Big\langle \cos\beta_i\Big\{(r_S - 2\Omega - 2\dot{\zeta}_i)\left[p_S\cos(\psi_i + \zeta_i) - q_S\sin(\psi_i + \zeta_i)\right]\Big\}\\
& + 2\dot{\beta}_i\sin\beta_i\left[p_S\sin(\psi_i + \zeta_i) + q_S\cos(\psi_i + \zeta_i)\right] - \sin\beta_i(p_S^2 + q_S^2 + \dot{\beta}_i^2))\Big\rangle
\end{aligned} \tag{3.28}$$

whereas the components of the mass matrix $\mathbb{M}_{FI,i_j}$ for $i = x,\ y,\ z$ and $j = V,\ \omega,\ \beta,\ \zeta$ are

$$\begin{aligned}
\mathbb{M}_{FI,x_V} = \;& (m_b,\ 0,\ 0)\\
\mathbb{M}_{FI,x_\omega} = \;& (0,\ -S_b\sin\beta_i,\ -S_b\cos\beta_i\sin(\psi_i + \zeta_i) - em_b\sin\psi_i)\\
\mathbb{M}_{FI,x_\beta} = \;& S_b\sin\beta_i\cos(\psi_i + \zeta_i)\\
\mathbb{M}_{FI,x_\zeta} = \;& S_b\cos\beta_i\sin(\psi_i + \zeta_i)\\
\mathbb{M}_{FI,y_V} = \;& (0,\ m_b,\ 0)\\
\mathbb{M}_{FI,y_\omega} = \;& (S_b\sin\beta_i,\ 0,\ -S_b\cos\beta_i\cos(\psi_i + \zeta_i) - em_b\cos\psi_i)\\
\mathbb{M}_{FI,y_\beta} = \;& S_b\sin\beta_i\sin(\psi_i + \zeta_i)\\
\mathbb{M}_{FI,y_\zeta} = \;& S_b\cos\beta_i\cos(\psi_i + \zeta_i)\\
\mathbb{M}_{FI,z_V} = \;& (0,\ 0,\ m_b)\\
\mathbb{M}_{FI,z_\omega} = \;& (S_b\cos\beta_i\sin(\psi_i + \zeta_i) + em_b\sin\psi_i,\ S_b\cos\beta_i\cos(\psi_i + \zeta_i) + em_b\cos\psi_i,\ 0)\\
\mathbb{M}_{FI,z_\beta} = \;& -S_b\cos\beta_i\\
\mathbb{M}_{FI,z_\zeta} = \;& 0
\end{aligned} \tag{3.29}$$

Inertial moments are generated by the inertial shear forces that the blade transmit to the hub at the flap/lag hinge, which is placed at a distance e with respect to the hub centre. Rotor inertial moments $\boldsymbol{M}_{I_S} = M_{I,x_S}\boldsymbol{i}_S + M_{I,y_S}\boldsymbol{j}_S + M_{I,z_S}\boldsymbol{k}_S$ in the nonrotating frame are thus evaluated as

$$\boldsymbol{M}_{I_S} = \boldsymbol{r}_S^e \times \boldsymbol{F}_{I_S} \tag{3.30}$$

where the position of the flap/lag hinge in nonrotating frame is $\boldsymbol{r}_S^e = (-e\cos\psi_i,\ e\sin\psi_i,\ 0)^T$. As in the inertial force case, the inertial moments contain state derivatives and thus can be rewritten as

$$\begin{bmatrix} \mathbb{M}_{MI,x} \\ \mathbb{M}_{MI,y} \\ \mathbb{M}_{MI,z} \end{bmatrix} \dot{\boldsymbol{x}}_c = \begin{bmatrix} f_{MI,x} \\ f_{MI,y} \\ f_{MI,z} \end{bmatrix} = \boldsymbol{r}_S^e \times \begin{bmatrix} \boldsymbol{f}_{FI,x} \\ \boldsymbol{f}_{FI,y} \\ \boldsymbol{f}_{FI,z} \end{bmatrix} \tag{3.31}$$

where

$$\begin{bmatrix} \mathbb{M}_{MI,x} \\ \mathbb{M}_{MI,y} \\ \mathbb{M}_{MI,z} \end{bmatrix} = \boldsymbol{r}_S^e \times \begin{bmatrix} \mathbb{M}_{FI,x} \\ \mathbb{M}_{FI,y} \\ \mathbb{M}_{FI,z} \end{bmatrix} \tag{3.32}$$

The i$^{\text{th}}$ blade inertial forces and moments can be summed up as:

$$\begin{aligned} \mathbb{M}_{FI,i}\dot{\boldsymbol{x}}_c = \boldsymbol{F}_{I,i_S} = \boldsymbol{f}_{FI} \\ \mathbb{M}_{MI,i}\dot{\boldsymbol{x}}_c = \boldsymbol{M}_{I,i_S} = \boldsymbol{f}_{MI} \end{aligned} \tag{3.33}$$

3.1.5 Blade equations of motion

The derivation of the blade equations of motion for articulated blades follows the approach proposed in Refs. [15, 17]. The flap and lag equations of motion are formulated by enforcing moment balance around the hinges. The applied moments can be divided into aerodynamic moments (M_{β_A} and M_{ζ_A}), inertial moments (M_{β_I} and M_{ζ_I}), hinge spring moments (M_{β_K} and M_{ζ_K}), and lag damper moments ($M_{\beta_{LD}}$ and $M_{\zeta_{LD}}$). The moment balance can be expressed as

$$\begin{aligned} M_{\beta_A} + M_{\beta_I} + M_{\beta_K} + M_{\beta_{ld}} &= 0 \\ M_{\zeta_A} + M_{\zeta_I} + M_{\zeta_K} + M_{\zeta_{ld}} &= 0 \end{aligned} \tag{3.34}$$

The expressions for aerodynamic moments are derived in section 3.1.3 whereas lag damper loads are presented in section 3.1.7. The inertial moments are derived by integrating the contribution of the acceleration of each differential blade element dr along blade span. If we define ρ_b as the linear mass density of the blade and take the acceleration of the blade element in blade span reference frame $\boldsymbol{a}_b^b$, as described in Eq. (3.13), the moment of inertial forces is given by

$$\begin{aligned} M_{\beta_I} &= -\int_e^R r\ \rho_b\ a_z\ dr \\ M_{\zeta_I} &= -\int_e^R r\ \rho_b\ a_x\ dr \end{aligned} \tag{3.35}$$

where a_x and a_z are the components of the acceleration $\boldsymbol{a}_b^b = a_x\boldsymbol{i}_b + a_y\boldsymbol{j}_b + \boldsymbol{k}_b$ along x and z axes evaluated in Eq. (3.13). The equations are written including the hinge stiffness term for the seek of generality. The UH-60A helicopter has no springs in the flap and lead/lag hinges and as a consequence no contribution of stiffness in the flap and lag equations. The resulting equation for the flap degree of freedom for the i^{th} blade is:

$$
\begin{aligned}
I_b\ddot{\beta}_i = \quad & S_b \langle \cos\beta_i \left\{ \ddot{w}_S + e \left[\dot{p}_S \sin\psi_i + \dot{q}_S \cos\psi_i + 2\Omega \left(p_S \cos\psi_i - q_S \sin\psi_i \right) \right] \right\} \\
& + \sin\beta_i \cos\zeta_i \Big[\dot{v}_S \sin\psi_i - \dot{u}_S \cos\psi_i - e \left(r_S - \Omega \right)^2 \Big] \Big\rangle \\
& + I_b \{ \dot{p}_S \sin\left(\psi_i + \zeta_i\right) + \dot{q}_S \cos\left(\psi_i + \zeta_i\right) \\
& + \cos\beta_i^2 \Big[\cos\zeta_i - 2 \left(\dot{\zeta}_i + \Omega \right) \left(q_S \sin\psi_i - p_S \cos\psi_i \right) \\
& - \sin\zeta_i 2\Omega \left(p_S \sin\psi_i + q_S \cos\psi_i \right)] \\
& - \sin\beta_i \cos\beta_i \left(r_S - \Omega - \dot{\zeta} \right)^2 \Big\} \\
& - M_{\beta_{ld}} - M_{\beta_A} - M_{\beta_K}
\end{aligned}
\tag{3.36}
$$

For the lag degree of freedom one gets

$$
\begin{aligned}
I_b \cos\beta_i \ddot{\zeta}_i = \quad & S_b \Big\{ \sin\zeta_i \Big[-\dot{u}_S \cos\psi_i + \dot{v}_S \sin\psi_i - e \left(r_S - \Omega \right)^2 \Big] \\
& + \cos\zeta_i \left(-\dot{u}_S \sin\psi_i - \dot{v}_S \cos\psi_i + e\dot{r}_S \right) \} \\
& + I_b \Big\{ \sin\beta_i \Big[2\dot{\beta}_i \left(\Omega + \dot{\zeta}_i - r_S \right) - \dot{p}_S \cos\left(\psi_i + \zeta_i\right) + \dot{q}_S \sin\left(\psi_i + \zeta_i\right) \Big] \\
& + \cos\beta_i \dot{r}_S + 2 \cos\beta_i \dot{beta}_i \left[\cos\zeta_i \left(q_S \sin\psi_i - p_S \cos\psi_i \right) \right. \\
& \left. + \sin\zeta_i \left(p_S \sin\psi_i + q_S \cos\psi_i \right) \right] \} \\
& - M_{\zeta_{ld}} - M_{\zeta_A} - M_{\zeta_K}
\end{aligned}
\tag{3.37}
$$

These equations can not be directly used in the simulation, as flap and lag accelerations depend on the derivative of rigid body velocity variables, that is, flap and lag dynamics are inertially coupled to fuselage degrees of freedom, as outlined in section 2.5. As in the previous section dedicated to the inertial forces and moments, the elements of the coupling matrix here described are referred to the i^{th} blade. A subscript i is omitted for the seek of conciseness. The flap and lag equation can be cast in matrix form as

$$
\begin{aligned}
\mathbb{M}_{\beta} \dot{\boldsymbol{x}}_c = \quad & f_{\beta} \\
\mathbb{M}_{\zeta} \dot{\boldsymbol{x}}_c = \quad & f_{\zeta}
\end{aligned}
\tag{3.38}
$$

where the coupling matrices $\mathbb{M}_{\beta}$ and $\mathbb{M}_{\zeta}$ are given by:

$$
\begin{aligned}
\mathbb{M}_{\beta} = \quad & \left(\mathbb{M}_{\beta_V} \boldsymbol{L}_{SB},\ \mathbb{M}_{\beta_V} \boldsymbol{L}_{SB} \tilde{\boldsymbol{r}}_B^H + \mathbb{M}_{\beta_\omega} \boldsymbol{L}_{SB},\ \mathbb{M}_{\beta_\beta},\ \mathbb{M}_{\beta_\zeta} \right) \\
\mathbb{M}_{\zeta} = \quad & \left(\mathbb{M}_{\zeta_V} \boldsymbol{L}_{SB},\ \mathbb{M}_{\zeta_V} \boldsymbol{L}_{SB} \tilde{\boldsymbol{r}}_B^H + \mathbb{M}_{\zeta_\omega} \boldsymbol{L}_{SB},\ \mathbb{M}_{\zeta_\beta},\ \mathbb{M}_{\zeta_\zeta} \right)
\end{aligned}
\tag{3.39}
$$

and the state derivative vector is the same as Eq. (3.26).The right hand side of the flap equations is thus given by

$$
\begin{aligned}
f_{\beta} = \quad & S_b \Big[2\Omega e \cos\beta_i \left(p_S \cos\psi_i - q_S \sin\psi_i \right) + \sin\beta_i - e \cos\zeta_i \left(r_S - \Omega \right)^2 \\
& + \left(-p_S w_S + r_S u_S \right) \sin\beta_i \cos\zeta_i \sin\psi_i + \left(-q_S u_S + p_S v_S \right) \cos\beta_i \\
& - \left(-r_S v_S + q_S w_S \right) \sin\beta_i \cos\zeta_i \cos\psi_i] \\
& + I_b \Big[\cos\beta_i^2 - 2 \cos\zeta_i \left(\dot{\zeta}_i + \Omega \right) \left(q_S \sin\psi_i - p_S \cos\psi_i \right) - \sin\beta_i \cos\beta_i \left(r_S - \Omega - \dot{\zeta}_i \right)^2 \\
& - \cos\beta_i^2 \sin\zeta_i 2\Omega \left(p_S \sin\psi_i + q_S \cos\psi_i \right)] + M_{\beta_{ld}} - M_{\beta_A}
\end{aligned}
\tag{3.40}
$$

For the lag equation one gets

$$\begin{aligned} f_\zeta = \; & -S_b\left[-e\sin\zeta_i(r_S-\Omega)^2-(q_Sw_S-r_Sv_S)\sin(\psi_1+\zeta_1)-(r_Su_S-p_Sw_S)\cos(\psi_1+\zeta_1)\right] \\ & -I_b\sin\beta_i\Big\{2\dot\beta_i\left(\Omega+\dot\zeta_i-r_S\right) \\ & +2\cos\beta_i\dot\beta_i\left[\cos\zeta_i\left(q_S\sin\psi_i-p_S\cos\psi_i\right)+\sin\zeta_i\left(p_S\sin\psi_i+q_S\cos\psi_i\right)\right]\Big\} \\ & -M_{\zeta_{ld}}+M_{\zeta_A} \end{aligned} \tag{3.41}$$

The elements $\mathbb{M}_{j_k}$ of the coupling matrices, with $j=\beta,\ \zeta$ and $k=V,\ \omega,\ \beta,\ \zeta$ for the i^{th} blade are

$$\begin{aligned} \mathbb{M}_{\beta_V} &= (S_b\sin\beta_i\cos\zeta_i\cos\psi_i,\ -S_b\sin\beta_i\cos\zeta_i\sin\psi_i,\ -S_b\cos\beta_i) \\ \mathbb{M}_{\beta_\omega} &= (-eS_b\cos\beta_i\sin\psi_i-I_b\sin(\psi_i+\zeta_i),\ -eS_b\cos\beta_i\cos\psi_i-I_b\cos(\psi_i+\zeta_i),\ 0) \\ \mathbb{M}_{\beta_\beta} &= I_b \\ \mathbb{M}_{\beta_\zeta} &= 0 \end{aligned} \tag{3.42}$$

and

$$\begin{aligned} \mathbb{M}_{\zeta_V} &= (-S_b\sin(\psi_i+\zeta_i),\ -S_b\cos(\psi_i+\zeta_i),\ 0) \\ \mathbb{M}_{\zeta_\omega} &= (-I_b\sin\beta_i\cos(\psi_i+\zeta_i),\ I_b\sin\beta_i\sin(\psi_i+\zeta_i),\ I_b\cos\beta_i+eS_b\cos\zeta_i) \\ \mathbb{M}_{\zeta_\beta} &= 0 \\ \mathbb{M}_{\zeta_\zeta} &= -I_b\cos\beta_i \end{aligned} \tag{3.43}$$

3.1.6 Dynamic twist

Together with pilot control (θ_0, A_{1_S} and B_{1_S}) and built–in twist (θ_{tw}), the local feathering angle $\theta_G(r)$ of the section at station r along the blade span is affected by aerodynamic loads, that twist the rotor blades. The value of θ_G is thus given by

$$\theta_G=\theta_0+A_{1_S}\cos\psi+B_{1_S}\cos\psi+\theta_{tw}+\theta_{dt}; \tag{3.44}$$

The dynamic twist θ_{dt} is expressed in terms of the product of a shape function times a generalized state variable as

$$\theta_{dt}=\varphi\left[0.28+0.72\sin\left(\epsilon+r/R\right)\right] \tag{3.45}$$

The dynamics of φ is described in terms of a second order dynamical system, so that the evolution of θ_{dt} is described by two states (twist amplitude and twist rate). The dynamic twist is driven by the x and z components of the aerodynamic load on the blade F_A:

$$\frac{\ddot\varphi\left(i\right)}{\omega_\theta^2}+\frac{2\zeta_\theta}{\omega_\theta}\dot\varphi\left(i\right)+\varphi\left(i\right)=K_\theta\sqrt{F_{Ax}^2+F_{Az}^2}\quad for\quad i=1,...,N_b \tag{3.46}$$

where

$$\begin{aligned}\zeta_\theta =&\quad 0.3\\ \omega_\theta =&\quad 23.63\\ K_\theta =&\quad -1.17\cdot 10^{-5} - 1.72\cdot 10^{-8}(u_B - 51.42)\end{aligned}$$

K_θ is expressed in rad/N and is bounded, to $-2.04\cdot 10^{-6} \leq K_\theta \leq -1.17\cdot 10^{-5}$ so that the twist is always negative. As a consequence, when dynamic twist is accounted for, the rotor requires more collective pitch to generate a given force compared to the case when dynamic twist is neglected. To convert the constant K_θ to metric system, and therefor be measured in rad/N, it must be multiplied by 0.0039.

The dynamic twist equation can be divided into two first order differential equations, assuming $\varphi_1 = \varphi$ and $\varphi_2 = \dot{\varphi}$, Eq. 3.46 can be cast as

$$\begin{aligned}\dot{\varphi}_1 =&\quad \varphi_2\\ \dot{\varphi}_2 =&\quad \omega_\theta^2\left(K_\theta\sqrt{F_{Ax}^2 + F_{Az}^2} - \varphi_1\right) - 2\zeta_\theta\omega_\theta\varphi_2\end{aligned} \tag{3.47}$$

3.1.7 Lag damper

The lag damper model used in the present analysis is taken from Ref. [15]. Figure 3.1 presents the lag damper geometry, the reference frames involved in the analysis as well as all the main features such as the lag damper attachment points on the hub and blade sides.

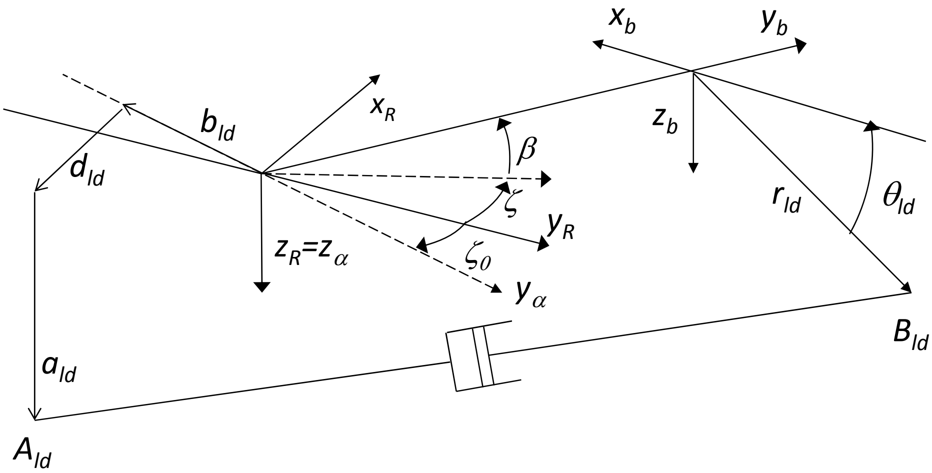

Figure 3.1. UH-60A Lag damper geometry.

To describe the lag damper, the attention should be focused on the relative motion of the two attach points: A_{ld} on the rotor hub, B_{ld} on the rotor blade. The present formulation is based on the peculiar geometry of the UH-60A lag damper, but the same approach can be used for any helicopter given the knowledge of its geometry.

For the description of lag damper geometry, a new reference frame, named α, is defined. This reference frame is centred at the flap/lag hinge (as the blade span one) and is rotated ζ_0 around the z axis with respect to the rotating shaft frame. The rotation matrix $L_{\alpha R}$ between the rotating and the α reference frames is given by

$$L_{\alpha R} = \begin{bmatrix} \cos\zeta_0 & \sin\zeta_0 & 0 \\ -\sin\zeta_0 & \cos\zeta_0 & 0 \\ 0 & 0 & 1 \end{bmatrix} \tag{3.48}$$

The position $\boldsymbol{r}_\alpha^{c,A_{ld}}$ of the lag damper attach point on the rotor hub A_{ld} with respect to the flap/lag hinge in the α reference frame is given by

$$\boldsymbol{r}_\alpha^{c,A_{ld}} = (-d_{ld}, -b_{ld}, a_{ld})^T \tag{3.49}$$

The position $\boldsymbol{r}_b^{c,B_{ld}}$ of the lag damper attach point on the blade B_{ld} with respect to the flap/lag hinge in the blade span reference frame is equal to:

$$\boldsymbol{r}_b^{c,B_{ld}} = (-r_{ld}\cos\theta_{ld}, c_{ld}, r_{ld}\sin\theta_{ld})^T \tag{3.50}$$

where a_{ld}, b_{ld}, c_{ld}, d_{ld}, r_{ld}, θ_{ld} are parameters which define the geometry of the lag damper. The attach point A_{ld} in blade reference frame is evaluated as

$$\boldsymbol{r}_b^{c,A_{ld}} = L_{bR} L_{R\alpha} \boldsymbol{r}_\alpha^{c,A_{ld}} \tag{3.51}$$

where its components are

$$\boldsymbol{r}_b^{c,A_{ld}} = \begin{pmatrix} b_{ld}\sin(\zeta+\zeta_0) - d_{ld}\cos(\zeta+\zeta_0) \\ -b_{ld}\cos\beta\cos(\zeta+\zeta_0) - d_{ld}\cos\beta\sin(\zeta+\zeta_0) - a_{ld}\sin\beta \\ -b_{ld}\sin\beta\cos(\zeta+\zeta_0) - d_{ld}\sin\beta\sin(\zeta+\zeta_0) + a_{ld}\cos\beta \end{pmatrix} \tag{3.52}$$

The vector which connects the two lag damper attach points is evaluated as $\boldsymbol{r}_b^{B_{ld},A_{ld}} = \boldsymbol{r}_b^{c,A_{ld}} - \boldsymbol{r}_b^{c,B_{ld}}$ and its length is equal to $l_{ld} = \left\|\boldsymbol{r}_b^{B_{ld},A_{ld}}\right\|$. As the lag damper force is proportional to its speed, its deformation speed $\boldsymbol{v}_b^{B_{ld},A_{ld}}$ is given by

$$\boldsymbol{v}_b^{B_{ld},A_{ld}} = \begin{pmatrix} b_{ld}\dot\zeta\cos(\zeta+\zeta_0) + d_{ld}\dot\zeta\sin(\zeta+\zeta_0) - r_{ld}\dot\theta_{ld}\sin\theta_{ld} \\ \\ b_{ld}\dot\beta\sin\beta\cos(\zeta+\zeta_0) + b_{ld}\dot\zeta\cos\beta\sin(\zeta+\zeta_0) + d_{ld}\dot\beta\sin\beta\sin(\zeta+\zeta_0) \\ -d_{ld}\dot\zeta\cos\beta\cos(\zeta+\zeta_0) - a_{ld}\dot\beta\cos\beta \\ \\ -b_{ld}\dot\beta\cos\beta\cos(\zeta+\zeta_0) + b_{ld}\dot\zeta\sin\beta\sin(\zeta+\zeta_0) - d_{ld}\dot\beta\cos\beta\sin(\zeta+\zeta_0) \\ -d_{ld}\dot\zeta\sin\beta\cos(\zeta+\zeta_0) - a_{ld}\dot\beta\sin\beta - r_{ld}\dot\theta_{ld}\cos\theta_{ld}; \end{pmatrix} \tag{3.53}$$

The absolute speed V_{ld} of the lag damper is given by

$$V_{ld} = ((\boldsymbol{r}_b^{B_{ld},A_{ld}})^T \boldsymbol{v}_b^{B_{ld},A_{ld}})/l_{ld} \tag{3.54}$$

and is used to evaluate the damping force generated by the lag damper $F_{ld} = F_{ld}(V_{ld})$. In the case of the UH-60A a lookup table is used to evaluate the lag damper force as the relation between F_{ld} and V_{ld} is highly nonlinear. The moment generated by the lag damper in blade span reference is given by

$$\boldsymbol{M}_{ld_b} = \frac{F_{ld}}{l_{ld}}(\boldsymbol{r}_b^{c,B_{ld}} \times \boldsymbol{r}_b^{c,A_{ld}}) \tag{3.55}$$

The components along the flap and lag degrees of freedom needed in Eq. (3.34) are evaluated assuming $\boldsymbol{M}_{ld_b} = (M_{\beta_{ld}},\ 0,\ M_{\zeta_{ld}})^T$.

3.1.8 Equations summary

Equations (3.22) and (3.33) describe the aerodynamic and inertial forces and moments of the i^{th} blade expressed in nonrotating shaft. Rotor forces and moments are obtained adding the contribution of all blades.

$$\boldsymbol{F}_{r_S} = \sum_{i=1}^{N_b}(\boldsymbol{F}_{I,i_S} + \boldsymbol{F}_{A,i_S}) \tag{3.56}$$

and

$$\boldsymbol{M}_{r_S} = \sum_{i=1}^{N_b}(\boldsymbol{M}_{I,i_S} + \boldsymbol{M}_{A,i_S} + \boldsymbol{M}_{ld,i_S}) \tag{3.57}$$

where $\boldsymbol{M}_{ld,i_S}$ is the moment generated by the i^{th} lag damper in non rotating shaft reference frame and evaluated as $\boldsymbol{M}_{ld,i_S} = \boldsymbol{L}_{SR}\boldsymbol{L}_{Rb}\boldsymbol{M}_{ld,i_b}$. A similar approach is followed in the coupling matrix where the effect of all blades is added

$$\mathbb{M}_{FI_S} = \sum_{i=1}^{N_b}\mathbb{M}_{FI,i} \tag{3.58}$$

and

$$\mathbb{M}_{MI_S} = \sum_{i=1}^{N_b}\mathbb{M}_{MI,i} \tag{3.59}$$

Finally rotor force and moments in body–fixed frame can be evaluated as

$$\begin{aligned} \boldsymbol{F}_r =& \quad \boldsymbol{L}_{Sb}^{-1}\boldsymbol{F}_{r_S} \\ \boldsymbol{M}_r =& \quad \boldsymbol{L}_{Sb}^{-1}\boldsymbol{M}_{r_S} + \boldsymbol{r}_B^H \times \boldsymbol{F}_r \end{aligned} \tag{3.60}$$

and

$$\begin{aligned} \mathbb{M}_{F_r} =& \quad \boldsymbol{L}_{Sb}^{-1}\mathbb{M}_{FI_S} \\ \mathbb{M}_{M_r} =& \quad \boldsymbol{L}_{Sb}^{-1}\mathbb{M}_{MI_S} + \boldsymbol{r}_B^H \times \mathbb{M}_{F_r} \end{aligned} \tag{3.61}$$

Blade flapping and lagging equations (Eq.(3.38)) are already written in a proper reference frame and need no transformation.

Assuming $\boldsymbol{x}_c = \left(u_B, v_B, w_B, p_B, q_B, r_B, \dot{\beta}_i, \cdots, \dot{\beta}_{N_b}, \dot{\zeta}_i, \cdots, \dot{\zeta}_{N_b}\right)^T$, the part of the coupling matrix which depends on the rotor can be assembled using $\mathbb{M}_{F_r}$, $\mathbb{M}_{M_r}$ (Eq. (3.61)), $\mathbb{M}_{\beta}$, and $\mathbb{M}_{\zeta}$ (Eq. (3.39)) as

$$\mathbb{M}_{r_c} = \begin{bmatrix} \mathbb{M}_{F_r} \\ \mathbb{M}_{M_r} \\ \mathbb{M}_{\beta_i} \\ \vdots \\ \mathbb{M}_{\beta_{N_b}} \\ \mathbb{M}_{\zeta_i} \\ \vdots \\ \mathbb{M}_{\zeta_{N_b}} \end{bmatrix} \tag{3.62}$$

This matrix is added to the contribution of the fuselage in Eq. (2.66) to generate the complete coupling matrix $\mathbb{M}_c$.

When dynamic twist is accounted for, Eq. (3.47) needs to be added to set of equations which describe main rotor dynamic behaviour.

3.2 Tip–Path–Plane models

The mathematical representation of main rotor behaviour in terms of Tip–Path–Plane (TPP) variables allows for a time invariant representation of the rotor dynamics. The equations derived in the sequel describe a fully articulated rotor, but they can also be used with a few minor modifications to represent teetering rotors (i.e. by setting eccentricity of the rotor $\epsilon = 0$, the number of blades $N_b = 2$ and blade flap angle $\beta_2 = -\beta_1$). The development of TPP models is derived from the works of Chen et al. [12, 13, 14], Prouty [8], and Leishman [10].

3.2.1 Assumptions

The mathematical representation of the main rotor in terms of TPP dynamics explicitly accounts for inertial coupling of rotor modes with fuselage ones. This is an important feature, since some rotor modes lie in the frequency range which is characteristic of flight qualities. The model includes only blade flap degree of freedom. Lag dynamics is thus neglected, but this is a minor drawback, as it will be demonstrated in Chapters 4 and 5, since lag dynamics has a minor impact on flight dynamics. In the derivation of the TPP models the following simplifying assumption are used:

- Rotor blade is rigid in torsion and bending;
- Blade flapping is approximated by means of the first harmonic terms $\beta(t) = a_0(t) - a_1(t)\cos\psi - b_1(t)\sin\psi$, where a_0, a_1, and b_1 are TPP states;
- The flapping angle is assumed to be small so that $\sin\beta_i = \beta_i$ and $\cos\beta_i = 1$;

- Aerodynamic loads are evaluated by means of a simple strip theory, where the angle of attack at the blade element is evaluated analytically as a function of rotorcraft states, azimuth position ψ and radial position along the blade r;
- The angle of attack is assumed to be small, and a linear relation $C_L = a\alpha$ is adopted;
- The reversed flow region is not accounted for;
- Compressibility effects and stall are neglected;
- A dynamic, 3–states inflow is used (see Section 2.4);
- No tip loss (tip loss factor is assumed $B = 1$);

3.2.2 Generation of model equations

Blade flapping equation is easily derived from Eq. (3.36) dropping the lag degree of freedom and the lag damper contribution. Note that in the individual blade model the aerodynamic load on the blade is evaluated numerically with strip theory and lookup tables. Conversely, the assumption of a simple linear relation between lift coefficient and blade element angle of attack allows for an analytical evaluation of aerodynamic loads in the case of TPP models. The load is then integrated over the blade span and averaged over one rotor revolution.

In the tip-path-plane description of rotor dynamics, flapping motion is described by means of its zero and first order harmonics as

$$\beta(t) = a_0(t) - a_1(t)\cos\psi - b_1(t)\sin\psi \tag{3.63}$$

where the TPP states $\boldsymbol{x}_{TPP} = (a_0, a_1, b_1)^T$ describe coning angle (a_0), longitudinal (a_1) and lateral (b_1) TPP tilt angles. The first and second time derivative of blade flapping in terms of TPP variables are:

$$\begin{aligned} \dot{\beta}(t) =& \quad \dot{a}_0(t) - [\dot{a}_1(t) + b_1(t)\Omega]\cos\psi - \left[\dot{b}_1(t) - a_1\Omega\right]\sin\psi \\ \ddot{\beta}(t) =& \quad \ddot{a}_0(t) - \left[\ddot{a}_1(t) + 2\dot{b}_1(t)\Omega - a_1(t)\Omega^2\right]\cos\psi - \left[\ddot{b}_1(t) - 2\dot{a}_1(t)\Omega - b_1(t)\Omega^2\right]\sin\psi \end{aligned} \tag{3.64}$$

In the sequel the explicit dependence on time of TPP states will be dropped for the sake of conciseness. Time derivatives of TPP states are written in nondimensional form by scaling them by means of rotor angular speed, so that $a_0' = \dot{a}_0/\Omega$, $a_1' = \dot{a}_1/\Omega$, $b_1' = \dot{b}_1/\Omega$. Similarly $a_0'' = \ddot{a}_0/\Omega^2$, $a_1'' = \ddot{a}_1/\Omega^2$, $b_1'' = \ddot{b}_1/\Omega^2$, $\beta' = \dot{\beta}/\Omega$ and $\beta'' = \ddot{\beta}/\Omega^2$. Equations (3.63) and (3.64) can be rewritten as

$$\begin{aligned} \beta =& \quad a_0 - a_1\cos\psi - b_1\sin\psi \\ \beta' =& \quad [a_0' - (a_1' + b_1)\cos\psi - (b_1' - a_1)\sin\psi] \\ \beta'' =& \quad [a_0'' - (a_1'' + 2b_1' - a_1)\cos\psi - (b_1'' - 2a_1' - b_1)\sin\psi] \end{aligned} \tag{3.65}$$

Tip path plane longitudinal and lateral tilt angles can be evaluated with respect to the nonrotating shaft reference frame or with respect to the hub wind axes. In the evaluation of inertial forces the equation are more easily written in the nonrotating frame, so that a_{0_S}, a_{1_S}, and b_{1_S} describe coning and tilt with respect to the x_S and y_S axes. Furthermore the TPP states need to be integrated with time and the integration is done in the nonrotating shaft frame as the hub wind reference frame rotates with respect to the body reference frame as a function of the instantaneous value of airstream direction at the rotor hub centre.

Provided that a 2nd order dynamics will be obtained in the next paragraph for TPP variables, rotor states in nonrotating shaft frame can be written as

$$\boldsymbol{x}_{r_S} = (\boldsymbol{x}_{TPP_S}, \dot{\boldsymbol{x}}_{TPP_S})^T = \left(a_{0_S},\ a_{1_S},\ b_{1_S},\ \dot{a}_{0_S},\ \dot{a}_{1_S},\ \dot{b}_{1_S}\right)^T \tag{3.66}$$

On the converse, aerodynamic forces are more easily written in the hub wind reference frame. In this case no subscripts are added to identify the TPP states in this frame to maintain the same notation introduced in Ref. [14]. Rotor states in hub wind reference frame are written as

$$\boldsymbol{x}_{r_w} = (\boldsymbol{x}_{TPP_w}, \dot{\boldsymbol{x}}_{TPP_w})^T = \left(a_0,\ a_1,\ b_1,\ \dot{a}_0,\ \dot{a}_1,\ \dot{b}_1\right)^T \tag{3.67}$$

The transformation matrix between the two reference frames is given by

$$\boldsymbol{x}_{TPP_w} = \tilde{\boldsymbol{L}}_{wS}\boldsymbol{x}_{TPP_S} \tag{3.68}$$

where

$$\tilde{\boldsymbol{L}}_{wS} = \begin{bmatrix} 1 & 0 & 0 \\ 0 & \cos\beta_w & -\sin\beta_w \\ 0 & \sin\beta_w & \cos\beta_w \end{bmatrix} \tag{3.69}$$

and β_w is the rotation angle between the two reference frame (see Sec. 2.2.4). A similar transformation is required for the main rotor commands, which are given as inputs to the rotor model in shaft axes as $\boldsymbol{\Theta}_S = (\theta_0,\ A_{1_S},\ B_{1_S})^T$. The corresponding values for rotor commands in hub wind axes are given by $\boldsymbol{\Theta}_w = (\theta_0,\ A_{1_w},\ B_{1_w})^T$ where the latter are evaluated as

$$\boldsymbol{\Theta}_w = \tilde{\boldsymbol{L}}_{wS}\boldsymbol{\Theta}_S \tag{3.70}$$

3.2.3 TPP equations

Following the simplifying assumption introduced in Sec. 3.2.1 the equilibrium of the blade around the flapping hinge can be written as

$$M_{\beta_A} + M_{\beta_I} + M_{\beta_K} = 0 \tag{3.71}$$

We consider the aerodynamic contribution first, then inertia and hinge elastic moment. As described in the individual blade model, the angle of attack of a blade element is evaluated as

$$\alpha = \theta_G + \tan^{-1}\frac{U_P}{U_T}$$

Some modification and simplification with respect to the individual blade models are introduced. In particular the geometric pitch θ_G at the considered blade element is evaluated as

$$\theta_G = \theta_0 + A_{1_w}\cos\psi + B_{1_w}\sin\psi + \theta_{tw} - K_{PC}\beta \tag{3.72}$$

where in this case the blade twist θ_{tw} is assumed to be a linear function of the blade element radial position

$$\theta_{tw} = \theta_{tw_x} x \tag{3.73}$$

where x is the nondimensional radial position of the blade element defined as

$$x = \frac{e+r}{R} \tag{3.74}$$

Only for a simple linear relation, it is possible to easily derive a fully analytic aerodynamic model for average rotor loads. The term $K_{PC}\beta$ accounts for pitch–flap coupling. The tangential and vertical components of blade element velocity are obtained from Eq. (3.15), by dropping the lag degree of freedom. One gets

$$\begin{aligned} U_T = \;& u_S\sin\psi + v_S\cos\psi - e(r_S - \Omega) \\ & + r\left[\sin\beta\,(p_S\cos\psi - q_S\sin\psi) - (r_S - \Omega)\cos\beta\right] \\ \\ U_P = \;& -u_S\sin\beta\cos\psi + v_S\sin\beta\sin\psi + w_S\cos\beta \\ & + e\cos\beta(q_S\cos\psi + p_S\sin\psi) \\ & + r\left(-\dot\beta + q_S\cos\psi + p_S\sin\psi\right) + U_{P_\lambda} \end{aligned} \tag{3.75}$$

where U_{P_λ} is obtained from Eq. (3.16).

If the components U_T and U_P of blade element velocity with respect to the air are transformed into hub–wind axes and written in nondimensional form by dividing by ΩR, the following expression are obtained:

$$\begin{aligned} \tilde U_T = \;& \mu\sin\psi + x\,(1 - \tilde{r_S}) + r\sin\beta\left[\tilde p_S\cos(\psi - \beta_w) - \tilde q_S\sin(\psi - \beta_w)\right] \\ \\ \tilde U_P = \;& -\mu\cos\psi\sin\beta + \lambda\cos\beta - x(\nu_c\cos\psi + \nu_s\sin\psi) \\ & - \beta'(x - \epsilon) + x\left[\tilde p_S\sin(\psi - \beta_w) + \tilde q_S\cos(\psi - \beta_w)\right] \end{aligned} \tag{3.76}$$

where $\tilde U_T = U_T/(\Omega R)$, $\tilde U_P = U_P/(\Omega R)$, $\tilde p_S = p_S/\Omega$, $\tilde q_S = q_S/\Omega$, and $\tilde r_S = r_S/\Omega$. Enforcing the small angle assumption on β, the final formulation of the velocity components is obtained:

$$\begin{aligned}
\tilde{U}_T = & \quad \mu \sin\psi + x\,(1 - \tilde{r_S}) \\
\tilde{U}_P = & \quad -\mu\beta\cos\psi + \lambda - x(\nu_c\cos\psi + \nu_s\sin\psi) \\
& \quad -\beta'(x-\epsilon) + x\,[\tilde{p}_S\sin(\psi - \beta_w) + \tilde{q}_S\cos(\psi - \beta_w)]
\end{aligned} \tag{3.77}$$

The local angle of attack is evaluated as $\alpha = \theta_G + \tilde{U}_P/\tilde{U}_T$. Due to the small angle assumption, the vertical force is equal to the lift, so that the infinitesimal vertical force increment dF_{A_z} generated by the blade element dr is evaluated as

$$dF_{A_z} = \frac{\rho}{2}V^2ca(\theta_G + \tilde{U}_P/\tilde{U}_T)dr \tag{3.78}$$

Assuming that the vertical component of the velocity has almost no impact on the velocity norm, so that $V \approx U_T$, it is $V^2 \approx (\Omega R)^2\tilde{U}_T$, so that dF_{A_z} becomes equal to

$$dF_{A_z} = \frac{\rho}{2}(\Omega R)^2ca(\theta_G\tilde{U}_T^2 + \tilde{U}_P\tilde{U}_T)dr \tag{3.79}$$

Finally, the aerodynamic moment around flap hinge can be evaluated as

$$M_{\beta_A} = \int_0^{R-e} rdF_{A_z} = \frac{\rho}{2}(\Omega R)^2R^2ca\int_\epsilon^1 x(\theta_G\tilde{U}_T^2 + \tilde{U}_P\tilde{U}_T)dx \tag{3.80}$$

Substituting the expressions for $\beta(\psi)$ and $\beta'(\psi)$ expressed in Eqs. (3.65) into equations (3.77) and (3.80), a representation of aerodynamic moment based on the first harmonic of the flapping motion is obtained. To evaluate TPP states dynamics it is necessary to isolate the contribution of the aerodynamic moment on coning, longitudinal and lateral flapping of the tip path plane, named M_{A_0}, M_{A_c}, M_{A_s} respectively. These contributions are evaluated as $\boldsymbol{M}_{A_w} = (M_{A_0},\ M_{A_c},\ M_{A_s})^T$, with

$$\begin{aligned}
M_{A_0} &= \tfrac{1}{2\pi}\textstyle\int_0^{2\pi} M_{\beta_A}d\psi \\
M_{A_c} &= -\tfrac{1}{\pi}\textstyle\int_0^{2\pi} M_{\beta_A}\cos\psi d\psi \\
M_{A_s} &= -\tfrac{1}{\pi}\textstyle\int_0^{2\pi} M_{\beta_A}\sin\psi d\psi
\end{aligned}$$

The aerodynamic moments are then written in the nonrotating shaft frame as $\boldsymbol{M}_{A_S} = \tilde{L}_{wS}^T\boldsymbol{M}_{A_w}$.

For the inertial contribution a similar approach is followed. Starting from Eq. (3.36) one

- drops the lag degree of freedom,
- enforces a small angle assumption on β,
- substitutes the individual blade flapping β with its 1st harmonic representation.

Finally, as in the aerodynamic case, the contribution of the inertial loads on coning, longitudinal and lateral tilt angle of the tip path plane is evaluated as $\boldsymbol{M}_{I_S} = (M_{I_0},\ M_{I_c},\ M_{I_s})^T$, with

$$\begin{aligned} M_{I_0} &= \tfrac{1}{2\pi}\int_0^{2\pi} M_{\beta_I} d\psi \\ M_{I_c} &= -\tfrac{1}{\pi}\int_0^{2\pi} M_{\beta_I}\cos\psi d\psi \\ M_{I_s} &= -\tfrac{1}{\pi}\int_0^{2\pi} M_{\beta_I}\sin\psi d\psi \end{aligned}$$

If stiffness is introduced in the flap hinges, the hinge spring moments $\boldsymbol{M}_{K_S} = (M_{K_0},\ M_{K_c},\ M_{K_s})^T$ in the nonrotating shaft reference frame is:

$$\begin{aligned} M_{K_0} &= \tfrac{1}{2\pi}\int_0^{2\pi} M_{\beta_K} d\psi \\ M_{K_c} &= -\tfrac{1}{\pi}\int_0^{2\pi} M_{\beta_K}\cos\psi d\psi \\ M_{K_s} &= -\tfrac{1}{\pi}\int_0^{2\pi} M_{\beta_K}\sin\psi d\psi \end{aligned}$$

where $M_{\beta_K} = K_\beta \beta_S = K_\beta(a_{0_S} - a_{1_S}\cos\psi - b_{1_S}\sin\psi)$. TPP dynamics can thus be represented as

$$\boldsymbol{M}_{I_S} + \boldsymbol{M}_{K_S} + \tilde{L}_{wS}^T \boldsymbol{M}_{A_w} = 0 \tag{3.81}$$

As for individual blade model, also TTP states are inertially coupled to fuselage states. The highest order derivatives of both rotor and fuselage velocity variables are collected in the inertial coupling matrix $\mathbb{M}_{TPP}$, and equation (3.81) is rewritten in the form

$$\mathbb{M}_{TPP}\dot{\boldsymbol{x}}_c = \bar{\boldsymbol{M}}_{I_S} + \boldsymbol{M}_{K_S} + \tilde{L}_{wS}^T \boldsymbol{M}_{A_w} \tag{3.82}$$

where $\bar{\boldsymbol{M}}_{I_S}$ is the portion of the inertial term that does not contain any highest-order state derivative, whereas the vector of state derivative $\boldsymbol{x}_c$ for the TPP model is equal to

$$\boldsymbol{x}_c = \left(u_B, v_B, w_B, p_B, q_B, r_B, \dot{a}_0, \dot{a}_1, \dot{b}_1\right)^T \tag{3.83}$$

The coupling matrix $\mathbb{M}_{TPP}$ can be written as

$$\mathbb{M}_{TPP} = \left[\mathbb{M}_{TPP_V}\boldsymbol{L}_{SB},\ \mathbb{M}_{TPP_V}\boldsymbol{L}_{SB}\tilde{\boldsymbol{r}}_B^H + \mathbb{M}_{TPP_\omega}\boldsymbol{L}_{SB},\ \mathbb{M}_{TPP_{TPP}}\right] \tag{3.84}$$

The aerodynamic contribution in the hub-wind reference frame $\boldsymbol{M}_{A_w}$ is usually rearranged in the form

$$\boldsymbol{M}_{A_w} = -\tilde{\boldsymbol{D}}(\dot{a}_0, \dot{a}_1, \dot{b}_1)^T - \tilde{\boldsymbol{K}}(a_0, a_1, b_1)^T + \tilde{\boldsymbol{f}} \tag{3.85}$$

3.2.4 Aerodynamic loads

The evaluation of rotor aerodynamic loads follows a similar path, starting from Eq. (3.79), which describes the vertical force increment due to aerodynamic loads. Two different contributions lead to the generation of rotor inplane force $dF_{A_x} = dF_{A_{in}} - dF_{A_{pr}}$. The first component is induced drag, which accounts for the projection of the lift coefficient along the x_b axis, such that $dF_{A_{in}} = dLU_P/U_T = dF_{A_{in}}U_P/U_T$. This term, due to the rotation of the lift direction towards the advancing side of the blade, is equal to

$$dF_{A_{in}} = \frac{\rho}{2}(\Omega R)^2 ca(\theta_G \tilde{U}\tilde{U}_P + \tilde{U}_P^2)dr \tag{3.86}$$

The second term is profile drag $dF_{A_{pr}}$, that is generated by each blade element. This second term is given by

$$dF_{A_{pr}} = \frac{\rho}{2}(\Omega R)^2 c\delta(\tilde{U}_T^2)dr \tag{3.87}$$

where the profile drag coefficient δ is determined as a function of rotor thrust coefficient (e.g. for a symmetric blade profile $\delta \approx 0.09 + 0.3(6C_T/a\sigma)^2$).

Main rotor thrust is the total component of the aerodynamic force generated along the perpendicular to the tip–path–plane, and therefore with a longitudinal a_1 and lateral b_1 tilt with respect the rotor shaft. Inplane forces are assumed to lie on the tip–path–plane. Under a small angle assumption their value can be approximated as if they lie on the plane perpendicular to the rotor shaft. The rotor aerodynamic force along the x and y directions takes into account both the inplane forces and the projection on the thrust due to TPP tilt angles. Main rotor aerodynamic force in hub-wind reference frame $\boldsymbol{F}_{A_w}$ can thus be evaluated as

$$\boldsymbol{F}_{A_w} = \frac{N_b}{2}\rho(\Omega R)^2 Rca \begin{pmatrix} C_X \\ C_Y \\ -C_T \end{pmatrix} \tag{3.88}$$

where

$$C_X = \frac{1}{\frac{N_b}{2}\rho(\Omega R)^2 Rca}\frac{1}{2\pi}\int_0^{2\pi}\int_0^{R-e}\left[dF_{A_z}\beta\cos\psi + \left(dF_{A_{in}} - dF_{A_{pr}}\right)\sin\psi\right]d\psi \tag{3.89}$$

$$C_Y = \frac{1}{\frac{N_b}{2}\rho(\Omega R)^2 Rca}\frac{1}{2\pi}\int_0^{2\pi}\int_0^{R-e}\left[-dF_{A_z}\beta\sin\psi + \left(dF_{A_{in}} - dF_{A_{pr}}\right)\cos\psi\right]d\psi \tag{3.90}$$

$$C_T = \frac{1}{\frac{N_b}{2}\rho(\Omega R)^2 Rca}\frac{1}{2\pi}\int_0^{2\pi}\int_0^{R-e} dF_{A_z}d\psi \tag{3.91}$$

The force coefficients can be rewritten as

$$C_X = \frac{1}{2\pi}\int_0^{2\pi}\int_0^{1-\epsilon}\left\{(\theta_G\tilde{U}_T^2 + \tilde{U}_P\tilde{U}_T)\beta\cos\psi + \left[(\theta_G\tilde{U}\tilde{U}_P + \tilde{U}_P^2) - (\tilde{U}_T^2\delta/a)\right]\sin\psi\right\}\ dx\ d\psi \tag{3.92}$$

$$C_Y = \frac{1}{2\pi}\int_0^{2\pi}\int_0^{1-\epsilon}\left\{-(\theta_G\tilde{U}_T^2 + \tilde{U}_P\tilde{U}_T)\beta\sin\psi + \left[(\theta_G\tilde{U}\tilde{U}_P + \tilde{U}_P^2) - (\tilde{U}_T^2\delta/a)\right]\cos\psi\right\}\ dx\ d\psi \tag{3.93}$$

$$C_T = \frac{1}{2\pi}\int_0^{2\pi}\int_0^{1-\epsilon}(\theta_G\tilde{U}_T^2 + \tilde{U}_P\tilde{U}_T)\ dx\ d\psi \tag{3.94}$$

Rotor moments about x_w and y_w are generated by blade shear loads evaluated at the flapping hinges, which are located at a distance e from the rotor centre. Rotor torque around the $z_w = z_S$ axis is the sum of profile and induced drag. These moments are expressed in hub wind axes as

$$\boldsymbol{M}_{Ar_w} = \frac{N_b}{2}\rho(\Omega R)^2 R^2 ca \begin{pmatrix} C_l \\ C_m \\ C_n \end{pmatrix} \tag{3.95}$$

where

$$C_l = \frac{1}{\frac{N_b}{2}\rho(\Omega R)^2 R^2 ca}\frac{\epsilon}{2\pi}\int_0^{2\pi}\int_0^{R-e} -dF_{A_z}\sin\psi d\psi \tag{3.96}$$

$$C_m = \frac{1}{\frac{N_b}{2}\rho(\Omega R)^2 R^2 ca}\frac{\epsilon}{2\pi}\int_0^{2\pi}\int_0^{R-e} -dF_{A_z}\cos\psi d\psi \tag{3.97}$$

$$C_n = \frac{1}{\frac{N_b}{2}\rho(\Omega R)^2 R^2 ca}\frac{1}{2\pi}\int_0^{2\pi}\int_0^{R-e} -r\left(dF_{A_{in}} - dF_{A_{pr}}\right) d\psi \tag{3.98}$$

The moments coefficient can be written in terms of nondimensional variables as

$$C_l = \frac{\epsilon}{2\pi}\int_0^{2\pi}\int_0^{1-\epsilon} -(\theta_G\tilde{U}_T^2 + \tilde{U}_P\tilde{U}_T)\sin\psi\ dx\ d\psi \tag{3.99}$$

$$C_m = \frac{\epsilon}{2\pi}\int_0^{2\pi}\int_0^{1-\epsilon} -(\theta_G\tilde{U}_T^2 + \tilde{U}_P\tilde{U}_T)\cos\psi\ dx\ d\psi \tag{3.100}$$

$$C_n = \frac{1}{2\pi}\int_0^{2\pi}\int_0^{1-\epsilon} x\left[(\theta_G\tilde{U}\tilde{U}_P + \tilde{U}_P^2) - (\tilde{U}_T^2\delta/a)\right]\ dx\ d\psi \tag{3.101}$$

Rotor aerodynamic forces and moments can then be transformed into the nonrotating shaft reference frame,

$$\begin{aligned} \boldsymbol{F}_{A_S} = &\ \boldsymbol{L}_{wS}^T\boldsymbol{F}_{A_w} \\ \boldsymbol{M}_{A_S} = &\ \boldsymbol{L}_{wS}^T\boldsymbol{M}_{A_w} \end{aligned} \tag{3.102}$$

3.2.5 Inertial loads

Rotor inertial forces and moments can be evaluated following a pattern similar to that used for the derivation of inertial terms for TPP equations. In this case Eq. (3.24) is used as the starting point. After the small angles simplifying assumption is enforced, the loads are integrated analytically over blade span and averaged over a rotor revolution. Inertial force $\boldsymbol{F}_{I_S}$ and moment $\boldsymbol{M}_{I_S}$ are thus expressed directly in nonrotating shaft reference frame. When stiffness in the flap hinges is added, a moment is transmitted to the fuselage given by

$$\boldsymbol{M}_{K_S} = \left(K_\beta b_{1_S},\ K_\beta a_{1_S},\ 0\right)^T \tag{3.103}$$

Again, some terms in the inertial force and moment components depend on higher order state derivatives. Rotor total forces and moments can be written as

$$\begin{aligned} \mathbb{M}_{FI}\dot{\boldsymbol{x}}_c = &\quad \boldsymbol{F}_{A_S} + \bar{\boldsymbol{F}}_{I_S} \\ \mathbb{M}_{MI}\dot{\boldsymbol{x}}_c = &\quad \boldsymbol{M}_{A_S} + \boldsymbol{M}_{K_S} + \bar{\boldsymbol{M}}_{I_S} \end{aligned} \tag{3.104}$$

where $\bar{\boldsymbol{F}}_{Ir_S}$ and $\bar{\boldsymbol{M}}_{Ir_S}$ are respectively the terms in the inertial force and moment that do not depend on highest order derivatives of velocity variables, whereas expressions of the coupling matrices $\mathbb{M}_{FI}$ and $\mathbb{M}_{MI}$ are built as follows:

$$\begin{aligned} \mathbb{M}_{FI} = &\quad \left[\mathbb{M}_{FI_V}\boldsymbol{L}_{SB},\ \mathbb{M}_{FI_V}\boldsymbol{L}_{SB}\tilde{\boldsymbol{r}}_B^H + \mathbb{M}_{FI_\omega}\boldsymbol{L}_{SB},\ \mathbb{M}_{FI_{TPP}}\right] \\ \mathbb{M}_{MI} = &\quad \left[\mathbb{M}_{MI_V}\boldsymbol{L}_{SB},\ \mathbb{M}_{MI_V}\boldsymbol{L}_{SB}\tilde{\boldsymbol{r}}_B^H + \mathbb{M}_{MI_\omega}\boldsymbol{L}_{SB},\ \mathbb{M}_{MI_{TPP}}\right] \end{aligned} \tag{3.105}$$

3.2.6 Equations summary

Equation (3.104) describes the total forces and moments (aerodynamic, inertial, and elastic) that the main rotor transmit to the fuselage, with Eq. (3.105) providing the coupling matrices in the evaluation of inertial forces and moments. As for the individual blade model, rotor force and moments in body–fixed frame can be evaluated as

$$\begin{aligned} \boldsymbol{F}_r = &\quad \boldsymbol{L}_{Sb}^{-1}\boldsymbol{F}_{r_S} \\ \boldsymbol{M}_r = &\quad \boldsymbol{L}_{Sb}^{-1}\boldsymbol{M}_{r_S} + \boldsymbol{r}_B^H \times \boldsymbol{F}_r \end{aligned} \tag{3.106}$$

and

$$\begin{aligned} \mathbb{M}_{F_r} = &\quad \boldsymbol{L}_{Sb}^{-1}\mathbb{M}_{FI_S} \\ \mathbb{M}_{M_r} = &\quad \boldsymbol{L}_{Sb}^{-1}\mathbb{M}_{MI_S} + \boldsymbol{r}_B^H \times \mathbb{M}_{F_r} \end{aligned} \tag{3.107}$$

Tip–path–plane equations (Eq.(3.82)) are already written in a proper reference frame and need no transformation. Assuming $\boldsymbol{x}_c = \left(u_B, v_B, w_B, p_B, q_B, r_B, \dot{a}_0, \dot{a}_1, \dot{b}_1\right)^T$, the part of the coupling matrix which depends on the rotor can be assembled using $\mathbb{M}_{F_r}$, $\mathbb{M}_{M_r}$ (Eq. (3.107)), and $\mathbb{M}_{TPP}$ (Eq. (3.84)):

$$\mathbb{M}_r = \begin{bmatrix} \mathbb{M}_{F_r} \\ \mathbb{M}_{M_r} \\ \mathbb{M}_{TPP} \end{bmatrix} \tag{3.108}$$

3.3 Improvements of TPP models

Section 3.2 describes in detail the approach for the development of a TPP rotor model that represents well both articulated and teetering rotors. The simplifying assumptions used for the development of the rotor model described in section 3.2.1 present some differences with respect to those used in Talbot et al. [14] and in particular

- a 3-states dynamic inflow is added;
- the rotor is fully inertially coupled with fuselage linear and angular accelerations (only angular acceleration was considered in the original formulation)
- fuselage yaw angular speed and acceleration are introduced in the analysis

In spite of a more accurate representation of rotor-fuselage inertial interactions, preliminary results obtained with this approach were not satisfactory, when compared to higher order models. Some modifications have thus been introduced in order to provide a more reliable representation of helicopter performance and handling qualities by means of simplified models.

3.3.1 Tip loss correction factor

Due to the different aerodynamic operating conditions experienced by the top an bottom sides of the helicopter blades, an extremity vortex is released at the blade tip. This vortex has an effect on the pressure distribution on blade elements close to the wing tip, which are not able to generate lift, but which generate drag nevertheless. This effect can be accounted for by introducing a tip loss correction factor (i.e. an efficiency factor). The tip loss factor B determines the portion of the blade which can generate lift, i.e. it means that the blade is able to generate lift up to a blade element placed at a distance BR from the rotor centre. A value $B = 0.97$ is used as it represents correctly the behaviour of blades in normal operating conditions. Models based on TPP states representation can be upgraded by introducing the tip loss factor B. To implement this change, in Eq. (3.80) the upper limit of integration on dx in Eq.(3.80) should be changed from 1 to B, whereas in equations (3.92) to (3.94) and (3.99) to (3.101) the upper limit of integration should bu changed from $1 - \epsilon$ to $B - \epsilon$.

3.3.2 Compressibility effects on advancing side

Induced drag, and the corresponding portion of induced power, is usually sufficiently well represented by means of even the simplest inflow model. Conversely, profile drag is often significantly underestimated. In their original versions, the evaluation of profile drag for models based on TPP representation is based on a quadratic relation with the rotor thrust coefficient, C_T. Among many other effects, this assumption does not account for drag coefficient increase due to Mach number. This effect is particularly relevant on the advancing blade at high speed and it is one of the effects that limit helicopter maximum speed. An empirical correction which takes into account the rise of profile drag at high speed based on compressibility loss [10] is introduced in all the models where rotor loads are evaluated analytically. With respect to the usual simplified quadratic relation with thrust, an additional term for profile power coefficient is summed up in the region of the rotor disk where the local Mach number is greater than M_d, the drag divergence Mach number. The additional term is expressed in the form:

$$\frac{\Delta C_P}{\sigma} = \frac{1}{4\pi} \int_{\psi_1}^{\psi_2} \int_{r_{dd}}^{1} (r + \mu \sin \psi)^3 \, \Delta C_D r \; dr \; d\psi \tag{3.109}$$

For the NACA 0012 profile, Prouty suggests [8] the following simple cubic formula for ΔC_d:

$$\Delta C_D(M) = \begin{cases} 12.5(M - M_d)^3 & \text{for} \quad M > M_d \\ 0 & \text{otherwise.} \end{cases} \tag{3.110}$$

with $M_d = 0.74$. The values of ψ_1, ψ_2 and r_{dd} limit the region of the rotor disk represented in polar coordinates where the local Mach number is higher than M_d. Since the shape of the region with compressibility losses and the losses themselves can be evaluated analytically in integral form and averaged over one rotor revolution, the correction is easily introduced in all the simplified models providing, among other improvements, a much more accurate estimation of maximum speed.

3.3.3 Bounded rotor lift coefficient

The analytical integration of aerodynamic loads is allowed by the assumption of a simple linear relation between local angle of attack and blade section lift coefficient, C_L. This assumption has a great impact on performance evaluation, especially in the determination of ceiling limits, as it will be outlined below.

The use of linear aerodynamics does not allow to account for the presence of a limiting value for C_L at stall, eventually producing arbitrarily large values of lift, whereas the actual rotor thrust is clearly bounded by blade airfoil stall limits. This oversimplified rotor model underestimate required power and, even more significantly, ceiling limits are largely overestimated. This happens because at high altitude, due to the lower air density, rotor blades are required to operate at higher angles of attack to balance the same helicopter weight, in the absence of stall limits for the maximum available blade lift coefficient. Two different empirical approaches are thus developed and compared in the next Section of Results, in order to provide a better estimate of ceiling limits.

In the first case, rotor maximum lift is associated to the flight condition at which an estimate of rotor averaged lift coefficient becomes higher than a prescribed threshold. The averaged lift coefficient, $\bar{C}_L$ is evaluated at $0.75R$. After indicating with the symbol α_{ll} the linearity limit for the C_L vs α curve (that is, the limit value for the validity of the linear approximation for C_l), maximum rotor performance in terms of thrust coefficient are assumed to be reached when the average angle of attack, $\bar{\alpha} = \bar{C}_L/C_{L_\alpha}$ become equal or greater than $0.95\alpha_{ll}$. In the absence of more precise information, a reference value for α_{ll} like that valid for the linearity limit for the lift curve of a NACA 0012 airfoil can be adopted, providing reasonable results. The logic for this first approach is that, when the linearity limit for the C_L vs α curve is approached on average for a blade station corresponding to the representative section at $0.75R$, a large portion of the rotor disk is working close or beyond stall limits.

The second approach is based on a different, more "local" logic. Let $\alpha_{\max}$ be the peak value of the angle of attack estimated at $0.75R$ for the retreating blade. This value can be analytically estimated from tip–path–plane and control variables. Maximum performance in terms of either helicopter speed or ceiling are assumed to be reached when $\alpha_{\max}$ exceeds 10% of the stall limit, α_{st}. When the region where the blade work at hight angle of attack becomes large on the retrating side, the original purely linear model underestimate the required power and overestimate the thrust produced by the rotor disk, so that an empirical limit is set for the maximum angle of attack attainable by the representative blade section, in order to avoid unrealistically high values of C_T.

3.4 Equation generation with ordering scheme and symbolic toolbox

Even if simpler than individual blade models, rotor model developed using TPP states are described by means of very complex mathematical expression, especially when aerodynamic force and moment coefficients are taken into consideration, as can be easily seen in Ref. [14]. Integration over blade span and averaging over one rotor revolution, as described in section 3.2.4, lead to very long equations which include terms with very different order of magnitude. As an example, aerodynamic forces include terms where the rotor eccentricity ,ϵ, a very small number, is present with high exponent, such as ϵ^3 or ϵ^4. Because of small number elevated at high powers, these terms have a negligible effect on the evaluation of rotor forces and moments, but, when included in the model, they damage the computational performance as unnecessary calculations are performed.

A solution to this problem is to write all the equations in the model with a consistent level of detail. For this purpose, two tasks have been done. First of all a symbolic toolbox has been developed to write rotor TPP dynamics equations and forces, as described in section 3.2.4, starting from the kinematic description of the blade element motion. This tool, based on Symbolic Math Toolbox $^{\text{TM}}$, provides as output the rotor equations including all terms (no terms are discarded in this process).

Secondly an ordering scheme for all the states, variables and coefficients of both aerodynamic and inertial contribution has been developed. Given that all the equations are written in symbolic form, this tool evaluates the order of magnitude of every term in the equations, depending on the relative weight provided by the users for every variable. The tool identifies the most important terms and discards the unimportant ones. The tool deletes from the equations all terms whose order of magnitude is less important than a threshold. The user can select the relative order of magnitude to be included in the models. The routine, implemented in Symbolic Math Toolbox $^{\text{TM}}$ as well, removes from the equation all terms with lower order of magnitude with respect to the desired one while it maintains all important terms.

The ordering scheme used for the UH–60A rotor with tip–path–plane dynamics is proposed in table 3.1. All states and parameters are given a relative order of magnitude by scaling them to a reference value (e.g. the speed are scaled with respect to blade tip speed). If the variable has the same order of magnitude when compared to the reference value, the relative order is $\mathcal{O}(1)$, if the relative order is lower $\mathcal{O}(\varepsilon)$ or $\mathcal{O}(\varepsilon^2)$ etc. This analysis has to performed on both aerodynamic and inertial terms. For the UH–60A helicopter aerodynamic and inertial terms share similar relative order of magnitude (they are therefore truncated using the same threshold) as the Lock number, which scales aerodynamic terms on inertial ones, is $\gamma = (\rho acR^4)/I_b \approx 8$.

This technique has been applied to the model of the UH-60A rotor based on TPP states representation. The equations reported in the sequel are evaluated using the symbolic toolbox and the ordering scheme. All the terms whose relative order is $\mathcal{O}\leq\ (\varepsilon^3)$ are included in the equations. The other terms are discarded.

Table 3.1. Articulated rotor ordering scheme.

variable	$\mathcal{O}$
angles	
θ_0	ε
A_{1_w}, B_{1_w}	ε
θ_{tw_x}	ε
a_0, a_1, b_1	ε
$\sin\beta_w$, $\cos\beta_w$	1
angular velocities r.v. Ω	
Ω	1
$\dot{a}_0$, a_0'	ε
$\dot{a}_1$, a_1'	ε
$\dot{b}_1$, b_1'	ε
p_S, $\tilde{p}_S$	ε
q_S, $\tilde{q}_S$	ε
r_S, $\tilde{r}_S$	ε
angular accelerations r.v. Ω^2	
$\ddot{a}_0$, a_0''	ε
$\ddot{a}_1$, a_1''	ε
$\ddot{b}_1$, b_1''	ε
$\dot{p}_S$, $\dot{q}_S$,$\dot{r}_S$	ε
lengths r.v. R	
R	1
e, ϵ	ε
linear velocities r.v. ΩR	
u_S, v_S, w_S	ε
linear accelerations r.v. $\Omega^2 R$	
$\dot{u}_S$, $\dot{v}_S$, $\dot{w}_S$	ε
inertial and stiffness properties r.v. $\Omega^2 R$	
I_b, S_b, m_b	1
K_b	1
nondimensional coefficients	
K_{PC}	1
λ	ε
ν_s, ν_c	ε
μ	ε
δ	ε
a	1
B	1

Table 3.2. Aerodynamic load matrices and components of the TPP dynamics equation (Eq. 3.85).

$$\tilde{\boldsymbol{D}} = -\frac{\gamma\Omega}{2}\begin{bmatrix} (\frac{B^4}{4} - \frac{2B^3}{3}\epsilon + \frac{B^2}{2}\epsilon^2)(1-\tilde{r}_S) & 0 & -(\frac{B^3}{6} - \frac{B^2}{2}\epsilon + \frac{B}{2}\epsilon^2)\mu \\ 0 & (\frac{B^4}{4} - \frac{2B^3}{3}\epsilon + \frac{B^2}{2}\epsilon^2)(1-\tilde{r}_S) & 0 \\ -(\frac{B^3}{3} - B^2\epsilon + B\epsilon^2)\mu & 0 & (\frac{B^4}{4} - \frac{2B^3}{3}\epsilon + \frac{B^2}{2}\epsilon^2)(1-\tilde{r}_S) \end{bmatrix}$$

$$\tilde{\boldsymbol{K}} = -\frac{\gamma\Omega^2}{2}\begin{bmatrix} \begin{array}{c} K_{PC}\Big[\mu^2(\frac{B^2}{4} - \frac{B}{2}\epsilon) + \\ +(\frac{B^4}{4} - \frac{B^3}{3}\epsilon)(1-\tilde{r}_S)^2\Big] \end{array} & \begin{array}{c} -\mu\Big[(\frac{B^2}{4}\epsilon - \frac{B}{2}\epsilon^2) + \\ -(\frac{B^3}{6} - \frac{B^2}{4}\epsilon)\tilde{r}_S\Big] \end{array} & -\mu K_{PC}(\frac{B^3}{3} - \frac{B^2}{2}\epsilon)(1-\tilde{r}_S) \\ \begin{array}{c} -\mu\Big[(\frac{B^3}{3} - \frac{B^2}{2}\epsilon) + \\ -(\frac{B^3}{3} - \frac{B^2}{2}\epsilon)\tilde{r}_S\Big] \end{array} & \begin{array}{c} K_{PC}\Big[\mu^2(\frac{B^2}{8} - \frac{B}{4}\epsilon) + \\ +(\frac{B^4}{4} - \frac{B^3}{3}\epsilon)(1-\tilde{r}_S)^2\Big] \end{array} & \begin{array}{c} (\frac{B^4}{4} - \frac{2B^3}{3}\epsilon + \frac{B^2}{2}\epsilon^2)(1-\tilde{r}_S) + \\ +(\frac{B^2}{8} - \frac{B}{4}\epsilon)\mu^2 \end{array} \\ -\mu K_{PC}(\frac{2B^3}{3} - B^2\epsilon)(1-\tilde{r}_S) & \begin{array}{c} -(\frac{B^4}{4} - \frac{2B^3}{3}\epsilon + \frac{B^2}{2}\epsilon^2)(1-\tilde{r}_S) + \\ +(\frac{B^2}{8} - \frac{B}{4}\epsilon)\mu^2 \end{array} & \begin{array}{c} K_{PC}\Big[\mu^2(\frac{3B^2}{8} - \frac{3B}{4}\epsilon) + \\ +(\frac{B^4}{4} - \frac{B^3}{3}\epsilon)(1-\tilde{r}_S)^2\Big] \end{array} \end{bmatrix}$$

$$\tilde{\boldsymbol{f}} = \frac{\gamma\Omega^2}{2}\begin{bmatrix} \begin{array}{l} \theta_0\Big[\frac{B^4}{4}(1-\tilde{r}_S)^2 - \frac{B^3}{3}\epsilon(1-2\tilde{r}_S) + \mu^2\frac{B^2}{4}\Big] + B_{1_w}\Big[-\mu(\frac{B^3}{3}(1-\tilde{r}_S) - \frac{B^2}{2}\epsilon)\Big] + \\ +\theta_{tw}(\frac{B^5}{5}(1-\tilde{r}_S)^2 - \frac{B^4}{4}\epsilon(1-2\tilde{r}_S) + \mu^2\frac{B^3}{6}) + \mu(\tilde{p}_S\cos\beta_w + \tilde{q}_S\sin\beta_w)(\frac{B^3}{6} - \frac{B^2}{4}\epsilon) + \\ +(\lambda - \mu\nu_s\frac{1}{2})(\frac{B^3}{3} - \frac{B^2}{2}\epsilon)(1-\tilde{r}_S) \end{array} \\ \\ \begin{array}{l} A_{1_w}\Big[\frac{B^4}{4}(1-\tilde{r}_S)^2 - \frac{B^3}{3}\epsilon(1-2\tilde{r}_S) + \mu^2\frac{B^2}{8}\Big] + (\tilde{p}_S\sin\beta_w - \tilde{q}_S\cos\beta_w)(\frac{B^4}{4} - \frac{B^3}{3}\epsilon)(1-\tilde{r}_S) + \\ +(\frac{B^4}{4} - \frac{B^3}{3}\epsilon)(1-\tilde{r}_S)\nu_c \end{array} \\ \\ \begin{array}{l} \theta_0\Big[-\mu(\frac{2B^3}{3}(1-\tilde{r}_S) - B^2\epsilon)\Big] + B_{1_w}\Big[\frac{B^4}{4}(1-\tilde{r}_S)^2 - \frac{B^3}{3}\epsilon(1-2\tilde{r}_S) + \mu^2\frac{3B^2}{8}\Big] + \\ +\theta_{tw}\Big[\mu(-\frac{B^4}{2} + \frac{2B^3}{3}\epsilon)(1-\tilde{r}_S)\Big] - (\tilde{p}_S\cos\beta_w + \tilde{q}_S\sin\beta_w)(\frac{B^4}{4} - \frac{B^3}{3}\epsilon)(1-\tilde{r}_S) + \\ +\lambda\mu(-\frac{B^2}{2} + B\epsilon) + \nu_s(\frac{B^4}{4} - \frac{B^3}{3}\epsilon)(1-\tilde{r}_S) \end{array} \end{bmatrix}$$

The components of the inertial contribution $\bar{\boldsymbol{M}}_{I_S}$ to TPP dynamics equation (Eq. (3.82)) are given by:

$$
\begin{aligned}
\bar{\boldsymbol{M}}_{I,x_S} = \; & -\tfrac{1}{2}\left(2K_\beta a_{0_S} - 4S_b\epsilon R r_S \Omega a_{0_S} + 2S_b\epsilon R\Omega^2 a_{0_S} + 2I_b r_S^2 a_{0_S}\right. \\
& +2I_b\Omega^2 a_{0_S} + S_b r_S u_S b_{1_S} - S_b q_S w_S a_{1_S} - 4I_b r_S \Omega a_{0_S} + S_b r_S v_S a_{1_S} \\
& \left. -S_b p_S w_S b_{1_S} + 2S_b g + 2S_b q_S u_S - 2S_b p_S v_S\right)/I_b \\
\bar{\boldsymbol{M}}_{I,y_S} = \; & \left(2S_b\epsilon R r_S \Omega a_{1_S} + S_b q_S w_S a_{0_S} - S_b r_S v_S a_{0_S} - S_b\epsilon R\Omega^2 a_{1_S} - K_\beta a_{1_S}\right. \\
& \left. +2I_b r_S \Omega a_{1_S} - 2I_b\Omega p_S - I_b r_S^2 a_{1_S} - 2S_b\epsilon R\Omega p_S - 2I_b\Omega \dot{b}_{1_S}\right)/I_b \\
\bar{\boldsymbol{M}}_{I,z_S} = \; & -\left(I_b r_S^2 b_{1_S} - 2S_b\epsilon R\Omega q_S + S_b\epsilon R\Omega^2 b_{1_S} + K_\beta b_{1_S} - 2I_b\Omega \dot{a}_{1_S}\right. \\
& \left. -2I_b r_S \Omega b_{1_S} - 2S_b\epsilon R r_S \Omega b_{1_S} - S_b p_S w_S a_{0_S} - 2I_b\Omega q_S + S_b r_S u_S a_{0_S}\right)/I_b
\end{aligned}
\tag{3.111}
$$

whereas the terms which are proportional to the derivatives of velocity variables in Eq. (3.84) are

$$
\mathbb{M}_{TPP_V} = \begin{bmatrix} -\frac{1}{2}/I_b S_b a_{1_S} & \frac{1}{2}/I_b S_b b_{1_S} & -1/I_b S_b \\ -1/I_b S_b a_{0_S} & 0 & 0 \\ 0 & 1/I_b S_b a_{0_S} & 0 \end{bmatrix} \tag{3.112}
$$

$$
\mathbb{M}_{TPP_\omega} = \begin{bmatrix} 0 & 0 & 0 \\ 0 & 1 + 1/I_b S_b \epsilon R & 0 \\ 1 + 1/I_b S_b \epsilon R & 0 & 0 \end{bmatrix} \tag{3.113}
$$

$$
\mathbb{M}_{TPP_{TPP}} = \begin{bmatrix} 1 & 0 & 0 \\ 0 & 1 & 0 \\ 0 & 0 & 1 \end{bmatrix} \tag{3.114}
$$

Rotor aerodynamic force coefficients in shaft axes (Eq. (3.94) for C_T, Eq. (3.92) for C_X, and Eq. (3.93) for C_Y) are given by

$$
C_T = \begin{aligned}[t]
& (\theta_0 - K_{PC} a_0)\left[\tfrac{B^3}{3}(1-\tilde{r}_S)^2 + \mu^2 \tfrac{B}{2}\right] \\
& +(B_{1_w} - K_{PC} b_1)\left[-\tfrac{B^2}{2}\mu(1-\tilde{r}_S)\right] \\
& +\theta_{tw}\left[\tfrac{B^4}{4}(1-\tilde{r}_S)^2 + \tfrac{B^2}{4}\mu^2\right] \\
& +\tfrac{B^2}{4}\mu(\tilde{p}_S \cos\beta_w + \tilde{q}_S \sin\beta_w) + a_0'(1-\tilde{r}_S)(-\tfrac{B^3}{3} + \tfrac{B^2}{2}\epsilon) \\
& +(b_1' - a_1)\mu(\tfrac{B^2}{4} - \tfrac{B}{2}\epsilon) + \lambda(\tfrac{B^2}{2}(1-\tilde{r}_S) - \tfrac{1}{2}\epsilon^2) \\
& -\tfrac{B^2}{4}\mu\nu_s + \tfrac{B^2}{4}\mu(1-\tilde{r}_S)a_1
\end{aligned}
\tag{3.115}
$$

$$
C_X = \begin{array}{l}
\frac{\delta}{a}\mu\left[-\frac{1}{2}(1-\tilde{r}_S)+\frac{1}{2}\epsilon^2\right] \\
+(\theta_0 - K_{PC}a_0)\left[\lambda\mu\frac{B}{2} - \nu_s\frac{B^3}{6}(1-\tilde{r}_S) - a_0'\mu\frac{B^2}{4} + (b_1'-a_1)(\frac{B^3}{6}(1-\tilde{r}_S)-\frac{B^2}{4}\epsilon)\right. \\
\left.+(\tilde{p}_S\cos\beta_w + \tilde{q}_S\sin\beta_w)\frac{B^3}{6}(1-\tilde{r}_S) - a_1\frac{B^3}{6}(1-2\tilde{r}_S)\right] \\
+(A_{1_w} - K_{PC}a_1)\left[\nu_c\mu\frac{B^2}{16} - (a_1'+b_1)\mu\frac{B^2}{16} + (\tilde{p}_S\sin\beta_w - \tilde{q}_S\cos\beta_w)\mu\frac{B^2}{16}\right. \\
\left.-a_0\frac{B^3}{6}(1-2\tilde{r}_S) + b_1\mu\frac{B^2}{16}\right] \\
+(B_{1_w} - K_{PC}b_1)\left[-\lambda\frac{B^2}{4}(1-\tilde{r}_S) + \nu_s\mu\frac{3B^2}{16} + a_0'(\frac{B^3}{6}(1-\tilde{r}_S)-\frac{B^2}{4}\epsilon) - (b_1'-a_1)\mu\frac{3B^2}{16}\right. \\
\left.-(\tilde{p}_S\cos\beta_w + \tilde{q}_S\sin\beta_w)\mu\frac{3B^2}{16} + a_1\mu\frac{B^2}{16}\right] \\
+\theta_{tw}\left[\lambda\mu\frac{B^2}{4} - \nu_s\frac{B^4}{8}(1-\tilde{r}_S) - a_0'\mu\frac{B^3}{6} + (b_1'-a_1)(\frac{B^4}{8}(1-\tilde{r}_S)-\frac{B^3}{6}\epsilon)\right. \\
\left.+(\tilde{p}_S\cos\beta_w + \tilde{q}_S\sin\beta_w)\frac{B^4}{8}(1-\tilde{r}_S) - a_1\frac{B^4}{8}(1-2\tilde{r}_S)\right] \\
+\lambda\left[-a_1\frac{B^2}{4}(1-\tilde{r}_S) - \nu_s\frac{B^2}{2}\right] \\
+a_0'\left[\nu_s(\frac{B^3}{3}-\frac{B^2}{2}\epsilon) - b_1'(\frac{B^3}{3}-B^2\epsilon) + a_1(\frac{B^3}{2}-\frac{B^3}{6}\tilde{r}_S-\frac{5B^2}{4}\epsilon)\right] \\
+(a_1'+b_1)\left[a_0(\frac{B^3}{6}(1-\tilde{r}_S)-\frac{B^2}{4}\epsilon) + b_1\mu\frac{B^2}{16}\right] \\
+(b_1'-a_1)\left[\lambda(\frac{B^2}{2}-B\epsilon) + \mu a_1\frac{B^2}{16}\right] \\
+(\tilde{p}_S\cos\beta_w + \tilde{q}_S\sin\beta_w)\left[\lambda\frac{B^2}{2} + a_0'(-\frac{B^3}{3}+\frac{B^2}{2}\epsilon) + a_1\mu\frac{B^2}{16}\right] \\
+(\tilde{p}_S\sin\beta_w - \tilde{q}_S\cos\beta_w)\left[-a_0\frac{B^3}{6}(1-\tilde{r}_S) - \mu b_1\frac{B^2}{16}\right] \\
+a_0\left[\nu_c\frac{B^3}{6}(-1+\tilde{r}_S) - \mu a_0\frac{B^2}{4}\right] - \mu(a_1\nu_s + b_1\nu_c + 3a_1^2 + b_1^2)\frac{B^2}{16}
\end{array}
\tag{3.116}
$$

$$
\begin{aligned}
C_Y = \quad & (\theta_0 - K_{PC}a_0)\Big[-\nu_c\tfrac{B^3}{6}(1-\tilde{r}_S) + (a_1' + b_1)(\tfrac{B^3}{6}(1-\tilde{r}_S) - \tfrac{B^2}{4}\epsilon) \\
& -(\tilde{p}_S\sin\beta_w - \tilde{q}_S\cos\beta_w)\tfrac{B^3}{6}(1-\tilde{r}_S) - a_0\mu\tfrac{3B^2}{4} + b_1\tfrac{B^3}{6}(1-2\tilde{r}_S)\Big] \\
& +(A_{1_w} - K_{PC}a_1)\Big[-\lambda\tfrac{B^2}{4}(1-\tilde{r}_S) + \nu_s\mu\tfrac{B^2}{16} + a_0'(\tfrac{B^3}{6}(1-\tilde{r}_S) - \tfrac{B^2}{4}\epsilon) - (b_1' - a_1)\mu\tfrac{B^2}{16} \\
& -(\tilde{p}_S\cos\beta_w + \tilde{q}_S\sin\beta_w)\mu\tfrac{B^2}{16} - a_1\mu\tfrac{5B^2}{16}\Big] \\
& +(B_{1_w} - K_{PC}b_1)\Big[\nu_c\mu\tfrac{B^2}{16} - (a_1' + b_1)\mu\tfrac{B^2}{16} \\
& +(\tilde{p}_S\sin\beta_w - \tilde{q}_S\cos\beta_w)\mu\tfrac{B^2}{16} + a_0\tfrac{B^3}{6}(1-2\tilde{r}_S) - b_1\mu\tfrac{7B^2}{16}\Big] \\
& +\theta_{tw}\Big[-\nu_c\tfrac{B^4}{8}(1-\tilde{r}_S) + (a_1' + b_1)(\tfrac{B^4}{8}(1-\tilde{r}_S) - \tfrac{B^3}{6}\epsilon) \\
& -(\tilde{p}_S\sin\beta_w - \tilde{q}_S\cos\beta_w)\tfrac{B^4}{8}(1-\tilde{r}_S) - a_0\mu\tfrac{B^3}{2} + b_1\tfrac{B^4}{8}(1-2\tilde{r}_S)\Big] \\
& +\lambda\Big[b_1\tfrac{B^2}{4}(1-\tilde{r}_S) - \nu_c\tfrac{B^2}{2} - a_0\mu\tfrac{3B}{2}\Big] \\
& +a_0'\Big[\nu_c(\tfrac{B^3}{3} - \tfrac{B^2}{2}\epsilon) - a_1'(\tfrac{B^3}{3} - B^2\epsilon) - b_1(\tfrac{B^3}{2} - \tfrac{B^3}{6}\tilde{r}_S - \tfrac{5B^2}{4}\epsilon) + \mu a_0\tfrac{3B^2}{4}\Big] \\
& +(a_1' + b_1)\Big[\lambda(\tfrac{B^2}{2} - B\epsilon) + \mu a_1\tfrac{7B^2}{16}\Big] \\
& +(b_1' - a_1)\Big[-a_0(\tfrac{B^3}{6}(1-\tilde{r}_S) - \tfrac{B^2}{4}\epsilon) + b_1\mu\tfrac{5B^2}{16}\Big] \\
& +(\tilde{p}_S\cos\beta_w + \tilde{q}_S\sin\beta_w)\Big[-a_0\tfrac{B^3}{6}(1-\tilde{r}_S) + \mu b_1\tfrac{5B^2}{16}\Big] \\
& +(\tilde{p}_S\sin\beta_w - \tilde{q}_S\cos\beta_w)\Big[-\lambda\tfrac{B^2}{2} + a_0'(\tfrac{B^3}{3} - \tfrac{B^2}{2}\epsilon) - a_1\mu\tfrac{7B^2}{16}\Big] \\
& +a_0\nu_s\tfrac{B^3}{6}(1-\tilde{r}_S) - \mu(7a_1\nu_c + 5b_1\nu_s - 2a_1b_1)\tfrac{B^2}{16}
\end{aligned}
\tag{3.117}
$$

Rotor aerodynamic moment coefficients in shaft axes (Eq. (3.99) for C_l, Eq. (3.100) for C_m, and Eq. (3.101) for C_n) are given by

$$
\begin{aligned}
C_l = \quad & (\theta_0 - K_{PC}a_0)\Big[-\mu\tfrac{B^2}{2}(1-\tilde{r}_S)\Big] \\
& +(B_{1_w} - K_{PC}b_1)\Big[\tfrac{B^3}{6}(1-\tilde{r}_S)^2 + \mu^2\tfrac{3B}{8}\Big] \\
& +\theta_{tw}\Big[-\mu\tfrac{B^3}{3}(1-\tilde{r}_S)\Big] \\
& +\lambda\mu(-\tfrac{B}{2} + \tfrac{\epsilon}{2}) + \nu_s\tfrac{B^3}{6}(1-\tilde{r}_S) + a_0'\mu(\tfrac{B^2}{4} - \tfrac{B}{2}\epsilon) \\
& +(b_1' - a_1)(1-\tilde{r}_S)(-\tfrac{B^3}{6} + \tfrac{B^2}{4}\epsilon) - (\tilde{p}_S\cos\beta_w + \tilde{q}_S\sin\beta_w)\tfrac{B^3}{6}(1-\tilde{r}_S) - \mu^2a_1\tfrac{B}{8}
\end{aligned}
\tag{3.118}
$$

$$
\begin{aligned}
C_m = \quad & (A_{1_w} - K_{PC}a_1)\Big[\tfrac{B^3}{6}(1-\tilde{r}_S)^2 + \mu^2\tfrac{B}{8}\Big] \\
& +\nu_c\tfrac{B^3}{6}(1-\tilde{r}_S) + (a_1' + b_1)(1-\tilde{r}_S)(-\tfrac{B^3}{6} + \tfrac{B^2}{4}\epsilon) \\
& +(\tilde{p}_S\sin\beta_w - \tilde{q}_S\cos\beta_w)\tfrac{B^3}{6}(1-\tilde{r}_S) + a_0\mu\tfrac{B^2}{4}(1-\tilde{r}_S) - \mu^2b_1\tfrac{B}{8}
\end{aligned}
\tag{3.119}
$$

$$
\begin{aligned}
C_n = \; & \tfrac{\delta}{a}\left[\tfrac{1}{4}(1-\tilde{r}_S)^2+\tfrac{1}{4}\mu^2\right] \\
& +(\theta_0-K_{PC}a_0)\Big[-\tfrac{B^3}{3}(1-\tilde{r}_S)\lambda+a_0'(\tfrac{B^4}{4}(1-\tilde{r}_S)-\tfrac{B^3}{3}\epsilon) \\
& +\mu\tfrac{B^3}{6}(-(b_1'-a_1)-(\tilde{p}_S\cos\beta_w+\tilde{q}_S\sin\beta_w)-a_1+\nu_s)\Big] \\
& +(A_{1_w}-K_{PC}a_1)\Big[(a_1'+b_1)(\tfrac{B^4}{8}(1-\tilde{r}_S)-\tfrac{B^3}{6}\epsilon)- \\
& (\tilde{p}_S\sin\beta_w-\tilde{q}_S\cos\beta_w)\tfrac{B^4}{8}(1-\tilde{r}_S)-\mu a_0\tfrac{B^3}{6}-\nu_c\tfrac{B^4}{8}(1-\tilde{r}_S)\Big] \\
& +(B_{1_w}-K_{PC}b_1)\Big[(b_1'-a_1)(\tfrac{B^4}{8}(1-\tilde{r}_S)-\tfrac{B^3}{6}\epsilon)+ \\
& (\tilde{p}_S\cos\beta_w+\tilde{q}_S\sin\beta_w)\tfrac{B^4}{8}(1-\tilde{r}_S)+\mu\lambda\tfrac{B^2}{4}-\mu a_0'\tfrac{B^3}{6}-\nu_s\tfrac{B^4}{8}(1-\tilde{r}_S)\Big] \\
& +\theta_{tw}\Big[-\tfrac{B^4}{4}(1-\tilde{r}_S)\lambda+a_0'(\tfrac{B^5}{5}(1-\tilde{r}_S)-\tfrac{B^4}{4}\epsilon) \\
& +\mu\tfrac{B^4}{8}(-(b_1'-a_1)-(\tilde{p}_S\cos\beta_w+\tilde{q}_S\sin\beta_w)-a_1+\nu_s)\Big] \\
& -\lambda\tfrac{B^2}{2}(\mu a_1+\lambda) \\
& +a_0'\left[\lambda(-B^2\epsilon+\tfrac{2B^3}{3})+\mu a_1\tfrac{B^3}{3}\right]+a_0'^2(\tfrac{2B^3}{3}\epsilon-\tfrac{B^4}{4}) \\
& +\left[(a_1'+b_1)\nu_c+(b_1'-a_1)\nu_s\right](\tfrac{B^4}{4}-\tfrac{B^3}{3}\epsilon) \\
& +\left[(a_1'+b_1)^2+(b_1'-a_1)^2\right](-\tfrac{B^4}{8}+\tfrac{B^3}{3}\epsilon)+(a_1'+b_1)\mu a_0\tfrac{B^3}{3} \\
& +(\tilde{p}_S\cos\beta_w+\tilde{q}_S\sin\beta_w)\left[(b_1'-a_1)(-\tfrac{B^4}{4}+\tfrac{B^3}{3}\epsilon)+\nu_s\tfrac{B^4}{4}\right] \\
& +(\tilde{p}_S\sin\beta_w-\tilde{q}_S\cos\beta_w)\left[(a_1'+b_1)(\tfrac{B^4}{4}-\tfrac{B^3}{3}\epsilon)-\nu_c\tfrac{B^4}{4}-\mu a_0\tfrac{B^3}{3}\right] \\
& -\mu a_0\nu_c\tfrac{B^3}{3}-\tfrac{B^4}{8}(\nu_s^2+\nu_c^2+\tilde{p}_S^2+\tilde{q}_S^2)
\end{aligned}
\tag{3.120}
$$

Rotor inertial forces in Eq. (3.104) are evaluated as

$$
\begin{aligned}
\bar{\boldsymbol{F}}_{I_S,x} = \; & S_b\dot{a}_{1_S}\dot{a}_{0_S}-S_br_Sa_{0_S}\Omega a_{1_S}+S_br_Sb_{1_S}\dot{a}_{0_S}+m_br_Sv_S+S_br_Sa_{0_S}\dot{b}_{1_S}+ \\
& \\
& +S_br_Sp_Sa_{0_S}-m_bq_Sw_S+1/2S_ba_{0_S}\Omega^2a_{1_S}+2S_bq_S\dot{a}_{0_S} \\
\bar{\boldsymbol{F}}_{I_S,y} = \; & m_bp_Sw_S-m_br_Su_S-S_b\dot{b}_{1_S}\dot{a}_{0_S}-2S_bp_S\dot{a}_{0_S}-1/2S_ba_{0_S}\Omega^2b_{1_S}+ \\
& +S_br_Sq_Sa_{0_S}+S_br_Sa_{1_S}\dot{a}_{0_S}+S_br_Sa_{0_S}\dot{a}_{1_S}+S_br_Sa_{0_S}\Omega b_{1_S} \\
& \\
\bar{\boldsymbol{F}}_{I_S,z} = \; & S_bp_Sa_{0_S}\Omega a_{1_S}-S_bq_Sa_{0_S}\Omega b_{1_S}+S_ba_{0_S}\Omega\dot{b}_{1_S}a_{1_S}-S_ba_{0_S}\Omega\dot{a}_{1_S}b_{1_S}-S_ba_{0_S}\dot{a}_{0_S}^2+ \\
& -1/2S_ba_{0_S}\dot{a}_{1_S}^2-1/2S_ba_{0_S}\dot{b}_{1_S}^2-m_bp_Sv_S+m_bq_Su_S-S_bq_S^2a_{0_S}-S_bp_S^2a_{0_S}+ \\
& -1/2S_ba_{0_S}\Omega^2b_{1_S}^2-1/2S_ba_{0_S}\Omega^2a_{1_S}^2-S_bb_{1_S}p_S\dot{a}_{0_S}-S_bb_{1_S}\dot{b}_{1_S}\dot{a}_{0_S}+ \\
& -S_bq_Sa_{0_S}\dot{a}_{1_S}-S_bp_Sa_{0_S}\dot{b}_{1_S}-S_bq_Sa_{1_S}\dot{a}_{0_S}-S_ba_{1_S}\dot{a}_{1_S}\dot{a}_{0_S} \\
& \\
\bar{\boldsymbol{M}}_{I_S,x} = \; & 1/2K_betab_{1_S}+S_b\epsilon R\Omega q_S+1/2S_b\epsilon R\Omega^2b_{1_S}+\epsilon RS_b\Omega\dot{a}_{1_S}+ \\
& -1/2\epsilon RS_br_Sq_S+\epsilon^2R^2m_b\Omega q_S \\
& \\
\bar{\boldsymbol{M}}_{I_S,y} = \; & 1/2K_betaa_{1_S}+1/2S_b\epsilon R\Omega^2a_{1_S}-S_b\epsilon R\Omega p_S-\epsilon RS_b\Omega\dot{b}_{1_S}+ \\
& +1/2\epsilon RS_br_Sp_S-\epsilon^2R^2m_b\Omega p_S \\
\bar{\boldsymbol{M}}_{I_S,z} = \; & -2\epsilon RS_b\Omega a_{0_S}\dot{a}_{0_S}-\epsilon RS_bq_S\Omega a_{1_S}-\epsilon RS_bp_S\Omega b_{1_S}+\epsilon RS_bq_S\dot{b}_{1_S} \\
& -\epsilon RS_b\Omega b_{1_S}\dot{b}_{1_S}-\epsilon RS_b\Omega a_{1_S}\dot{a}_{1_S}-\epsilon RS_bp_S\dot{a}_{1_S}
\end{aligned}
\tag{3.121}
$$

whereas the terms in Eq. (3.105) which depend on derivatives of velocity variables are:

$$\mathbb{M}_{FI_V} = \begin{bmatrix} m_b & 0 & 0 \\ 0 & m_b & 0 \\ 0 & 0 & m_b \end{bmatrix} \tag{3.122}$$

$$\mathbb{M}_{FI_\omega} = \begin{bmatrix} 0 & -S_b a_{0_S} & 0 \\ S_b a_{0_S} & 0 & 0 \\ 0 & 0 & 0 \end{bmatrix} \tag{3.123}$$

$$\mathbb{M}_{FI_{TPP}} = \begin{bmatrix} -\frac{1}{2} S_b a_{1_S} & -\frac{1}{2} S_b a_{0_S} & 0 \\ \frac{1}{2} S_b b_{1_S} & 0 & \frac{1}{2} S_b a_{0_S} \\ -S_b & 0 & 0 \end{bmatrix} \tag{3.124}$$

$$\mathbb{M}_{MI_V} = \begin{bmatrix} 0 & 0 & 0 \\ 0 & 0 & 0 \\ 0 & 0 & 0 \end{bmatrix} \tag{3.125}$$

$$\mathbb{M}_{MI_\omega} = \begin{bmatrix} \frac{1}{2} S_b \epsilon R + \frac{1}{2} \epsilon^2 R^2 m_b & 0 & 0 \\ 0 & \frac{1}{2} S_b \epsilon R + \frac{1}{2} \epsilon^2 R^2 m_b & 0 \\ \frac{1}{2} S_b \epsilon R a_{1_S} & -\frac{1}{2} S_b \epsilon R b_{1_S} & S_b \epsilon R + \epsilon^2 R^2 m_b \end{bmatrix} \tag{3.126}$$

$$\mathbb{M}_{MI_{TPP}} = \begin{bmatrix} 0 & 0 & \frac{1}{2} S_b \epsilon R \\ 0 & \frac{1}{2} S_b \epsilon R & 0 \\ 0 & 0 & 0 \end{bmatrix} \tag{3.127}$$

In the inflow model, the aerodynamic moment around the x_w and y_w axes are required in Eqs. (2.56) and (2.57) and are given by:

$$C_{l_\lambda} = \begin{array}{l} (\theta_0 - K_{PC} a_0) \left[\mu(-\frac{B^3}{3} + \frac{B^2}{2} \epsilon)(1 - \tilde{r}_S) \right] \\ +(B_{1_w} - K_{PC} b_1) \left[\frac{B^4}{8} (1 - \tilde{r}_S)^2 - \frac{B^3}{6} \epsilon (1 - 2\tilde{r}_S) + \frac{3B^2}{16} \mu^2 \right] \\ +\theta_{tw} \left[\mu(-\frac{B^4}{4} + \frac{B^3}{3} \epsilon)(1 - \tilde{r}_S) \right] \\ -(\tilde{p}_S \cos \beta_w + \tilde{q}_S \sin \beta_w)(1 - \tilde{r}_S)(\frac{B^4}{8} - \frac{B^3}{6} \epsilon) + a_0' \mu (\frac{B^3}{6} - \frac{B^2}{2} \epsilon) \\ +(b_1' - a_1)(-\frac{B^4}{8} + \frac{B^3}{3} \epsilon - \frac{B^2}{4} \epsilon^2)(1 - \tilde{r}_S) - \lambda \mu (\frac{B^2}{4} - \frac{B}{2} \epsilon) \\ -\nu_s(-1 + \tilde{r}_S)(\frac{B^4}{8} - \frac{B^3}{6} \epsilon) - \frac{B^2}{16} \mu^2 a_1 \end{array} \tag{3.128}$$

$$C_{m_\lambda} = \begin{array}{l} (A_{1_w} - K_{PC} a_1) \left[\frac{B^4}{8} (1 - \tilde{r}_S)^2 - \frac{B^3}{6} \epsilon (1 - 2\tilde{r}_S) + \frac{B^2}{16} \mu^2 \right] \\ +(\tilde{p}_S \sin \beta_w - \tilde{q}_S \cos \beta_w)(1 - \tilde{r}_S)(\frac{B^4}{8} - \frac{B^3}{6} \epsilon) \\ +(a_1' + b_1)(-\frac{B^4}{8} + \frac{B^3}{3} \epsilon - \frac{B^2}{4} \epsilon^2)(1 - \tilde{r}_S) + \nu_c (1 - \tilde{r}_S)(\frac{B^4}{8} - \frac{B^3}{6} \epsilon) \\ +\mu a_0 (\frac{B^3}{6} - \frac{B^2}{4} \epsilon)(1 - \tilde{r}_S) - \frac{B^2}{16} \mu^2 b_1 \end{array} \tag{3.129}$$

3.5 Teetering rotors

The aim of this section is to present the mathematical description of a teetering rotor used in simulation. Teetering rotor is described as a rigid beam, considering the effects of undersling (δ) and preconing (β_p). The description which follows is similar to the approach followed in the description of the articulated rotor dynamics and it can be used together with the same description of aerodynamic loads.

For the derivation of the mathematical model of a teetering rotor, three reference systems are used, represented in figure 3.2: a non rotating shaft reference frame ($\mathcal{F}_S$), a rotating reference frame ($\mathcal{F}_R$) and a blade reference frame ($\mathcal{F}_b$). The three references share the same origin, at the intersection of rotor axis and teetering hinge.

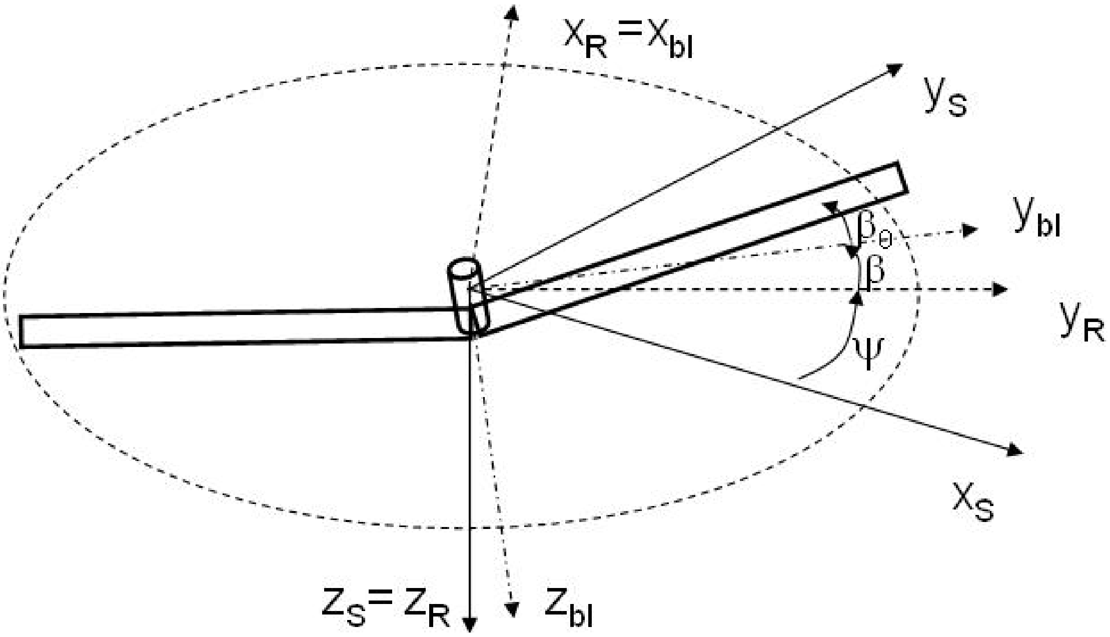

Figure 3.2. Teering rotor reference systems.

The teetering rotor has only two blades. One of the two blades is used as a reference to evaluate the anomaly ψ between nonrotating and rotating shaft reference frames, and the teetering (flapping) angle β_0, which is assumed positive when the reference blade is over its unperturbed rotation plane. As the two bladed are cantilevered, $\beta_1 = \beta_0$ (by definition) implies $\beta_2 = -\beta_0$. The notation β_0 in place of β is used in order to maintain consistency with the gimballed rotor model (see section 3.6). The rotating matrix between rotating and non rotating frames is

$$\boldsymbol{L}_{RS} = \begin{bmatrix} \sin\psi & \cos\psi & 0 \\ -\cos\psi & \sin\psi & 0 \\ 0 & 0 & 1 \end{bmatrix} \tag{3.130}$$

whereas the rotating matrix between rotating and blade frames is

$$\boldsymbol{L}_{bR} = \begin{bmatrix} 1 & 0 & 0 \\ 0 & \cos\beta_0 & -\sin\beta_0 \\ 0 & \sin\beta_0 & \cos\beta_0 \end{bmatrix} \tag{3.131}$$

Two other quantities are used in the description of the rotor: the undersling δ and the preconing β_p which are design features of the teetering rotor. Using the reference frame defined above, the position of a blade element along the blade span is given by

$$\boldsymbol{r}_b^{R,b} = \begin{bmatrix} 0 \\ r \\ \delta - |r| \tan\beta_p \end{bmatrix} \tag{3.132}$$

where $-R < r < R$. The absolute sign $|r|$ is introduced to take into account that both blades have a positive preconing. This notation is not used in the following derivations, but the effects of preconing are taken into account in when writing the equations.

3.5.1 Blade element kinematics

Linear and angular speed in the nonrotating reference system are assumed to be known, indicated as $\boldsymbol{v}_S = [u_S \;\; v_S \;\; w_S]$ and $\boldsymbol{\omega}_S = [p_S \;\; q_S \;\; r_S]$, respectively. Similarly to the articulated rotor, velocity components in the rotating reference system can be written as:

$$\boldsymbol{v}_R = \boldsymbol{L}_{RS}\boldsymbol{v}_S \tag{3.133}$$

and

$$\boldsymbol{\omega}_R = \boldsymbol{L}_{RS}\boldsymbol{\Omega}_S - \boldsymbol{\omega}_R^{R/S} \tag{3.134}$$

The components of $\boldsymbol{v}_R$ and $\boldsymbol{\omega}_R$ are equal to

$$\boldsymbol{v}_R = \begin{bmatrix} u_S \sin\psi + v_S \cos\psi \\ -u_S \cos\psi + v_S \sin\psi \\ w_S \end{bmatrix} \tag{3.135}$$

and

$$\boldsymbol{\omega}_R = \begin{bmatrix} p_S \sin\psi + q_S \cos\psi \\ -p_S \cos\psi + q_S \sin\psi \\ r_S - \Omega \end{bmatrix} \tag{3.136}$$

where $\boldsymbol{\omega}_R^{R/S} = \Omega\,[0{,}0{,}1]^T$ is the relative angular speed of the rotating axes with respect to the nonrotating frame.

The position of the blade element in rotating frame is expressed as:

$$\boldsymbol{x}_R^{R,b} = \boldsymbol{L}_{Rb}\boldsymbol{x}_b^{R,b} = \begin{bmatrix} 0 \\ r\left(\cos\beta_0 - \tan\beta_p \sin\beta_0\right) + \delta\sin\beta_0 \\ -r\left(\sin\beta_0 + \tan\beta_p \cos\beta_0\right) + \delta\cos\beta_0 \end{bmatrix} \tag{3.137}$$

The blade element speed $\boldsymbol{v}_R^b$ can be written as:

$$\boldsymbol{v}_R^b = \boldsymbol{v}_R + \boldsymbol{\omega}_R \times \boldsymbol{x}_R^{R,b} + \dot{\boldsymbol{x}}_R^{R,b} \tag{3.138}$$

where

$$\dot{\boldsymbol{x}}_R^{R,b} = \begin{bmatrix} 0 \\ \dot{\beta}_0 \left[-r \left(\sin\beta_0 + \tan\beta_p \cos\beta_0\right) + \delta \cos\beta_0\right] \\ \dot{\beta}_0 \left[-r \left(\cos\beta_0 - \tan\beta_p \sin\beta_0\right) + \delta \sin\beta_0\right] \end{bmatrix} \tag{3.139}$$

The components of the blade element speed $\boldsymbol{v}_R^b$ in rotating frame are thus given by

$$\boldsymbol{v}_R^b = \begin{bmatrix} u_S \sin\psi + v_S \cos\psi + \left(-p_S \cos\psi + q_S \sin\psi\right)\left[-r\left(\sin\beta_0 + \tan\beta_p \cos\beta_0\right) + \delta\cos\beta_0\right] \\ -\left(r_S - \Omega\right)\left[r\left(\cos\beta_0 - \tan\beta_p \sin\beta_0\right) + \delta \sin\beta_0\right] \\ \\ -u_S \cos\psi + v_S \sin\psi + \left(\dot{\beta}_0 - p_S \sin\psi - q_S \cos\psi\right)\left[-r\left(\sin\beta_0 + \tan\beta_p \cos\beta_0\right) + \delta \cos\beta_0\right] \\ \\ w_S + \left(p_S \sin\psi + q_S \cos\psi - \dot{\beta}_0\right)\left[r\left(\cos\beta_0 - \tan\beta_p \sin\beta_0\right) + \delta \sin\beta_0\right] \end{bmatrix} \tag{3.140}$$

Blade element velocity, expressed in blade reference frame is evaluated as

$$\boldsymbol{v}_b = \boldsymbol{L}_{bR} \boldsymbol{v}_R^b \tag{3.141}$$

where its components are:

$$\boldsymbol{v}_b = \begin{bmatrix} u_S \sin\psi + v_S \cos\psi + \left(-p_S \cos\psi + q_S \sin\psi\right)\left[-r\left(\sin\beta_0 + \tan\beta_p \cos\beta_0\right) + \delta\cos\beta_0\right] \\ -\left(r_S - \Omega\right)\left[r\left(\cos\beta_0 - \tan\beta_p \sin\beta_0\right) + \delta \sin\beta_0\right] \\ \\ \left(-u_S \cos\psi + v_S \sin\psi\right)\cos\beta_0 - w_S \sin\beta_0 + \left(\delta - r\tan\beta_p\right)\left(\dot{\beta}_0 - p_S \sin\psi - q_S \cos\psi\right) \\ \\ \left(-u_S \cos\psi + v_S \sin\psi\right)\sin\beta_0 + w_S \cos\beta_0 - r\left(\dot{\beta}_0 - p_S \sin\psi - q_S \cos\psi\right) \end{bmatrix} \tag{3.142}$$

Blade element accelerations, needed for inertial forces and moments evaluation can be expressed as follows:

$$\boldsymbol{a}_R^b = \dot{\boldsymbol{v}}_R^b + \boldsymbol{\omega}_R \times \boldsymbol{v}_R^b \tag{3.143}$$

where its components are:

$$
\begin{aligned}
\left(a_R^b\right)_x = \;& \dot{u}_S \sin\psi + \dot{v}_S \cos\psi + w_S \left(-p_S \cos\psi + q_S \sin\psi\right) - r_S \left(-u_S \cos\psi + v_S \sin\psi\right) \\
& + \left[-r \left(\sin\beta_0 + \tan\beta_p \cos\beta_0\right) + \delta \cos\beta_0\right] \Big[\left(-\dot{p}_S \cos\psi + \dot{q}_S \sin\psi\right) \\
& -2\dot{\beta}_0 \left(r_S - \Omega\right) + r_S \left(p_S \sin\psi + q_S \cos\psi\right)\Big] \\
& + \left[r \left(\cos\beta_0 - \tan\beta_p \sin\beta_0\right) + \delta \sin\beta_0\right] \Big[-\left(\dot{r}_S - \dot{\Omega}\right) + \left(p_S \cos\psi - q_S \sin\psi\right) \\
& \left(2\dot{\beta}_0 - p_S \cos\psi - q_S \sin\psi\right)\Big] \\
\\
\left(a_R^b\right)_y = \;& -\dot{u}_S \cos\psi + \dot{v}_S \sin\psi - w_S \left(p_S \sin\psi + q_S \cos\psi\right) + r_S \left(u_S \sin\psi + v_S \cos\psi\right) \\
& + \left[-r \left(\sin\beta_0 + \tan\beta_p \cos\beta_0\right) + \delta \cos\beta_0\right] \Big[\ddot{\beta}_0 - \dot{p}_S \sin\psi - \dot{q}_S \cos\psi \\
& + r_S \left(-p_S \cos\psi + q_S \sin\psi\right)\Big] \\
& - \left[r \left(\cos\beta_0 - \tan\beta_p \sin\beta_0\right) + \delta \sin\beta_0\right] \left[\left(\dot{\beta}_0 - p_S \sin\psi - q_S \cos\psi\right)^2 + \left(r_S - \Omega\right)^2\right] \\
\\
\left(a_R^b\right)_z = \;& \dot{w}_S + p_S v_S - q_S u_S \\
& - \left[-r \left(\sin\beta_0 + \tan\beta_p \cos\beta_0\right) + \delta \cos\beta_0\right] \Big[\left(\dot{\beta}_0 - p_S \sin\psi - q_S \cos\psi\right)^2 \\
& + \left(-p_S \cos\psi + q_S \sin\psi\right)^2\Big] \\
& + \left[r \left(\cos\beta_0 - \tan\beta_p \sin\beta_0\right) + \delta \sin\beta_0\right] \Big[-\ddot{\beta}_0 + \dot{p}_S \sin\psi + \dot{q}_S \cos\psi \\
& + \left(2\Omega - r_S\right) \left(p_S \cos\psi - q_S \sin\psi\right)\Big]
\end{aligned}
\tag{3.144}
$$

The blade element acceleration written in blade reference system is given by

$$
\boldsymbol{a}_b = \boldsymbol{L}_{bR} \boldsymbol{a}_R^b \tag{3.145}
$$

where its components are:

$$
\begin{aligned}
(a_b)_x = \;& (a_R^r)_x \\
(a_b)_y = \;& \left[-\dot{u}_S \cos\psi + \dot{v}_S \sin\psi - w_S \left(p_S \sin\psi + q_S \cos\psi\right) + r_S \left(u_S \sin\psi + v_S \cos\psi\right)\right] \cos\beta_0 \\
& - \left(\dot{w}_S + p_S v_S - q_S u_S\right) \sin\beta_0 + \left(\ddot{\beta}_0 - \dot{p}_S \sin\psi - \dot{q}_S \cos\psi\right) \left(\delta - r \tan\beta_p\right) \\
& -r \left(\dot{\beta}_0 - p_S \sin\psi - q_S \cos\psi\right)^2 - \left(r_S - \Omega\right)^2 \left[r \left(\cos\beta_0 - \tan\beta_p \sin\beta_0\right) + \delta \sin\beta_0\right] \cos\beta_0 \\
& + \left(-p_S \cos\psi + q_S \sin\psi\right)^2 \left[-r \left(\sin\beta_0 + \tan\beta_p \cos\beta_0\right) + \delta \cos\beta_0\right] \sin\beta_0 \\
& -2\Omega \left(p_S \cos\psi - q_S \sin\psi\right) \left[r \left(\cos\beta_0 - \tan\beta_p \sin\beta_0\right) + \delta \sin\beta_0\right] \sin\beta_0 \\
& +r_S \left(-p_S \cos\psi + q_S \sin\psi\right) \left[-r \left(\sin\left(2\beta_0\right) + \tan\beta_p \cos\left(2\beta_0\right)\right) + \delta \cos\left(2\beta_0\right)\right] \\
(a_b)_z = \;& \left[-\dot{u}_S \cos\psi + \dot{v}_S \sin\psi - w_S \left(p_S \sin\psi + q_S \cos\psi\right) + r_S \left(u_S \sin\psi + v_S \cos\psi\right)\right] \sin\beta_0 \\
& + \left(\dot{w}_S + p_S v_S - q_S u_S\right) \cos\beta_0 - r \left(\ddot{\beta}_0 - \dot{p}_S \sin\psi - \dot{q}_S \cos\psi\right) \\
& - \left(\delta - r \tan\beta_p\right) \left(\dot{\beta}_0 - p_S \sin\psi - q_S \cos\psi\right)^2 \\
& - \left(r_S - \Omega\right)^2 \left[r \left(\cos\beta_0 - \tan\beta_p \sin\beta_0\right) + \delta \sin\beta_0\right] \sin\beta_0 \\
& - \left(-p_S \cos\psi + q_S \sin\psi\right)^2 \left[-r \left(\sin\beta_0 + \tan\beta_p \cos\beta_0\right) + \delta \cos\beta_0\right] \cos\beta_0 \\
& +2\Omega \left(p_S \cos\psi - q_S \sin\psi\right) \left[r \left(\cos\beta_0 - \tan\beta_p \sin\beta_0\right) + \delta \sin\beta_0\right] \cos\beta_0 \\
& +r_S \left(-p_S \cos\psi + q_S \sin\psi\right) \left[-r \left(\cos\left(2\beta_0\right) + \tan\beta_p \sin\left(2\beta_0\right)\right) + \delta \sin\left(2\beta_0\right)\right]
\end{aligned}
\tag{3.146}
$$

3.5.2 Inertial loads

Moment of inertia loads are calculated integrating acceleration components over rotor mass increments,

$$
\boldsymbol{M}_{I_b} = -\int_m \boldsymbol{r}_b \times \boldsymbol{a}_b dm \tag{3.147}
$$

where, given the linear density ρ, the mass increment is defined as $dm = \rho dr$. The mass moments of inertia are defined as follows:

$$
\begin{aligned}
I_x = \;& \int_m x_b^2 dm = \int_{-R}^{R} \rho x_b^2 dr \\
I_y = \;& \int_m y_b^2 dm = \int_{-R}^{R} \rho y_b^2 dr \\
I_z = \;& \int_m z_b^2 dm = \int_{-R}^{R} \rho z_b^2 dr
\end{aligned}
\tag{3.148}
$$

where x_b, y_b, and z_b are the components of the position vector of the blade element in blade element reference frame $\boldsymbol{r}_b = (x_b,\ y_b,\ z_b)^T$. The static moment in the z direction is defined as:

$$
S_z = \int_m z_b dm = \int_{-R}^{R} \rho z_b dr \tag{3.149}
$$

If the mass distribution $\rho(r)$ along the blade (r) is assumed to be uniform, the moments of inertia and the static moments are given by

$$\begin{aligned}
I_x =& \quad m_b\left[\tfrac{2}{3}\left(1+\tan{\beta_p}^2\right)R^2-2\delta R\tan\beta_p+2\delta^2\right]\\
I_y =& \quad m_b\left[\tfrac{2}{3}R^2\tan{\beta_p}^2-2\delta R\tan\beta_p+2\delta^2\right]\\
I_z =& \quad \tfrac{2}{3}m_bR^2\\
S_z =& \quad m_b\left(2\delta-R\tan\beta_p\right)
\end{aligned} \tag{3.150}$$

where m_b is the mass of a single blade. Substituting Eq. (3.150) into Eq. (3.147) and performing the integrations, one gets

$$\begin{aligned}
M_{I,x_b} =& \quad \left(\ddot{\beta}_0-\dot{p}_S\sin\psi-\dot{q}_S\cos\psi\right)I_x-\left(-p_S\cos\psi+q_S\sin\psi\right)^2\left(I_Z-I_y\right)\tfrac{\sin 2\beta_0}{2}\\
&+\left(r_S-\Omega\right)^2\left(I_Z-I_y\right)\tfrac{\sin 2\beta_0}{2}-2\Omega\left(p_S\cos\psi-q_S\sin\psi\right)\left[\left(I_z-I_y\right)\cos{\beta_0}^2+I_y\right]\\
&+r_S\left(-p_S\cos\psi+q_S\sin\psi\right)\left(I_z-I_y\right)\cos 2\beta_0\\
&+\{[-\dot{u}_S\cos\psi+\dot{v}_S\sin\psi-w_S\left(p_S\sin\psi+q_S\cos\psi\right)\\
&+r_S\left(u_S\sin\psi+v_S\cos\psi\right)]\cos\beta_0-\left(\dot{w}_S+p_Sv_S-q_Su_S\right)\sin\beta_0\}\,S_z\\
\\
M_{I,y_b} =& \quad -\left[\dot{u}_S\sin\psi+\dot{v}_S\cos\psi+w_S\left(-p_S\cos\psi+q_S\sin\psi\right)-r_S\left(-u_S\cos\psi+v_S\sin\psi\right)\right]S_z\\
&-\left[-\dot{p}_S\cos\psi+\dot{q}_S\sin\psi-2\dot{\beta}_0\left(r_S-\Omega\right)+r_S\left(p_S\sin\psi+q_S\cos\psi\right)\right]I_y\cos\beta_0\\
&-\left[-\dot{r}_S+\dot{\Omega}+\left(p_S\cos\psi-q_S\sin\psi\right)\left(2\dot{\beta}_0-p_S\sin\psi-q_S\cos\psi\right)\right]I_y\sin\beta_0\\
\\
M_{I,z_b} =& \quad -\left[-\dot{p}_S\cos\psi+\dot{q}_S\sin\psi-2\dot{\beta}_0\left(r_S-\Omega\right)+r_S\left(p_S\sin\psi+q_S\cos\psi\right)\right]I_z\sin\beta_0\\
&+\left[-\dot{r}_S+\dot{\Omega}+\left(p_S\cos\psi-q_S\sin\psi\right)\left(2\dot{\beta}_0-p_S\sin\psi-q_S\cos\psi\right)\right]I_z\cos\beta_0
\end{aligned} \tag{3.151}$$

In the rotating reference frame the moment of inertia is equal to

$$\boldsymbol{M}_{I_R}=\boldsymbol{L}_{Rb}\boldsymbol{M}_{I_b} \tag{3.152}$$

The inertia forces are expressed directly in the rotating reference frame

$$\boldsymbol{F}_{I_R}=-\int_m \boldsymbol{a}_R^b dm \tag{3.153}$$

Performing the integration, the components in a rotating reference frame are thus given by

$$\begin{aligned}
F_{I,x_R} = \;& -2m_b\left[\dot{u}_S\sin\psi + \dot{v}_S\cos\psi + w_S\left(-p_S\cos\psi + q_S\sin\psi\right) - r_S\left(-u_S\cos\psi + v_S\sin\psi\right)\right] \\
& -S_z\cos\beta_0\left[-\dot{p}_S\cos\psi + \dot{q}_S\sin\psi - 2\dot{\beta}_0\left(r_S - \Omega\right) + r_S\left(p_S\sin\psi + q_S\cos\psi\right)\right] \\
& -S_z\sin\beta_0\left[-\dot{r}_S + \dot{\Omega} + \left(p_S\cos\psi - q_S\sin\psi\right)\left(2\dot{\beta}_0 - p_S\sin\psi - q_S\cos\psi\right)\right] \\
\\
F_{I,y_R} = \;& -2m_b\left[-\dot{u}_S\cos\psi + \dot{v}_S\sin\psi - w_S\left(p_S\sin\psi + q_S\cos\psi\right) + r_S\left(u_S\sin\psi + v_S\cos\psi\right)\right] \\
& -S_z\cos\beta_0\left[\ddot{\beta}_0 - \dot{p}_S\sin\psi - \dot{q}_S\cos\psi + r_S\left(-p_S\cos\psi + q_S\sin\psi\right)\right] \\
& +S_z\sin\beta_0\left[\left(\dot{\beta}_0 - p_S\sin\psi - q_S\cos\psi\right)^2 + \left(r_S - \Omega\right)^2\right] \\
\\
F_{I,z_R} = \;& -2m_b\left[\dot{w}_S + p_S v_S - q_S u_S\right] \\
& -S_z\sin\beta_0\left[-\ddot{\beta}_0 + \dot{p}_S\sin\psi + \dot{q}_S\cos\psi + \left(2\Omega - r_S\right)\left(p_S\cos\psi - q_S\sin\psi\right)\right] \\
& +S_z\cos\beta_0\left[\left(\dot{\beta}_0 - p_S\sin\psi - q_S\cos\psi\right)^2 + \left(-p_S\cos\psi + q_S\sin\psi\right)^2\right]
\end{aligned} \tag{3.154}$$

3.6 Gimballed Rotor

A two–bladed gimballed rotor configuration is being considered in this study as a possible way for alleviating some of the drawbacks that affect conventional teetering rotors. As to the authors' knowledge, such a configuration is novel and original and a limited number of studies is available for supporting its design.

The rotor configuration considered in this study features (i) a fly–bar with paddles, (ii) a rigid yoke connected to the shaft by means of a spherical homokinetic hinge, realized by means of a set of elastomeric springs to improve the handling qualities of the helicopter at low load factor, and (iii) coning hinges with pitch–coning links.

From the purely mechanical standpoint, this configuration allows one more degree–of–freedom to the blades in the rotating frame with respect to a conventional teetering rotor, as the flapping motion around the axis perpendicular to both the shaft and blade axes is accompanied by a feathering motion around the blade axis itself, this latter rotation corresponding to the flap angle for the paddles. The pitch angle of each blade thus results from the combination of a direct command, delivered by a conventional swash–plate, and the feathering motion of the rotor.

The introduction of coning hinges further increases model complexity, because of the significant variation of rotor inertial properties associated to blade rotations around coning hinges. Both ideal frictionless coning hinges and realistic ones, with friction induced by the centrifugal load, will be considered. Finally, the presence of a pitch–coning link varies blade pitch as a function of coning angles, a feature introduced in order to alleviate gust loads. It will be shown that, at the same time, the pitch–coning gain significantly affects system stability.

The presence of a sustained wobbling motion is the ost relevant characteristic of the two-bladed gimballed rotor, as already observed in Refs. [23] and [83]. This motion is interpreted as the result of the difference in the tip–path–planes described by blades and paddles, for the rigid rotor case [78]. Moreover, these previous studies demonstrated how the inertial properties of the feathering axis have a marginal effect on rotor behaviour, whereas the presence of paddles at the tips of the fly-bar is necessary for stabilizing the motion and avoid the departures experienced by the rotor in the presence of periodic forcing terms. These features are basically maintained even in the presence of coning degrees of freedom, although pitch–coning coupling significantly affects rotor stability. Relevant differences are present with respect to three–bladed gimballed rotors featuring coning hinges, where polar symmetry of the inertia tensor gyroscopically stabilize the rotor and pitch–coning coupling only affect rotor load [84, 85].

The homokinetic rotor hub with elastomeric bearings, represented in Figs. 3.3 and 3.4, is designed in order to make the hub rotate about its axis with the same angular speed of the shaft even when they are not aligned, thus making hub angular speed constant. This is obtained by means of elastomeric bearing assemblies that provide a link between the shaft and a carrier, and between the carrier and the hub. The mechanism is at the moment patent pending and it cannot be disclosed. The details of the design are not relevant for the study of the aeromechanic characteristics of this rotor. In what follows, the joint will be always represented as a spheric gimbal.

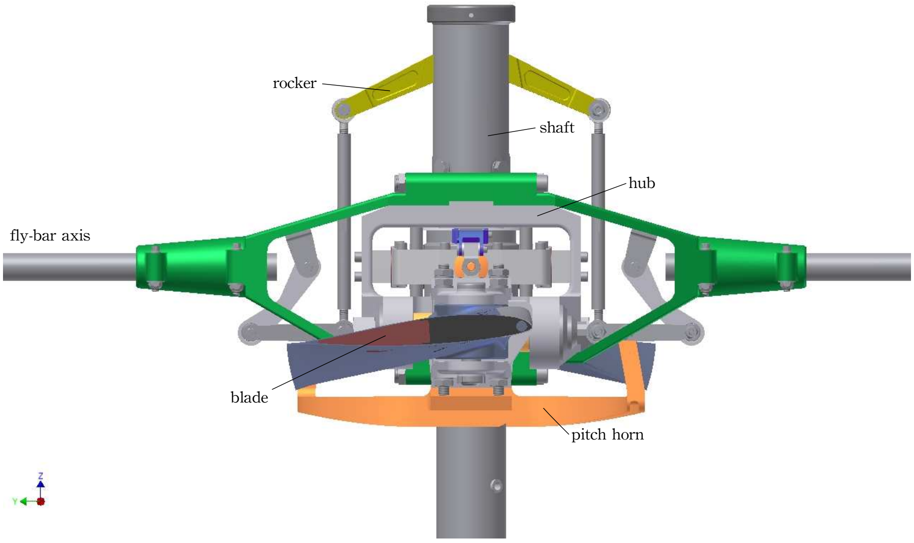

Figure 3.3. Sketch of the KA-2H homokinetic joint.

Two blades and the fly-bar are attached to the hub, the latter perpendicular to the rotor blades (Fig. 3.5). As outlined above, the blade pitch command has two contributions:

- a direct command from the swashplate (collective θ_0 and cyclic θ_{cyc}), where $\theta_{cyc} = \theta_{SW} \cos\psi + \phi_{SW} \sin\psi$ corresponds to the inclination of the swashplate about an axis parallel to the feathering axis of the blade, and θ_{SW} and ϕ_{SW} are the longitudinal and lateral rotations of the swashplate.

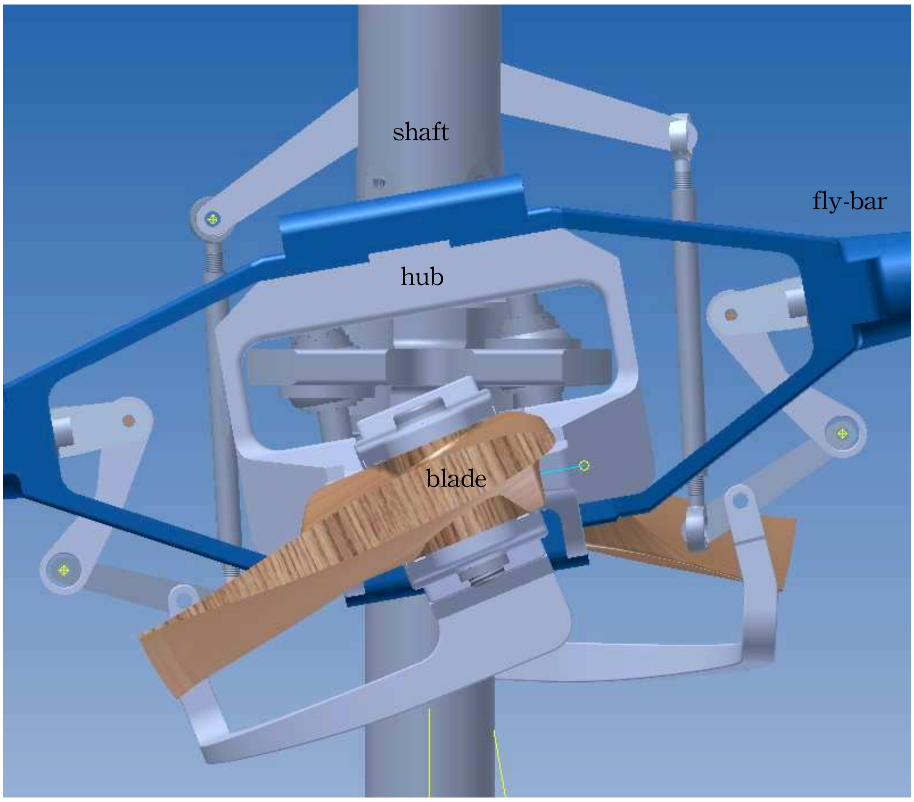

Figure 3.4. Sketch of the KA-2H homokinetic joint tilted and with a cyclic command from the swashplate.

- a secondary command (limited to cyclic pitch) due to the inclination of the hub from the shaft axis: in particular this command θ_{fb} is proportional to the rotation angle of the hub about the blade feathering axis, that corresponds to the flapping of the fly-bar.

The cyclic command on the blade, defined with respect to the plane perpendicular to the shaft, is then equal to $\theta_b = K_H \theta_{cyc} + (1 - K_H)\theta_{fb}$ where K_H is a fly-bar/swashplate command ratio. When the swashplate and the hub planes are parallel, the pitch command gain is 1. This is a typical architecture for teetering rotors, where the secondary command is simply the fly-bar flapping angle.

Figure 3.5 shows the cyclic command mechanism. With $K_H = 0.57$, a $\theta_{sw} = 10$ deg cyclic command from the swashplate results into a feathering angle of the blade $\theta_b = 5.7$ deg, when the hub is not tilted. Only when the hub becomes parallel to the swashplate, the resulting pitch angle of the blade is $\theta_b = 5.7 + 4.3 = 10$ deg. In this manner the blade Non-Feathering Plane (NFP) is parallel to the blade TPP.

From a modelling point of view, these characteristics are taken into consideration in the following way.

1. The condition of constant angular speed must be imposed to the hub axis rather

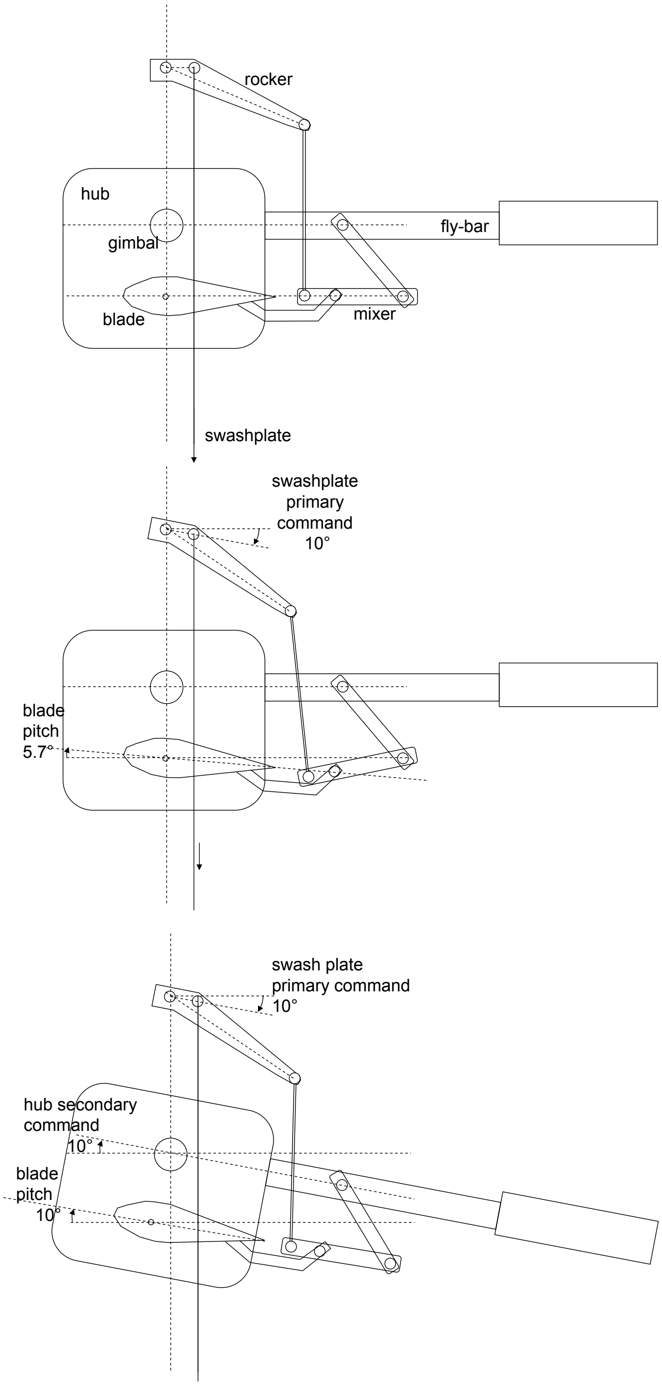

Figure 3.5. Gimballed rotor blade pitch command.

than the shaft axis, in order to enforce the condition $\dot{\psi}_H = \Omega$ =const. This was done using a non-conventional sequence for describing the rotations (2-1-3) from the non rotating shaft (NRS) to the rotating hub (RH) frames. In the classical approach used for teetering/articulated rotors ([17, 86]) the rotation about the shaft axis precedes the flapping rotation of the blades.

2. The homokinetic joint transmits to the helicopter body only the elastic, propulsive and friction moments. In particular
    (a) the torque of the engine Q_{mot} is directed along the hub axis
    (b) the elastic moments of the joint lie in the hub plane
    (c) the elastic/friction moments due to the blade feathering hinges lie in the hub plane
3. The inertial and aerodynamic forces are transmitted to the fuselage.

To describe the behaviour of the main rotor, it is necessary to define four reference systems:

- The shaft coordinate system (or Non Rotating Shaft - NRS) $\mathcal{F}_S$ $\{x_S, y_S, z_S\}$ is a non rotating frame centred on the hub gimbal. In the analysis of the behaviour of the isolated rotor, this is the fixed (inertial) frame. The system is represented in Fig. 3.6;
- The Non Rotating Hub (NRH) coordinate system $\mathcal{F}_{NRH}$ $\{x', y'', z_H\}$ has the same origin of the NRS system (the hub gimbal centre), it is tilted with respect to the NRS by means of two rotations: a first rotation θ_H about the y_S axis, that brings x_s in x' and z_s in z', then a rotation about the x' axis of an angle ϕ_H that brings the y_s axis in y'' and z' in z_H;
- The Rotating Hub (RH) coordinate system $\mathcal{F}_H$ $\{x_H, y_H, z_H\}$ is rotated from the NRH about the z_H of an angle $\psi = 90^o - \tilde{\psi}_H$ in order to have at $\psi = 0$ the first blade in the aft position, and ψ increasing with time;
- Blade Span coordinate systems $\mathcal{F}_{BS_j}\{x_{BS_j}, y_{BS_j}, z_{BS_j}\}$ with j = 1,2, have their origins at the root of the j^{th} blade (that does not coincide with the centre of the joint because of an undersling δ and eccentricity r_c of coning hinges) and their y_{BS_j} axis oriented along the blade span, such that it is rotated about the x_H axis of a coning angle $\pm\beta_c$.

Once defined the hub plane angular position, the position of the fly-bar is univocally defined, since the fly-bar feathering axis is in the hub plane. It is important to note that in this configuration the blades and the fly-bar are rigidly fixed to the hub, and therefore they are forced to belong to the same (hub) plane. This is different from the teetering rotor case, where the flapping dynamics of the blades and of the fly-bar are independent.

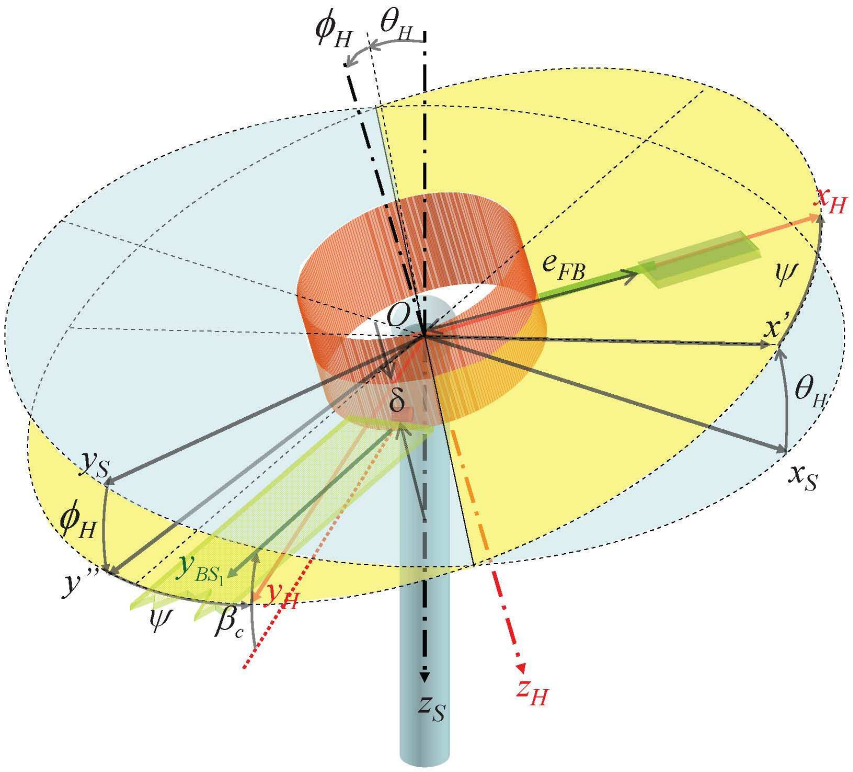

Figure 3.6. Sketch of the gimballed rotor system: rotations and reference frames.

3.6.1 Individual blade models

The equations of motion of the gimballed rotor with an individual blade approach are derived in detail in [78]. As in the case of the articulated rotor, the starting point for the description of the rotor is the position of the blade (or paddle) element. As a difference with the articulated rotor where the equation of motions are derived with a Newtonian approach, the gimballed rotor equations of motion were derived in Ref. [78] using a Lagrangian approach. A few simplifying assumptions can be made to alleviate the difficulties of the study of this novel (and unusual) rotor configuration, representing the dynamics of a gimballed rotor with reasonable accuracy. In particular it is necessary to describe accurately the rotor inertial loads so that all the nonlinear inertial terms are kept to correctly represent the wobbling motion.

With this respect, the Lagrangian approach has been selected as it allows to express the constraints easily, and it is suited for multi-body dynamics description (fuselage, hub, blades). Thanks to the Lagrangian approach it is possible to modify the model with additional degrees of freedom, such as coning hinges or feathering dynamics, or other design variations, with limited effort. In spite of the simplifications, the equations derived for gimballed rotor dynamics are quite cumbersome. To deal with such complex equations, a symbolic processor [86] was used to evaluate the inertial term of the equations of motion, as well as the expression in the general case of the blade element velocity components needed for the computation of aerodynamic loads, and then automatically generate the MATLAB^{ő} code used in the simulation model.

Due to the Lagrangian approach, the position of the blade element is expressed in the inertial frame [86]. The Lagrangian is composed of a kinetic contribution and a potential one (which depends only on elastic energy due to stiffness in rotor and feathering hinges whereas it does not depend on gravitational forces). Aerodynamic loads which determine the work of external forces on the rotor are evaluated by means of strip theory. To obtain the kinetic energy of rotor blades (paddles), the position of the blade element (or paddle element) is differentiated with respect to time and integrated along the blade (paddle) span.

The main features of this model are

- The rotor blades and paddles are rigidly connected to the hub;
- Lift and drag coefficients of blade sections are in tabular form for $-180 \leq \alpha \leq 180$ deg, and for Mach number between 0 and 0.8;
- Aerodynamic loads are computed by numerical integration over the blade span in the framework of blade element approach;
- A three–state Pitt-Peters dynamic inflow model (see section 2.4) is used whereas dynamic stall and unsteady aerodynamics effects are not included;
- Dynamic stall effects are not included, and static stall is considered in the lift and drag coefficients;
- Tip losses due to 3D effects are neglected;

- The shaft angular speed is constant, and the model of the propulsive system is not considered;
- The rotor is homokinetic.

These simplifying assumptions are similar to those used for the articular rotor individual blade models, if one acknowledges the minor differences related to the peculiarities of the gimballed rotor. The individual blade model has been used in a previous work for performance analysis, stability and handling qualities assessment [87]. In the present work the individual blade model is used to validate simplified models and to analyse rotor stability.

3.6.2 Simplified models

The full model provides a reliable description of helicopter behaviour, and its rotor in particular. Nevertheless the level of detail in the individual blade model does not allow to easily identify how single rotor configuration parameters affect the resulting dynamic behaviour. Nor it is possible to define simple linear models to analyse stability as the time–variant model requires Floquet analysis to evaluate stability regions and modes.

Furthermore the gimballed rotor configuration may include coning hinges with pitch–coning coupling and friction in the coning hinges. When the coning degrees of freedom are introduced (together with the difficulties in modelling friction), the individual blade model leads to an overly complex dynamics with relevant numerical problems due to different time scales of fuselage and rotor modes, compared to aerodynamic response characteristic times and the high frequency vibrations induced by the switching of the stick-slip friction model.

A simplified model of the gimballed rotor has thus been developed in order to analyse systematically the effect of rotor configuration parameters and of coning hinges. The simplified model has been validated against the full–order model by comparing rotor response, forces transmitted to the fuselage, and stability characteristics.

The gimballed rotor with coning hinges features a yoke connected to the main rotor shaft through a spherical joint, that allows two relative angular degrees of freedom for feathering and teetering, indicated in Fig. 3.7 as γ and β_0, respectively. The blades are connected to the yoke through coning hinges, placed at a distance r_c from the rotor axis, with a geometrical undersling h_c with respect to the centre of the gimbal.

The configuration is similar, in some respect, to the teetering rotor mounted on the Robinson R-22 helicopter, with the major difference that the spherical joint replaces the teetering hinge, thus allowing one more degree of freedom to the yoke. The isolated gimballed rotor model will be compared with an equivalent teetering one in terms of dynamic behaviour and response to controls. A simplified helicopter model is also derived, that features a vertical translational degree of freedom only (heave motion) with uniform dynamic inflow, in order to investigate the loads transmitted during a gust encounter and the effects of the pitch–coning link.

To generate the rotor model, three equations in vector form are written: one for the angular momentum balance of the whole rotor, considered as an articulated body,

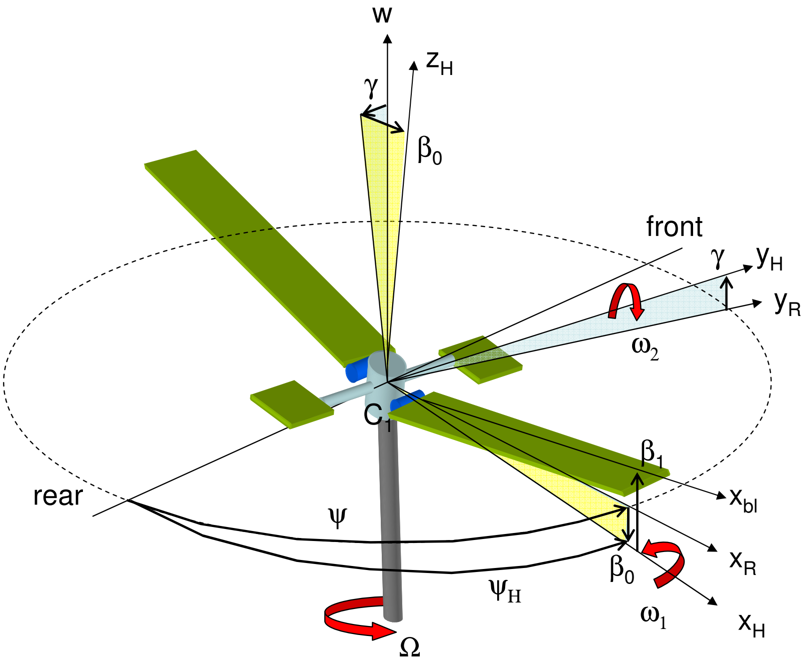

Figure 3.7. Gimballed rotor geometry.

the attitude of which is described by means of teetering and feathering angles (β_0 and γ) representing the inclination of the yoke with respect to the rotor shaft around the spherical gimbal; and two equations for the coning motion of each blade with respect to the yoke, β_i, i = 1,2 being the coning angles. The geometry of the hub-blade assembly and the position of coning hinges are shown in Fig. 3.8

Hub equations

In what follows, vector quantities are indicated with an arrow when they are not projected in any particular frame. According to the generalized Euler equations [5], hub motion is described using the centre of the spherical joint, O, as the pole for moments. Accordingly, angular momentum balance of the entire rotor is written as

$$\frac{\mathrm{d}\vec{\boldsymbol{h}}_O}{\mathrm{d}t} + m_{rot}\vec{\boldsymbol{r}}_{CM} \times \vec{\boldsymbol{a}}_O = \vec{\boldsymbol{m}}_O \tag{3.155}$$

where external torques $\vec{\boldsymbol{m}}_O$ and angular momentum $\vec{\boldsymbol{h}}_O$ are referred to O, $m_{rot}\vec{\boldsymbol{r}}_{CM}$ is the static moment of the rotor, $\vec{\boldsymbol{r}}_{CM}$ is the position vector of rotor centre of mass with respect to O and $\vec{\boldsymbol{a}}_O$ the absolute acceleration of the gimbal centre, O. The total angular momentum of the rotor with respect to O is given by

$$\vec{\boldsymbol{h}}_O = \boldsymbol{I}(\beta_1, \beta_2)\vec{\boldsymbol{\omega}} + \vec{\boldsymbol{h}}_1^{rel} + \vec{\boldsymbol{h}}_2^{rel}$$

where $\boldsymbol{I}(\beta_1, \beta_2)$ is the inertia tensor which, in the most general case, depends on the time–varying coning angles, β_1 and β_2, and $\vec{\boldsymbol{\omega}}$ is the hub angular velocity. The relative angular

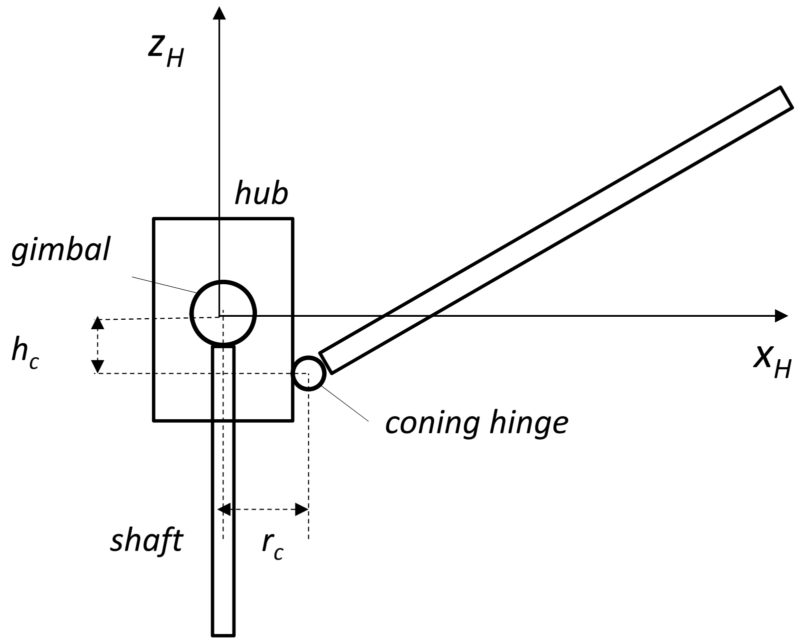

Figure 3.8. Gimballed rotor hub-blade geometry with coning hinges.

momentum due to the motion of the i–th blade relative to a reference frame fixed to the hub, $\vec{\boldsymbol{h}}_i^{rel}$, is expressed as

$$\vec{\boldsymbol{h}}_i^{rel} = \int_0^\ell \mu(x_b) \left[(\vec{\boldsymbol{r}}_{OC} + \vec{\boldsymbol{r}}_{CP}) \times \vec{\boldsymbol{v}}_P^{rel} \right] \mathrm{d}x_b \tag{3.156}$$

where $\mu(x_b)$ is the linear density of the blade, $\vec{\boldsymbol{r}}_{OC}$ is the position of the coning hinge with respect to the rotor centre, and $\vec{\boldsymbol{r}}_{CP}$ is the position of the blade element of the blade element $\mu(x_b)\mathrm{d}x$ with respect to the coning hinge, placed in P, at a distance x_b from the coning hinge along the blade span. The speed of the blade element $\mu(x_b)\mathrm{d}x$ relative to the hub is thus given by

$$\vec{\boldsymbol{v}}_P^{rel} = \frac{\mathrm{d}\vec{\boldsymbol{r}}_{CP}}{\mathrm{d}t}$$

Moments of Inertia

As outlined above, the inertia tensor of the rotor varies as a function of the coning angles. The inertia of the rotor is the sum of the contributions from central hub, $\boldsymbol{J}_H = \mathrm{diag}(J_{H_F}, J_{H_T}, J_{H_P})$, flybar $\boldsymbol{J}_{fb} = \mathrm{diag}(J_{fb}, 0, J_{fb})$, (where the fly–bar, aligned with the teetering axis, is assumed to have negligible inertia around it, its remaining moments of inertia being approximately equal) and blades. The contributions of the blades around teetering, feathering and polar axes are given respectively by

$$\begin{aligned}
J_{bl_T} &= 2\left\{m_b(r_C^2+h_C^2)+I_b+S_b\left[r_C(\cos\beta_1+\cos\beta_2)+h_C(\sin\beta_1+\sin\beta_2)\right]\right\}\\
J_{bl_F} &= 2\left[m_b h_C^2+S_b h_C(\sin\beta_1+\sin\beta_2)\right]+I_b(\sin^2\beta_1+\sin^2\beta_2)\\
J_{bl_P} &= 2\left[m_b r_C^2+S_b r_C(\cos\beta_1+\cos\beta_2)\right]+I_b(\cos^2\beta_1+\cos^2\beta_2)
\end{aligned}$$

where reference is made to the Nomenclature section for the meaning of the symbols. The blades also cause the presence of an off–diagonal term in the inertia tensor, equal to

$$J_{bl_{xz}} = S_b\left[r_C(\sin\beta_1-\sin\beta_2)+h_C(\cos\beta_1+\cos\beta_2)\right]+I_b(\sin\beta_1\cos\beta_1-\sin\beta_2\cos\beta_2)$$

Blade equations

Blade motion around the coning hinge is described by means of a vector equation formally identical to Eq. (3.155)

$$\frac{\mathrm{d}\vec{\boldsymbol{h}}_{C,i}^{rel}}{\mathrm{d}t}+m_b\vec{\boldsymbol{r}}_{CG,i}\times\vec{\boldsymbol{a}}_{C,i}=\vec{\boldsymbol{m}}_{C,i} \tag{3.157}$$

where moments are evaluated with respect to the coning hinge, C_i, and a single relative degree of freedom, β_i, is available around the hinge axes, $\mp\hat{\boldsymbol{j}}$, parallel to the y_H axis of the hub–fixed frame, $\mathcal{F}_H$, where the $-$ sign is used for blade #1, placed on the positive side of the x_H axis.

The relative angular momentum of the i–th blade $\vec{\boldsymbol{h}}_{C,i}^{rel}$ with respect to the hinge C_i is equal to

$$\vec{\boldsymbol{h}}_{C,i}^{rel}=\int_0^{\ell}\mu(x_b)\left(\vec{\boldsymbol{r}}_{CP}\times\vec{\boldsymbol{v}}_P^{rel}\right)\mathrm{d}x_b,\quad i=1,2 \tag{3.158}$$

where $m_b\vec{\boldsymbol{r}}_{CG,i}$ is the static moment of the blade with respect to C_i and

$$\vec{\boldsymbol{a}}_{C,i}=\frac{\mathrm{d}^2\vec{\boldsymbol{r}}_{OC}}{\mathrm{d}t^2}$$

is the absolute acceleration of C_i. The relative speed $\vec{\boldsymbol{v}}_P^{rel}$ of the mass element $\mu(x_b)\mathrm{d}x_b$ in P, with abscissa x_b counted along the blade span, is

$$\vec{\boldsymbol{v}}_P^{rel}=\vec{\boldsymbol{v}}_P-\vec{\boldsymbol{v}}_{C,i}.$$

Aerodynamics and controls

The moments of aerodynamic forces around coning hinges, $\boldsymbol{m}_{C,i},\ i=1,2$, and the corresponding torques around teetering and feathering axes, m_F e m_T, are expressed following the same simplifying approach described in Ref. [23], although the presence of aerodynamic paddles and additional coning degrees of freedom needs to be accounted for. The lift of each blade is expressed as

$$L_i\approx\frac{1}{6}\rho\Omega^2R^3c(1\pm3\mu\sin\psi)C_{L_\alpha}\alpha_i,\ i=1,2$$

It is assumed that L_i is applied at $0.7R$, where the upper and lower signs apply to the first and second blade, respectively. This convention will be adopted throughout the paragraph. Rotor inflow and blade drag are not included in the simplified model, as they were shown to have negligible effects on the dynamic behaviour of the gimballed rotor around the teetering and feathering axes, which is the focus of the present analysis.

The most relevant variation in the aerodynamic model with respect to that adopted in Ref. [23] are (i) the pitch–coning coupling, that introduces a variation in blade pitch as a function of coning angle, and (ii) the variation of blade incidence induced by coning rates. As a consequence of this latter effect, aerodynamic damping around the teetering axis, expressed in Ref. [23] simply as $-B\omega_2$ (where $B = 1.4/6 \cdot \rho R^4 c\Omega C_{L_\alpha}$), is now given by $-B[\omega_2 - \tau(\dot\beta_1 - \dot\beta_2)]$, where $\tau = (0.7R - r_c)/(0.7R)$, r_c accounts for the effect of the eccentricity of the coning hinge.

As for coning dynamics, the aerodynamic forcing term is given by lift acting with a moment arm equal to $0.7R - r_C$ with respect to the coning hinge. Note that in Ref. [23] it was not necessary to express the lift of the single blade, but only the lift unbalance between the two blades of the rotor.

In the presence of a coning rate and pitch–coning coupling, the angle of attack of the reference section at $0.7R$ is equal to

$$\alpha_i \approx \theta_0 \pm \theta_{cyc} \pm \omega_2/\Omega - K_{PC}\beta_i - \tau\dot\beta_i/\Omega + \Delta\alpha_{g_i} \tag{3.159}$$

where, together with standard control variables, namely, collective and cyclic pitch, θ_0 and θ_{cyc} , the effects of coning rate, $\dot\beta_i$, and pitch–coning coupling, $-K_{PC}\beta_i$, are accounted for. Variations of angle of attack due to a vertical gust, $\Delta\alpha_{g_i}$, are also considered, assuming that the two blades may enter the gust at different times, so that, in general, it is $\Delta\alpha_{g_1} \neq \Delta\alpha_{g_2}$.

The pitch command (considered as the blade rotation around the feathering axis with respect to the gimbaled yoke) is expressed as

$$\theta = \theta_0 \mp K_H(\phi_{SW}\cos\psi - \theta_{SW}\sin\psi + \gamma) \tag{3.160}$$

where the gain K_H gives the swash–plate/blade–pitch command ratio. This is something similar to what happens in teetering rotors equipped with a fly–bar, with the major difference that, in the present case, the fly–bar is rigidly connected to the yoke and it directly drives it by means of its flapping motion.

In order to maintain the validity of the small angle assumption, a reference condition at hovering is considered and response of rotor is considered only for small values of the advance ratio, $\mu = V/(\Omega R)$. At hovering, cyclic pitch commands are close to zero and each blade provides a constant lift force equal to half of the total weight of the vehicle, such that

$$L_1 = L_2 = \frac{1}{6}\rho\Omega^2 R^3 c C_{L_\alpha}(\theta_0 - K_{PC}\beta_h) = \frac{W}{2} \tag{3.161}$$

Coning and incidence angles can thus be expressed in the form

$$\begin{array}{rcl} \beta_i & = & \beta_h + \Delta\beta_i \\ \alpha_i & = & \alpha_h + \Delta\alpha_i \end{array} \quad i = 1,2$$

where

$$\Delta\alpha_i = \Delta\theta_0 \pm \theta_{cyc} \pm \omega_2/\Omega - K_{PC}\Delta\beta_i - \tau\dot{\beta}_i/\Omega + \Delta\alpha_{g_i}$$

At hovering $\beta_i = \beta_h$ and $\alpha_i = \alpha_h$, $i = 1{,}2$. Considering flight conditions at low advance ratio μ, the angular variables remain small and it is possible to express the lift developed by the blades in the form

$$L_i \approx \frac{W}{2}(1 \pm 3\mu\sin\psi) + \frac{1}{6}\rho\Omega^2 R^3 c C_{L_\alpha}\Delta\alpha_i$$

It is now possible to evaluate the moments acting on the elements of the gimballed rotor. Blade coning motion is driven by aerodynamic moment with respect to the coning hinge

$$m_{C_i}^{aero} = (0.7R - r_C) \times L_i$$

whereas the total moment acting on the rotor around the teetering axis passing through the centre of the spherical hinge is given by

$$\begin{aligned} N_2 = 0.7R \times (L_2 - L_1) = \\ = -2.1\mu W R\sin\psi - 0.233\rho\Omega^2 R^4 c C_{L_\alpha}(\theta_{cyc} + \omega_2/\Omega) \ + \\ +0.1167\rho\Omega^2 R^4 c C_{L_\alpha} \cdot [K_{PC}(\beta_1 - \beta_2) + \tau(\dot{\beta}_1 - \dot{\beta}_2)/\Omega - \Delta\alpha_{g_1} + \Delta\alpha_{g_2}] \end{aligned}$$

The last term includes the effects of possible aerodynamic load unbalance between the blades induced by a difference in either their coning motion or variation of local angle of attack induced by a gust.

The expression of the aerodynamic moment generated by the paddles around the rotor feathering axis is not affected by the configuration of the coning hinges. In dimensional terms the expression is

$$N_1 = -0.25\rho\Omega^2 R_{fb}^3 S_{fb} C_{L_{\alpha fb}}(\omega_1/\Omega)$$

Rotor equations of motion

After introducing the small angle assumption, such that $\cos\vartheta_i \approx 1$ and $\sin\vartheta_i \approx \vartheta_i$ with $\vartheta_i \in \{\gamma, \beta_0, \beta_1, \beta_2\}$, and writing all the equations in terms of the relevant vector components, a set of linear ordinary differential equations with periodic coefficients is derived for describing the motion of the central hub and blades, in terms of feathering and teetering degrees of freedom, and coning angles, respectively.

Feathering and teetering dynamics are expressed by the equations

$$\left[J_{H_F} + J_{FB} + 2m_b h_C^2\right]\dot{\omega}_1 = -\left[J_{FB} + (J_{H_P} - J_{H_T}) - 2m_b h_C^2\right]\omega_2\Omega + m_{H_F}$$

$$\begin{aligned} \left[J_{H_T} + 2I_b + 2m_b(r_C^2 + h_C^2) + 4S_b r_C\right]\dot{\omega}_2 + (I_b + S_b r_C)(\ddot{\beta}_2 - \ddot{\beta}_1) \\ = -\left[J_{H_F} - J_{H_P} + 2m_b(h_C^2 - r_C^2) - 4S_b r_C - 2I_b\right]\omega_1\Omega - (I_b + S_b r_C)(\beta_2 - \beta_1)\Omega^2 + m_{H_T} \end{aligned} \tag{3.162}$$

where $m_{H_F} = N_2 - K\gamma$ and $m_{H_T} = N_1 - K\beta_0$ are the external aerodynamic and elastic moments acting around the feathering and teetering axes of the spherical joint.

The equations for the relative motion of the blades with respect to the yoke are given by

$$I_b\ddot{\beta}_i \mp (I_b + S_b r_c)\dot{\omega}_2 + (I_b + S_b r_c)(\Omega^2\beta_1 \pm \Omega\omega_1) = m_{C_i} \tag{3.163}$$

where m_{C_i} is the total external moment applied around the coning hinge, which may include, together with the aerodynamic term, contributions from elastic, viscous or dry friction terms in the coning hinges.

The kinematic model is written in terms of teetering, feathering and coning angles, namely β_0, γ, β_1, and β_2. Under the small angle assumption, β_0 and γ represent the flapping and feathering rotations of the hub with respect to the rotating shaft–fixed frame (x_R, y_R, z_R), such that

$$\begin{aligned} \dot{\beta} &= -\tilde{\omega}_2 + \Omega\gamma && (3.164)\\ \dot{\gamma} &= \omega_1 - \Omega\beta && (3.165) \end{aligned}$$

The derivatives of the coning angles are simply equal to the coning rates, $\dot{\beta}_1$ and $\dot{\beta}_2$.

Note that the inclination of the hub with respect to the direction of the shaft can also be described by means of the angles u_1 and u_2 in a non-rotating frame, defined as

$$\begin{aligned} \vartheta_H &= -\beta\cos\psi + \eta\sin\psi && (3.166)\\ \varphi_H &= -\beta\sin\psi - \eta\cos\psi && (3.167) \end{aligned}$$

where the angle ϑ_H is positive when the hub is tilted in the rear direction, while φ_H is positive when it is tilted to the right.

Finally, a constant rotor angular rate Ω is assumed, so that it is possible to transform all the differential equations from the time domain into the angular variable ψ by means of the chain rule for derivatives, such that $\dot{x} = \mathrm{d}x/dt = (\mathrm{d}x/d\psi)(\mathrm{d}\psi/dt) = x'\Omega$. For second order derivatives, it is $\ddot{x} = x''\Omega^2$.

3.6.3 Teetering and rigid gimballed rotors

Teetering rotor models are derived from those representing the dynamics of a fully gimballed one by setting feathering angle and rate, γ and $\dot{\omega}_1$, equal to zero. The corresponding equations of motion, easily obtained from Eqs. (3.162) and (3.163) are not reported for the sake of conciseness.

In a similar way, freezing the coning degrees of freedom, such that $\beta_i = \beta_H$ and $\dot{\beta}_i = 0$, $i = 1{,}2$, the rigid gimballed rotor analysed in Ref. [23] is recovered, if the centre of mass of the resulting rigid rotor coincides with the centre of the spherical joint. In this case, after defining nondimensional angular velocity components as $\tilde{\omega}_i = \omega_i/\Omega$, $i = 1{,}2$, and dividing for $\dot{\omega}_i$ by $J_i\Omega^2$, the equations of motion achieve the compact form

$$\boldsymbol{x}' = \mathbf{A}(\psi)\boldsymbol{x} + \mathbf{B}(\psi)\mathbf{u}$$

where the state and control vectors are, respectively, $\mathbf{x} = (\tilde{\omega}_1, \tilde{\omega}_2, \gamma, \beta)^T$ and $\mathbf{u} = (\theta_{SW}, \phi_{SW})^T$. The state–matrix of the system is given by

$$\boldsymbol{A}(\psi) = \begin{bmatrix} -\frac{\gamma_{fb}}{2} & -1 & \frac{\gamma_{fb}}{2} J\mu^2 \cos\psi \sin\psi - k_1 - 2k_T K_H & 0 \\ 1 & -\frac{\gamma_b}{8} & \frac{\gamma_b}{8} K_H (1 + 2\mu^2 \sin^2\psi) & \frac{\gamma_b}{4}\mu^2 \cos\psi \sin\psi + k_2 \\ 1 & 0 & 0 & -1 \\ 0 & -1 & 1 & 0 \end{bmatrix} \tag{3.168}$$

whereas

$$\boldsymbol{B}(\psi) = \begin{bmatrix} 2k_T \sin\psi & 2k_T \cos\psi \\ \frac{\gamma_b}{8} & \frac{\gamma_b}{8} \\ 0 & 0 \\ 0 & 0 \end{bmatrix} \tag{3.169}$$

3.6.4 Friction

Due to the centrifugal load, a dry friction term in the coning hinge is introduced. A value equal to 100 Nm is assumedfor the considered blade mass and coning hinge geometry. The effects of friction on rotor dynamics and stability will be demonstrated to be significant. A simple friction model is adopted, letting

$$m_{C_i}^{fric} = -k_{fr}\text{sign}(\dot{\beta}_i) \tag{3.170}$$

where k_{fr} is a friction coefficient that depends on hinge characteristics and centrifugal force, whereas the sign function is defined as

$$\text{sign}(x) = \begin{cases} 1 & \text{if} \quad x > 0 \\ -1 & \text{if} \quad x < 0 \end{cases}$$

The friction torque is constant in magnitude and it works against the direction of coning motion. Note that within this simple friction model, stick–slip phenomena are not taken into account. Moreover, the sudden changes in sign of the friction torque introduce problems for (i) the numerical integration of the equations of motion and (ii) the evaluation of inertial loads, especially when the coning motion is close to an equilibrium and $\dot{\beta}_i \approx 0$.

A fixed–step integration algorithm was adopted for performing the numerical simulations, with an integration step $\delta\psi$ that resulted into a reasonable CPU time for the simulations, while maintaining rotor behaviour independent of $\delta\psi$ itself. At the same time a small "viscous interval" was introduced around the stick condition $\dot{\beta}_i \approx 0$, which avoids non–physical high–frequency variations of inertial forces.

3.6.5 Coupled rotor–fuselage heave motion

In order to investigate rotor loads during gust encounters and the effects of the pitch–coning coupling, a vertical translational degree of freedom for the fuselage is introduced (heave motion). Furthermore, a uniform first–order dynamic inflow model was included in the model , resulting in a 11^{th} order system, to consider all the time–scales relevant to the response.

Rotor thrust sustains both vehicle's weight and its drag, evaluated by means of an equivalent parasite area. The intensity of the flow impinging on the fuselage is given by the vector sum of helicopter vertical speed and inflow. Inertial coupling between coning motion and fuselage vertical displacement is also significant and it is included in the model.

Chapter 4

Steady–state performance

This chapter and the following one are dedicated to the description of techniques for the evaluation of rotorcraft behaviour and the analysis of the effects of model complexity on prediction of performance and handling qualities. In particular the present chapter presents steady–state performance which can be obtained by means of rotorcraft trim. Chapter 5 is dedicated to helicopter handling qualities with a focus on linearization and inverse simulation. A wide set of models with different complexity all representing the same rotorcraft (the UH-60A “Blackhawk” helicopter) has been developed.

4.1 Reference models for the analysis

A set of models ranging from a medium complexity one to lower order simulators has been developed in the framework of helicopter performance and dynamic behaviour analysis. Table 4.1 summarizes the characteristics of all the models considered in the analysis in form of a test matrix. Line types and markers used for all the plots in chapters 4 and 5 are also reported for each model.

Rotor models of decreasing complexity are listed top–down in the rows from 1 to 9, whereas fuselage aerodynamic models of decreasing complexity are listed in the columns labeled A and B. The resulting number of states for the models is indicated in the fourth column. A combination of letter (A or B) and number identifies each model. A static model for helicopter at trim is derived from Ref. [5] and it is indicated as Model C at the bottom of the list. As the simplest model it has no dynamic states as it is based only on force and moments balance and no equation of motion is written.

Also some of the dynamic models share a strong link with models proposed in literature. In particular, Model A1 corresponds to the UH-60 “Blackhawk” helicopter model described in [15]. Minor differences are present in the fuselage aerodynamic model, which was modified removing a few discontinuities, thus making it able to simulate a wide range of manoeuvres, including backward flight. Model A6 describes the same helicopter modeled according to the approach discussed in Ref. [14]. The simplest model, indicated as B9, was developed according to the guidelines reported in Ref. [11]. These four reference models, indicated by boldface letters in Tab. 4.1, represent the backbone of the analysis, whereas intermediate ones will be used in order to highlight the relevance of specific aspects of the simplifications adopted on performance and handling qualities analysis.

The impact of fuselage aerodynamic model on helicopter performance evaluation has been taken into due consideration, an analysis often neglected in other studies. The models have been tested either with a complete fuselage aerodynamic force and moment coefficient database or with a much simpler model based on parasite drag area. The following sections presents the models used in the analysis in greater detail, describing the main features and differences among them.

Table 4.1. Rotorcraft models test matrix (with line–style legend for the plots).

Main rotor				**Fuselage aerodynamics**	
Blade dynamics		Inflow model	No. of states	From database	Parasite area
Articulated	flap, lag & twist	3 state dynamics	37	**A1** —■—	
	flap & lag	3 state dynamics	29	A2 —●—	
	flap only	3 state dynamics	21	A3 —▲—	
2^{nd} order TPP dynamics	coning, lat. & long. flap coeff.	3 state dynamics	19	A4 -▼ -	
	coning, lat. and long. flap coeff.	unif. dyn. inflow	17	A5 -□ -	
	coning, lat. and long. flap coeff.	unif. static inflow	15	**A6** -○ -	B6 -× -
1^{st} order TPP dynamics	coning, lat. & long. flap coeff.	unif. dyn. inflow	14		B7 -·*·-·
	coning, lat. and long. flap coeff.	unif. static inflow	12		B8 -·+-·
	decoup. lat. & long. flap coeff.	unif. static inflow	11		**B9** —·—
no dynamics	decoup. lat. & long. flap coeff.	unif. static inflow	n.a.		**C** ··△·

4.1.1 Individual blade models

A first set of 3 rotor models is considered, which features an individual blade dynamic model. In the most complex version, the model features a full nonlinear description of fuselage aerodynamics; rigid articulated blades with a dynamic twist model; an accurate representation of the lag damper; a 3 state dynamic model of main rotor inflow, and a simple tail rotor model with dynamic uniform inflow. The equation of these models are developed following the approach described in the articulated rotor, individual blade description (section 3.1).

The evaluation of aerodynamic loads on the blades is based on airfoil lift and drag coefficients given in tabular form for $-180 \leq \alpha \leq 180$ deg and $0 \leq M \leq 1$.

A1: Individual blade with flap, lag, and twist DoFs

The baseline reference model for the present analysis is representative of an articulated blade, single main rotor transport helicopter, the Sikorsky UH-60. A fully nonlinear description of fuselage and empennage aerodynamics is coupled with a rotor model which features rigid articulated blades with an accurate representation of the lag damper. Effects of blade torsional deformation are included, while blade, shaft and fuselage elastic modes and engine dynamics are neglected (constant rotor rotational speed is assumed). Power required from the main and tail rotor is evaluated from the shaft torques in order to estimate vehicle limiting performance as a function of flight condition and engine expected maximum available power at the considered altitude.

Aerodynamic loads are obtained by numerical integration in the framework of blade element theory, where airfoil lift and drag coefficients are given in tabular form for $-180 \leq \alpha \leq 180$ deg and $0 \leq M \leq 1$, in order to take into account at least approximately the effects of stall and reverse flow on the retreating blade and those of compressibility on the advancing blade. Among other minor differences with respect to the original model described in [15] and [17], the formulation adopted for the evaluation of rotor aerodynamic loads is based on a conventional definition of the blade element $c\,\mathrm{d}y_b$, lying in a direction perpendicular to the blade axis y_b, with effective velocity and angle of attack evaluated as the magnitude of the velocity component perpendicular to the blade axis and its inclination with respect to the blade chord, respectively. Five blade elements were considered for each blade. No 3-D aerodynamic effects, such as blade–vortex interaction, nor other important 2-D aerodynamic effects, such as circulation hysteresis are included in the model.

The fuselage aerodynamic database is extended by means of an interpolation in spherical coordinates of available data, providing aerodynamic force and moment coefficients in tabular form for every possible set of values of aerodynamic angles in the range $-180 \leq \alpha \leq 180$ deg and $-90 \leq \beta \leq 90$ deg.

A 3–DoF dynamic model of main rotor inflow (see section 2.4), and a simple tail–rotor model with dynamic uniform inflow are assumed. Rotor wake coupling with fuselage and empennage aerodynamics is considered by means of simple velocity composition and some empirical coefficients [15], but no rotor wake distortion is included in the model. In this respect, the rotor model is a Level 1.4 model, as far as blade dynamics is concerned, while it is an intermediate model between Level 1 and 2 for the evaluation of aerodynamics loads on the blades. Fuselage aerodynamic model is represented by a database of force and moment coefficients depending on aerodynamic angles α_f and β_f.

In compact form, the reference model is defined by a set of 37, time variant, nonlinear ordinary differential equations

$$\begin{aligned} \dot{\boldsymbol{x}} &= \boldsymbol{f}\left(\boldsymbol{x}, \boldsymbol{u}, t\right) \\ \boldsymbol{y} &= \boldsymbol{g}\left(\boldsymbol{x}\right) \end{aligned} \tag{4.1}$$

where the helicopter state vector can be partitioned as follows:

$$\boldsymbol{x} = (\boldsymbol{x}_f,\ \boldsymbol{x}_r,\ \boldsymbol{x}_\lambda)^T$$

where $\boldsymbol{x}_f = (u, v, w, p, q, r, \phi, \theta, \psi)^T$ collects fuselage rigid body states, $\boldsymbol{x}_r = (\boldsymbol{x}_{r_1}^T, \boldsymbol{x}_{r_2}^T, ..., \boldsymbol{x}_{r_{N_b}}^T)^T$, with $\boldsymbol{x}_{r_i} = \left(\beta_i, \dot{\beta}_i, \zeta_i, \dot{\zeta}_i, \varphi_i, \dot{\varphi}_i\right)^T$, lists rotor flap, lag and twist angles and their derivatives for all the blades, and finally the vector $\boldsymbol{x}_\lambda = (\nu_0, \nu_c, \nu_s, \nu_{0_{tr}})^T$ features main rotor and tail rotor inflow states. The control vector $\boldsymbol{u} = (\theta_0, A_{1_S}, B_{1_S}, \theta_{0_{tr}})^T$ contains pilot commands on main rotor collective, lateral and longitudinal cyclic pitch and tail rotor collective pitch. Finally the reference model output vector $\boldsymbol{y}$ contains all the output variables needed for the guidance and inverse simulation step. The choice of a suitable set of output variables will be discussed in Chapter 5.

A2: Individual blade with flap and lag DoFs

Model A2 is obtained from model A1 by removing blade twist degrees of freedom while keeping every other aspect of the original helicopter model, including, in particular, the inflow model and blade airfoil and fuselage aerodynamic coefficients. Only the equivalent blade torsional stiffness is no longer necessary, so that the overall amount of information necessary for developing this models is not significantly reduced, the major savings being related to the reduction of system order, from 37 to 29 state variables for model A2. Compared to model A1, only the rotor state is different so that $\boldsymbol{x}_{r_i} = \left(\beta_i, \dot{\beta}_i, \zeta_i, \dot{\zeta}_i\right)^T$. The dynamic twist has a very limited impact on performance evaluation apart from generating a constant shift in main rotor collective. For this reason Model A2 will not be used in the steady–state performance analysis as its results almost perfectly overlap those derived from Model A1.

A3: Individual blade with flap DoFs

Model A3 is obtained from model A1 by removing blade twist and lag degrees of freedom while keeping every other aspect of the original helicopter model, including, in particular, the inflow model and blade airfoil and fuselage aerodynamic coefficients. The equivalent blade torsional stiffness and lag damper data are no longer necessary, the latter representing a significant simplification of the blade model, when one acknowledges the level of detail necessary for a complete description of the lag damper. Moreover, major savings in terms of computational time are obtained from to the reduction of system order, from 37 to 21 state variables and the reduction of the coupling matrix. Model A3 rotor state vector is $\boldsymbol{x}_{r_i} = \left(\beta_i, \dot{\beta}_i\right)^T$

4.1.2 2^{nd} order TPP dynamics

A more compact representation of rotor dynamics is obtained in terms of rotor flapping coefficients (Chapter 3.2). In this case the flap angle of each blade is expressed in terms of a Fourier series expansion, truncated at the fundamental frequency Ω,

$$\beta(\psi) = a_0 - a_1 \cos\psi - b_1 \sin\psi$$

where, coning, longitudinal and lateral flapping coefficients represent “global” rotor state variables, $\boldsymbol{x}_r = (a_0, a_1, b_1)^T$, and the individual blade model is lost. Assuming small flap angles and linear aerodynamics, a second order dynamics for $\boldsymbol{x}_r$ is obtained in the form (see Eq.(3.85)):

$$\mathbb{M}_{TPP}\ddot{\boldsymbol{x}}_r + \tilde{\boldsymbol{D}}\dot{\boldsymbol{x}}_r + \tilde{\boldsymbol{K}}\boldsymbol{x}_r = \tilde{\boldsymbol{f}}(t) \tag{4.2}$$

Under these assumptions, rotor loads are evaluated analytically, in terms of average values over one revolution for forces and moments transmitted to the rotor hub. With respect to the original rotor model developed by Chen [12], a more accurate rotor inflow model is assumed, featuring a triangular induced velocity distribution (Model A4), which is then simplified into a uniform dynamic inflow model (A5) and a uniform, quasi–steady one for both main and tail rotors (A6), as in the original version. The number of states thus decreases from 19, for model A4, to 17 for A5 and only 15 for A6.

At the latter level, the effects of different fuselage aerodynamic models is also considered, where in the absence of a complete set of wind–tunnel experiments, only parasite area estimate (B6) is available. This aspect does not affect the number of dynamic states, but only the amount of information necessary for building the vehicle model.

4.1.3 1^{st} order TPP dynamics

An even simpler representation of rotor dynamics is obtained by neglecting inertial coupling between rotor and fuselage. This is equivalent to assuming that, starting from the rotor model described in Section 3.2, the term $\mathbb{M}_{TPP}\ddot{\boldsymbol{x}}_r$ in Eq. (4.2) is negligible with respect to the others, so that rotor response can be modeled as

$$\dot{\boldsymbol{x}}_r = \tilde{\boldsymbol{D}}^{-1}\left[\tilde{\boldsymbol{f}}(t) - \tilde{\boldsymbol{K}}\boldsymbol{x}_r\right] \tag{4.3}$$

where only aerodynamic coupling between lateral and longitudinal flapping coefficients and the effects of forward speed on rotor response are thus retained in the model. Only the simplest fuselage aerodynamic model and uniform main rotor inflow are considered in this framework, featuring either a dynamic variation of induced velocity as a function of thrust coefficient (Model B7, with 14 states) or a quasi–static one (12^{th} order model, B8).

In the simplest model B9, equivalent to that described in Ref. [11], decoupled first–order dynamics for lateral and longitudinal flapping coefficients is assumed. Time–constants are held fixed over a wide portion of the flight envelope, and a correction for low values of the advance ratio is included in order to simulate the so–called rotor dihedral effect at low speed [11].

In the analysis of steady–state conditions, a 2^{nd} order model and its equivalent 1^{st} oder one provide the same results. In fact trim conditions are evaluated by forcing to zero rates and accelerations of tip–path–plane variables together with derivatives of fuselage states. As the tip–path–plane states velocity are required to be equal to zero, the same trim result is obtained by a 2^{nd} and 1^{st} order TPP models based on the same assumptions. For this reason no 1^{st} oder model is included in the performance analysis, whereas they are used extensively in the section that deals with handling qualities.

4.1.4 Static models

Model C (i.e. Level 0 complexity) is based on Bramwell's analysis of helicopter performance [5]. This approach does not allow to derive a dynamical model (no equations of motion are written), but helicopter equilibrium conditions are evaluated balancing forces and moments acting on the fuselage. Forces and moments generated by the rotor are expressed as a function of attitude angles, collective and cyclic pitch, and flapping angles which are described by means of first-order harmonic approximation. The major simplifying assumptions are related to the description of the main rotor, where blade element theory is adopted for estimating main rotor thrust and inplane force. Fuselage drag is evaluated assuming a constant parasite fuselage area independent of aerodynamic angles and flight condition. Lateral trim (i.e. lateral cyclic pitch and roll attitude), is evaluated after the longitudinal variables are set to their equilibrium conditions, by balancing roll moments and lateral forces, taking into account the sidewise projection of rotor thrust, tail rotor thrust (which is calculated as to compensate main rotor torque) and the projection of gravity acceleration along the pitch axis. The configuration data required for Model C are reported in Tab. A.2. It should be noted how a few parameters are sufficient, in this case, to obtain information on helicopter expected performance and command travel, within the simplifying assumptions discussed here. Note also that, for a conventional, articulated blade helicopter, this simple model is expected to perform relatively well, in spite of these simplifying assumptions.

4.2 Trim techniques

One of the objective of the work is to analyse the effect of model complexity on steady–state performance evaluation, as a consequence a trim technique is required for each model used in the analysis. Among all models described in table 4.1, Models A1 and A3 represent individual blade models, Models A4, A6 and B6 TPP models, and finally Model C an example of simple descriptions for preliminary performance evaluation. This section is dedicated to the solution of the trim problem, while the following collects the performance results evaluated on the basis of all the models.

As outlined by Peters and Barwey [28], the word *trim* may undergo different interpretations when dealing with its application to a helicopter. In what follows, the problem of *trimming a helicopter model* will be considered as *the determination of a set of controls that result in a steady flight condition with prescribed properties (in terms of velocity, rate of climb and turn rate) at least in an average sense.* Even in the framework of this particular definition, the problem of helicopter trim remains strongly coupled with rotorcraft modeling level.

The definition of a suitable set of mathematical conditions to be enforced also depends on the model but, in general, two sets of equations are always present in the formulation of a trim problem: (i) a set of requirements for enforcing a steady flight condition and (ii) a set of trim constraints for enforcing the desired flight conditions.

4.2.1 Algebraic trim

When individual rotor blade dynamics is not included in the model (Models A4, A6, and B6), TPP orientation and rotor loads averaged over a rotor revolution are analytically determined as functions of flight condition and main and tail rotor control settings. In this case the trim problem can be formulated in a form very similar to the fixed–wing aircraft case, where the equations of motion for fuselage and rotor variables are cast in the form of a set of nonlinear ordinary differential equations,

$$\dot{\boldsymbol{x}} = \boldsymbol{f}(\boldsymbol{x}, \boldsymbol{u}) \tag{4.4}$$

where $\boldsymbol{x} = (\boldsymbol{x}_F^T\ \boldsymbol{x}_R^T)^T$, $\boldsymbol{x}_F^T = (u, v, w, p, q, r, \phi, \theta, \psi)^T$ are fuselage states, $\boldsymbol{x}_R^T$ are rotor states and $\boldsymbol{u} = (\theta_0, A_{1s}, B_{1s}, \theta_{0_{TR}})^T$ are control variables. As an example, in Model A4, where the rotor is described by 2$^{\text{nd}}$ order TPP dynamics and 3-states inflow, the rotor state vector is equal to $\boldsymbol{x}_R^T = (\dot{a}_0, \dot{a}_1, \dot{b}_1, a_0, a_1, b_1, \nu_0, \nu_c, \nu_s)^T$

The steady–state condition requires that state and control variables at trim, $\boldsymbol{x}_e$ and $\boldsymbol{u}_e$, satisfy the equilibrium conditions

$$\boldsymbol{f}(\boldsymbol{x}_e, \boldsymbol{u}_e) = \boldsymbol{0} \tag{4.5}$$

whereas the trim constraints require that

$$u_e^2 + v_e^2 + w_e^2 = \bar{V}^2 \tag{4.6}$$

$$u_e \sin\theta_e - v_e \sin\phi_e \cos\theta_e - w_e \cos\phi_e \cos\theta_e = \bar{\dot{h}} \tag{4.7}$$

$$(q_e \sin\phi_e + r_e \cos\phi_e)/\cos\theta_e = \bar{\dot{\psi}} \tag{4.8}$$

where the bar denotes desired values of variables at trim. In a steady-state coordinate turn the rate of turn (which is enforced by Eq. (4.7)) can be related to angular velocities as $\bar{\dot{\psi}}^2 = \bar{\omega}^2 = p_e^2 + q_e^2 + r_e^2$. Since there are 11 equations and 13 unknowns, two additional conditions are required for closing the problem. Note that this is a minor difference with respect to the fixed wing aircraft where the yaw angle ψ can always be assumed 0 at trim, without loss of generality. In particular either the heading or the yaw angles can be assumed equal to 0 without loss of generality. For the helicopter case one constraint is derived from the relation between yaw, sideslip and heading angles. The simplest approach is to assume the heading angle equal to 0. This is equivalent to assuming the projection of the velocity vector on the horizontal plane as reference direction. The yaw angle, counted with respect to this reference direction, is maintained among the trim variables, providing the information on the misalignment of the vehicle longitudinal axis with respect to the direction of motion. A further trim condition is still required to close the problem. Several alternatives are possible, the most common ones being flight at zero sideslip ($v_e = 0$) or zero roll angle ($\phi_e = 0$) for rectilinear flight or zero lateral acceleration in a steady turn (that is, a requirement for a coordinated turn). Different choices are also interesting, such as minimum control effort or minimum power, etc. When the zero sideslip condition is enforced, due to the relation between the Euler and aerodynamic angles, roll angle can be evaluated as [88]:

$$\tan\phi_e = \frac{\sin\psi_e\cos\bar{\gamma}}{\sin\theta_e\cos\psi_e\cos\bar{\gamma} + \cos\theta_e\sin\bar{\gamma}}$$

It is possible to exploit kinematic relations at equilibrium in order to solve analytically at least some of the equilibrium and trim conditions, thus reducing the order of the algebraic system to be solved. In this way the number of unknowns can be reduced to 6 [6]. This means that only ψ_e and θ_e plus the 4 control variables are left as unknowns, to be determined from the equilibrium conditions for force and moments equations, $\dot{u} = \dot{v} = \dot{w} = 0$, and $\dot{p} = \dot{q} = \dot{r} = 0$.

For steady rectilinear flight, these latter conditions are equivalent to the equilibrium of external force and moments acting on the helicopter fuselage. Bramwell [5] proposes an analytical procedure for evaluating trim conditions by enforcing equilibrium in the longitudinal plane first and then along the lateral axis. This approach was used to evaluate trim conditions for Model C. On the converse, when TPP and inflow states are included in the model (Models A1 to B6), an equilibrium is obtained when the time derivatives these states are equal to zero, together with fuselage force and moment equilibrium conditions. The resulting set of algebraic equations is solved numerically by means of a Newton-Raphson scheme.

If the model features rotor blade dynamics, a steady–state flight condition is periodic in nature. In this case, two different approaches have been followed in the evaluation of trim conditions: a novel trim technique based on rotor shooting with average forces and moments equilibrium on the fuselage and full–order periodic–shooting for the complete helicopter model.

4.2.2 Nested trim

In order to enforce a rotor periodic equilibrium, each blade and inflow variable is required to achieve the same conditions after one revolution. If one neglects the small variations of fuselage rigid–body variables, the values of $\boldsymbol{v}_B$ and $\boldsymbol{\omega}_B$ become constant and the effects of fuselage acceleration on blades dynamics are thus neglected. In such a way it is possible to identify rotor steady states by means of a shooting algorithm, where the blades equations of motion are numerically integrated from a given set of initial conditions that are adjusted until the periodicity conditions are satisfied [17].

Remembering that, for a correctly balanced rotor, all the blades follow the same trajectory at steady state, the shooting problem for a single blade is solved over a whole revolution or for the whole set of blades over a fraction $2\pi/N_b$ of a revolution [26], where the periodicity conditions are substituted by the requirements that each blade at the end of the $2\pi/N_b$ integration period achieves a final state equal to the initial condition of the following one. This condition is expressed in mathematical term by the equations:

$$\boldsymbol{x}_R(\psi_0 + 2\pi/N_b) = \boldsymbol{P}_{N_b}\boldsymbol{x}_R(\psi_0) \quad ; \quad \dot{\boldsymbol{x}}_R(\psi_0 + 2\pi/N_b) = \boldsymbol{P}_{N_b}\dot{\boldsymbol{x}}_R(\psi_0) \tag{4.9}$$

where $\boldsymbol{P}_{N_b}$ is the $N_b \times N_b$ permutation matrix

$$\boldsymbol{P}_{N_b} = \begin{bmatrix} 0 & 1 & 0 & \dots & 0 & 0 \\ 0 & 0 & 1 & \dots & 0 & 0 \\ \dots & \dots & \dots & \dots & \dots & \\ 0 & 0 & 0 & \dots & 1 & 0 \\ 0 & 0 & 0 & \dots & 0 & 1 \\ 1 & 0 & 0 & \dots & 0 & 0 \end{bmatrix}$$

and $\boldsymbol{x}_R$ represents either the flap, lag or twist states.

Once rotor blade periodic motion is known, average inertial and aerodynamic loads transmitted via the rotor hub to the helicopter fuselage are evaluated. The problem of fuselage trim is thus rephrased exactly in the same form as that outlined in the pure algebraic trim in the previous subsection, requiring force and moment equilibrium plus a proper set of trim conditions [89]. In this way a nested trim algorithm is derived where, at the inner level, the current value of rigid–body states and control variables is adopted for determining rotor blade periodic motion, while at the outer level, the unknowns related to rigid–body states and controls are varied until the average loads satisfy the required equilibrium. The resulting set of shooting (for rotor states) and algebraic trim conditions (for fuselage states) are solved by means of a numerical technique, such as the Newton–Raphson method. The approach was tested on Model A1 and results tested against a full–order model shooting.

4.2.3 Periodic trim for full-order model

In those cases when a detailed analysis of the trim condition is sought, it is necessary to take into account the coupled periodic variation of all fuselage, rotor and inflow states. The shooting technique can be applied to the whole set of ordinary differential equations representing rotorcraft dynamics. In order to solve for the 4 control variables while setting the desired trim flight condition, 4 additional constraints need to be enforced. Because of the time–varying nature of the problem, these trim conditions are enforced in an average sense, in the form

$$\int_0^{2\pi/N_b} \left(\bar{V} - \sqrt{u^2 + v^2 + q^2}\right) \mathrm{d}\psi \;=\; 0 \tag{4.10}$$

$$\int_0^{2\pi/N_b} \left[\bar{\dot{h}} - (u\sin\theta - v\sin\phi\cos\theta - w\cos\phi\cos\theta)\right] \mathrm{d}\psi \;=\; 0 \tag{4.11}$$

$$\int_0^{2\pi/N_b} \left[\bar{\dot{\psi}} - (q\sin\phi + r\cos\phi)/\cos\theta\right] \mathrm{d}\psi \;=\; 0 \tag{4.12}$$

$$\int_0^{2\pi/N_b} \left[\sin\phi - \frac{\dot{\psi}}{g}(u\cos\phi + w\tan\theta)\right] \mathrm{d}\psi \;=\; 0 \tag{4.13}$$

Equation (4.13) represents the additional trim condition with a requirement for zero average lateral acceleration a_y. For a desired turn rate $\bar{\dot{\psi}} \neq 0$ this condition results into a requirement for a coordinated turn, whereas for $\bar{\dot{\psi}} = 0$ a zero average value of the yaw angle is requires. For steady rectilinear flight at advance rations $\mu = \bar{V}/(\Omega R) < 0.1$, Eq. (4.13) is replaced by

$$\int_0^{2\pi/N_b} [\sin\phi(\sin\theta\cos\psi\cos\bar{\gamma} + \cos\theta\sin\bar{\gamma}) - \cos\phi\sin\psi\cos\bar{\gamma}]\,\mathrm{d}\psi = 0 \tag{4.14}$$

that is, a requirement for zero average sideslip angle [17].

4.3 Validation

In the development of helicopter mathematical models, the validation phase is a fundamental step to assess the validity of the approach. Unfortunately flight data or even wind tunnel test data are available only for a limited set of helicopter, while most of the information is proprietary. As an example Yeo et al. [90] compare the results of the CAMRAD/II comprehensive analysis software with the flight test results obtained by means of the UH60 airload project [91] during which an extensive flight–testing campaign was conducted. For the present work, model A1 is compared with flight test data published in [92] and used as a reference also in [17]. Trim data in level flight are evaluated for a helicopter mass of 6,600 kg and at an altitude of 5400 ft. The results are also compared with a model developed in Flightlab [36] with a similar level of complexity (no dynamic twist).

Figure 4.1 compares the command required to trim the helicopter. Main rotor collective and longitudinal cyclic pitch show a very good agreement between model developed for this analysis, Flightlab and flight test, meaning that the longitudinal behaviour is well represented. Lateral behaviour is less well described, as can be seen for the lateral cyclic pitch and the tail rotor in particular. As can be seen in figure 4.2 a different trimming approach has been used for model A1 and for the model analysed in Flightlab. Model A1 trim enforces zero roll angle when $\mu > 0.1$, conversely Flightlab trim requires nonzero roll angle even at high advance speeds. For this reason, as well as differences in the tail rotor model, lateral direction commands show some disagreement at low to medium speeds between the models and flight tests.

Finally figure 4.3 represent necessary power as a function of advancing speed. Although Model A1 and Flightlab tend to underestimate power requirement at high speed, the results are nevertheless close to flight tests. Given its ability to correctly represent command, attitude as well as power, model A1 will be used in the sequel as a reference to evaluate the ability of lower order models to provide a reliable estimate of helicopter steady–state behaviour.

4.4 Maximum performance in steady flight conditions

Limiting performance (maximum speed, ceiling, rate of climb and rate of turn) are obtained from the determination of the flight conditions where power required at trim matches the

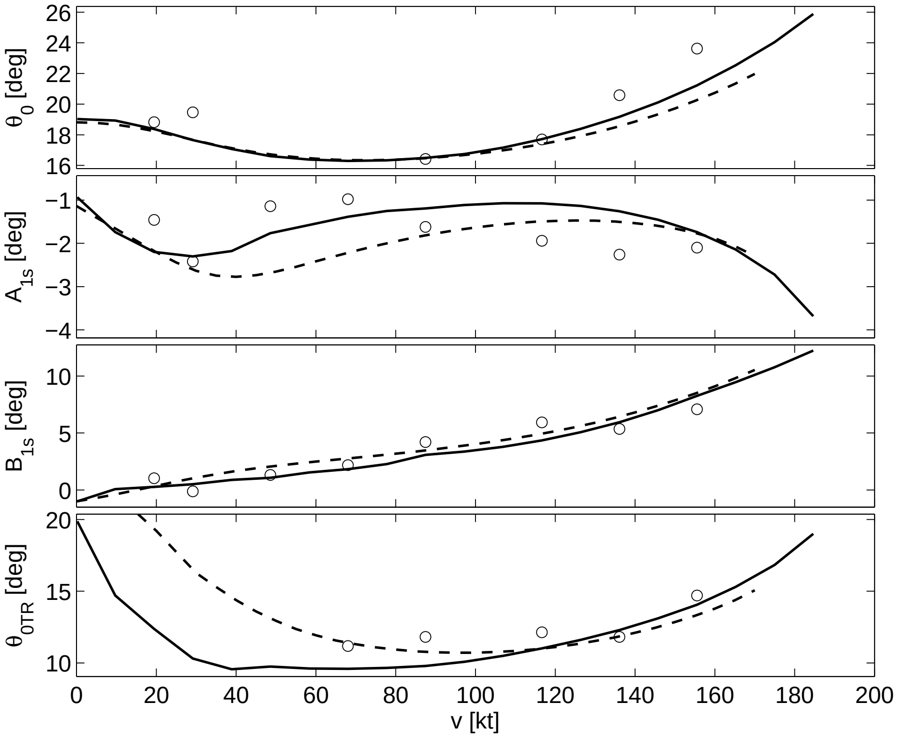

Figure 4.1. Validation of UH–60A commands evaluation for a 6,600 kg fuselage mass at 5400 ft altitude: model A1 (—), Flightlab (- - -), flight test (o).

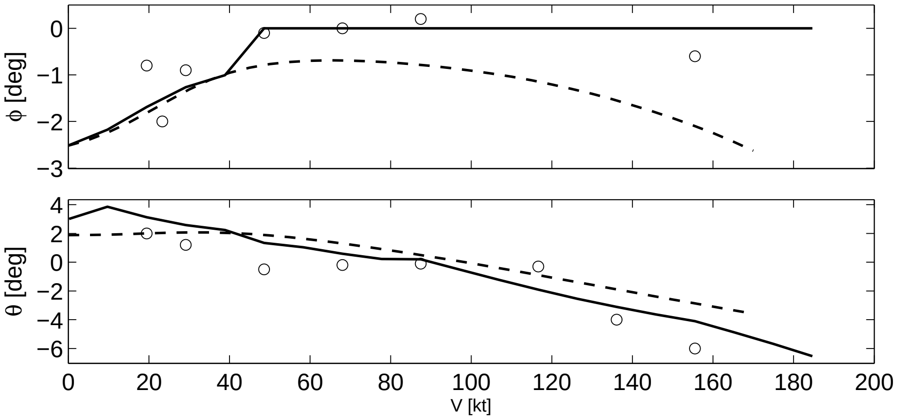

Figure 4.2. Validation of UH–60A attitude evaluation for a 6,600 kg fuselage mass at 5400 ft altitude: model A1 (—), Flightlab (- - -), flight test (o).

maximum available power. Available power is evaluated as a function of sea level maximum power and altitude. No correction for helicopter speed is introduced and all data are for a standard atmosphere temperature (15°C at sea level). Required power is evaluated adding main rotor and tail rotor power absorption plus a 5% margin for secondary power system

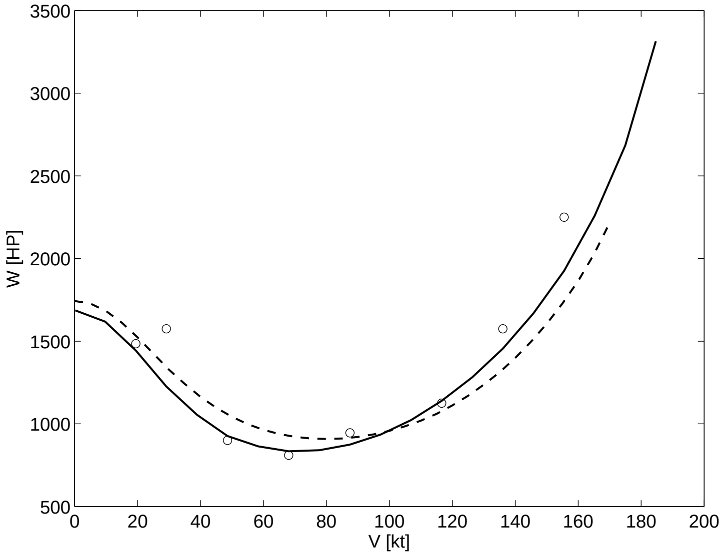

Figure 4.3. Validation of UH–60A required power for a 6,600 kg fuselage mass at 5400 ft altitude: model A1 (—), Flightlab (- - -), flight test (o).

and transmission losses.

The flight envelope is evaluated by merging data on maximum speed in level flight at increasing altitude with ceiling limits determined at different flight speed. Ceiling is evaluated as the maximum altitude at which the helicopter is able to sustain level flight at the desired speed. Maximum rate of climb (ROC) and rate of turn (ROT) are evaluated at various flight velocities ranging between hover and maximum speed. Trim in turning flight is determined assuming a coordinated turn condition (that is, zero average lateral acceleration, $\bar{a}_y = 0$).

In the evaluation of trim conditions, individual blade models (namely, Models A1 and A3) require a shooting algorithm and a complete set of data for the considered helicopter. Data from Ref. [15] were used for the Sikorsky UH–60 helicopter, in the present analysis. The shooting technique is applied over a fraction $2\pi/N_b$ of rotor revolution with averaged trim conditions [17] . The corresponding performance limits are regarded as the most accurate estimate of the UH–60 operational envelope, on the basis of the available model. These data are compared with flight test results found in the literature [92].

The trim algorithm with nested shooting and averaged rotor loads [89] is also tested on Model A. The results are compared with those obtained for the full–order shooting method, in all the considered flight conditions. A very good agreement between the results is obtained, either when command travel or maximum performance are compared.

The algebraic conditions corresponding to the definition of steady state flight for Models A4, A6, and B6 are determined by enforcing that all time–derivatives of rotor, inflow and fuselage states are equal to zero (see Eq. (4.5), and that horizontal and vertical speeds and rate of turn are equal to prescribed desired values (Eqs. (4.6) to (4.7)). The algebraic Model F provides an analytical approach for the determination of steady rectilinear flight conditions [5], and, as a consequence, it does not allow for the analysis of trim conditions in turning flight. Data for performance in steady coordinated turns are thus evaluated for Models A1 to B6 only.

Limiting performance are determined by means of an algorithm which starts from a reference level flight condition. The parameter under analysis (speed, altitude, ROC, or ROT) is then increased and trim conditions evaluated until the required power P_r exceeds the available one, $P_a(h)$. A secant method is then used to evaluate the limit value of the considered performance index, where required power exactly matches the available power, that is, $P_r = P_a$, within a prescribed relative tolerance ε. In the present analysis a value of $\varepsilon = |P_r - P_a| = 10$ HP was selected, equal to 0.4% of the maximum available power at sea level $P_{\max,SL}$.

4.4.1 Steady level flight

Figure 4.4.a shows the UH–60 estimated flight envelope in the $h - V$ plane for a reference Aerial Recovery Mission. The three models based on individual blade description predict the same flight envelope. Models based on analytically evaluated rotor loads are able to correctly predict maximum speed and ceiling up to a speed of about 40 kt. On the contrary they fail in the prediction of ceiling for medium to high speed. The simplified analytical model based on Bramwell description is able to correctly predict the flight envelope only at low speeds, while it greatly overestimates ceiling at medium to high advance ratios as well as maximum speeds. The ceiling limit in hover and at low speed is dominated by induced power, which all models are able to describe thanks to the presence of uniform inflow state. To improve the predictive capabilities of simpler models several different approaches have been used as described in par 3.3. When a 0.95 rotor C_L limit is enforced, only a limited improvement in the prediction of ceiling is achieved. In order to provide a better performance estimation a second technique has been used. As described in figure 4.4.b, enforcing the limit on the retreating blade provides a much better performance estimation at medium speed. In all cases the effect of the lateral and longitudinal inflow coefficient is marginal (model A6 compared to model A4), while the aerodynamic description of the fuselage has an impact on the maximum speed evaluation (model B6 compared to model A6). More in general simpler aerodynamic models tend to overestimate maximum performance.

Figures 4.5 to 4.8 represent the behaviour of the helicopter in advancing trimmed flight. Commands, attitude, rotor states as well as required power are plotted for a light configuration flying at 5400 ft. Full-order model trim is evaluated with roll attitude depending on advance ratio, as described in Sec. 4.2.3 and represented in Fig. (4.6). At low speed roll attitude needs to compensate disequilibrium of forces in the lateral plane through rotation of the gravity vector with respect to $\mathcal{F}_B$. At higher speed roll attitude is set to zero, while sideslip becomes a trim variable as the vertical tail is able to generate the lateral force needed to guarantee lateral equilibrium. This trim approach is used for all models excluding the nested trim approach and Bramwell's approach, where roll angle is determined by forces equilibrium .

Figure 4.5 describes command excursion: collective pitch, lateral and longitudinal

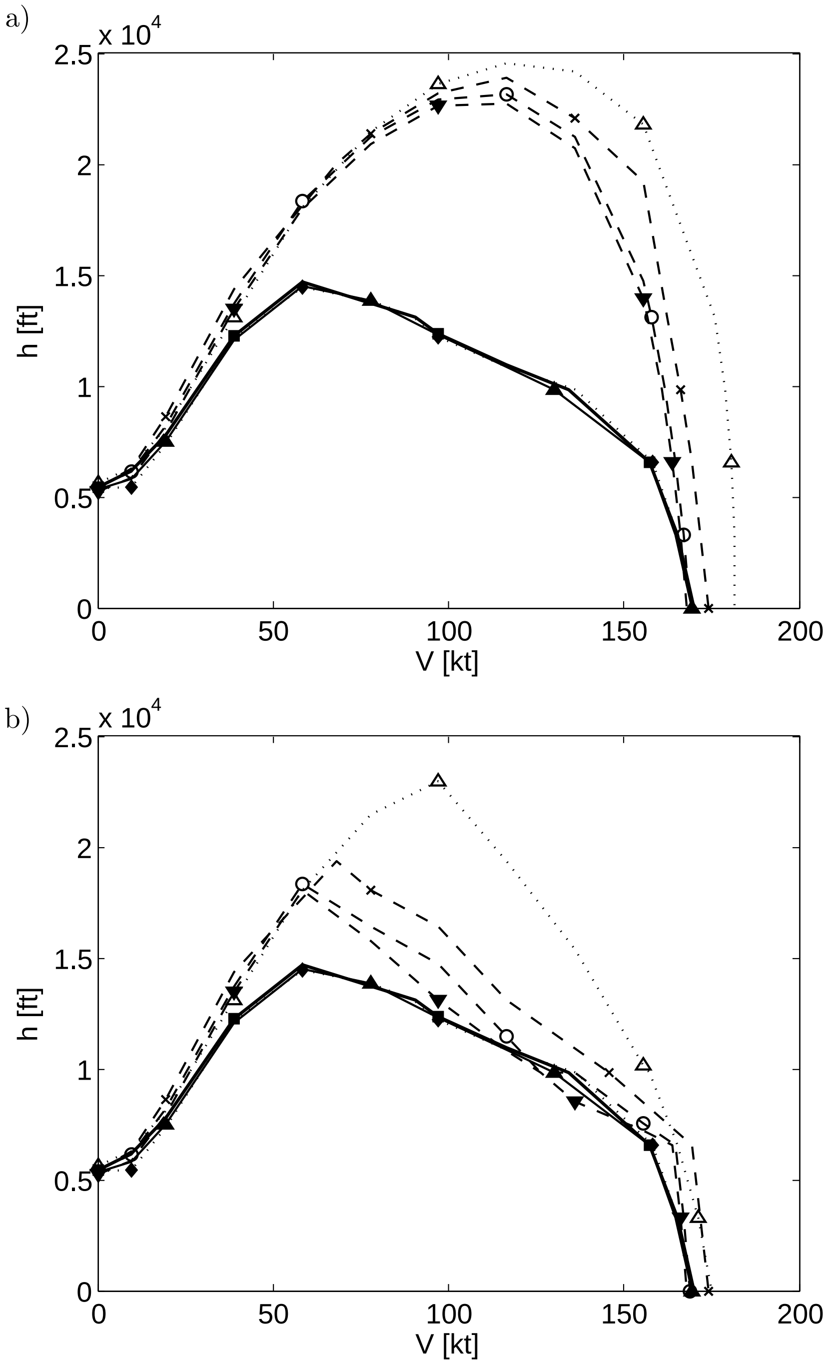

Figure 4.4. Flight envelope (V–h plane) for a design Aerial Recovery Mission [15] (a) with no C_L limit, (b) with C_L limit enforced for the retreating blade: A1 (■—), A1 nested (▷ · · ·), A3 (▲—), A4 (▼ - - -), A6 (○ - - -), B6(× - - -), C (△ · · ·).

pitch, tail rotor collective. The evaluated collective pitch is similar for all the models. The difference between model A1 and A3 is given by the absence of the dynamic twist in model A3 while the absence of the lag degree of freedom has a limited effect. Collective pitch in model A1 is therefore higher to compensate the dynamic twist of the blade. Model B6 provides a slightly different solution due to the simpler fuselage mode which takes into account only fuselage aerodynamic drag while lift, lateral forces and moments are neglected. Longitudinal pitch B_{1s} is correctly evaluated by all the models and trim techniques. Discrepancies between the models are more evident in lateral pitch A_{1s}. Although for longitudinal variables trim evaluated for model A1 with full shooting technique and with nested algorithm provides the same results, it is not possible to enforce the zero roll angle for the nested algorithm. As a consequence there is a small difference between lateral commands given by the different trim roll angle (see figure 4.6). Model A4 is able to evaluate lateral command quite precisely, on the contrary model A6 present some significant differences given the absence of lateral and longitudinal inflow states. The absence of a 3-states inflow has a detrimental effect on the ability of correctly describe the off-axis behaviour of the rotorcraft. Model B6 lateral cyclic pitch and tail rotor collective are quite far from the actual value especially at medium to high speeds because of the simplified fuselage model. Model C successfully evaluates longitudinal controls (main rotor collective pitch and longitudinal cyclic pitch), while significant errors are present in the evaluation of lateral controls (lateral cyclic pitch and tail rotor collective pitch). In particular, the oversimplified tail rotor model provides a greatly overestimated tail rotor collective pitch. This error is due, at least partially, to the particular configuration of the UH–60 helicopter that features a large tail rotor cant angle, so that tail rotor thrust significantly couples equilibrium conditions in the longitudinal plane and in the lateral direction. This coupling is neglected in model C which evaluates lateral states trim only after the longitudinal trim is solved, thus preventing also the enforcement of the requirement on zero roll angle at high advance ratios.

Figure 4.6 represent the helicopter attitude in forward flight. The roll angle differences of models A6 and B6 compared to A4 at low speeds are given by the simpler inflow model. Pitch angle is very similar for all the models except for model B6 because of its fuselage model.

Rotor states in advancing flight are represented in Figure 4.7. Model A1 with nested trim provides a higher coning due to the discarded inertial coupling between rotor states and fuselage states compared to the full shooting algorithm. All models are within a 0.5 degrees error band, with the exceptions of models B6 and C at high speed. The longitudinal tilt β_{1c} of the TPP is similar for all models, while the lateral tilt β_{1s} is affected by both the inflow model and the fuselage aerodynamic description. In general, model based on individual blade dynamics show a smaller variation in lateral TPP position than models based on TPP dynamics and analytically evaluated loads.

Total required power for trimmed flight is represented in figure 4.8. Models A1 to A6 provide the same results thanks to the nonlinear correction of profile drag coefficient used in model A4 to B6. Model B6 underestimate required power because of it simpler aerodynamic model. Model C uses a constant profile drag coefficient over the entire speed range. Such approach, while maintaining the model as simple as possible, has the drawback

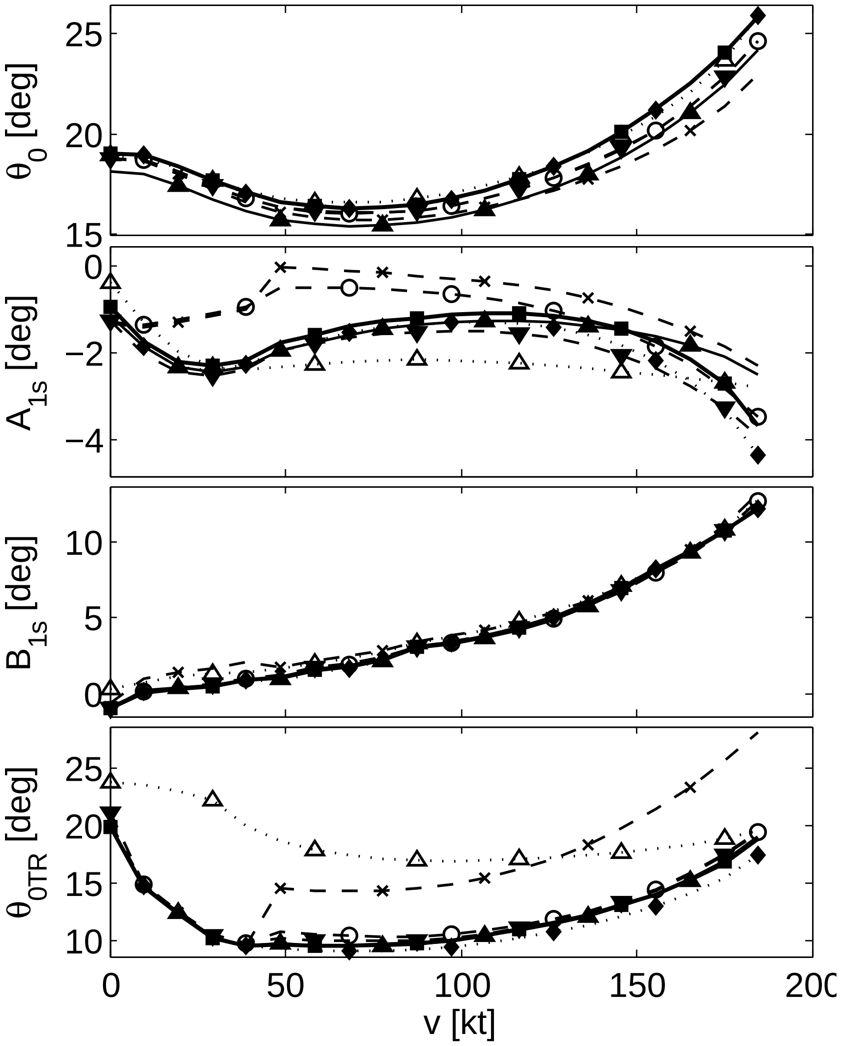

Figure 4.5. Commands for a Design Mission-Troop [15] at 5400 ft altitude: A1 (■—), A1 nested (▷···), A3 (▲—), A4 (▼ - - -), A6 (○ - - -), B6(× - - -), C (△ ···).

of overestimating power requirement at low speeds and underestimating it a high speed, where nonlinearities in profile drag emerge.

4.4.2 Climbing flight

In spite of the large error in the definition of the flight envelope, the simplified models are sufficiently accurate in evaluating rate of climb at all speed range, as demonstrated in Fig. 4.9, where the maximum rate of climb for the heavier configuration at sea level is represented. This is due to the fact that while ceiling is limited by nonlinearities in the C_{L_α} and C_{D_α} relations which are not included in simpler models, rate of climb

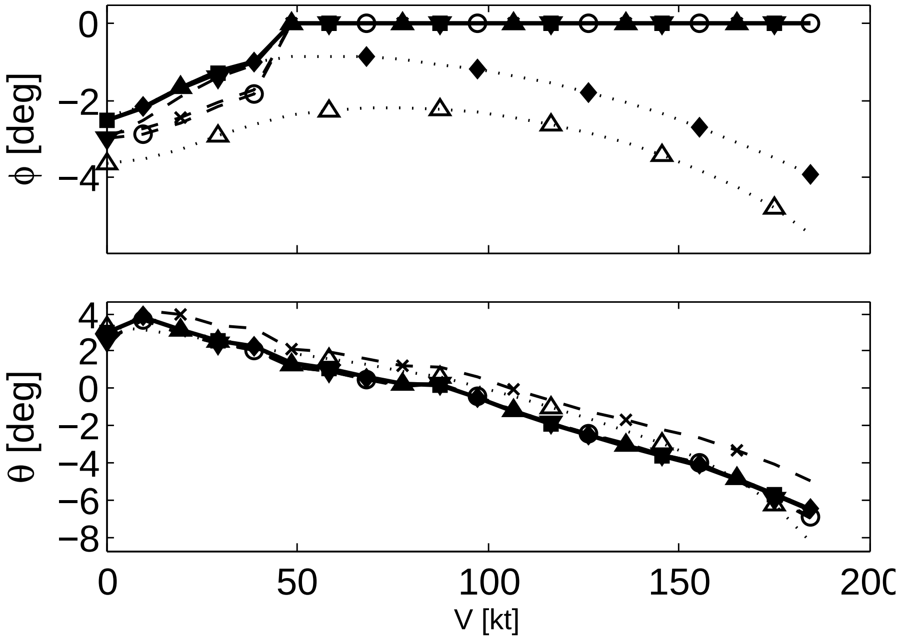

Figure 4.6. Attitudes for a Design Mission-Troop [15] at 5400 ft altitude: A1 (■—), A1 nested (▷···), A3 (▲—), A4 (▼ - - -), A6 (○ - - -), B6(× - - -), C (△ ···).

is mainly dominated by induced power. Since models A4 to B6 have quite accurate descriptions of induced power, they are able to correctly predict ROC performance. Model B6 provides lower accuracy due to the limitations of a pure drag aerodynamic description of the fuselage. On the contrary major differences are clearly visible in model C which significantly underestimates the climb performance of the helicopter at low speed, while it overestimate maximum speed. Among many other reasons, the major assumption that affects the result is the constant fuselage parasite surface, assumed independent of flight condition (on the contrary the direction of the wind impinging on the fuselage varies substantially with the speed and rate of climb). Another critical aspect is the simple inflow model adopted by this model. In its original formulation it does not take into account the vertical component of velocity in body axes and therefore provides much underestimated results for the climb performance. A more realistic result has been obtained by introducing a more accurate inflow model in the model description, taking into account the reduction of the inflow speed at increasing rate of climb, even though the climb performance is still underestimated due to the poor modelling of fuselage drag.

4.4.3 Turning flight

The maximum turn–rate at sea–level is reported in Fig. 4.10. In nonsymmetrical maneuvers, including turning flight, the structure of the main rotor downwash impinging the fuselage and tail surface is very complex. The description of these phenomena requires a more comprehensive model (e.g. featuring a free-wake description). Nevertheless the

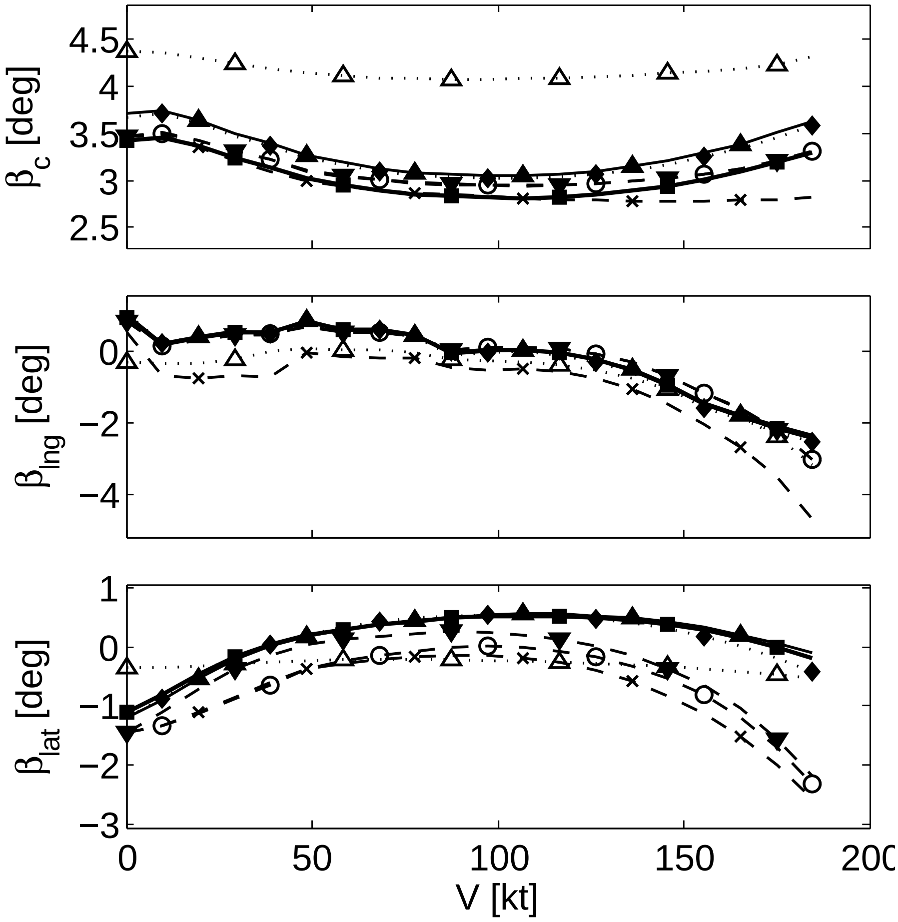

Figure 4.7. Coning and TPP inclination for a Design Mission-Troop [15] at 5400 ft altitude: A1 (■—), A1 nested (▷···), A3 (▲—), A4 (▼ - - -), A6 (○ - - -), B6(× - - -), C (△ ···).

model is able to catch some nonsymmetrical characteristics of turning performance. As illustrated in Fig. 4.10, the helicopter performance is very similar in both right and left turns. Figure 4.11 describes power requirements for coordinated turns at increasing rate at a speed of 100 kt. Models based on individual blade dynamics predict a slightly better performance in left turn, while models based on analytically loads predict a better performance on right turns (especially A6 and B6 models). In general simpler models tend to overestimate turning performance of the rotorcraft (which on the present analysis are only based on total necessary power). This is due to the much simpler representation of the blade operating conditions (i.e. the correct analysis of the local angle of attack and as a consequence of the lift and drag coefficient) which can be accurately described only using an individual blade approach. Nevertheless model A4 is able to represent quite precisely required power on low to medium turn rates as shown in figure 4.11.

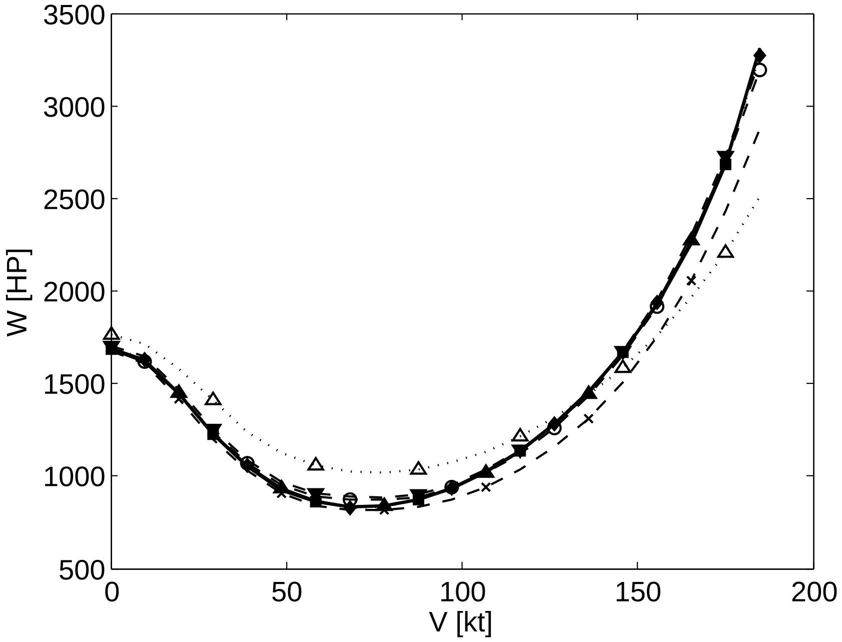

Figure 4.8. Required power for a Design Mission-Troop [15] at 5400 ft altitude: A1 (■—), A1 nested (▷···), A3 (▲—), A4 (▼ - - -), A6 (○ - - -), B6(× - - -), C (△ ···).

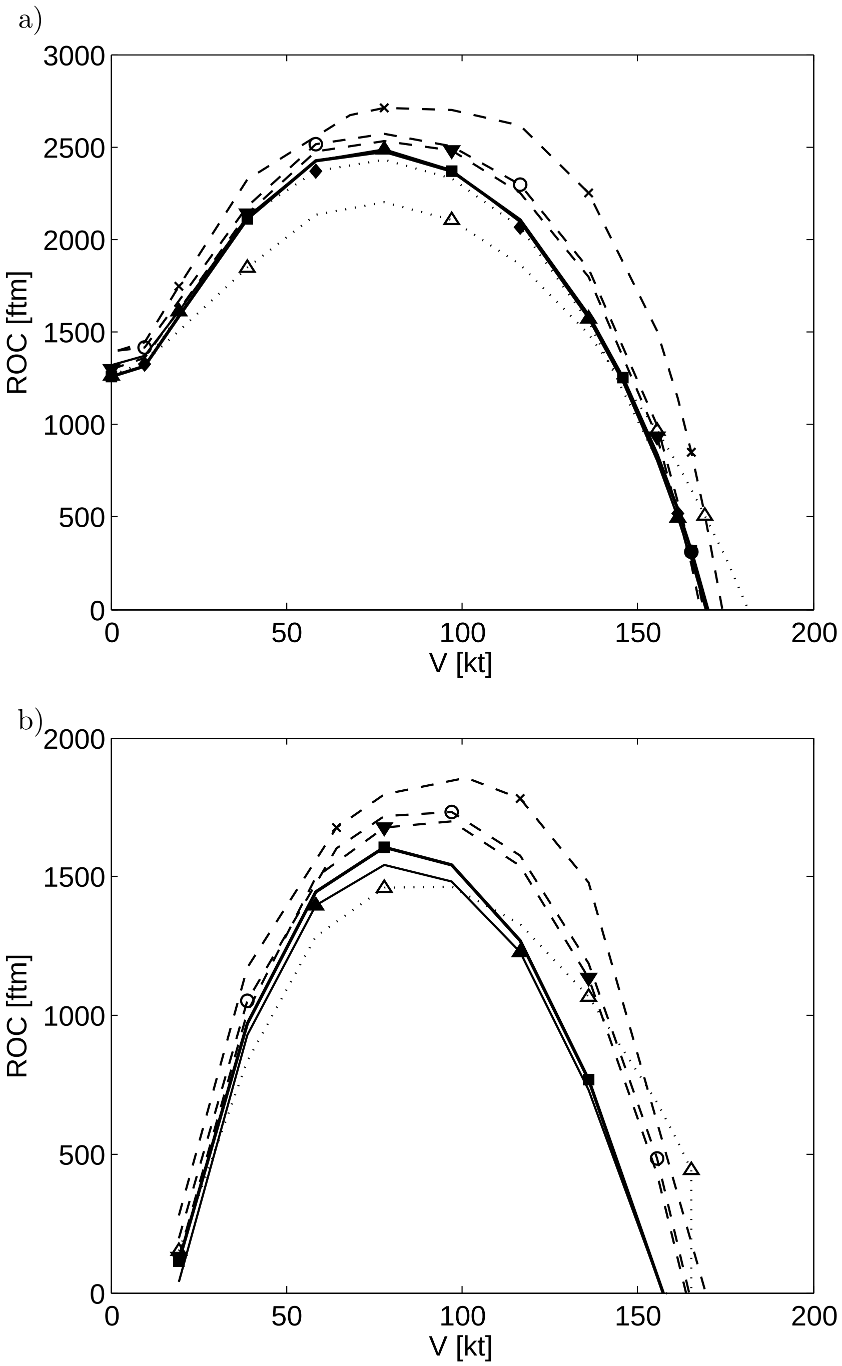

Figure 4.9. Maximum Rate of Climb for a design Aerial Recovery Mission [15] at (a) sea level, (b) 2240 m: A1 (■—), A1 nested (▷···), A3 (▲—), A4 (▼ - - -), A6 (○ - - -), B6(× - - -), C (△ ···).

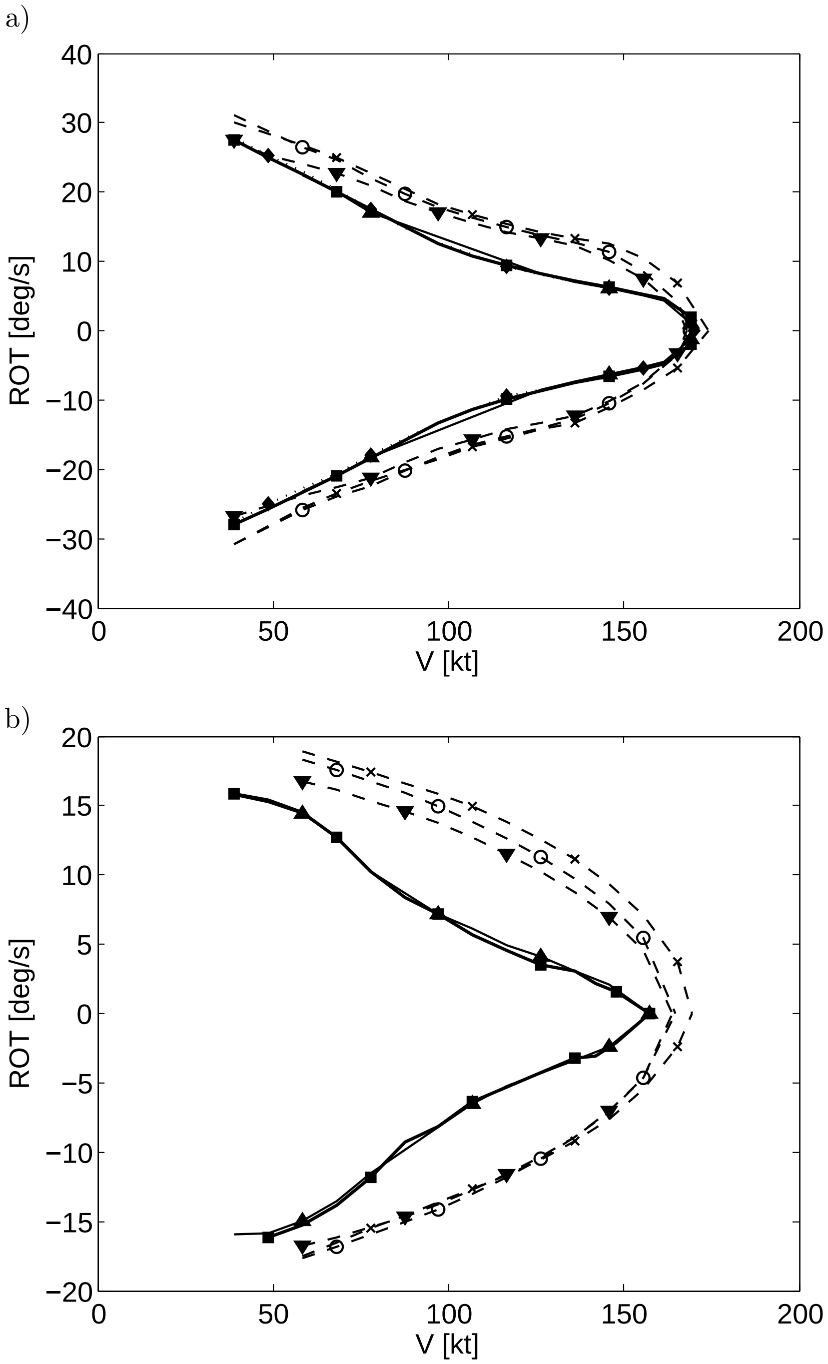

Figure 4.10. Maximum Rate of Turn for a design Aerial Recovery Mission [15] at (a) sea level, (b) 2240 m: A1 (■—), A1 nested (▷· · ·), A3 (▲—), A4 (▼ - - -), A6 (○ - - -), B6(× - - -), C (△ · · ·).

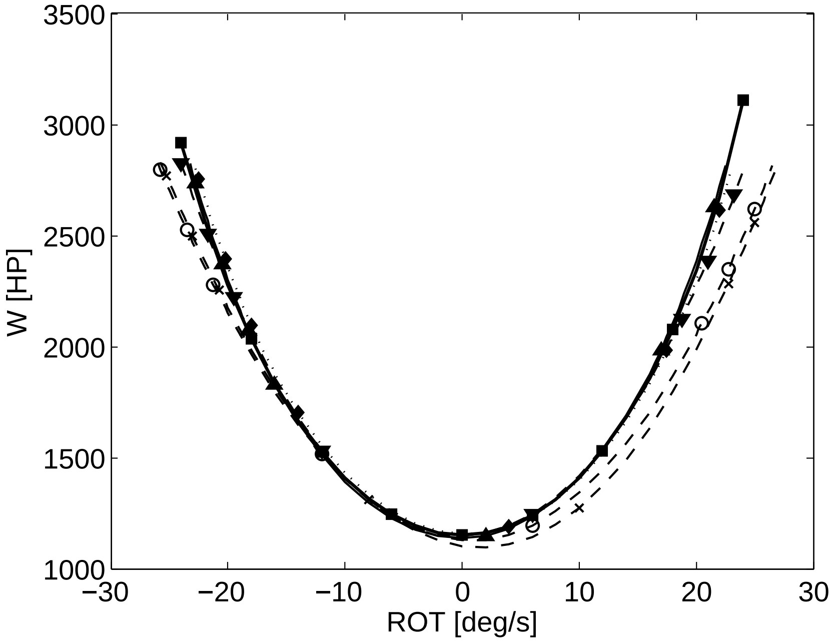

Figure 4.11. Power required for a 100 kt turn at sea level. Aerial Recovery Mission configuration [15] : A1 (■—), A1 nested (▷· · ·), A3 (▲—), A4 (▼ - - -), A6 (○ - - -), B6(× - - -), C (△ · · ·).

4.4.4 Effects of truncation due to ordering scheme

The previous analysis aimed at highlighting the effects of model complexity on performance evaluation. A similar approach is here used to analyse the effects of an ordering scheme (i.e. the equations are written including terms only to a prescribed level of detail, using the symbolic tool for the automatic generation of aerodynamic and inertial equations in a TPP formulation) on the evaluation of rotorcraft performance. For this reason, the approach described in section 3.4 was followed. Three different versions of model A4 were generated truncating the equation at the 2^{nd} (i.e. all terms which satisfy $< \mathcal{O}(\varepsilon^2)$ are included), 3^{rd} and 4^{th} order, respectively. The possibility of considering only the 1^{st} order terms is ruled out by the fact that such approach would include only main rotor collective pitch while lateral and longitudinal flap as well as commands would be excluded from the analysis. At the same time the equations which include 4^{th} order terms are sufficiently detailed so that adding higher order terms would not provide any significant change in the results. Model A4 is used as a reference for the analysis.

Figure 4.12 represents command required to trim the helicopter at increasing speeds in level flight. Truncating terms to 2^{nd} order provides a very poor estimation of lateral command and an overestimation of collective pitch. As higher order terms are discarded, the lateral–direction description is poor due to the importance of higher order terms in the description of off-axis behaviour. This can be seen even better in figure 4.13 where the attitude is pictured and in figure 4.14 where the rotor states in multiblade coordinates are represented. If the model is limited to 3^{rd} order terms the behaviour is very similar to model with higher order terms with the exception of higher speeds where the advance ratio μ plays a more important role.

All models provide a similar description of required power in level flight, as represented in figure 4.15. This leads to comparable results in the evaluation of maximum climb performance at sea level, as in figure 4.16, even if models with less terms tend to underestimate performance. A similar behaviour can be seen in figure 4.17 where the flight envelope with no correction of maximum C_L is represented as evaluated with the three models. As a conclusion the introduction of 4^{th} order terms provide more reliable results only at very high speeds, while in all flight conditions, truncation to 3^{rd} order is able to correctly represent the helicopter behaviour in steady–state conditions.

4.4.5 Discussion

The trim results of full-order model obtained with complete shooting and nested trim with averaged rotor loads show a very good agreement in all trim conditions despite the slightly different roll angle. Since the nested algorithm is faster, it can replace the full–order shooting in all test cases here proposed. Although removing blade lag and twist degrees of freedom the results of helicopter performance estimation show a very good agreement with full-order model and the trim routine is faster, the model still requires the almost complete set of configuration data.

Models bases on TPP dynamics with the improvements described in section 3.3 provide a good estimate of the helicopter performance in straight flight at a computational cost one

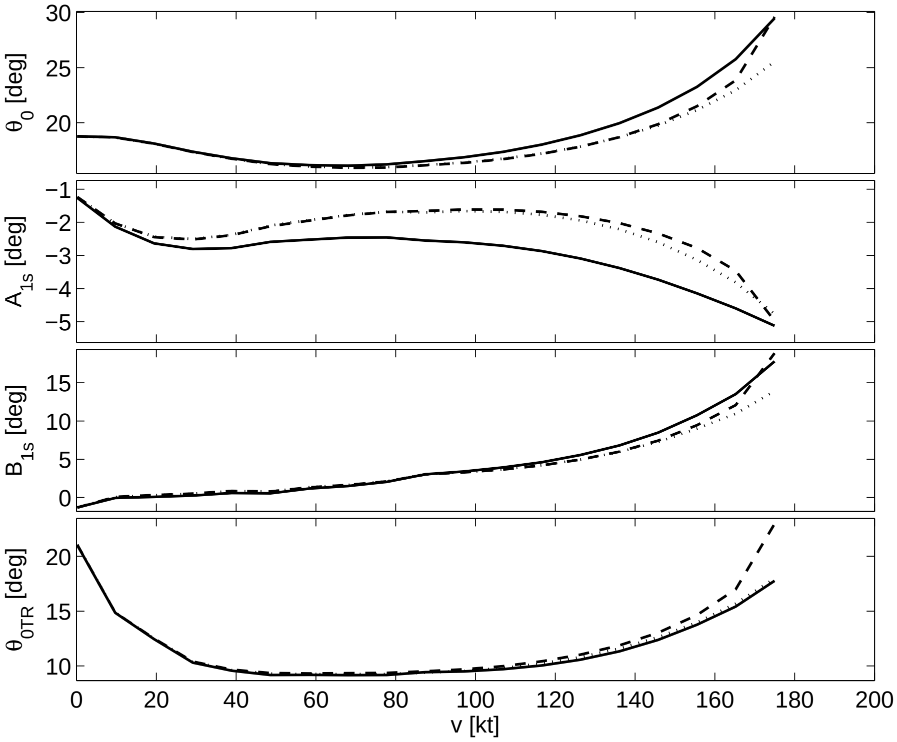

Figure 4.12. Commands for a Design Mission-Troop [15] at 5400 ft altitude: model A4 with equations truncated at 2^{nd} (—), 3^{rd} (- - -), and 4^{th} (· · ·) order terms.

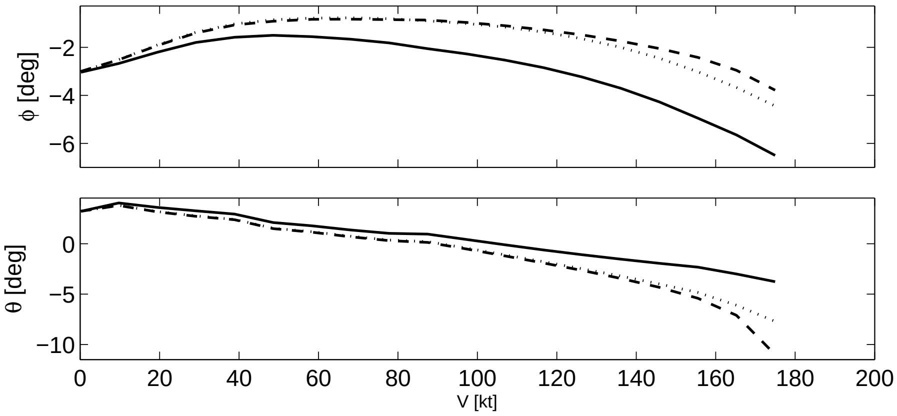

Figure 4.13. Attitudes for a Design Mission-Troop [15] at 5400 ft altitude: model A4 with equations truncated at 2^{nd} (—), 3^{rd} (- - -), and 4^{th} (· · ·) order terms.

to two orders of magnitude lower than full order models, though the TPP description and the linear aerodynamic formulation do not allow for a precise description of blade behaviour in the complex environment of turning flight, leading to overestimation of performance. Comparing the results of the different model, a uniform inflow degrades the evaluation

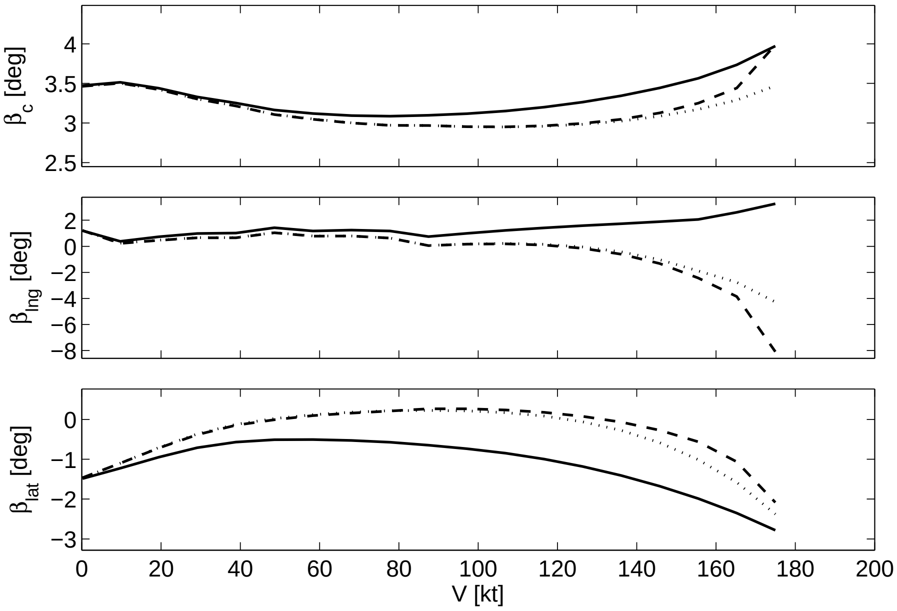

Figure 4.14. Coning and TPP inclination for a Design Mission-Troop [15] at 5400 ft altitude: model A4 with equations truncated at 2^{nd} (—), 3^{rd} (- - -), and 4^{th} ($\cdots$) order terms.

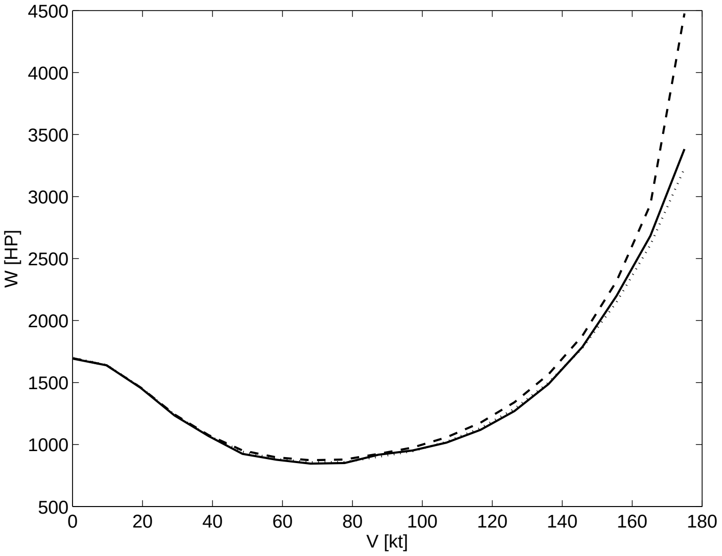

Figure 4.15. Required power for a Design Mission-Troop [15] at 5400 ft altitude: model A4 with equations truncated at 2^{nd} (—), 3^{rd} (- - -), and 4^{th} ($\cdots$) order terms.

of off-axis behaviour, while the description of fuselage aerodynamic forces by means of parasite drag area leads to overestimation of rotorcraft performance. The results of the lowest order Model C, which is based on separate longitudinal and lateral trim and a very

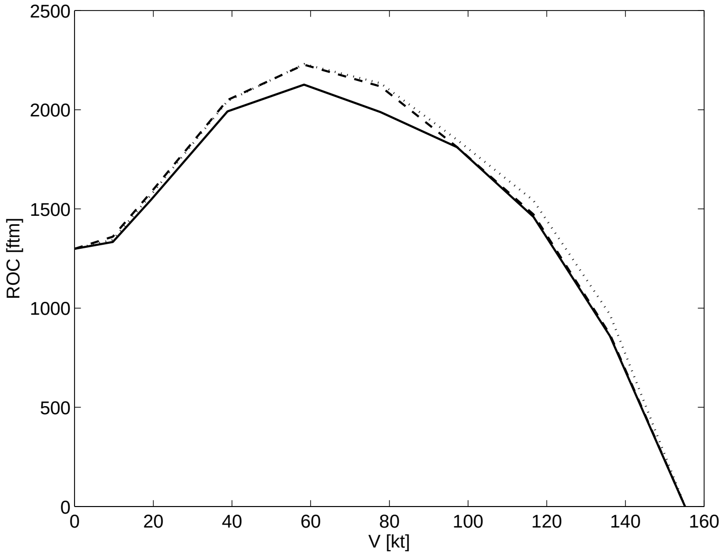

Figure 4.16. Maximum Rate of Climb for a design Aerial Recovery Mission [15] at sea level: model A4 with equations truncated at 2^{nd} (—), 3^{rd} (- - -), and 4^{th} (· · ·) order terms.

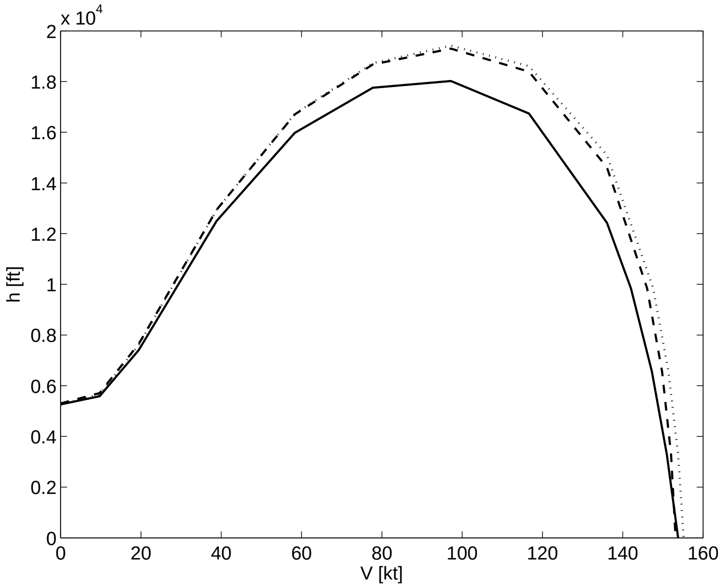

Figure 4.17. Flight envelope (V–h plane) for a design Aerial Recovery Mission [15] with no C_L limit: model A4 with equations truncated at 2^{nd} (—), 3^{rd} (- - -), and 4^{th} (· · ·) order terms.

limited set of parameters, are reliable only for maximum speed and rate of climb, while the estimation of lateral variables needs a significant improvement.

Chapter 5

Handling qualities

5.1 Stability analysis

The evaluation of flying qualities of an helicopter requires the determination of several different properties, among them static and dynamic stability (in particular the long-period roots), control displacements, force gradients, transient response characteristics, control coupling, control sensitivity [7].

In this chapter some aspects of the static and dynamic stability characteristics are analysed, with particular attention to how the main rotor dynamics affect the stability of the helicopter. The results are then analysed with reference to the specifications for light helicopters CS-27 [93], that give reference values for the frequencies and dampings of the modes.

The stability analysis of the main rotor and helicopter dynamics were undertaken following different approaches. The purposes are

1. to investigate the accuracy of approximate solutions comparing them to the solutions for the nonlinear time-periodic system associated to the complete helicopter model (obtained through the Poincaré map analysis), and

2. to propose a guideline for the interpretation of the results of the complete helicopter model analysis thanks to the formulation of models of reduced order with uncoupled dynamics, and approximate solutions.

For these purposes, it is necessary to provide some tools to evaluate the stability of periodic systems. to this end, a widely used method is the Floquet Transition Matrix method, based on the Floquet-Liapunov Theory [63, 94]. Another possible solution is the use of Poincaré maps [95].

For the analysis of the main rotor stability the adopted tools are:

1. Classical eigenstructure analysis of the simplified linear model of the main rotor obtained neglecting the harmonic terms in the rotating frame equations or through harmonic balance methods in the non-rotating frame. This analysis is carried out with the aim of providing a first approximation of the eigenvalues. Since it deals with

very basic equations of motion, the eigenvalues can be calculated semi-analytically to analyse the influence of parameters on frequency and damping of main rotor modes. The analysis was undertaken both in the rotating and the non-rotating frames to determine the frequencies and damping of single-blade and TPP modes. In the hovering condition this approach gives reference points for the study of the periodic system, as the solutions obtained using this technique and the Floquet analysis should coincide.

2. Floquet analysis of the linear time-periodic rotor model. This is an intermediate step between linear analysis and Poincaré maps as Floquet analysis gives a reference solution (of a linear time-periodic system) to interpret the results of the Poincaré map.

3. Poincaré map analysis of the complete nonlinear rotor model. This is the most complete and accurate methodology, since it takes into account all the nonlinearities of the model, including inflow states. However, the frequency of the characteristic modes cannot be determined univocally [63]. To this end the frequencies obtained are compared using the methods 1. or 2. The Poincaré map was determined for the rotor states $\boldsymbol{x}_r$, with and without the inflow states. Inflow states dynamics were investigated separately.

When the whole helicopter model was considered, two different approaches were used for the stability analysis:

4. The linearization of the quasi-static model of the helicopter degrees of freedom [96]. Using this method, the rigid-body rotorcraft modes (frequency and damping) are easily determined. Among other aspects, the coupling of longitudinal and lateral dynamics of the helicopter are analysed as an important factor for the evaluation of handling qualities [6].

5. The Poincaré map analysis of the complete helicopter model is the most accurate method also in this case. It provides information regarding the stability of the roots of the complete system. However the linearized Poincaré map does not allow to determine univocally the frequencies of the roots so that the identification of the characteristic modes is far from trivial.

A complete analysis of this activities is the main purpose of [78], from which part of this chapter is inspired.

5.1.1 Rigid gimballed rotor for model validation

As a first step, validation of the simplified model is carried out using a full nonlinear, single–blade simulation model of the gimbaled rotor with blades rigidly connected to the hub [78] formulated without small angles assumptions or linearizing techniques in order to analyse the rotor behaviour in a variety of motions not limited to small perturbations.

Assuming no coning angle, no twist and no undersling of the blades, Fig. 5.1 shows a comparison of the hub response (in the u_1-u_2 plane) to a cyclic command $\theta_{SW} = 5^\circ$ in hovering with $K = 3{,}610$ Nm/rad, as obtained from the simplified and complete models, with the trim value of the rotor thrust $T = 6{,}400$ N. Rotor data in both cases are shown in Table 1.

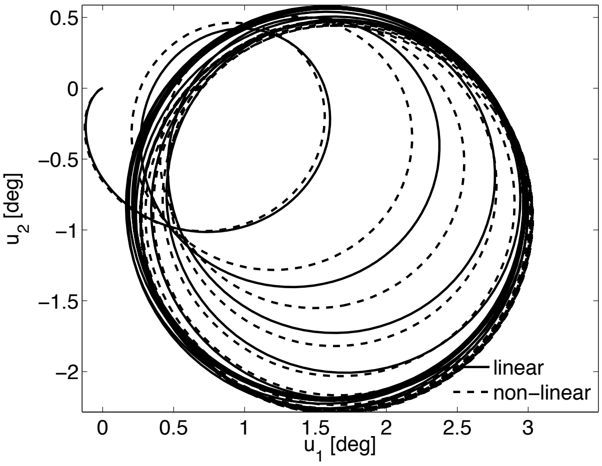

Figure 5.1. Comparison of the simplified (linear) and general (nonlinear) rotor model responses to a longitudinal cyclic command $\theta_{SW} = 5$ deg; $\mu = 0$, $K = 3{,}610$ Nm/rad.

It is apparent that the rotor responses obtained from the two models are in good agreement in spite of the large value of the considered cyclic command. In forward flight, the description of the rotor behavior by means of the simplified model becomes less accurate even for relatively small advance ratios, mainly because of the effects of the nonuniform inflow. This is illustrated in Figs. 5.2 where the response of the tilt angles u_1 and u_2 to a step variation $\mu = 0.05$ of the advance ratio from hovering is reported. The significant differences in the two solutions visible in Fig. 5.2.a for a rather low advance ratio are due to the non–uniform inflow in the general model, whereas the response is again very similar when a uniform inflow is assumed (Fig. 5.2.b). If on one side this last result rules out the possibility of adopting the simplified model for a realistic simulation of the full vehicle, on the other one its capability of capturing the fundamental aspects of the motion is demonstrated.

Origin of the wobbling motion

As stated previously, one of the most relevant characteristics of the two–bladed gimballed rotor is the onset, in most operating conditions, of a wobbling motion of the rotor hub, which corresponds to a precession motion of the hub axis with respect to the shaft axis. The simplified model (Eqs. (3.164)–(3.165)), provides some physical insight into the system that allows for understanding how the wobbling motion is triggered by the periodic loads in the presence of a cyclic pitch command or forward flight condition.

A steady–state condition for the rotor with a constant tilt angle with respect to the shaft axis (that is, without wobbling motion) requires $\tilde{\omega}_1 = \tilde{\omega}_2 = 0$. To this end, the moments N_1 and N_2 need to be constantly zero, which is not true in general, as these

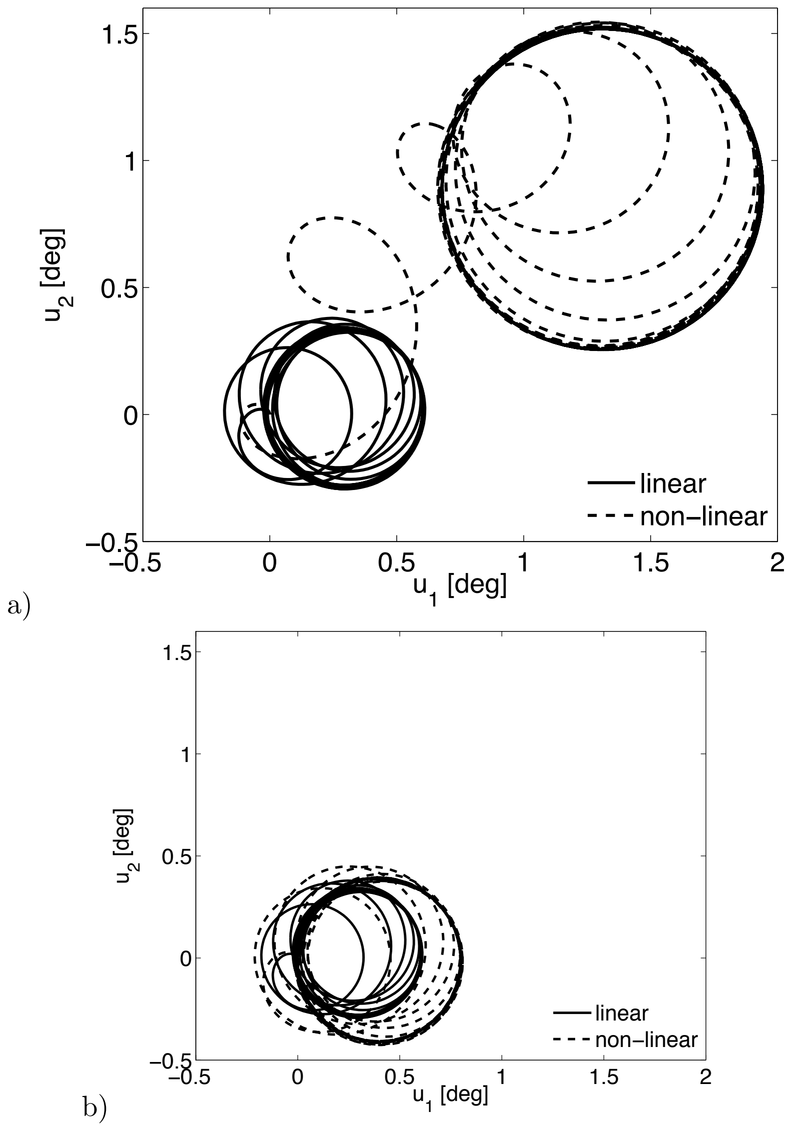

Figure 5.2. Comparison of the simplified and general rotor model responses to a perturbation of the advance ratio $\mu = 0.05$; $K = 3{,}610$ Nm/rad (a) general rotor model with 3–states inflow model, (b) general rotor model with uniform inflow.

terms represent periodic forcing functions.

With reference to Eq. (3.168), assuming a forcing term along the feathering (x_H) axis (Fig. 3.7) $N_1/(I_1\Omega^2) = A\cos\psi$, the resulting periodic motion at steady–state is $\tilde{\omega}_1' = -\tilde{\omega}_2 = (A/2)\cos\psi$ and $\tilde{\omega}_2' = \tilde{\omega}_1 = (A/2)\sin\psi$. This means that the angular speed components $\tilde{\omega}_1$ and $\tilde{\omega}_2$ continue to oscillate with constant amplitude $A/2$ and phase $\Delta\psi = \pi/2$, thus resulting in a precession motion of the hub axis, namely the wobbling. A similar argument holds for a periodic forcing term around the flapping, $N_2/(I_2\Omega^2) = B\cos\psi$ as, given the system linearity, the perturbed motions can be superimposed.

When considering the effects of cyclic commands in hovering ($\mu = 0$) with zero angular velocity of non–rotating frame ($\bar{p} = \bar{q} = 0$) and zero stiffness of the feathering hinges ($K_T = 0$), all higher–order harmonic terms are zero and the first two equations in system Eq. (3.168) become

$$\begin{aligned} \tilde{\omega}_1' &= -\tilde{\omega}_2 - \frac{\gamma_{fb}}{2}\tilde{\omega}_1 - K_{PC}\gamma && (5.1) \\ \tilde{\omega}_2' &= \tilde{\omega}_1 + \frac{\gamma_b}{8}[K_H(\phi_{SW}\cos\psi \\ &\quad -\theta_{SW}\sin\psi + \gamma) - \tilde{\omega}_2] + K_{PC}\beta && (5.2) \end{aligned}$$

With $K = 0$, the steady-state solution is

$$\begin{aligned} \beta &= -\phi_{SW}\sin\psi - \theta_{SW}\cos\psi && (5.3) \\ \gamma &= -\phi_{SW}\cos\psi + \theta_{SW}\sin\psi && (5.4) \end{aligned}$$

that gives constant hub tilt angles $u_1 = \theta_{SW}$ and $u_2 = \phi_{SW}$, as obtained by substituting Eqs. (5.3) and (5.4) into Eqs. (3.166) and (3.167), with the blade tip-path-plane (TPP) parallel to the swash–plate.

Figure 5.3 shows the system response as function of rotor revolutions in the two considered circumstances following a longitudinal cyclic command. In the ideal case with $K = 0$,the hub angular position achieves a constant value (Fig. 5.3.a), while in Fig. 5.3.b the flapping (continuous line) and feathering (dotted line) angles show a sinusoidal oscillation in quadrature, and the longitudinal (continuous line) and lateral (dotted line) tilt angles of the TPP, u_1 and u_2, become constant in a time interval corresponding to 15 revs, the time–constant being approximately proportional to the fly–bar inertia I_1.

On the converse, when $K \neq 0$, the TPP angles u_1, u_2 have periodic variations (Fig. 5.3.c) that prevent the system from achieving a constant equilibrium as the elastic moment about the feathering axis induces a nonzero $\tilde{\omega}_1$ rate that triggers the wobbling motion. In other words, in this case no equilibrium can be established about the feathering axis due to the effect of the periodic elastic moment as, also, the moment of inertia is minimum and the aerodynamic moment of the paddles is small. As far as the equilibrium about the flapping axis is concerned, note that the aerodynamic moment is orders of magnitude higher than the moment due to hub stiffness.

In order to gain some further insight in the wobbling motion characteristics, the feathering and flapping angles can be expressed as

$$\begin{aligned} \beta &= -a_1\cos\psi - b_1\sin\psi && (5.5) \\ \gamma &= c_1\sin\psi - d_1\cos\psi && (5.6) \end{aligned}$$

to introduce the longitudinal a_1, c_1, and lateral b_1, d_1 flapping angles of, respectively, blade and fly–bar TPP's. When Eqs. (5.5), (5.6) are substituted into Eqs. (5.1), (5.2) written in terms of γ and β, application of the harmonic balance method [27] yields a set of differential equations for the TPP flapping degrees of freedom.

Figure 5.4 shows the responses to a 10 deg longitudinal cyclic command (already illustrated in Fig. 5.3 considering hub flap and feathering angles) in terms of TPP flapping coefficients. It is worth to observe that after a few rotor revolutions, the orientations of the two planes carved out by blade and paddle tips become constant in spite of the sustained wobbling oscillations in the case with nonzero hub stiffness. As a consequence, the thrust vector direction is constant and, as a further observation, wobbling motion can be interpreted as a 2/rev oscillation of the hub plane between the blade and paddle TPP's, the amplitude of which depends on the relative orientation of the two TPP's. For $K = 0$, when the wobbling motion subsides at steady–state, the TPP's of blades and fly–bar are parallel to the swash–plate ($a_1 = c_1 = \theta_{SW} = 10$ deg, $b_1 = d_1 = \phi_{SW} = 0$). In the case $K \neq 0$, the fly–bar TPP mainly flaps to the left ($c_1 = 0.5$ deg, $d_1 = -2.2$ deg) while the blade TPP is flapping backward ($a_1 = 6$ deg) and to the left ($b_1 = -1$ deg), and the wobbling amplitude is about 6 deg.

When a the response to a step variation of forward speed is considered, Fig. 5.5 shows that the wobbling motion develops even for $K = 0$ as the moment equilibrium on the feathering axis is now unbalanced by the periodic variation of the aerodynamic moment of the paddles.

As for the effect of the K_H ratio, a lower K_H determines a reduction of the limit cycle amplitude together with a minor effectiveness of the command because the time constant of the rotor response is increased and, in the situation with nonzero K, the hub rotation is smaller for the same cyclic command amplitude.

As shown in Fig. 5.6, the effect of the feathering hinge stiffness on the evolution and amplitude of the wobbling motion is negligible for the nominal value $K_T = 150$ Nm/rad (the situation with $K_T = 0$ corresponds to the dotted line in Fig. 5.3.a). Increasing the value of K_T determines a reduction of the limit cycle amplitude together with a major effectiveness of the command at hovering.

As far as the influence of hinge stiffness on wobbling is concerned, it is apparent that the elastic moment along the feathering axis is proportional to θ_c and acts in the sense of reducing the relative orientation of the non-feathering–plane (NFP) and the fly–bar TPP. Therefore, a reduction of the wobbling amplitude due to a restrain action of the pitch hinges can be obtained only in the circumstances, such as hovering, when the angle between NFP and blade TPP is small, while in all the other operating conditions (i.e. advancing flight) the stiffness increases the relative orientation of blade and fly–bar TPP's with the already cited effect of increasing the amplitude of hub oscillatory motion.

Stability Analysis of the rigid configuration

The periodic terms in the state–matrix $\boldsymbol{A}$ (Eq. (3.168)) depend on forward speed so that the system achieves a time–invariant form in hovering. In this circumstance Eqs. (5.1)-(5.2) can be re–written in terms of flapping and feathering angles. Keeping only the homogeneous terms, the governing equations become

$$\begin{aligned}\beta'' &= -\frac{\gamma_b}{8}\beta' - (1 + K_{PC})\beta - \frac{\gamma_b}{8}(K_H - 1)\gamma \\ \gamma'' &= -\frac{\gamma_{fb}}{2}\gamma' - (1 + K_{PC} + 2k_T K_H)\gamma - \frac{\gamma_{fb}}{2}\beta\end{aligned} \tag{5.7}$$

Table 5.1. Eigenvalues of the uncoupled system with and without paddles at fly–bar tips.

a) Fly–bar Lock numb. $\gamma_{fb} = 0$		$K = 0$	K_{nom}
Natural frequency ω_n/Ω			
Flapping	$\sqrt{1 + k_2}$	1.	1.003
Feathering	$\sqrt{1 + k_1'}$	1.	1.282
Damping coefficient ζ			
Flapping	$\frac{\gamma_{bl}}{16}/\sqrt{1 + k_2}$	0.261	0.260
Feathering	$\frac{\gamma_{fb}}{4}/\sqrt{1 + k_1'}$	0.	0.

b) Fly–bar Lock numb. $\gamma_{fb} = 0.53$		$K = 0$	K_{nom}
Natural frequency ω_n/Ω			
Flapping	$\sqrt{1 + k_2}$	1.	1.004
Feathering	$\sqrt{1 + k_1'}$	1.	1.281
Damping coefficient ζ			
Flapping	$\frac{\gamma_b}{16}/\sqrt{1 + k_2}$	0.255	0.254
Feathering	$\frac{\gamma_{fb}}{4}/\sqrt{1 + k_1'}$	0.147	0.115

Table 2 shows the modal characteristics of this system for $K = 0$ and for $K = K_{nom} =$ 3,610 Nm/rad, when small coupling terms are neglected for the sake of simplicity and $k_1' = K_{PC} + 2K_T K_H$. Two configurations are considered: Case a (reported on the top portion of Tab. 2), when no aerodynamic paddle is present and the resulting fly–bar Lock number is 0; Case b (reported below), when paddles are present and $\gamma_{fb} = 0.53$. For $\gamma_{fb} = 0$ the damping of the feathering motion vanishes, so that a weakly stable system is obtained at hovering. This means that, as already observed in [23] and [83], a regressive motion would be induced on the rotor by the periodic aerodynamic load in forward flight. This characteristics strongly supports the need for the presence of paddles, which thus perform and important stabilizing action for the two–bladed gimbaled rotor, without affecting the characteristics of the flapping mode.

The dynamic analysis of the system supports the interpretation of the effect of hub stiffness on command response illustrated in Figs. 5.3 and 5.4. For $K = 0$. flapping and feathering modes are both at resonance so that, as already observed, the blade and fly–bar TTP's are both tilted backward. When the stiffness K takes its nominal value, the feathering frequency is increased and this motion, when represented in terms of TPP position, lags flapping by 77 deg, which turns out in the observed lateral flapping of the fly–bar TPP (Fig. 5.4). This means that, when the motion is referred to a single angular variable ψ, such that $\psi_{fb} = \psi + \pi/2$, γ lags β of 167 deg, which corresponds to what is observed in Fig. 5.3.

Note also that the sustained wobbling motion at steady–state induces a not negligible variation of the cyclic pitch command, with a 60% reduction of amplitude and a 9 deg phase delay with respect to the situation with $K = 0$. As a consequence, if on one side flapping frequency remains close to unity as K is varied (the unit circle corresponding to $\omega_n/\Omega = 1$ is shown in the figures), feathering frequency increases significantly with stiffness, due to the low inertia of the fly–bar, if compared with elastic moments, as demonstrated also by Figure 5.7. A similar effect on feathering eigenvalues is obtained by increasing the stiffness of the feathering hinges K_T. Figure 5.8 shows the eigenvalues for K_T varying from 0 to

150 Nm/rad, for the nominal value of K. Again, flapping eigenvalue presents a negligible variation.

Increasing the inertia of the fly–bar leads to the variation of two parameters of the system: the fly–bar Lock number $\gamma_{fb} = 2\rho a_{fb} S_{fb} R_{fb}^3 / I_1$ that decreases the damping of the feathering mode, and the elastic terms, $k_1' = (K + 2K_T K_H)/(\Omega^2 I_1)$, that decreases its natural frequency, resulting in significant variations for the feathering eigenvalue, as shown in Fig. 5.9. Also in this case only minor variations are observed on the flapping eigenvalue, but I_1 plays a significant role on TPP response to an angular velocity component.

In forward flight the eigenvalues of the linear, time–varying system Eq. (3.168) are determined using Floquet theory [94]. As usual, the state–equation is integrated over one period for each independent initial condition to obtain the Floquet Transition Matrix (FTM). Natural frequencies and damping ratios of the system modes are then obtained by taking the logarithm of the FTM eigenvalues, where use is made of the eigenvalues computed in the hovering condition to identify the origin of the curves. All the roots, reported in Fig. 5.10, are stable in the considered range of the advance ratio, μ, where the eigenvalues of the feathering mode remain complex, their frequency approximately given by $\omega/\Omega = 1.25$, while those relative to flapping become real for $\mu > 0.18$..

5.1.2 Gimballed and teetering rotors with coning hinges

In this section the behaviour of the gimballed rotor is compared to that of an equivalent teetering rotor, with and without the coning degrees of freedom. The stability of the rotor is analysed first, for different pitch–coning coupling and in the presence of dry friction in the coning hinges. Response to swashplate commands and gust disturbances are presented to highlight the peculiar behavior of the gimballed rotor.

Stability analysis

The impact of rotor configuration on rotor stability is here considered, and in particular the presence of coning hinges (CH), their location, pitch–flap coupling coefficient, damping or friction in the hinges. Table 5.2 collects the eigenvalues in hover of the basic rotor configuration.

Table 5.2. Eigenvalues for $K_{PC} = 1.36$ and $k_{fr} = 0$.

Gimballed rotor	**Teetering rotor**
with coning	
$0.1339 \pm 2.3686i$	$0.1254 \pm 2.3545i$
$-0.1871 \pm 1.2464i$	$-0.1871 \pm 1.2460i$
$-0.3745 \pm 0.8357i$	$-0.3758 \pm 0.8605i$
$-0.1263 \pm 0.9642i$	
without coning	
$-0.2170 \pm 0.9740i$	$-0.2179 \pm 0.9760i$
$-0.1187 \pm 0.9623i$	

Both the gimballed and the teetering rotor without CH are stable, nevertheless the introduction of the coning degree of freedom with a high pitch–coning coupling leads both configurations to instability. The first oscillatory mode in both the gimballed and teetering rotors is unstable and it excites all states which lies in the plane perpendicular to the coning hinges (i.e. β_0, β_1 and β_2). This mode is an anti–symmetric coning, where the blades exchange energy through the mechanical link represented by the teetering hub, with coning rotations β_1 and β_2 of opposite phase and β_0 in quadrature.

The rotor becomes stable if the pitch–coning coupling gain is sufficiently reduced and/or some form of dissipation in the coning hinges is introduced. Figure 5.11 shows the root–loci of when the pitch–coning coupling varies from $K_{PC} = 0$ to the nominal value, $K_{PC} = 1.36$ (blue line). The imaginary axis is crossed for $K_{PC} \approx 0.4$ and the rotor remains unstable for larger values of K_{PC}. When a viscous damping term proportional to the coning speed ($M_{vsc_i} = -c_{vsc}\dot{\beta}_i$) is introduced for $K_{PC} = 1.36$, the system turns stable again, for $c_{fric} > 0.15$. On the converse, the feathering mode for the gimballed rotor is always stable and almost unaffected by the presence of coning hinges (the feathering pole, $-0.1263 \pm 0.9642i$, being very close to that obtained for blades fixed to the hub, $-0.1187 \pm 0.9623i$) or the introduction of viscous damping (see Fig. 5.11).

The actual gimballed rotor does not features dampers, yet the high centrifugal load leads to the presence of dry friction in the coning hinges, that dissipates energy. This type of hard nonlinearity prevents the system from being linearized and, as a consequence, a stability analysis based on the eigenvalues is no longer available. Nonetheless, it is possible to identify a minimum value for k_{fr} which guarantees stability, on the basis of a Poincaré mapping approach: a perturbed state for the rotor is considered as the initial condition and the perturbation after a rotor revolution is evaluated by means of numerical simulation. If the norm of the perturbation after one revolution is smaller than the initial one the rotor is stable. Figure 5.12 shows the minimum level of friction in the coning hinges in order to guarantee stability as a function of the pitch–coning coupling. The nominal value of the friction $k_{fr} = 100\ Nm$ satisfies the stability condition for $K_{PC} = 1.36$.

5.1.3 Isolated rotor response

The behavior of gimballed and teetering rotors with and without CH is compared. The same set of initial conditions is considered in all the simulations, with the vehicle at trim in hover, rotor thrust balancing vehicle's weight and assuming cyclic pitch commands close to zero. A periodic forcing term is introduced assuming a step variation of advance ratio ($\mu = 0.1$) and cyclic pitch, where the latter command is chosen in order to trim the helicopter at the corresponding speed. Figures 5.13 reports the resulting behavior of the rotor with dry friction in CH and no stiffness in hub teetering and feathering hinges.

The presence of the feathering degree of freedom allows the gimballed rotor to tilt almost exactly in the direction commanded by the swashplate, if no stiffness is present in the spherical gimbal, a negative value indicating forward tilt. A minor difference between no–feathering–plane and tip–path–plane is present, due to the aerodynamic periodic term.

The hub tilt angle, seen in the non–rotating frame, presents oscillations of small amplitude. As a consequence the in–plane rotor load oscillations (aerodynamic and inertial force components perpendicular to the shaft axis) remain small. On the converse, the teetering rotor presents a more intense oscillation. The presence of CH in both the gimballed and teetering rotor leads to marginal variations in the behaviour of the system.

When a stiffness $K = 7219$ Nm/rad is introduced in hub teetering and feathering hinges, the gimballed rotor is no longer capable of tilting the hub exactly in the direction of the no–feathering–plane (Fig. 5.14), an equilibrium condition being no longer available, as discussed previously. Both hub and blades present a periodic behaviour. The shape of the oscillations of coning angles and rates is a consequence of the friction in the coning hinges, with intervals during which friction keeps $\dot{\beta}_i$ close to zero (stick phase). As for the rest, the behaviour resembles that of the rigid rotor with cantilevered blades considered in the previous section. The impact of CH in the case of response to commands and loads transmitted in forward flight is thus limited.

5.1.4 Gust response of the isolated rotor

The presence of CH and pitch–coning coupling is motivated by a better gust response which should limit the peak load transmitted to the fuselage during a gust encounter, and provide inherent stability to the rotor, as discussed in [[84]]. At the same time it must be recognized that the rigid blade model considered in the previous section would excessively penalize the configuration with no CH, as blade flexibility and torsional deformation (not accounted for in the model) would induce a significant coupling between local incidence and effective blade coning.

Figure 5.15 describes the behavior of a rotor in hover with longitudinal cyclic pitch which experiences a severe vertical gust. In the first 0.6 s the rotor responds to the 5° longitudinal cyclic command. The tip–path–plane of all rotor configurations (evaluated for $\psi = 0, \pi$ for a_1 and for $\psi = \pi/2, 3\pi/2$) tilts in the same direction of the swashplate. Rotors with coning hinges presents a longer settling time before reaching the equilibrium value due to the blade coning motion.

During gust penetration both blades move upwards and the coning angle a_0 reaches a higher equilibrium position, when an inertially fixed isolated rotor is considered. At the same time the pitch–coning coupling reduces the steady state value of the rotor vertical forces, if compared with a rotor with no CH.

5.1.5 Gust response with heave motion

Figure 5.16 compares the gust response in hovering for an isolated rotor with that obtained for the simplified fuselage–rotor model, featuring a vertical translational degree of freedom, described at the end of the Section on “Rotor Models”. In both cases a fully gimballed rotor is considered.

When fuselage heave motion is included in the model, the helicopter accelerates in the direction of the gust as shown in Fig. 5.17. The relative speed of the helicopter with respect to the surrounding air mass reduces the variation of the angle of attack generated by the gust.

The gimballed rotor with CH presents a better gust response from both an aerodynamic and a dynamic standpoint. On one side, the variation of pitch angle induced by the pitch–coning coupling reduces the angle–of–attack variation and, as a direct consequence, the peak load. At the same time, the vertical load on the fuselage is reduced, when part of the aerodynamic load excites the coning response.

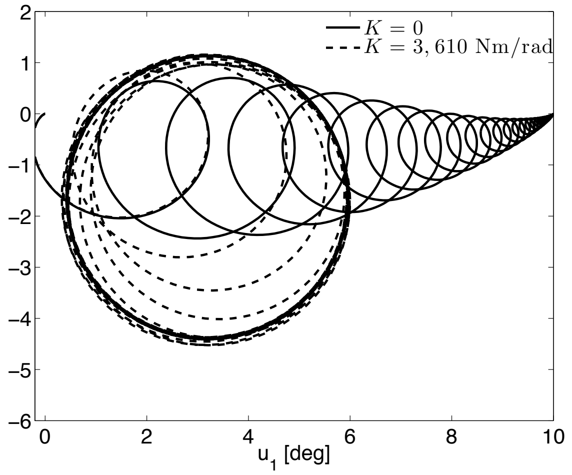

a) hub angular position

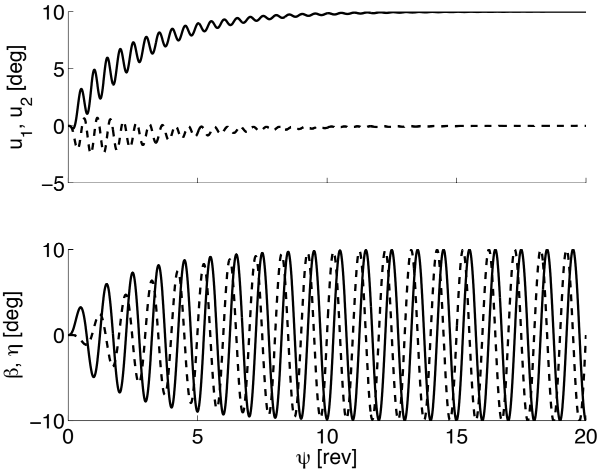

b) hub tilt angles $K = 0$

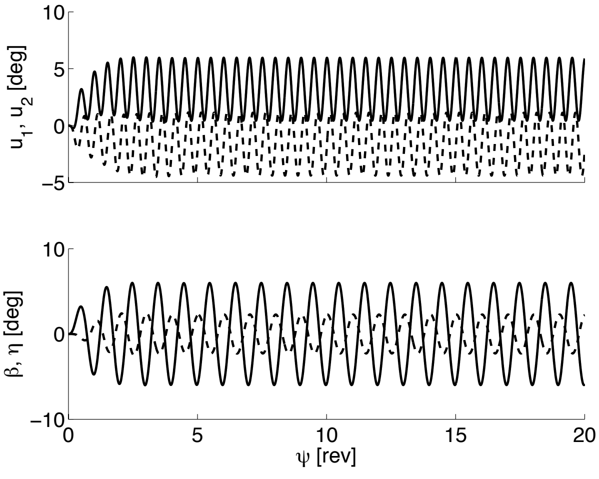

c) hub tilt angles $K = 3{,}610$ Nm/rad

Figure 5.3. Response to a longitudinal cyclic command $\theta_{SW} = 10$ deg.

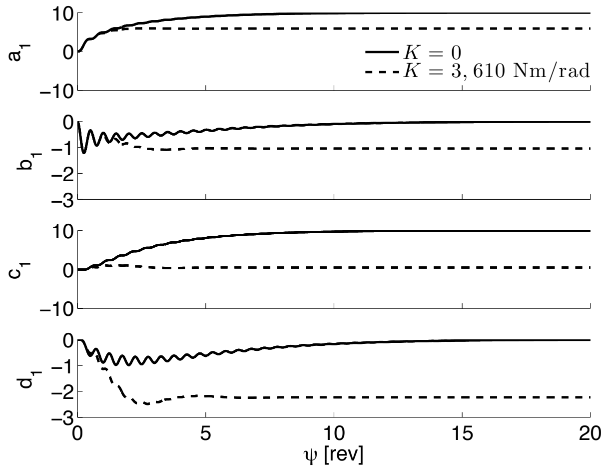

Figure 5.4. Response to a longitudinal cyclic command $\theta_{SW} = 10$ deg in terms of flapping coefficients.

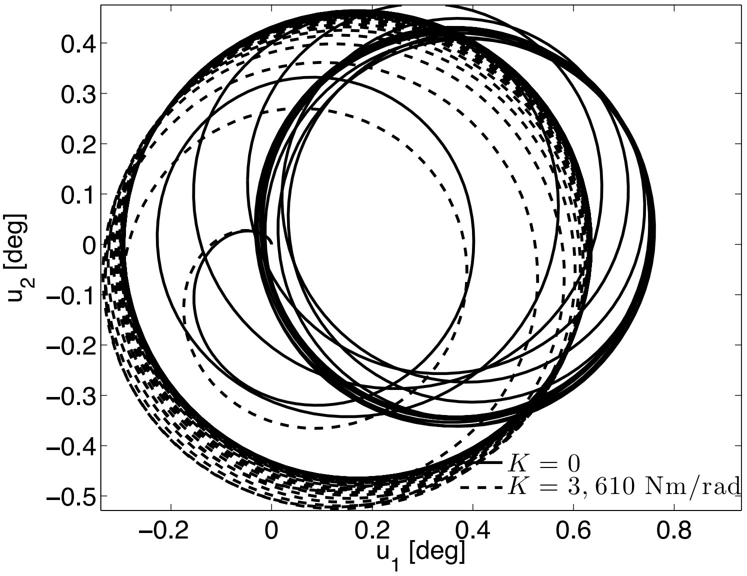

Figure 5.5. Response to a perturbation of the advance ratio $\mu = 0.05$.

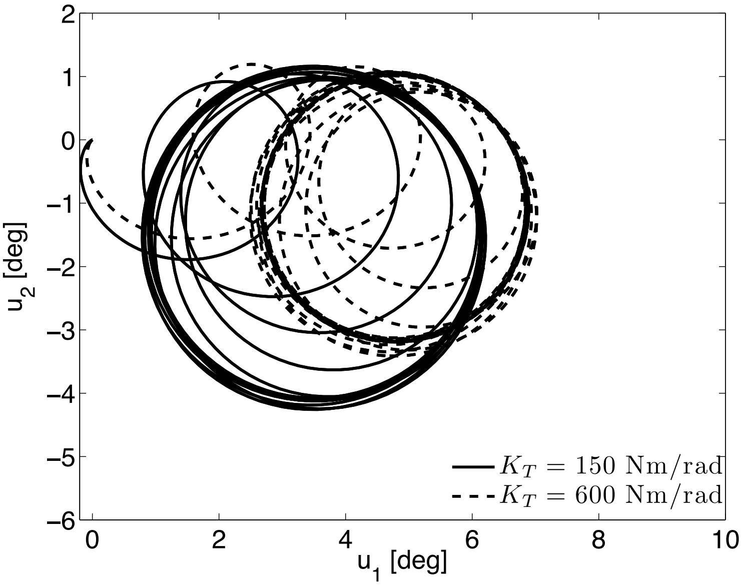

Figure 5.6. Response to a longitudinal cyclic command $\theta_{SW} = 10$ deg; $K_T \neq 0$.

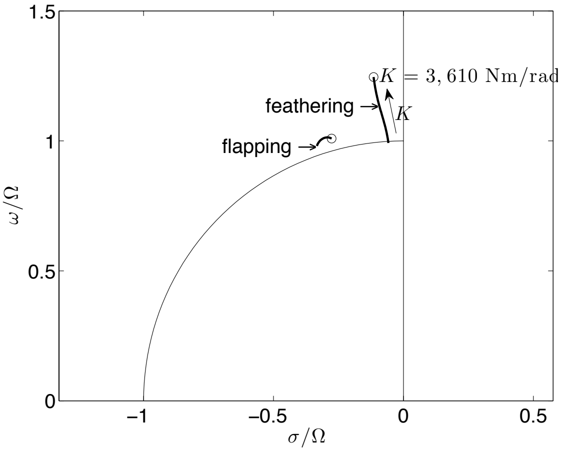

Figure 5.7. Root locus as a function of K; $\mu = 0$, $k_T = 0$.

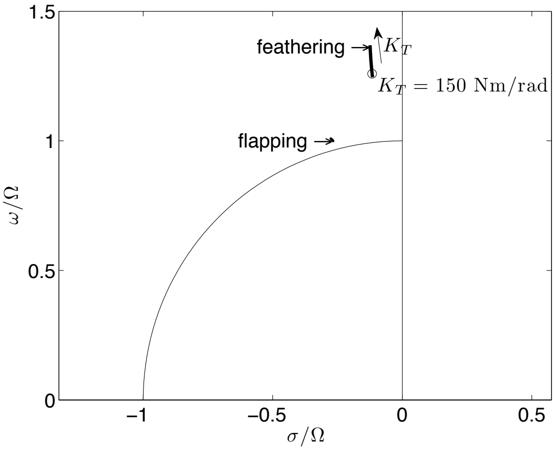

Figure 5.8. Root locus as a function of K_T; $\mu = 0$, $K = 3{,}610$ Nm/rad.

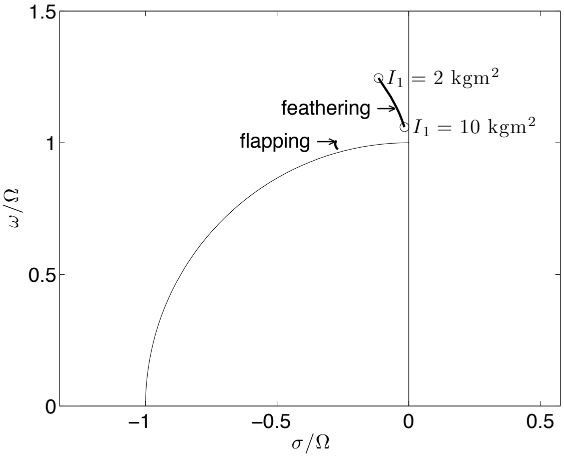

Figure 5.9. Root locus as a function of I_1; $\mu = 0$, $K = 3{,}610$ Nm/rad.

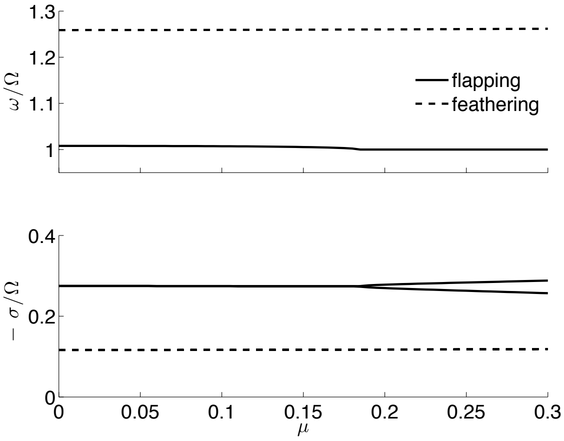

Figure 5.10. Frequency and damping as a function of μ from Floquet analysis for $K = 3{,}610$ Nm/rad.

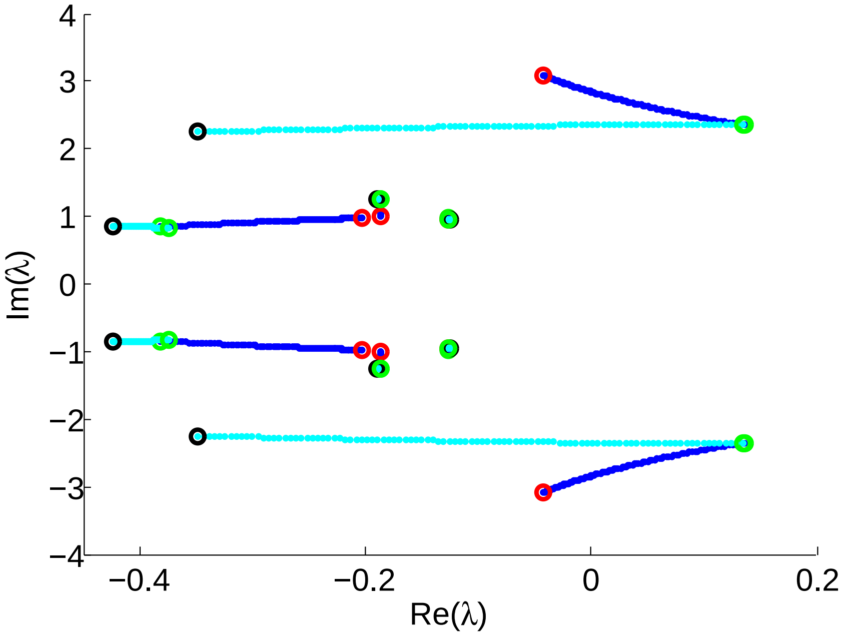

Figure 5.11. Root loci for the gimballed rotor in hover ($K_{PC} = 0$ and $c_{fr} = 0$: **o**; $0 < K_{PC} < 1.36$ with $c_{fr} = 0$: **...**; $K_{PC} = 1.36$ and $c_{fr} = 0$: **o**; $0 < c_{fric} < 0.4$ with $K_{PC} = 1.36$: **...**; $K_{PC} = 1.36$ and $c_{fr} = 0.4$:**o**).

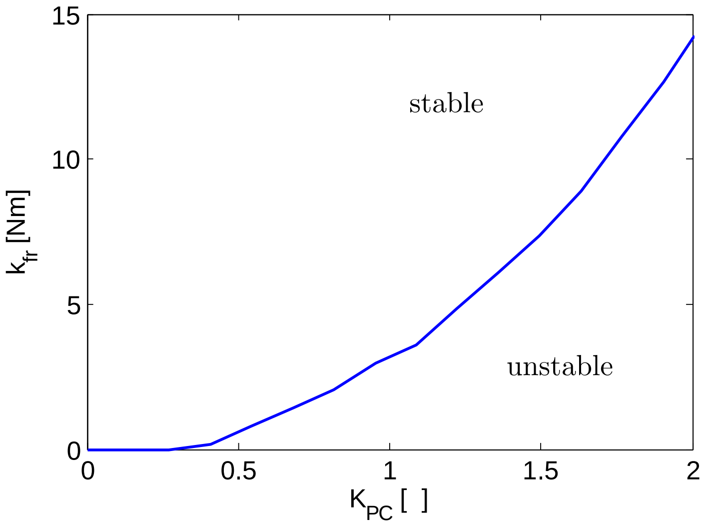

Figure 5.12. Stability limit in the k_{fr} vs k_{PC} plane.

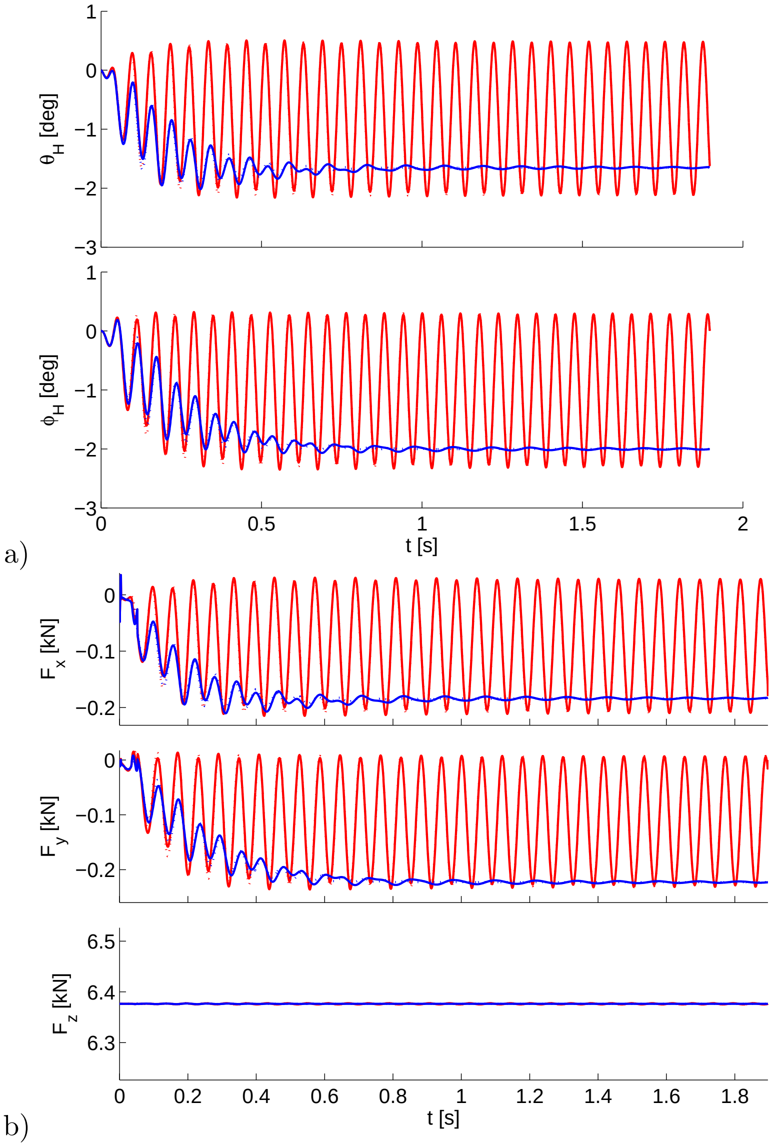

Figure 5.13. Rotor behavior at $\mu = 0.1$ with cyclic pitch and no hinge stiffness: a) hub tilt angles ; b) loads transmitted to the shaft. Gimb. rotor with CH (—), gimb. rotor without CH (···), teet. rotor with CH (—), teet. rotor without CH (···).

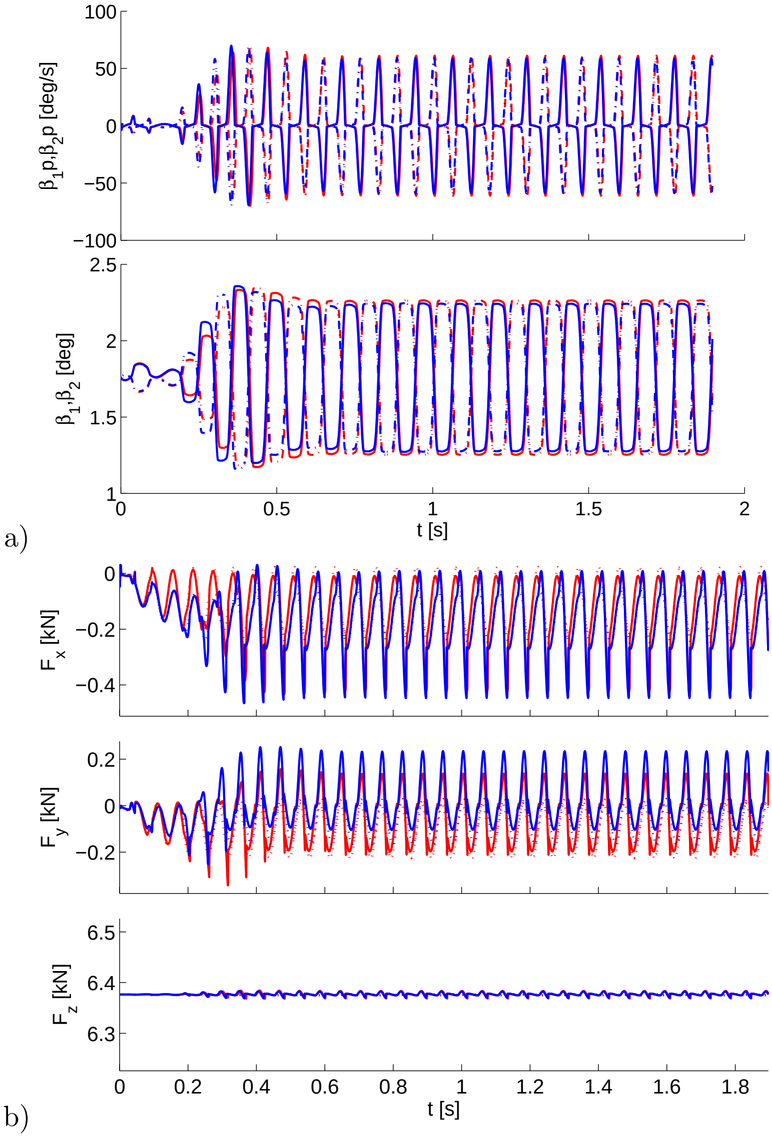

Figure 5.14. Rotor behavior at $\mu = 0.1$ with cyclic pitch and hinge stiffness: a) blade coning angles: Gimb. rotor: blade 1 (—) blade 2 (- · -), Teet. rotor: blade 1 (—) blade 2 (- · -), b) Force components in shaft axis: Gimb. rotor with CH (—), gimb. rotor without CH (· · ·), teet. rotor with CH (—), teet. rotor without CH (· · ·).

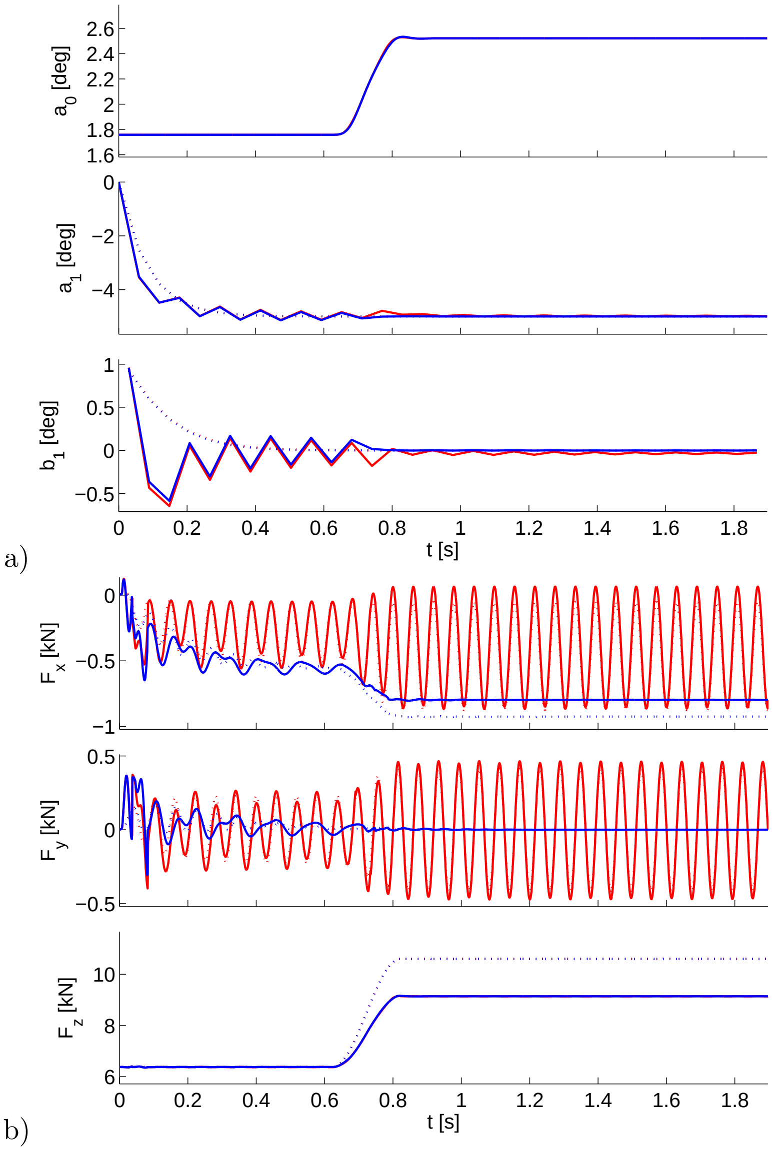

Figure 5.15. Rotor response to a step gust at $t = 0.6$ s in hover with 5° longitudinal cyclic: a) TPP states; b) loads transmitted to the shaft. Gimb. rotor with CH (—), gimb. rotor without CH (···), teet. rotor with CH (—), teet. rotor without CH (···).

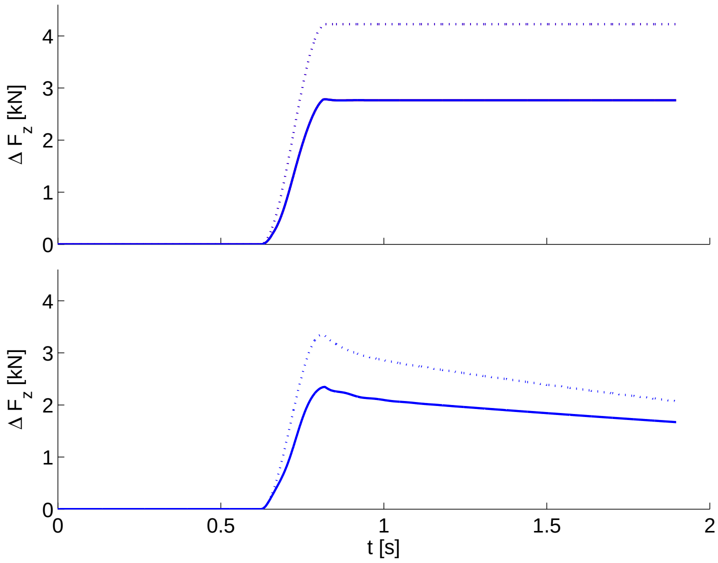

Figure 5.16. Rotor thrust response to a 0.2 s gust: a) rotor only; b) rotor and fuselage heave motion. Hover without cyclic pitch and no stiffness in rotor hub. Rotor with friction and $K_{PC} = 1.36$ (—), rotor without coning (···).

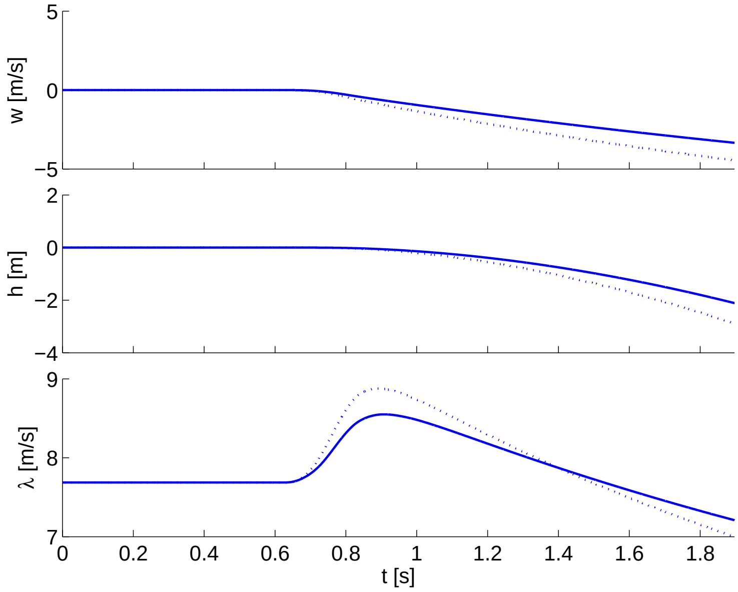

Figure 5.17. Fuselage and inflow states response to 0.2 s step gust. Rotor with friction and $K_{PC} = 1.36$ (—), rotor without coning (···).

5.2 Agility potential

As discussed in [43], inverse simulation is a very powerful tool for the analysis of rotorcraft agility potential. In particular, as handling qualities for modern helicopter are determined by means of ADS-33 standard [62], the evaluation of the rotorcraft behaviour in performing the required Mission Task Elements (MTE) by means of solution of inverse problems provides most of the most important information on agility potential. If on the one side the importance of technique such as inverse simulation and trajectory optimization [61] and [56] for agility potential evaluation is established, on the other hand a limited attention was devoted to the analysis of the effects of modelling issues on solution of these problems. These aspects are particularly relevant for the helicopter case, where model complexity can differ significantly depending on the approach chosen for representing vehicle dynamics. Different models of the same rotorcraft may result in a sizable different computational burden, sometimes even preventing the applicability of an algorithm because of the characteristics of the model itself. At the same time, and more important for the present study focused on the application of IS to the evaluation of helicopter HQ's, different models can provide significantly different inverse solutions for tracking the same manoeuvre, and this fact clearly poses some problems, if the inverse solution is derived with the objective of evaluating manoeuvring and agility potential of the vehicle.

5.2.1 Inverse Simulation algorithms

The subject of this section is the analysis of the effects of different choices in deriving a helicopter model suitable for flight dynamic studies on the results obtained from inverse simulation algorithms (IS). The objectives are:

1. to analyse the origin of the discrepancies between inverse solutions obtained from different models of the same vehicle, while performing a given task

2. to evaluate the uncertainty on command laws necessary to realize a specified flight task associated to a certain vehicle model.

The first objective requires the identification of those critical situations in which a given model fails to provide a reliable inverse solution for the considered task, whereas the definition of an uncertainty interval is a parameter of paramount importance for the development of robust control laws (*e.g.* stability and command augmentation systems that equips modern rotorcraft).

Quite obviously, differences are now expected when determining command travel during an aggressive manoeuvre by means of IS. The reliability of the result needs thus to be carefully analysed, particularly if the methodology is used in the framework of a preliminary design phase or handling quality assessment. Aim of this section is to perform a complete qualitative and quantitative analysis of the inverse solutions obtained for a set of manoeuvre tasks by means of different models of the Sikorsky UH–60 “Black Hawk” articulated blade single main rotor helicopter, described in section 4.1. Time–histories for control and state variables are compared, in order to identify the origin of discrepancies on the basis of a physical interpretation of the model characteristics. Metrics are then defined that quantify the confidence in the predicted control action with respect to a baseline helicopter model, used as a reference for the analysis. This provides a measure of control action uncertainty, an information of paramount importance in developing rotorcraft control systems.

The results obtained from the IS of the complete baseline model (Model A1) will be compared with those obtained for increasingly simpler models (A2 to B9), in order to identify whether and in which cases the predicted command travel and flight condition necessary for tracking the desired manoeuvres significantly differ from those obtained for the reference model. In particular, simpler rotor, inflow and fuselage aerodynamic models will be considered. As for the rotor, blade twist and lag degrees of freedom will be removed first from the individual blade model in order to reduce model order. Further simplifications are then obtained by considering rotor dynamics in terms of first harmonic flapping coefficients (coning, longitudinal and lateral). Main rotor inflow model is reduced from the classical Peters–Ha 3 state model with triangular velocity distribution to a single–state uniform dynamics and, finally, a quasi–static uniform inflow model, where inflow velocity is determined together with rotor thrust coefficient solving momentum balance equation by means of an iterative scheme [12]. Tail rotor inflow is always considered as uniform, featuring a single inflow velocity variable driven by tail rotor thrust, unless main rotor inflow dynamics is neglected, in which case also tail rotor inflow is assumed as quasi-steady. Also fuselage aerodynamic modelling is considered as amenable to simplification. In models Bs the force and moment database in tabular form is substituted by an estimate of parasite areas along the three–body axes. This will allow to highlight the relevance of fuselage aerodynamic model on the determination of the control action.

Main rotor collective (θ_0) and lateral and longitudinal cyclic pitch (A_{1_S} and B_{1_S}) and tail rotor collective ($\theta_{0_{tr}}$) are used as control variables for all the models. In this way the inverse solutions obtained for each one of the five considered tasks can be compared by analysing the difference in the control action on all the control channels, once the inverse solutions for the considered manoeuvre tasks are available. A global merit function is obtained from the root–mean–square (RMS) of the difference between the control displacement of the considered model and the control action for the reference one. The control action is always considered in terms of control displacement from the initial trim condition, inasmuch as different models may provide slightly different absolute command position and state variables at trim. Although marginal, this initial difference would be integrated over the whole duration of the manoeuvre, thus providing a bias to the metrics adopted for evaluating model reliability.

The global merit function is analysed in both absolute terms (RMS of the command activity difference) and relative ones (by scaling the RMS value of the difference with respect to the RMS of the control action). In the latter case an interesting index is obtained in terms of percentage of control action intensity, the reliability of which is partially compromised for those control channels along which control activity is less intense. In such a case, the (small) scaling value would result in high values of the average error with respect to the reference control action, that is, a (totally apparent) lack of reliability for the less important control action in the considered manoeuvre. This aspect makes the relative metric sometimes harder to interpret, inasmuch as the RMS of the total command travel (*i.e.* command action intensity) needs to be accounted for. As a consequence, also the RMS of the difference between the considered control actions needs to be considered for a complete and reliable analysis. The effect of manoeuvre intensity is accounted for by considering three different levels for each of the considered tasks (low, medium and high), where the level is modified increasing or decreasing one of the manoeuvre parameters (*i.e.* height variation in the hurdle–hop and pop–up manoeuvres, lateral displacement of vehicle centre of mass - CoG - in the slalom and lateral repositioning, manoeuvre time in the 180 deg turn), thus making the task more or less demanding.

As a further contribution, an uncertainty window for the control action is determined. This is done by evaluating the factor k_i for the RMS such that, given the control action on the i–th command channel, $u_i(t)$, its reference value, $u_i^r(t)$, and the resulting RMS of the difference, σ_i, at least 90% of control activity of the reference signal lies between $u_i(t) - k_i\sigma_i$ and $u_i(t) + k_i\sigma_i$. In such a way it is possible to obtain a quantitative evaluation of control uncertainty of the current helicopter model with respect to the reference baseline model. Such a technique could be extended to comparisons with actual flight tests, when available.

Three typical manoeuvres are considered first,[58, 97] in order to highlight major differences in command sequences for different tasks: (i) a longitudinal hurdle-hop; (ii) a slalom manoeuvre and (iii) a lateral repositioning. Reference values taken from HQ requirements are considered for the manoeuvre intensity parameters (that is, vertical or lateral CoG displacement or manoeuvre time) in the medium intensity tasks. Low and high intensity manoeuvres are obtained by decreasing or increasing such reference values by approximately 30%. The IS method adopted for the analysis is an integration method directly derived from the local optimization technique presented in Ref. [54]. The obtained results allowed for the determination of the RMS of the difference in the control action for all the considered helicopter models and the corresponding value of k_i for each manoeuvre.

The reliability of the findings is further investigated by analysing two more manoeuvres, a pop–up–pop–down manoeuvre and a 180 deg fast turn, again considering three different intensity levels. The resulting control action are shown to lie within the confidence levels derived from the previous test cases, thus demonstrating that the technique provides a valid method for the quantitative evaluation of uncertainty on control activity for the various helicopter models.

In the following paragraph a brief description of the numerical scheme adopted for solving the IS problem will be provided. The results obtained on the considered test cases for the different models will then be compared and discussed, in order to identify those models that provide a reasonable estimate of the required control action and HQ potential, while keeping model complexity (and consequently the overall amount of information necessary to develop it) down to a minimum level. After that, a technique for a faster solution of inverse simulation problems based on complex models which maintains a high level of reliability reducing the computational cost is provided.

5.2.2 Integration algorithm

Among other methods, the inverse simulation problem is solved by means of an integration algorithm [53, 54] as it provides the best compromise between computational cost and commonality (i.e. the possibility of using the same technique with all models). Assuming that helicopter dynamics is represented in terms of a system of n nonlinear ordinary differential equations in the form

$$\dot{\boldsymbol{x}} = \boldsymbol{f}(\boldsymbol{x}, \boldsymbol{u}) \; ; \quad \boldsymbol{y} = \boldsymbol{g}(\boldsymbol{x}) \tag{5.8}$$

where a dot indicates the time derivative, $\boldsymbol{x} \in \mathbb{R}^n$ is the state vector, $\boldsymbol{u} = (\theta_0, A_{1_S}, B_{1_S}, \theta_{0_{tr}})^T \in \mathbb{R}^m$ is the vector of $m = 4$ control variables (main rotor collective, lateral and longitudinal cyclic pitch coefficients, and tail rotor collective), and $\boldsymbol{y} \in \mathbb{R}^p$ is the vector of tracked output variables.

Once an output time history, $\boldsymbol{y}_{des}(t)$, is available (i.e. a manoeuvre profile like those required by ADS–33 specifications [62]), equations of motion are integrated from an initial condition $\boldsymbol{x}_I = \boldsymbol{x}_k$ at time t_k over a time interval Δt for a piece–wise constant value $\boldsymbol{u}_k^\star$ of the control variables. The resulting value $\boldsymbol{y}_F = \boldsymbol{g}(\boldsymbol{x}_F)$ of the output variables at time $t_F = t_{k+1} = t_k + \Delta t$ is thus a function $\boldsymbol{y}_F = \boldsymbol{F}(\boldsymbol{x}_k, \boldsymbol{u}_k^\star)$ of the (given) initial state $\boldsymbol{x}_k$ and of the (unknown) constant control action, $\boldsymbol{u}_k^\star$.

Control variables can then be determined in such a way that $\boldsymbol{y}_F$ matches the value of $\boldsymbol{y}_{des}$ at time t_F, that is, the inverse problem can be stated in terms of a set of p algebraic equations in the form

$$\boldsymbol{F}(\boldsymbol{x}_k, \boldsymbol{u}_k^\star) = \boldsymbol{y}_{des}(t_F) \tag{5.9}$$

with m unknowns. When $m = p$, the problem is nominal and, if well posed, it can be solved by means of standard numerical techniques, such as Newton–Raphson (NR) method [53]. If $m > p$ the problem is redundant, as in many aeronautical applications for fixed and rotary–wing aircraft, when 4 controls are available for tracking 3 trajectory variables.

Hess & Gao [53] solved this problem by use of the so–called Moore–Penrose pseudo–inverse during NR iterations, which results into the minimum–norm control vector that solves the problem. A more general approach was proposed by De Matteis *et al.* [54], where an optimization problem was solved in order to enforce, together with the constraints on trajectory variables, relevant properties to the inverse solution by defining a suitable merit function to be minimized locally at each time step of the inverse simulation. As an alternative, an additional constraint can be enforced in order to obtain a nominal inverse problem. In particular in the thesis the additional constraints zero lateral acceleration or zero sideslip are used.

A further problem relevant for aeronautical applications of IS integration methods is represented by undesirable oscillations in the control action or even instabilities in the inverse solution, discussed in some details in Refs. [43, 98, 99, 100]. These problems are related to the presence of transmission zeros, uncontrolled states and possible difficulties in the correct numerical evaluation of Jacobian matrix $\boldsymbol{J} = \partial \boldsymbol{y}_F / \partial \boldsymbol{u}_k^\star$ for the output variables. These issues can be circumvented, at the cost of increasing the computational burden, by solving the inverse problem stated by Eq. (5.9) over a longer time–horizon, that is, choosing $t_F^\star = t_k + N\Delta t > t_{k+1}$, that is, the piece–wise constant control action is propagated for a longer time interval in order to allow for uncontrolled dynamics to settle down. The initial condition $\boldsymbol{x}_{k+1}$ for the next step is then evaluated at time t_{k+1} [54].

As a variation to a standard integration method, a different definition of the algebraic system is adopted, where, rather than solving Eq. (5.9) in terms of the actual value of the tracked variables at time t_F, their increments over the time step between t_I and $t_F^\star$ are required to be equal. Equation (5.9) is thus replaced with

$$\begin{aligned} \Delta\boldsymbol{y} &= \boldsymbol{F}(\boldsymbol{x}_k, \boldsymbol{u}_k^\star) - \boldsymbol{g}(\boldsymbol{x}_k) = \\ &= \boldsymbol{y}_{des}(t_F) - \boldsymbol{y}_{des}(t_I) + K\left[\boldsymbol{y}_{des}(t_I) - \boldsymbol{g}(\boldsymbol{x}_k)\right] \end{aligned} \tag{5.10}$$

where the additional term in square brackets multiplied by a gain K avoids that the actual solution "drifts" away from the desired path because of the incomplete implementation of the considered step during the forward propagation, as outlined above. This term also enforces asymptotic convergence on the tracked variables when they achieve a steady value. By some simple manipulation, Eq. (5.10) can be rearranged as

$$\boldsymbol{F}(\boldsymbol{x}_k, \boldsymbol{u}_k^\star) = \boldsymbol{y}_{des}(t_F) + (K-1)\left[\boldsymbol{y}_{des}(t_I) - \boldsymbol{g}(\boldsymbol{x}_k)\right]$$

where for $K = 0$ the additional term $[\boldsymbol{y}_{des}(t_I) - \boldsymbol{g}(\boldsymbol{x}_k)]$ disappears and one simply requires that the increment of the actual output variables at the end of the whole inverse simulation step $\Delta t = t_F - t_I$ equals the increment for the desired variation of $\boldsymbol{y}$. Note that when $K = 1$ the inverse simulation scheme delivers a solution that exactly tracks the desired value of $\boldsymbol{y}_{des}$ at time $t_F^\star$. An intermediate value between 0 and 1 usually provides reasonable inverse solution for the considered application. A value $K = 0.3$ was used for producing all the results discussed in the sequel.

5.2.3 Test manoeuvres

The inverse simulation algorithm is tested, for all the different models briefly described in the previous Section, on 5 different manoeuvres:

(i) hurdle–hop

(ii) slalom manoeuvre

(iii) lateral repositioning

(iv) a pop–up–pop–down manoeuvre

(v) fast turn

Most of the analysis is based on manoeuvres (i) to (iii), that are used for the determination of the effects of model simplifications on the inverse solution and for the evaluation of model reliability metrics. Manoeuvres (iv) and (v) are used for validating the results obtained for the determination of the uncertainty on the control action.

Manoeuvres (i), (ii) and (v) start from a horizontal trim flight condition (the first one being a purely longitudinal manoeuvre) and are performed at constant speed, whereas the lateral repositioning and the pop–up–pop–down manoeuvres, (iii) and (iv), require the recovery of a hover condition after a lateral and a vertical displacement, respectively.

In the first case a purely longitudinal manoeuvre is considered, with a commanded altitude variation given by

$$\begin{aligned}
\Delta z &= 0 && \text{for } t \leq t_0, t \geq t_0 + T \\
\Delta z &= \frac{\Delta h}{16} \left\{ 9\cos\left[\frac{2\pi(t-t_0)}{T}\right] + \right. \\
&\qquad \left. - \cos\left[\frac{6\pi(t-t_0)}{T}\right] - 8 \right\} && \text{for } t_0 < t < t_0 + T
\end{aligned}$$

In the second case, the helicopter is required to perform a sequence of 4 turns, in order to follow a lateral path defined by the equation

$$\begin{aligned}
\Delta y &= 0 && \text{for } t \leq t_0, t \geq t_0 + T \\
\Delta y &= \frac{\Delta Y}{27\sqrt{3}} \left\{ 32\sin\left[\frac{2\pi(t-t_0)}{T}\right] - 20\sin\left[\frac{4\pi(t-t_0)}{T}\right] + \right. \\
&\qquad \left. + 2\sin\left[\frac{8\pi(t-t_0)}{T}\right] \right\} && \text{for } t_0 < t < t_0 + T
\end{aligned}$$

The third manoeuvre starts from a hovering condition that needs to be recovered after a lateral displacement of $Y_F = 120$ m, where the lateral coordinate is expected to vary as

$$\begin{aligned}
y &= 0 && \text{for } t \leq t_0 \\
y &= \frac{Y_F}{16} \left\{ 8 + \cos\left[\frac{3\pi(t-t_0)}{T}\right] + \right. \\
&\qquad \left. - 9\cos\left[\frac{\pi(t-t_0)}{T}\right] \right\} && \text{for } t_0 < t < t_0 + T \\
y &= Y_F && \text{for } t \geq t_0 + T
\end{aligned}$$

The data used for specifying the three manoeuvres are reported in Tab. 5.3. Note that the parameters for manoeuvres (ii) and (iii) are defined according to the standards set by ADS–33 requirements [62]. On the converse, manoeuvre (i) is not one of those specified in [62], but it is nonetheless one of the classic test–cases adopter in the literature on IS. A graphical representation of the desired variation of the relevant trajectory variables for the three manoeuvres is also reported (Fig. 5.18).

Commands necessary for tracking the desired manoeuvres will be represented in the following sub–sections in terms of main rotor collective, longitudinal and lateral cyclic pitch and tail rotor collective, by means of the percentage of the total available travel. A variation between 0 and 1 is considered for main rotor collective pitch, while ranges of variation between -1 and 1 are assumed for the other commands. Attitude variables (*i.e.* roll, pitch and yaw angles) and rotor states (in terms of multi–blade variables, when individual blade models are considered, or first harmonic flapping coefficients, when TPP dynamics is adopted) will also be analysed. On the converse, trajectory variables will not

Table 5.3. IS manoeuvres test matrix.

Manoeuvre	Initial	Manoeuvre attributes:			Value		Unit
	Velocity	Duration	Parameter	Low	Medium	High	
Test cases							
Hurdle Hop	30 m/s	20 s	Δh	20	30	40	m
Lateral reposit.	0 m/s	16 s	Δy	90	120	150	m
Slalom	35 m/s	13 s	Δy	9	15	21	m
Validation							
Pop-up-pop-down	0 m/s	10 s	Δh	6	9	12	m
Fast turn	30 m/s	T_m	T_m	18	15	12	s

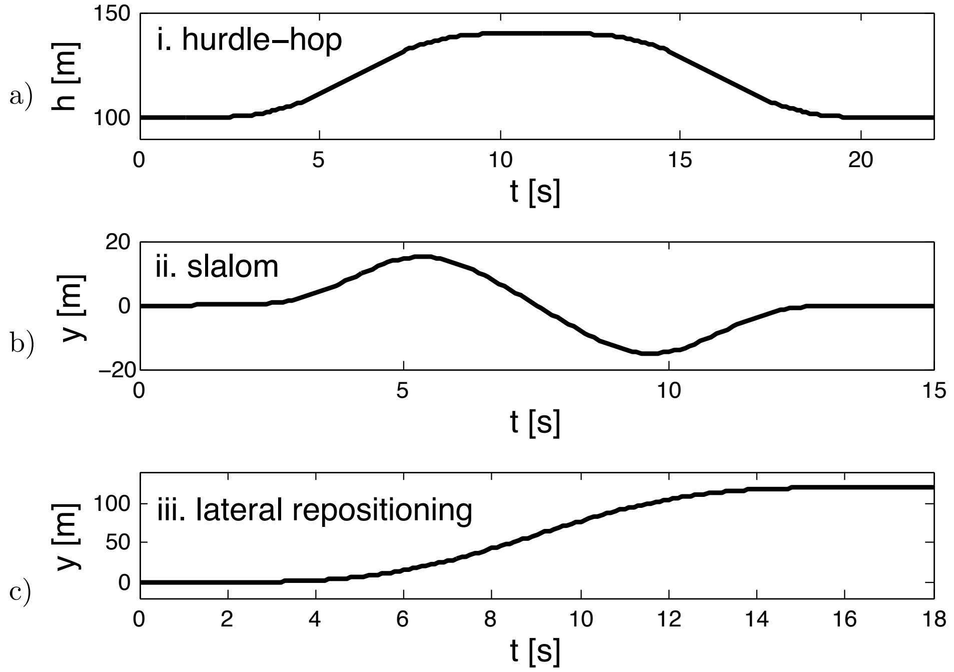

Figure 5.18. Geometry of the desired trajectories.

be shown, as far as the IS algorithm successfully tracks the desired trajectories, in all the considered test–cases.

The IS algorithm adopts a piece–wise constant control over a time step $\Delta t = 0.2$ s. For the individual blade models (A.1 to A.3) $N = 3$ is used, so that the inverse simulation problem is solved over an interval $\Delta t^\star = t_F^\star - t_I = 0.6$ s. For all the other models (A.4 to C.9), $N = 2$ is chosen, resulting in an inverse simulation time–step $\Delta t^\star = 0.4$ s. In all the considered cases a gain $K = 0.3$ in Eq. (5.10) is selected.

5.2.4 Model reliability metrics

Model reliability is evaluated on the basis of two metrics: (i) a global measure of the performance of lower order models in determining the control action when compared with the inverse solution of a more complete, higher order one used as a reference, and (ii) an estimate of the uncertainty on the command, that is, the identification of an interval centred around the command time–history of the simplified model that includes most of the control action derived for the reference baseline model. Both metrics will be based on the definition of suitable root–mean–square (RMS) values of relevant signals.

As far as the uncertainty window is concerned, the objective is to derive an estimate of its size from a given set of reference manoeuvres, where the inverse solution of the reference model is known, in terms of parameters related to control activity for the lower order model only. In this way it will be possible to use it in the form of a confidence interval for different manoeuvres without any *a priori* knowledge on a reference solution of any kind. On the converse, the determination of model global performance, which evaluates the discrepancies with respect to the reference solution, is available only in the presence of the latter.

The knowledge of the expected uncertainty for all the command lines is a piece of information of paramount importance in the derivation of closed–loop robust control laws. At the same time, the approach discussed in the sequel can be easily extended to the comparison of model inverse solutions with actual flight tests.

Global performance index

Command activity intensity $\bar{\bar{u}}_i$ for the i-th command line (e.g. $i = 3$ lateral cyclic for a hurdle–hop manoeuvre represented in figure 5.19.a) is evaluated as

$$\bar{\bar{u}}_i^2 = \frac{1}{T_m} \int_0^{T_m} u_i^2\,(t)\,dt \tag{5.11}$$

where u_i represents the variation of the command from the initial trim condition. As a consequence the values of command equilibrium have no influence on the evaluation of command activity intensity. Command intensity $\bar{\bar{u}}_i$ is determined for all command lines $\boldsymbol{u} = (\theta_0, A_{1_S}, B_{1_S}, \theta_{0_{tr}})^T$.

Model A1 is used as a reference for the current analysis, that is, the results $u_i^r\,(t)$ of the inverse simulation problem for model A1 are used as reference signals. The quantity σ_i, defined as the RMS of the difference of the two command signals, $u_i(t)$ and $u_i^r(t)$,

$$\sigma_i^2 = \frac{1}{T_m} \int_0^{T_m} \left[u_i\,(t) - u_i^r\,(t)\right]^2 dt \tag{5.12}$$

represents a measure of how well the model under analysis is able to capture the behaviour of the reference one on each command line (Fig. 5.19.b).

The value of σ_i may vary significantly for different command lines and manoeuvre tasks, as simplifying assumptions at the basis of each model may have a different impact on its ability to represent the system command response for different levels of the required

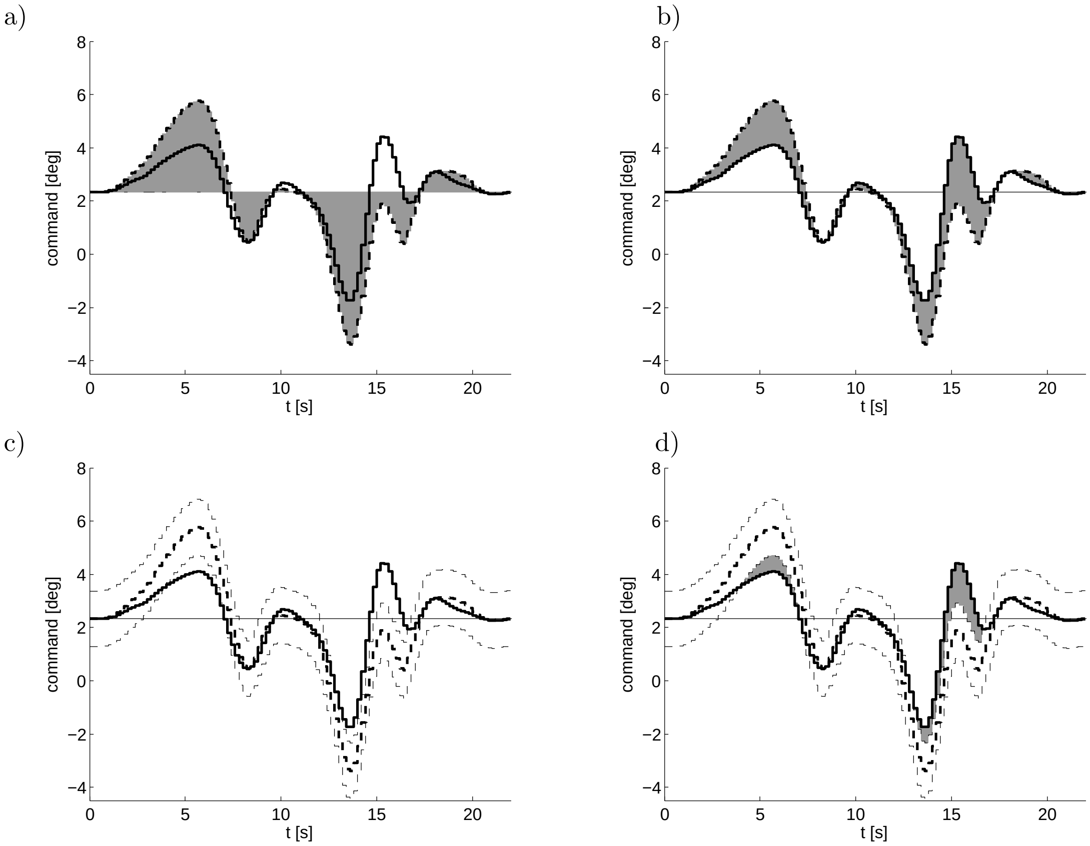

Figure 5.19. Comparison of control displacements: (a) RMS of command u_i; (b) RMS of the difference $u_i - u_i^r$; (c) uncertainty interval; (d) RMS of reference command outside of uncertainty interval.

control activity when flying in different flight conditions. A nondimensional ratio is thus defined, $\sigma_i^* = \sigma_i / \bar{\bar{u}}_i$, which represents the relative accuracy in the control action obtained by scaling the RMS of the error on the i–th command signal with respect to the RMS of the considered command, $\bar{\bar{u}}_i$, which is a rough measure of control activity. Clearly, a low value of σ_i^* indicates that the simplified model is capable of correctly reproducing the behaviour of the reference system. On the converse, higher values indicate either the presence of a very large peak in the error for a certain portion of the manoeuvre or a global inability of the simplified model to capture the physical behaviour of the system, at least in the considered task.

Determination of the uncertainty window

The second step of the procedure is the determination of the uncertainty window $k_i \sigma_i$ by means of an iterative process, starting from a reasonable first guess for k_i. Figure 5.19.c represents the uncertainty interval of size $k_i \sigma_i$ around the model command for $k_i = 1$. It is possible at this point to evaluate the portion $\delta_i(t)$ of the reference command that lies outside of the $u_i \pm k_i\sigma_i$ interval centred around the considered command trim history, that is

$$\delta_i(t) = \begin{cases} u^r(t) - [u(t) - k_i\sigma_i] & \text{if} \quad u^r(t) < u(t) - k_i\sigma_i \\ 0 & \text{if} \quad u(t) - k_i\sigma_i < u^r(t) < u(t) + k_i\sigma_i \\ u^r(t) - [u(t) + k_i\sigma_i] & \text{if} \quad u^r(t) > u(t) + k_i\sigma_i \end{cases} \tag{5.13}$$

The root mean square of the signal

$$\epsilon_i^2 = \frac{1}{T_m}\int_0^{T_m} \delta_i^2(t)\,dt \tag{5.14}$$

represents at this point a global measure of the portion of the reference signal $u^r(t)$ that, lying outside of the $\pm k_i\sigma_i$ window (5.19.d), is not correctly represented by $u_i(t)$.

Given the above mentioned definitions, the value k_i is evaluated for each command line in all the test manoeuvres considered, in such a way that the ratio $\tau = \epsilon_i/\sigma_i$ is equal to a given threshold, $\tau_{\max}$. It is clear that, by setting $\tau_{\max} = 0$, one requires that the reference signal $u_i^r(t)$ lies entirely within the uncertainty window, in which case its amplitude would be simply given by

$$k_i\sigma_i = \max_{t\in[0,T_m]} \left[u_i(t) - u_i^r(t)\right]$$

without the need for any iterative procedure. But the use of an uncertainty window that contains all the reference command control activity results into an excessively conservative estimate of the uncertainty that may unfairly penalize a relative good modelling approach because of a slight below average performance on a small time interval, whereas most of the manoeuvre is correctly represented. A value of $\tau_{\max} = 0.1$ is selected for the present analysis, such that at least 90% of the reference control activity lies within the uncertainty window, a value that, in the authors' opinion represents a reasonable compromise between reliability of the results and conservativeness. Larger values of $\tau_{\max}$ will result into smaller uncertainty interval that may fail to correctly point out those critical situations in which a model is not able to capture the actual control action over a limited yet significant portion of the manoeuvre.

5.2.5 Qualitative analysis

The main objective of a qualitative analysis is to correlate differences in the results with simplifying assumption at the base of each model. Such analysis is conducted on the three test manoeuvres, comparing the behaviour of all models.

Manoeuvre i: Hurdle–hop

Figure 5.20 represents the trajectories achieved by means of the inverse simulation algorithm. All models are able to track the desired trajectory with great precision. The lateral error, allowed in the integration approach with correction factor, is smaller than 0.3 m after a 22s manoeuvre.

Figure 5.21 depicts the command travel required for performing the hurdle–hop manoeuvre for all the considered models, the most relevant aspects of the manoeuvre appearing to be almost independent of the model, if not for the initial trim state, which is significantly affected by the inflow model. Figure 5.22 plots the command displacement from trim value and thus annihilates differences at trim among the models. In this respect, differences are particularly evident in the lateral cyclic pitch time–history, where two groups of solutions are clearly visible: the individual blade models (A1 to A3), together with model A4, featuring the 2^{nd} order TPP dynamics with triangular inflow on one side, and the models featuring uniform inflow (from A5 to B8).

The only minor difference in the first group of solutions (A1 to A4) is represented by θ_0, affected by the presence of the dynamic twist model which causes a 3% variation of main rotor collective pitch with respect to those models where a blade torsional degree of freedom is not present. This difference is hardly visible on the reported results and appears as truly negligible with respect to the command travel required for the manoeuvre. Similarly, a slight variation on commands is also apparent when fuselage aerodynamic moments are dropped (models B), a difference particularly evident on longitudinal cyclic pitch, where command values are shifted by almost 5%, but command travel is practically unaffected. If command displacement from trim value was reported instead of the absolute command, the first 9 models (A1 to B8) would provide almost identical results. The only exception is represented by model B9 which exhibit significant differences. In particular, a smaller command displacement from trim is apparent for A_{1_S} and $\theta_{0_{tr}}$, due to the fact that in–plane rotor forces are neglected, according to the elementary rotor model formulation reported in [11]. This fact clearly demonstrate that, even for this relatively simple, purely longitudinal manoeuvre, the most elementary model misses important aspects of the required control action, thus harming a correct analysis of vehicle manoeuvre potential.

A similar trend is apparent also for attitude (Fig. 5.23) and rotor variables (Fig. 5.24). The time–histories are almost identical for all these variables and attitude angles all lie within ±1 deg from the solution for the most complex model, A1. As for rotor variables, only model B9 presents a few more significant variations with respect to the trend identified on the basis of the other models. Some differences, from the quantitative point of view, are visible on the coning angle, β_c, for individual blade models (continuous lines in Fig. 5.24), which show wider variations in response to rotor loads changes along the manoeuvre. This means that TPP models underestimate coning angle variations. This could be detrimental, when a pitch–flap coupling is considered, but in the present case $\tan\delta_3 = 0$, and this difference does not affect significantly rotor manoeuvre loads. As far as every other aspect is concerned, the two classes of rotor models provide very similar results. A few minor but systematic differences on flapping coefficients are also apparent between 2^{nd} and 1^{st}–order TPP models and on lateral flapping coefficient, β_{1_s}, in relation to the inflow model, a difference that is compensated by the slight variation in rotor cyclic pitch, as outlined above, in order to provide the correct load for performing the desired manoeuvre.

As a general limitation for the validity of the results, it should be noted that a negative peak value of collective pitch is required during the descent phase (Fig. 5.21), which means that the manoeuvre cannot be completed at constant speed without violating a constraint

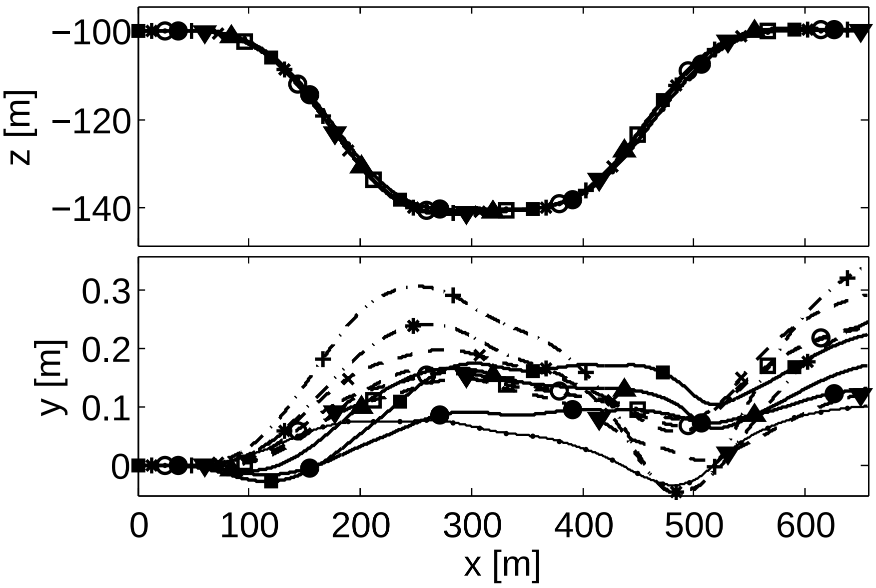

Figure 5.20. Achieved trajectories in hurdle-hop manoeuvre.

on command travel. Finally, figure 5.25 depicts power requirement during the hurdle-hop manoeuvre. All models but B9 are able to provide a realistic estimate of necessary power. The low peak in the collective pitch is matched in this case with a negative power requirement.

Manoeuvre ii: Slalom

A second set of test–cases is considered for a more complex, three–dimensional slalom manoeuvre. The command travel required around all control axes is quite large for all the considered models, which shares most of the qualitative features, but quantitative differences on control effort are rather significant, as it is evident from the plots reported in Fig. 5.26, where results for the 3 reference models A1, A6, and B9 are reported, together with those obtained for models A4 and B6. The other individual blade models exhibit a behaviour very close to that shown by A1.

If one drops model B9, that as for the hurdle–hop manoeuvre exhibits major differences with respect to all the other test cases, the control on lateral cyclic pitch appears similar for all the models, although the individual blade model requires significantly less command travel for performing the required turns. Differences are even more dramatic for the other commands: model A4 follows relatively well the command profile for θ_0, but control activity on longitudinal cyclic pitch and tail rotor collective is significantly more intense for models A4 to B6, if compared with A1. This is at least partially due to the need for a stronger filtering action on the command law obtained by the IS algorithm, when an individual blade model is dealt with, in order to avoid the insurgence of command oscillations, but it is also related to the effects of nonlinear dynamic terms not included in

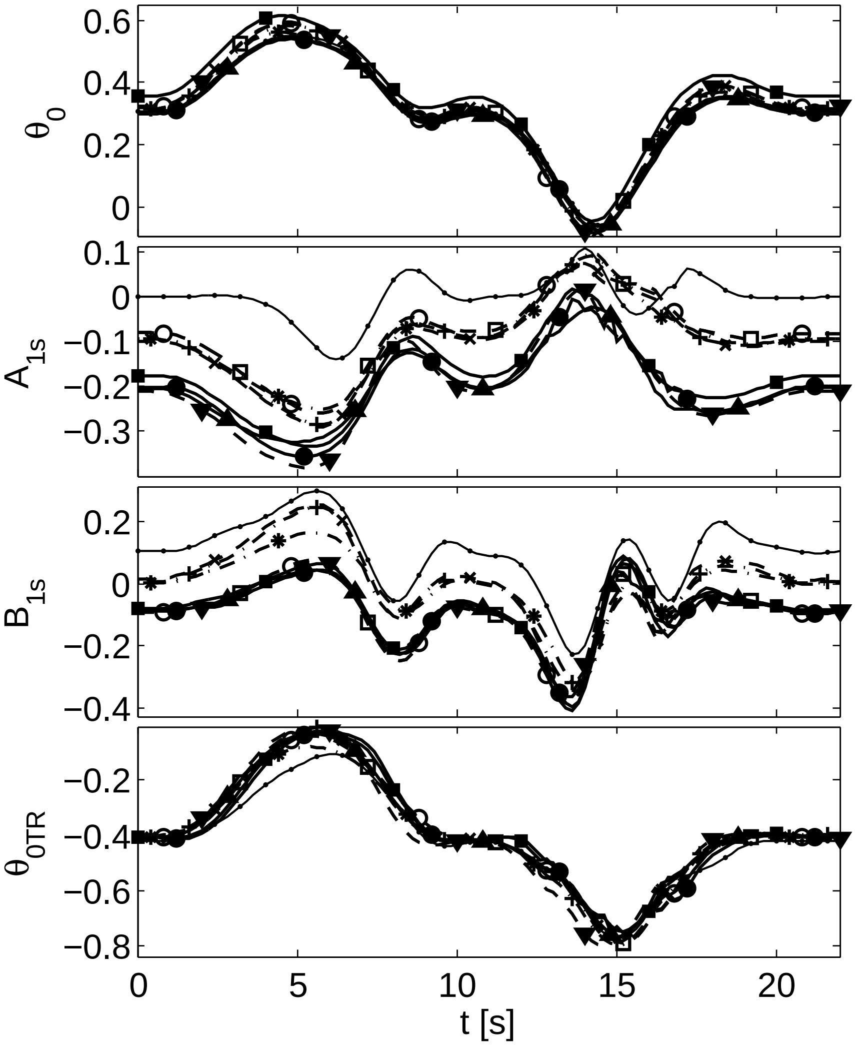

Figure 5.21. Total command travel time-histories in hurdle-hop manoeuvre.

the simplified TPP linear dynamic models and the related evaluation of rotor loads and inertial coupling terms.

As can be seen in figure 5.27, rotor states dynamics is very similar for all the model for the coning degree of freedom β_c while strong difference emerge for model B8 and B9 when longitudinal and alteral tilt are considered. As for attitude variable, roll and yaw angles (also not reported) show very similar variations, with differences limited to less than 2 deg for ϕ, over variations as high as ± 50 deg, and less than ± 1 deg for ψ over variations between -12 and 14 deg. On the converse, sizable differences are present on the pitch angle θ (Fig. 5.28), where differences as high as 5 deg are present, which are equivalent to the whole amplitude of the motion around the pitch axis. From this discussion it is apparent that, when more aggressive tasks are considered, the role of higher order terms

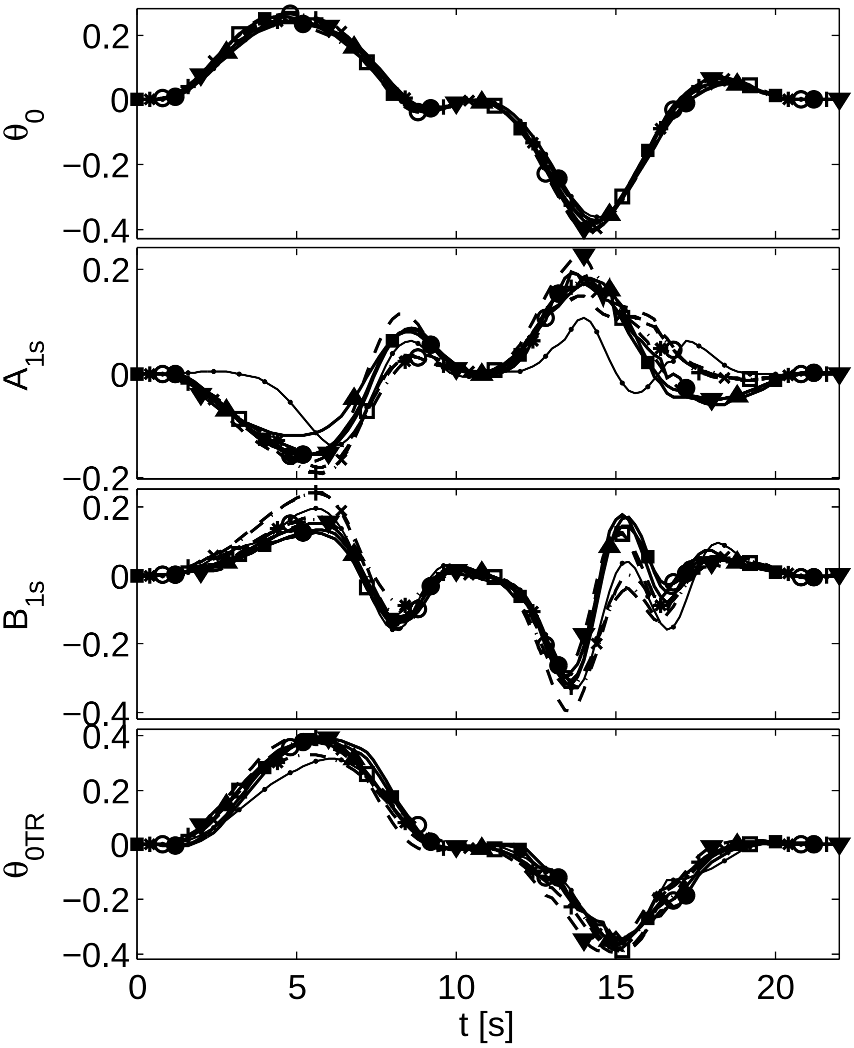

Figure 5.22. Command displacement from trim time-histories in hurdle-hop manoeuvre.

in rotor dynamics has a sizable effect on the simulated manoeuvre.

Manoeuvre iii: Lateral Repositioning

The last manoeuvre considered is the so–called lateral repositioning. The command travel on A_{1_S} and B_{1_S} is reported in Fig. 5.29 (the variation of main and tail rotor collective pitch is not represented as it is similar for all the models, with the usual exception of model B9, which follows the qualitative behaviour, but misses the correct amplitude of the command travel required). Major differences are visible on cyclic pitch commands, A_{1_S} and B_{1_S}, and lateral and longitudinal flapping coefficients, β_{lng} and β_{lat} (also not reported for the sake of conciseness). If, on the one side, differences in terms of required

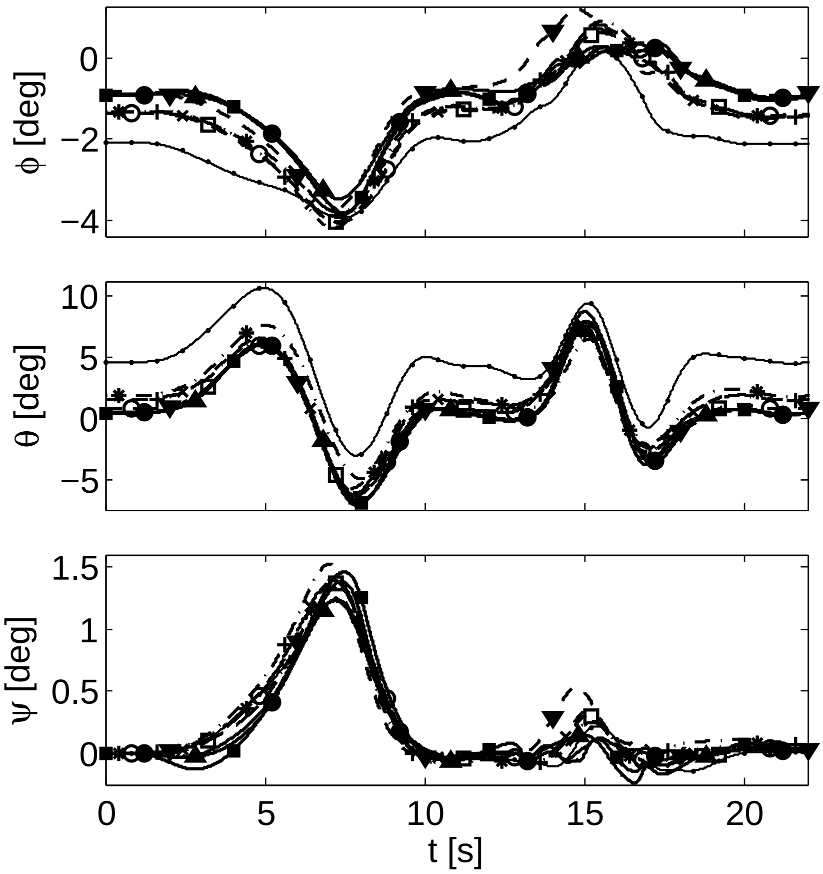

Figure 5.23. Attitude time-histories in hurdle-hop manoeuvre.

command travel remain rather limited, on the other one the qualitative trend shown by command and rotor state variables is significantly affected by the main rotor inflow model, where a triangular distribution at the peak lateral velocity close to 20 m/s clearly causes a significant variation on rotor loads that need to be compensated by a proper lateral and longitudinal control action, in order to keep a purely lateral velocity and constant fuselage heading.

In this latter situation, also the fuselage model appears to play a more significant role than in the previous cases. It is clear from Fig. 5.30, where roll and pitch angles are reported, that neglecting fuselage aerodynamic moments results into a significant difference in the attitude variables during the manoeuvre, up to 5 deg for ϕ and 4 deg for θ. Such a difference was not apparent in the previous two manoeuvres, when the flow impinges on the fuselage with small sideslip angles at high speed and most of the fuselage is outside of rotor wake. On the converse, when aggressive, lateral manoeuvres are dealt with, all the features of the flowfield around the fuselage play a more crucial role, especially considering the fact

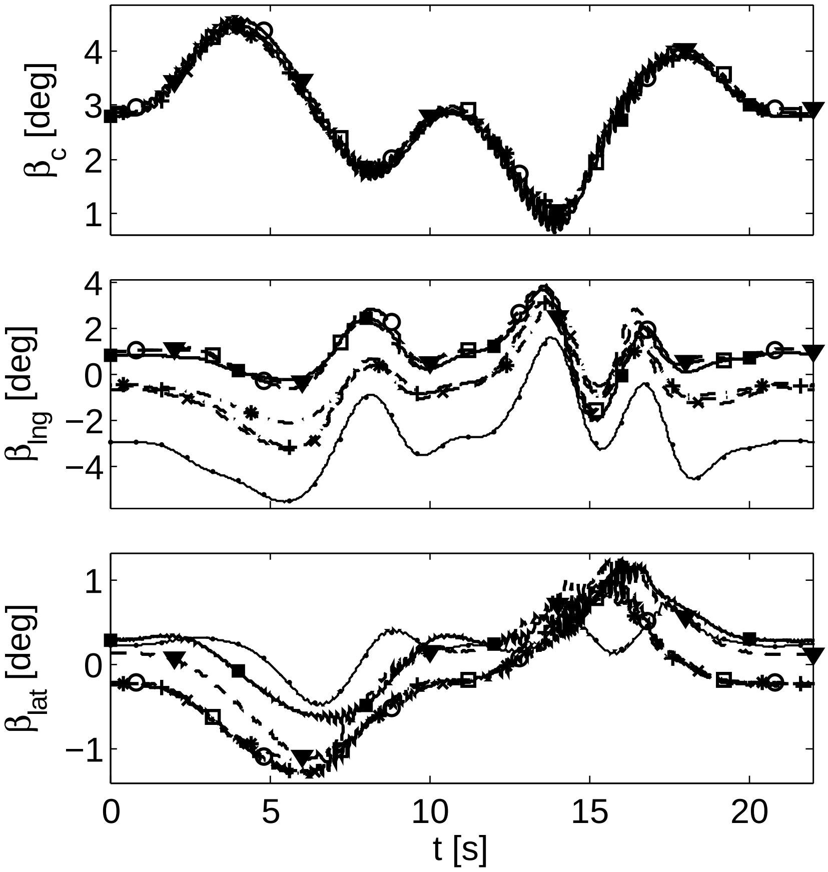

Figure 5.24. Rotor states time-histories in hurdle-hop manoeuvre.

that the manoeuvres starts and ends in a hover condition passing through a relatively high lateral speed, as high as 20 m/s in the considered case, where rotor wake impinges on the fuselage for a large portion of the manoeuvre and large variations of both aerodynamic angles, α and β are expected.

5.2.6 Quantitative analysis

As stated before, different “intensities” are considered for each manoeuvre. Together with the standard cases, defined according to HQ requirements or after similar manoeuvre examples found in the literature (and considered as medium tasks), less demanding (low intensity) and more demanding (high intensity) test cases were defined by decreasing or increasing the difficulty of the manoeuvre, by properly tailoring the manoeuvre parameter (*e.g.* the vertical or lateral displacement to be achieved during the manoeuvre or the manoeuvre time prescribed to complete it).

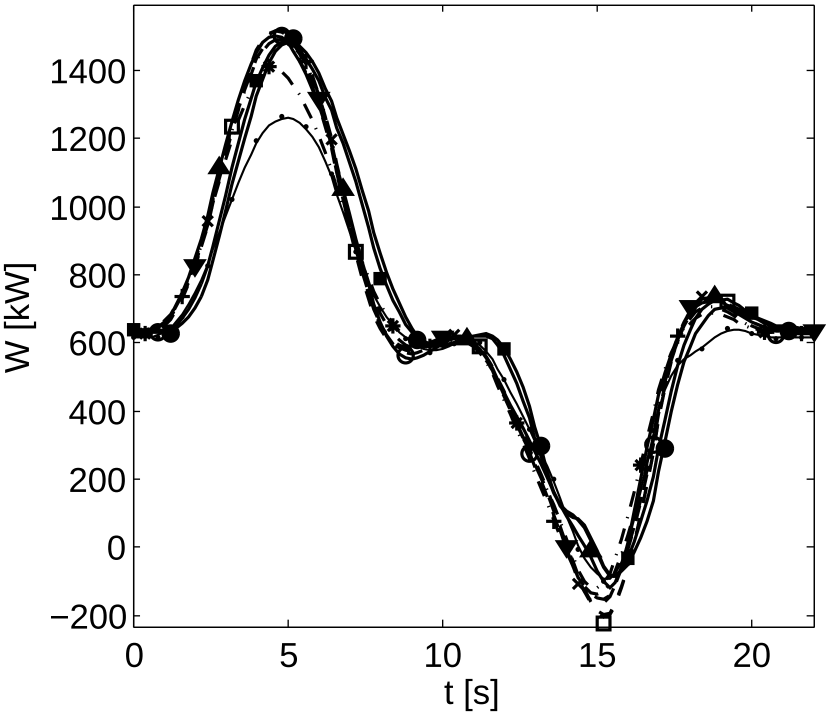

Figure 5.25. Required power in hurdle-hop manoeuvre.

After the evaluation of the uncertainty on each command line, two more manoeuvres are considered, a vertical pop–up–pop–down and a fast 180 deg turn, in order to validate the results obtained, by verifying that the uncertainty levels determined on the basis of the previous three manoeuvres correctly bracketed the control action for these additional tasks. For the latter one, the performance parameter that rules manoeuvre difficulty is the time required to complete the 180 deg turn, T_m, which makes the task more demanding when smaller values are considered.

A total of 3 tests for each of the 5 manoeuvres for as many as 10 helicopter models of various complexity (see Tab. 4.1) have been analysed, summing up a total of 150 test cases. 90 of these tests are used for the determination of the global model reliability metrics for the 4 command channels, σ_i, $i = 1, 2, 3, 4$, and the corresponding uncertainty intervals, $k_i\sigma_i$ according to the procedure outlined in the previous paragraph. The remaining 60 tests are used with the purpose of validating the obtained results, as discussed above.

5.2.7 Determination of the model reliability metric

By considering the results obtained from the IS of the 90 test cases, the values of the relative accuracy in the control action, σ_i^*, defined in the previous paragraph, are computed. A selection of these data, for models A4, A6, B6, B8 and B9 is reported in Tab. 5.4. It

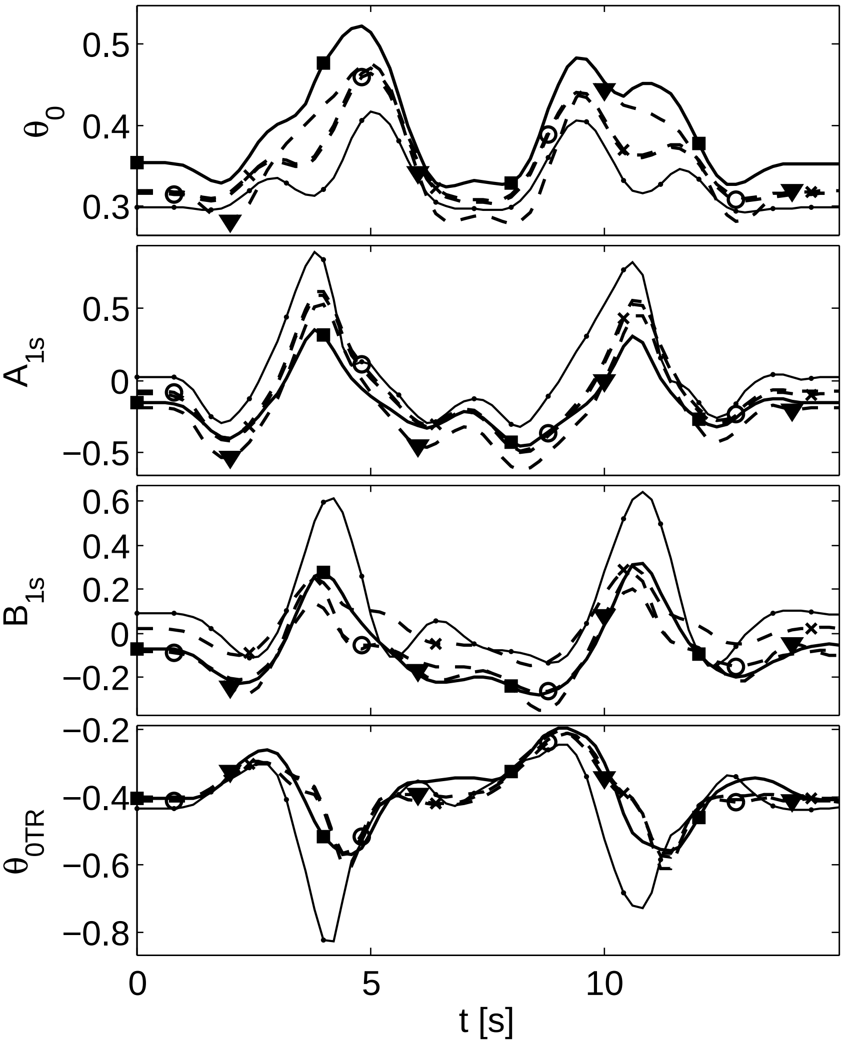

Figure 5.26. Command travel in slalom manoeuvre.

is possible to observe that these values present a sizable variation, over the various test cases, also for the same command channel, whereas a single, reference value for globally quantifying the performance of the considered model would be highly desirable.

Starting from these rough data, a single reference value, $\hat{\sigma}_i$, that represents a global index for the RMS of the error over the whole set of tests, is selected as

$$\hat{\sigma}_i = \bar{\sigma}_i + 0.25[\max_i(\sigma_i^*) - \bar{\sigma}_i]$$

an empirical value between the average value $\bar{\sigma}_i$ of σ_i^* over the different manoeuvres and the worst case, represented by the maximum value of the scaled RMS. The values of $\hat{\sigma}_i$, reported in the last column of Tab. 5.4, are highlighted in boldface characters. Their choice is necessary in the attempt of providing a single value for the amplitude of the uncertainty

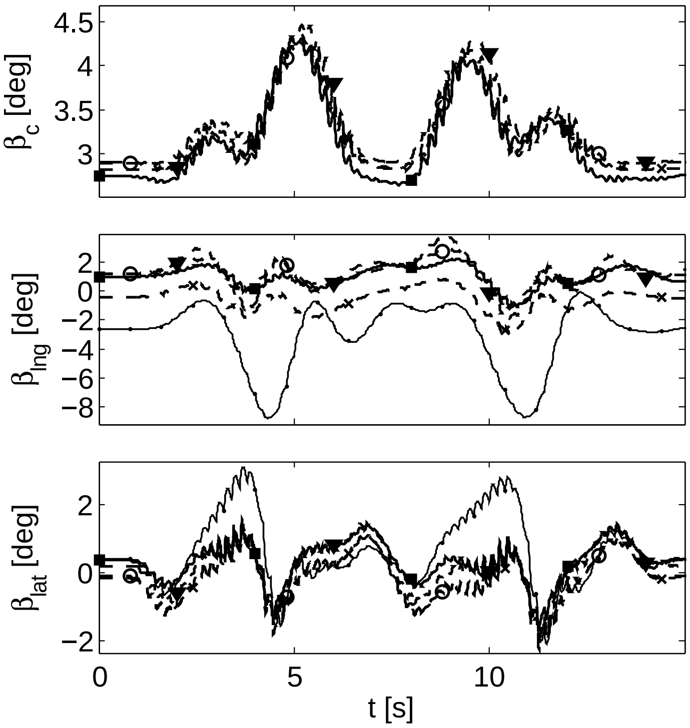

Figure 5.27. Rotor states time-histories in slalom manoeuvre.

window in the form $\pm k\hat{\sigma}_i$, at the next step of the procedure, when the uncertainty needs to be scaled with respect to control activity RMS, $\bar{\bar{u}}_i$. In such a way it is possible to provide an estimate of the uncertainty window for any given level of control activity, an important information in the synthesis of robust control laws (e.g. control and stability augmentation systems, SCAS).

In the choice of $\hat{\sigma}_i$, a few cases appear as critical, inasmuch as they were affected by a clear inadequacy of the considered model in representing a particular manoeuvre, as already reported in the previous section. In particular, for the lateral repositioning task, reduced–order rotor models and, even more seriously, simplified fuselage aerodynamic models clearly cause a significant loss in overall simulation model reliability, with values of σ_i^* that become as high as 3 or 4 for the longitudinal cyclic pitch, that is, the RMS of the error on this command channel is 3 or 4 times the value of the RMS of the control activity. If these data are dropped in the definition of $\hat{\sigma}_i$, the data reported between parentheses in the last column are obtained, in the same range of the other values, at the expenses of limiting the validity of the results, as not all the manoeuvres are included in the definition of this corrected reference value of the RMS of the error.

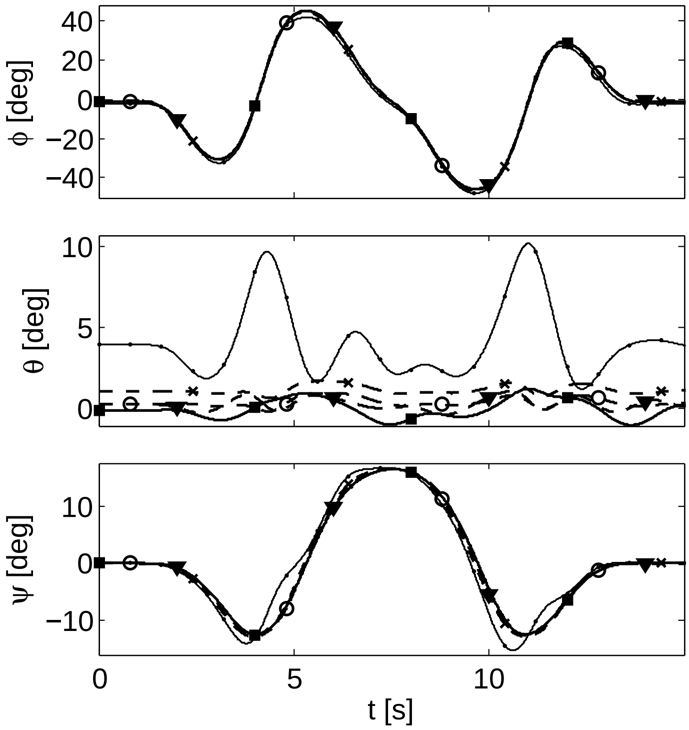

Figure 5.28. Attitude time-histories in slalom manoeuvre.

5.2.8 Definition of the uncertainty window

The following step in the analysis is the identification of the uncertainty interval for the given control action, as discussed in the previous paragraph. Table 5.5 reports the values of k_i to obtain a confidence level equal to 90% of the RMS of the error $u_i - u_i^r$, considering the same models at the basis of the results reported in Tab. 5.4. Again, a compromise between the average value and the reported worst cases (*e.g.* longitudinal cyclic pitch and tail rotor collective in a low–intensity hurdle–hop) is needed, where one should remember that the values, scaled with respect to the RMS of the control displacement, are penalized for those command lines less important for the considered task. Following an approach similar to the reliability metrics, the final value is evaluated as

$$k = \bar{k} + 0.25[\max_i(k_i) - \bar{k}]$$

where $\bar{k}$ is the average value of k_i. The value $k = 2.1$ obtained with such approach is used for all models and commands lines in the rest of the analysis. With this choice, somewhat arbitrary but practically effective, a single parameter can be used to characterize the uncertainty level on all command lines, once a reference value $\hat{\sigma}_i$ for the RMS of the error with respect to the reference command signal is known.

Once a uniform value for the parameter k is chosen for all the considered tests, as

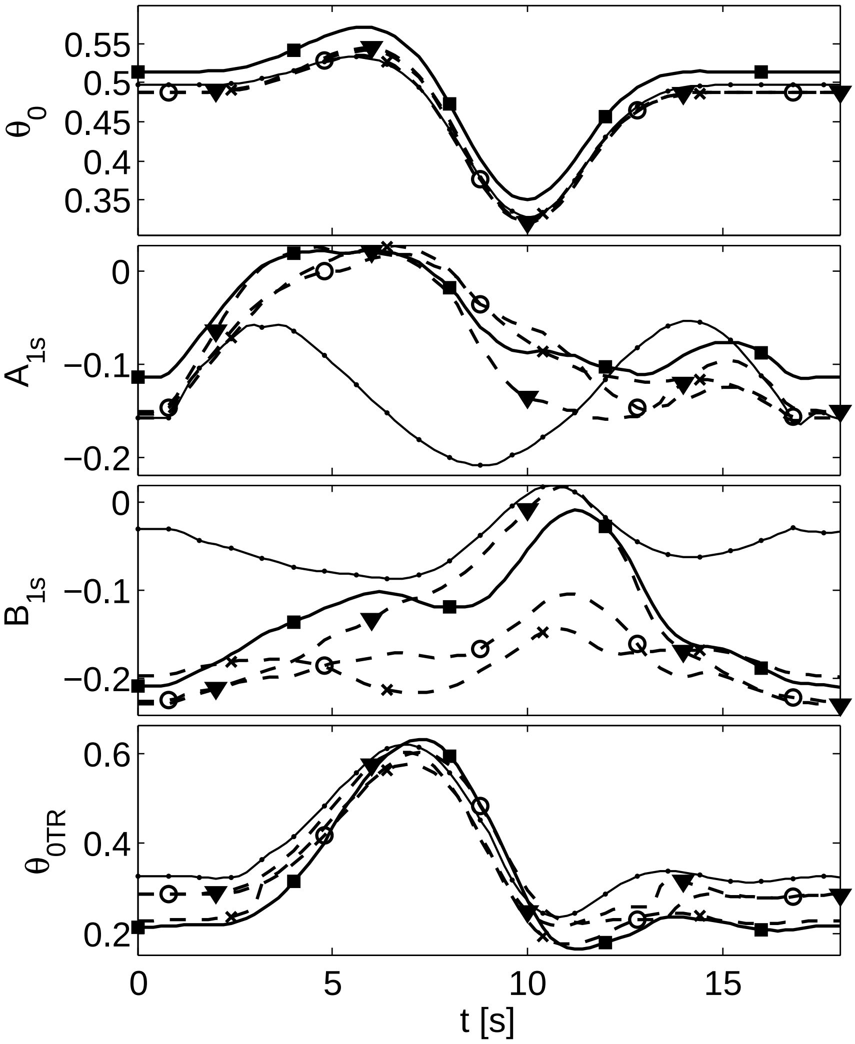

Figure 5.29. Command travel in lateral repositioning manoeuvre.

indicated above, a target window for the command, $u_i(t) \pm (k\hat{\sigma}_i)\bar{\bar{u}}_i$, is easily obtained for any control law, $u_i(t)$, and its corresponding RMS, $\bar{\bar{u}}_i$. Most of the command signal of the reference model, that is, approximately 90% of the error with respect to $u_i^r(t)$, is now expected to lie within this interval. As a matter of fact, Fig. 5.31 demonstrates that this holds for three of the four command lines for lateral repositioning manoeuvres of increasing intensity, with a strong violation for the longitudinal cyclic pitch, as expected from the analysis of the previous data, inasmuch as a smaller uncertainty window was selected. Note that model A4 performs definitely better than all the other ones, thus confirming that fuselage and inflow models play a crucial role in this manoeuvre for the correct representation of off–axis response.

It should also be noted that, when the RMS of the violation of the considered target

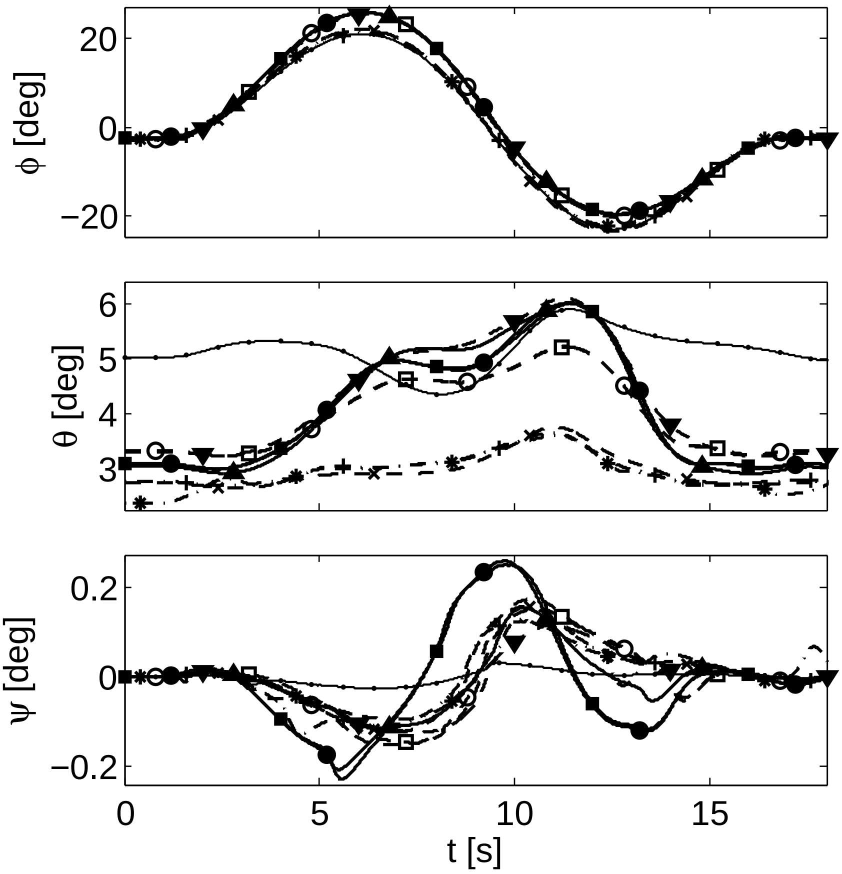

Figure 5.30. Attitude time-hystories in lateral repositioning manoeuvre.

window for the time–histories of the control variables is scaled with respect to the RMS of the command, $\bar{\bar{u}}_i$ (Fig. 5.32), relatively small figures are obtained also for model A6, with less than 10% of the reference command signal lost outside of the uncertainty window. On the converse, model C6, with the same rotor and inflow models, but simplified fuselage aerodynamics, is not correctly bracketed, that is, the uncertainty is higher than what indicated by the proposed procedure.

Good results in the definition of the uncertainty window are obtained for the hurdle–hop and the slalom manoeuvre as shown in Fig. 5.33 and 5.34, with the exceptions of the longitudinal cyclic pitch in the first case and main rotor collective in the latter one, where the choice of a single value of k results in an overoptimistic prediction of the uncertainty interval. The interpretation of the slalom results is relatively straightforward, being related to a very aggressive, lateral–directional manoeuvre, with minor displacements of the collective command, whereas the major errors in the tail rotor channel are related to the difficulties in correctly representing a very aggressive manoeuvre with lower–order

Table 5.4. Model accuracy metrics (σ_i^*) for the 9 test manoeuvres.

COLLECTIVE

	hurdle hop (HH)			**lateral repositioning (LR)**			**slalom (SL)**			
	20 m	30 m	40 m	90 m	120 m	150 m	9 m	15 m	21 m	$\hat{\sigma}_i$
A4	0.118	0.118	0.119	0.044	0.053	0.049	0.163	0.160	0.219	**0.1**
A6	0.174	0.179	0.185	0.222	0.243	0.251	0.958	0.626	0.542	**0.4**
C6	0.178	0.184	0.191	0.209	0.237	0.255	0.955	0.621	0.539	**0.4**
C8	0.122	0.125	0.125	0.110	0.121	0.137	0.918	0.614	0.559	**0.4**
C9	0.142	0.145	0.144	0.153	0.158	0.168	1.202	0.802	0.721	**0.4**

LATERAL CYCLIC

	hurdle hop (HH)			**lateral repositioning (LR)**			**slalom (SL)**			
	20 m	30 m	40 m	90 m	120 m	150 m	9 m	15 m	21 m	$\hat{\sigma}_i$
A4	0.209	0.239	0.278	0.960	0.425	0.901	0.379	0.377	0.396	**0.6**
A6	0.475	0.472	0.465	1.022	0.902	0.843	0.361	0.371	0.400	**0.7**
C6	0.493	0.468	0.449	0.636	0.593	0.569	0.362	0.373	0.400	**0.7**
C8	0.375	0.369	0.379	0.642	0.600	0.576	0.399	0.413	0.448	**0.7**
C9	1.446	1.362	1.237	1.141	1.190	1.232	0.459	0.483	0.541	**1.2**

LONGITUDINAL CYCLIC

	hurdle hop (HH)			**lateral repositioning (LR)**			**slalom (SL)**			
	20 m	30 m	40 m	90 m	120 m	150 m	9 m	15 m	21 m	$\hat{\sigma}_i$
A4	0.203	0.236	0.270	0.223	0.092	0.268	0.272	0.322	0.394	**0.3 (0.3)**
A6	0.258	0.245	0.272	0.648	0.503	0.416	0.176	0.250	0.327	**0.5 (0.5)**
C6	0.465	0.551	0.591	3.403	2.348	1.691	0.179	0.256	0.331	**1.6 (0.7)**
C8	0.458	0.526	0.558	3.554	2.473	1.804	0.245	0.323	0.405	**1.8 (0.7)**
C9	0.407	0.442	0.462	4.550	3.386	2.543	0.324	0.402	0.549	**2.2 (1.2)**

TAIL ROTOR COLLECTIVE

	hurdle hop (HH)			**lateral repositioning (LR)**			**slalom (SL)**			
	20 m	30 m	40 m	90 m	120 m	150 m	9 m	15 m	21 m	$\hat{\sigma}_i$
A4	0.141	0.149	0.119	0.412	0.252	0.258	0.326	0.426	0.755	**0.4**
A6	0.146	0.141	0.117	0.409	0.289	0.215	0.276	0.377	0.756	**0.4**
C6	0.152	0.140	0.130	0.373	0.333	0.287	0.398	0.471	0.836	**0.4**
C8	0.143	0.139	0.118	0.391	0.366	0.314	0.564	0.621	0.913	**0.5**
C9	0.296	0.238	0.230	0.360	0.336	0.294	0.543	0.656	0.914	**0.5**

simplified models.

5.2.9 Validation manoeuvres

As a further proof of the validity of the approach, two more manoeuvres were considered for testing how well the uncertainty intervals defined on the basis of the previous test cases could capture the performance of each model on different tasks. For the pop–up–pop–down manoeuvre (Fig. 5.35) the uncertainty defined on the basis of different manoeuvres correctly captures the reference model control activity on all the command channels with the exception of the longitudinal cyclic pitch. But this fact, rather than being related to the quality of the simplified models, is caused by the small value of the RMS of the command time–history during a purely vertical manoeuvre, with minor longitudinal cyclic

Table 5.5. Factors k_i for the definition of the uncertainty interval.

		hurdle hop (HH)			**lateral repositioning (LR)**			**slalom (SL)**		
		20 m	30 m	40 m	90 m	120 m	150 m	9 m	15 m	21 m
Collective	**A4**	1.484	1.538	1.531	1.658	1.704	1.652	2.623	2.636	2.531
	A6	1.447	1.664	1.653	1.763	1.843	1.931	1.834	1.930	2.240
	C6	1.565	1.603	1.592	1.750	1.688	1.666	1.863	1.963	2.308
	C8	1.529	1.622	1.603	1.883	1.994	1.913	2.050	2.295	2.736
	C9	1.775	1.873	1.860	1.682	1.905	1.979	2.064	2.279	2.636
Lateral Cyclic	**A4**	1.851	1.746	2.397	1.691	1.625	1.747	1.859	1.824	1.920
	A6	1.624	1.734	1.749	1.707	1.687	1.602	1.947	1.959	2.037
	C6	1.791	1.953	1.944	1.755	1.654	1.571	1.976	2.000	2.010
	C8	1.934	2.191	2.058	1.757	1.664	1.590	2.138	2.043	2.145
	C9	1.604	1.520	1.581	1.600	1.689	1.767	2.099	2.013	2.267
Longitudinal Cyclic	**A4**	1.736	2.149	2.016	1.473	1.432	1.598	2.045	2.222	2.299
	A6	2.617	2.721	2.937	1.650	1.842	2.181	2.110	2.280	2.378
	C6	2.389	2.610	2.550	1.540	1.534	1.664	1.611	1.980	2.381
	C8	2.016	2.341	2.250	1.524	1.558	1.724	1.996	2.165	2.513
	C9	2.857	2.271	2.081	1.245	1.258	1.290	1.792	1.914	2.219
Tail rotor Collective	**A4**	1.839	2.258	2.519	2.101	2.515	1.586	2.085	2.261	3.129
	A6	2.336	2.479	1.926	1.982	1.625	1.507	1.878	2.177	3.385
	C6	2.273	2.358	1.628	2.375	1.842	1.997	1.881	2.231	3.219
	C8	2.052	2.220	2.229	2.253	1.934	2.068	1.786	2.113	3.475
	C9	3.156	2.279	2.005	2.326	1.965	2.115	2.228	2.501	3.387

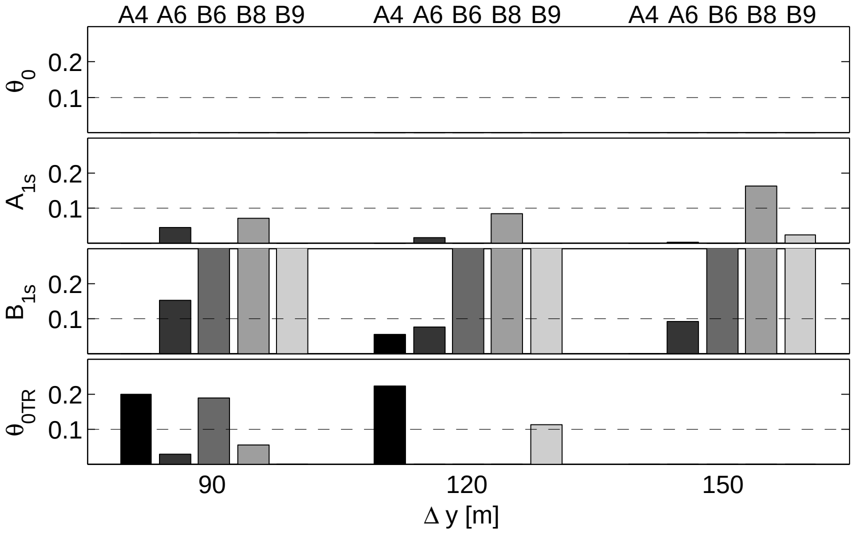

Figure 5.31. RMS of command lying outside of the target region for lateral repositioning manoeuvre: values scaled w.r.t. σ_i .

pitch displacements.

Something less trivial takes place with the fast 180 deg turn (Fig. 5.36), that provides excellent results for the collective and longitudinal cyclic pitch, not so good results for tail rotor collective and very poor ones for the most important command line, that is, lateral cyclic pitch. The analysis of the time–histories proves that this fact is related to a sort of bias on these command lines between different models during the quasi–steady portion of the turn. It is for this reason that in this case the most aggressive manoeuvre provides better results, because of its more dynamic nature.

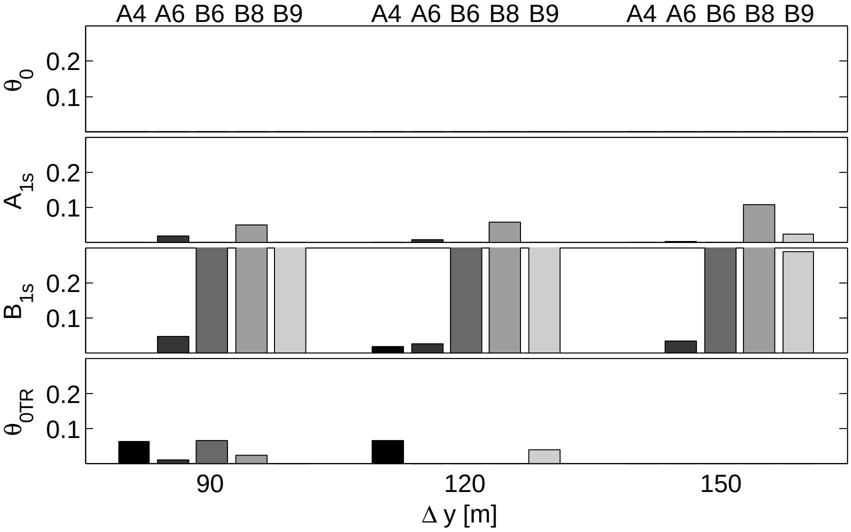

Figure 5.32. RMS of command lying outside of the target region for lateral repositioning manoeuvre: values scaled w.r.t. $\bar{\bar{u}}_i^r$.

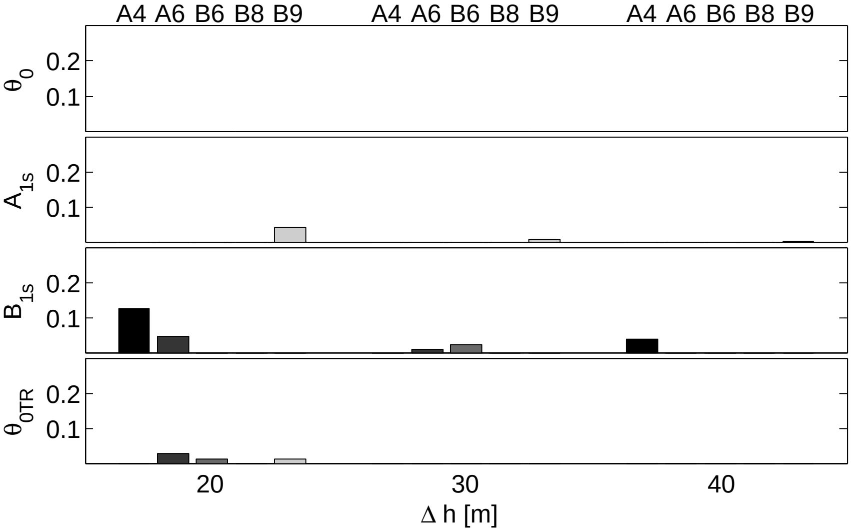

Figure 5.33. RMS of command lying outside of the target region scaled w.r.t. $\bar{\bar{u}}_i^r$ for a hurdle–hop manoeuvres.

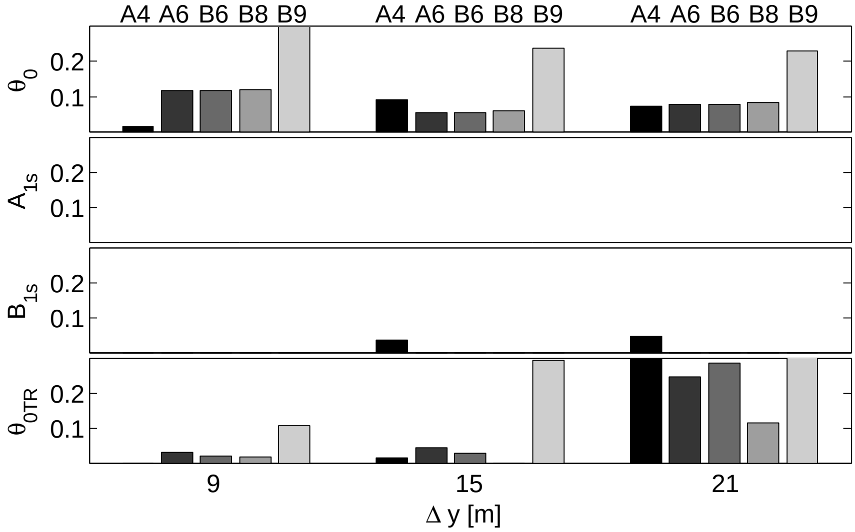

Figure 5.34. RMS of command lying outside of the target region scaled w.r.t. $\bar{\bar{u}}_i^r$ for a slalom manoeuvres.

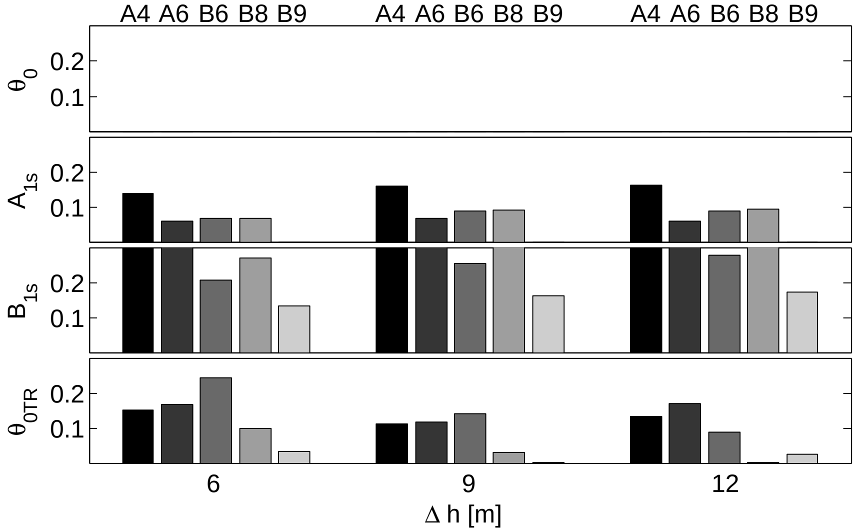

Figure 5.35. RMS of command lying outside of the target region scaled w.r.t. $\bar{\bar{u}}_i^r$ for for pop–up–pop–down manoeuvre.

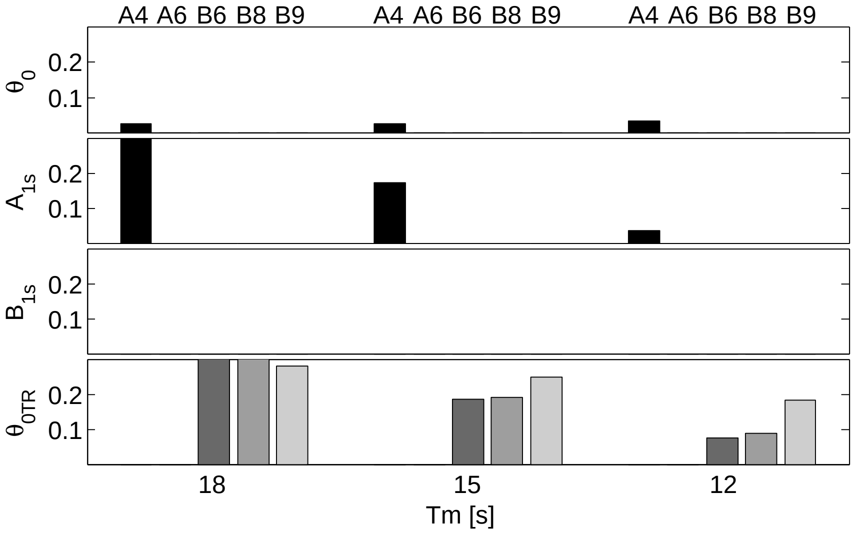

Figure 5.36. RMS of command lying outside of the target region scaled w.r.t. $\bar{\bar{u}}_i^r$ for for 180 deg fast turn.

5.3 MPC algorithm

The integration algorithm presented in the previous section is able to solve the inverse problem even with individual blade models. Nevertheless the iterative solution for the inverse simulation step based on an individual blade model has a high computational cost, leading to a slow solution to the problem. A new algorithm based on a Model Predictive Control (MPC) scheme for the solution of the inverse simulation problem for rotorcraft dynamics is proposed. The complex model which needs to be analysed is substituted in the inverse simulation scheme by a lower–order model that requires a significantly shorter CPU time to solve the inverse problem. The control action evaluated for the low–order model is then propagated forward in time on the most complex, high–order one.

The present section aims at demonstrating that Model Predictive Control (MPC) can also reduce the computational burden and alleviate the numerical issues that affect the inverse solution of high–order, individual blade helicopter models. The combined use of a high–order accurate model for forward simulation with a low–order one for the determination of the control action by means of the solution of an IS problem reduces the computational cost significantly.

In Model Predictive Control [101] the evaluation of the control law usually results from the solution of a finite horizon open-loop optimal control problem, using the current state of the plant as the initial state. The optimization yields an optimal control sequence and the first control in this sequence is applied to the plant which is then integrated until the next control step, when the same procedure is repeated. Usually, the control objective requires to follow a user defined trajectory $\boldsymbol{y}(t) = \boldsymbol{y}_{des}(t)$, where $\boldsymbol{y}_{des}(t)$ is the desired evolution for the components of the vector of tracked outputs. The optimization problem is aimed at minimizing a stage cost based on the difference between real and desired output variables as well as on control activity during each time step plus a terminal cost evaluated at the end of the integration, that is, at time $t_F = t_k + T$ (where T is the length of the receding horizon).

The reference model used for the analysis is Model A1 described in section 4.1.1. In the present analysis two lower–order models are used to test the technique, Models A4 and B8. Model A4 is described by a 19 elements state vector $\tilde{\boldsymbol{x}}$ which can be partitioned in the form $\tilde{\boldsymbol{x}} = (\tilde{\boldsymbol{x}}_f,\ \tilde{\boldsymbol{x}}_r,\ \tilde{\boldsymbol{x}}_\lambda)^T$, with the same fuselage rigid body and inflow states, $\tilde{\boldsymbol{x}}_f$ and $\tilde{\boldsymbol{x}}_\lambda$ as model A1 (see section 4.1.1), respectively. Rotor states represent first order flap harmonic coefficients and their derivatives, that is $\tilde{\boldsymbol{x}}_r = \left(\tilde{a}_0, \dot{\tilde{a}}_0, \tilde{a}_1, \dot{\tilde{a}}_1, \tilde{b}_1, \dot{\tilde{b}}_1\right)^T$, where $\tilde{a}_0$, $\tilde{a}_1$, and $\tilde{b}_1$ are coning, longitudinal and lateral flapping coefficients, respectively.

The dynamics of the simplified model is thus defined by means of a set of 19 nonlinear time–invariant ordinary differential equations, in the form

$$\begin{aligned} \dot{\tilde{\boldsymbol{x}}} &= \tilde{\boldsymbol{f}}\left(\tilde{\boldsymbol{x}}, \tilde{\boldsymbol{u}}\right) \\ \tilde{\boldsymbol{y}} &= \tilde{\boldsymbol{g}}\left(\tilde{\boldsymbol{x}}\right) \end{aligned} \tag{5.15}$$

where $\tilde{\boldsymbol{u}} = \left(\tilde{\theta}_0, \tilde{A}_{1_S}, \tilde{B}_{1_S}, \tilde{\theta}_{0_{tr}}\right)^T$ is the command vector and $\tilde{\boldsymbol{y}}$ is the output vector. Note that the states, commands and outputs of the model used for the inverse simulation step are defined by symbols with a ˜ in order to underline the fact that, in general, they may assume different values with respect to their counterparts in the reference models due to the difference in modelling level and tracking error of the output variables during the procedure.

The MPC–IS scheme is also tested by solving the IS step for a minimum–complexity model (Model B8), where further simplifying assumptions are used in order to drop inflow states and some rotor variables [11]. In particular, main and tail rotor inflow is assumed uniform and quasi–steady. The values for the inflow non–dimensional velocity parameters, ν_0 and $\nu_{0_{tr}}$, are determined at each time step by means of a simple iterative procedure based on momentum theory. Fuselage aerodynamic description is based on parasite drag area, thus dropping the aerodynamic database used for Models A1 and A4. Finally, a first–order dynamics is assumed for rotor states, namely coning, longitudinal and lateral flap coefficients.

The dynamics of this lowest–order model is thus described in terms of just 12 state variables. The state vector is partitioned in this case as $\hat{\boldsymbol{x}} = (\hat{\boldsymbol{x}}_f,\ \hat{\boldsymbol{x}}_r\ )^T$, where $\hat{\boldsymbol{x}}_f = \left(\hat{u}, \hat{v}, \hat{w}, \hat{p}, \hat{q}, \hat{r}, \hat{\phi}, \hat{\theta}, \hat{\psi}\right)^T$ represents as usual fuselage states and $\hat{\boldsymbol{x}}_r = \left(\hat{a}_0, \hat{a}_1, \hat{b}_1\right)^T$ represents rotor states. Note that a "hat" symbol is used for indicating Model B8 state and control variables, in order to mark the difference with respect to the corresponding ones for Models A1 and A4.

As anticipated above, the proposed model predictive control scheme allows for the evaluation of the solution of an inverse simulation problem for a complex rotorcraft model, starting from the solution of the inverse simulation step obtained for a lower–order, simplified model of the same vehicle. In this numerical scheme, indicated as MPC-IS in what follows, the complex model is used only in the forward simulation step, which is by far the computationally least demanding. A great amount of time and computational burden can be saved if a lower–order model is used in the inverse simulation step, which requires the numerical solution of a set of non–linear conditions on rotorcraft output at the final time of the discretization interval by means of an iterative procedure [46, 53]. A simple guidance scheme is sufficient for avoiding that the models drift away from the prescribed flight path. All the elements (helicopter models, IS algorithm and guidance scheme) will be presented in this Section together with the overall architecture of the MPC-IS scheme.

The approach for the solution of the inverse problem is described in Fig. 5.37. Three major blocks are at the basis of the architecture of the algorithm. The forward simulation block performs the forward simulation of the reference Model A1. The inverse simulation block evaluates the command increment $\Delta\boldsymbol{u}$ that achieves the desired increment $\Delta\boldsymbol{y}^\star$ for the tracked output variables on the basis of either Model A4 or B8. Finally, the guidance block generates the desired output increment $\Delta\boldsymbol{y}^\star$ for the inverse simulation block, based on the desired trajectory $\boldsymbol{y}_{des}(t)$ plus a correction $\Delta\boldsymbol{y}_{guid}$ that takes into account differences between the actual output function $\boldsymbol{y}$ of the reference Model A1 and $\boldsymbol{y}_{des}(t)$ at the beginning of the time step t_k.

The IS problem is solved by means of an integration algorithm. In a standard inverse simulation approach [97], once a desired variation with time $\boldsymbol{y}_{des}(t)$ of the output is prescribed (*i.e.* a manoeuvre profile like those required by ADS–33 specifications [62]), helicopter equations of motion are integrated from an initial condition $\boldsymbol{x}_I = \boldsymbol{x}_k$ at time

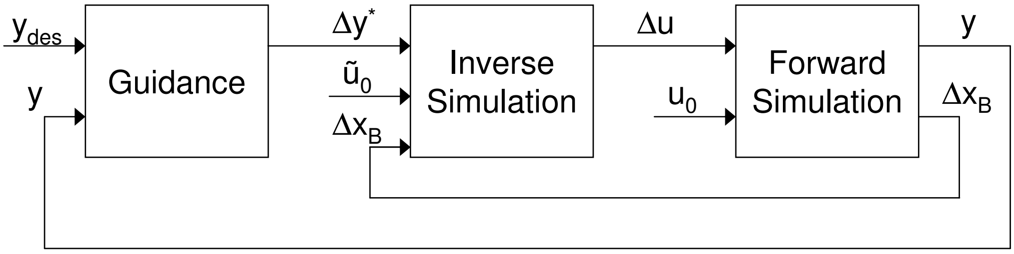

Figure 5.37. Architecture of the MPC–IS scheme.

t_k over a time interval T for a piece–wise constant value $\boldsymbol{u}_k^\star$ of the control variables. The resulting value $\boldsymbol{y}_F = \boldsymbol{g}(\boldsymbol{x}_F)$ of the output variables at time $t_F = t_k + T$ can thus be represented in terms of a function $\boldsymbol{y}_F = \boldsymbol{F}(\boldsymbol{x}_F, \boldsymbol{u}_k^\star)$ of the (given) initial state $\boldsymbol{x}_k$ and of the (unknown) constant control action, $\boldsymbol{u}_k^\star$. The unknown control vector, $\boldsymbol{u}_k^\star$, is evaluated iteratively by means of some suitable numerical approach (Newton–Raphson [97], local optimization [54], etc), until $\boldsymbol{y}_F$ matches the desired output at the final time, $\boldsymbol{y}_{des}(t_F)$. The control action is then propagated forward in time for only a fraction $\Delta t = T/N$ of the inverse simulation time interval [97].

In this latter respect, a proper choice of the receding horizon T and time–step Δt is crucial, in order to obtain adequate numerical performance and, at the same time, a feasible and reasonable inverse solution. The selection of T and N results from a trade-off between computational time and stability of the method. A short integration time may excite uncontrolled dynamics and lead to an unstable or highly oscillatory response of the system, both of which should be discarded as poor and/or impractical solutions of the inverse problem. The value of T must thus be sufficiently large, in order to allow non–minimum–phase response to settle down, but if N is large, large fractions of the time–history from the IS solution are dropped in the forward simulation step, and the computation time becomes obviously longer.

Note that this approach is common practice in Model Predictive Control, where the receding horizon used for the forward prediction of system behaviour and evaluation of control activity is usually 3 to 10 times the controller time step [101]. In the routine developed for the present work the integration time T is selected so that $T = N\Delta t$, with $N = 3$ and $\Delta t = 0.2$ s for all the results proposed in the next Section. Similar results are obtained with $N = 5$, with a corresponding increment of approximately 66% in terms of CPU time, whereas $N = 2$ results into an unacceptable solution for the inverse problem, during critical phases of the most aggressive manoeuvres.

The approach described above becomes even more demanding from the computational point of view for individual blade models featuring as many as 37 states, such as Model A1 for the present analysis. The resulting computational time becomes considerably high, also on modern CPUs, and a problem of uncontrolled states and non–minimum phase response can harm the convergence of the scheme and/or the practical feasibility of the command law, in the presence of large amplitude oscillations. In order to reduce the computational burden, the inverse problem is here solved on the basis of a lower–order, simplified helicopter model. Some changes to the inverse simulation integration method are required in order to achieve robustness and, more in general, better performance.

Assuming that Model A4 is used for the inverse solution of vehicle motion, at every time step t_k the inverse simulation block evaluates the control action $\tilde{\boldsymbol{u}}_k^\star$, that achieves the desired variation $\Delta\boldsymbol{y}^\star = \Delta\boldsymbol{y}_{des} + \Delta\boldsymbol{y}_{guid}$ at the end of the IS step, that is, for $t_F = t_k + T$, where $\Delta\boldsymbol{y}_{des} = \boldsymbol{y}_{des}(t_k + T) - \boldsymbol{y}_{des}(t_k)$ and $\Delta\boldsymbol{y}_{guid}$ is determined by the guidance block, on the basis of the difference between the output of Models A1 and the desired one at time t_k.

As in any other IS algorithm, the value $\tilde{\boldsymbol{y}}_F = \tilde{\boldsymbol{g}}(\tilde{\boldsymbol{x}}_F)$ of the output variables for the simplified model at time $t_F = t_k + T$ depends on a known initial state $\tilde{\boldsymbol{x}}_k$ at time t_k and on the unknown control action, $\tilde{\boldsymbol{u}}_k^\star$, assumed piece–wise constant. As usual, control variables are determined in such a way that the increment of the output variables obtained at the end of the IS step matches a given desired value, $\Delta\boldsymbol{y}^\star$. The value of the control increment $\Delta\tilde{\boldsymbol{u}}$ is then passed to the forward simulation as command displacement from trim condition, assuming $\Delta\boldsymbol{u} = \Delta\tilde{\boldsymbol{u}}$. From the knowledge of the initial condition for state variables at time t_k and controls at trim, $\boldsymbol{u}_0$, the forward simulator integrates the equations of motion for Model A1, assuming a constant value of the control variables, $\boldsymbol{u} = \boldsymbol{u}_0 + \Delta\boldsymbol{u}$, over a time step equal to the simulation step $\Delta t = T/N$.

A perfectly analogous scheme is easily implemented if Model B8 is used instead of Model A4 in the IS algorithm. But prior to implement this IS scheme, a few issues need to be properly taken into account: (i) the choice of constrained output variables, (ii) initialization of the IS step, and (iii) definition of a guidance logic. The first issue is typical of all aeronautical applications of IS schemes, whereas the remaining two characterize the development of the MPC–based IS scheme.

5.3.1 IS problem constraints

When the number of control variables, m, is equal to the number of the constrained output variables, p, the problem is nominal and, if well posed, it can be solved by means of standard numerical techniques, such as Newton–Raphson (NR) method. If $m > p$ the problem is redundant, as in many aeronautical applications for fixed and rotary–wing aircraft, when 4 controls are available for tracking 3 trajectory variables. The redundancy can be either exploited in order to minimize at every time–step a desired objective function [54] or, as an alternative, a further constraint can be added to make the problem nominal [97]. The additional constraint provides the manoeuvre with desired characteristics, such as nose pointing (when a value to either the yaw or the sideslip angle is assigned) or zero lateral acceleration, that results into the execution of coordinated turns only. In the next Section, additional constraints, that depend on the type of manoeuvre considered, are added to the basic velocity tracking task.

As a further issue, if the helicopter must follow a prescribed trajectory, the flight task element can be enforced by setting as constraints at every time step either the inertial position, or the inertial velocity components or the inertial acceleration, as discussed in Ref. [45]. Choosing the acceleration components as constraints makes the problem numerically more stable, but at the same time it may lead to large drift from the desired trajectory, as the system integrates twice the error on the considered constraints, whereas setting the position as desired variables may lead to instability in the algorithm. Inertial velocity components were thus chosen as the baseline desired output to be tracked by means of the inverse simulation technique.

5.3.2 Initial conditions and MPC–IS scheme initialization

All the manoeuvres dealt with in the next Section start from a given flight condition in forward flight. In order to start the MPC–IS algorithm it is thus necessary to provide both models with the correct initial trim condition. Model A1, based on an individual blade approach, is inherently time variant and oscillations in every state variable are expected at a frequency equal to (or multiple of) blade rotational speed, Ω, assumed constant in the sequel. As a consequence trim conditions cannot be enforced in an algebraic way by simply setting to zero all states derivatives as with fixed wing aircrafts. A periodic trim needs to be found by enforcing a periodicity condition on all the states in the form

$$\boldsymbol{x}\left(t\right) = \boldsymbol{x}\left(t + 2\pi/\Omega\right)$$

for a constant value of the controls, $\boldsymbol{u}_0$. The values of control variables are chosen so as to determine (on average) a desired flight condition, defined in terms of airspeed, V, climb rate, $\dot{h}$, and heading angle, χ (or turn rate, $\dot{\psi}$). The mean value of states over one rotor revolution

$$x_{i_0} = \frac{\Omega}{2\pi}\int_t^{t+2\pi/\Omega} x_i dt \tag{5.16}$$

is used for defining the state variables at trim. Several techniques can be found in the literature for solving the problem of helicopter periodic trim. In particular harmonic balance, periodic shooting, autopilot techniques have been proposed over the years and compared in Ref. [28]. In the present work, a periodic shooting approach derived from the work by McVicar and Bradley [26] is used for trimming Model A1.

Models A4 (or B8) is trimmed in the same flight condition. In this second case a set of nonlinear time–invariant ordinary differential equations, Eq. (5.15), describes vehicle's dynamics, so that the helicopter model can be trimmed by means of algebraic tools, simply enforcing the condition

$$\tilde{\boldsymbol{f}}\left(\tilde{\boldsymbol{x}}_0, \tilde{\boldsymbol{u}}_0\right) = 0$$

where $\tilde{\boldsymbol{x}}_0$ and $\tilde{\boldsymbol{u}}_0$ are the state and control variables at trim.

Since each model generates in general slightly different values for state and control variables at trim for the same flight condition, the variations of states and controls from their trim values is used during the simulation, rather than their absolute values, as far as the latter are biased by this slight initial difference. This difference, integrated over time, would result in a significant drift between the models used in the MPC-IS scheme. By means of this elementary procedure, the initial difference between equilibrium states for the two models has no impact on the evaluation of the dynamic behaviour of the vehicle.

In what follows, the symbols $\Delta\boldsymbol{u} = \boldsymbol{u} - \boldsymbol{u}_0$ will indicate control variable increments with respect to the considered reference trim condition for Model A1. Similarly, state vector increments for Model A1 are defined as $\Delta \boldsymbol{x}_r = \boldsymbol{x}_r - \boldsymbol{x}_{r_0}$, $\Delta \boldsymbol{x}_f = \boldsymbol{x}_f - \boldsymbol{x}_{f_0}$, $\Delta \boldsymbol{x}_\lambda = \boldsymbol{x}_\lambda - \boldsymbol{x}_{\lambda_0}$ for rotor, fuselage and inflow states, respectively. Similar definitions hold for Models A4 (*e.g.* $\Delta \tilde{\boldsymbol{u}} = \tilde{\boldsymbol{u}} - \tilde{\boldsymbol{u}}_0$) and B8 (*e.g.* $\Delta \hat{\boldsymbol{x}} = \hat{\boldsymbol{x}} - \hat{\boldsymbol{x}}_0$) as well. Note that each model has a different vector of rotor states. This characteristic affects the IS scheme, and it will be discussed in detail in the following subsection.

Since a reduced order model (either A4 or B8) is adopted for the IS step, both states $\Delta \boldsymbol{x}\left(t_k + \Delta t\right)$ and output variables $\boldsymbol{y}\left(t_k + \Delta t\right)$ achieved at the end of the simulation step for Model A1 are (hopefully only slightly) different from their counterparts for the IS step, $\Delta \tilde{\boldsymbol{x}}\left(t_k + \Delta t\right)$ and $\tilde{\boldsymbol{y}}\left(t_k + \Delta t\right)$, determined on the basis of a simplified model. These discrepancies need to be taken into account when the initial conditions for the simplified model at each initial time t_k are defined and the control objectives for the IS step prescribed. The second issue will be dealt with in the next subsection.

As for the initial conditions, the ideal choice of setting $\tilde{\boldsymbol{x}}_I = \boldsymbol{x}_k$ for Model A4 (or $\hat{\boldsymbol{x}}_I = \boldsymbol{x}_k$, when Model B8 is adopted in the IS scheme) is ruled out by the fact that the two state vectors contain different sets of variables. Moreover, some of the states would not be accessible to direct measurements, if the algorithm is implemented as an MPC controller for an actual vehicle, rather than an off–line inverse simulation method for a complex helicopter model. For this reason, the issue of state initialization for Models A4 (or B8) at the beginning of every IS time step t_k needs to be properly addressed. Note that for the forward simulation, the states at the beginning of the k–th step are obviously given simply by the values assumed at the end of the previous one, $\boldsymbol{x}_{I_k} = \boldsymbol{x}(t_k) = \boldsymbol{x}(t_{k-1} + \Delta t)$.

For the inverse simulation step, on the converse, the initialization of states must rely (at least partially) on the knowledge of the states of the reference model which is integrated forward in time, in order to prevent a drift between the two models and consequent loss of control when implementing the control action derived from the simplified model on the full–order one, which is flying a different condition. Two options are here considered. In the first case as much information as possible is passed from the complete model to the reduced order one. In what follows, this technique will be referred to as full state initialization, inasmuch as initial conditions for all the simplified model state variables are derived from the knowledge of the state for Model A1 at the end of the previous time–step Δt. In particular, increments for fuselage and inflow variables are evaluated and the initial states for the inverse simulation step are given by

$$\tilde{\boldsymbol{x}}_f\left(t_k\right) = \tilde{\boldsymbol{x}}_{f_0} + \left[\boldsymbol{x}_f\left(t_k\right) - \boldsymbol{x}_{f_0}\right] \tag{5.17}$$

$$\tilde{\boldsymbol{x}}_\lambda\left(t_k\right) = \tilde{\boldsymbol{x}}_{\lambda_0} + \left[\boldsymbol{x}_\lambda\left(t_k\right) - \boldsymbol{x}_{\lambda_0}\right] \tag{5.18}$$

where $\boldsymbol{x}_{f_0}$ and $\tilde{\boldsymbol{x}}_{f_0}$ are the values at trim of rigid body states for reference and inverse models, respectively, and $\boldsymbol{x}_f\left(t_k\right)$ is the vector of rigid body states at the end of the previous forward integration step. Similarly $\boldsymbol{x}_{\lambda_0}$ and $\tilde{\boldsymbol{x}}_{\lambda_0}$ represent inflow states for the reference and inverse models, and $\boldsymbol{x}_\lambda\left(t_k\right)$ is the reference model inflow state at the end of the previous forward integration step.

As for rotor states, coning, longitudinal and lateral flapping coefficients at time t_k are evaluated by means of multiblade coefficients:

$$\begin{aligned}\beta_c\left(t_k\right) &= \frac{1}{N_b}\sum_{j=1}^{N_b}\beta_j\left(t_k\right)\\ \beta_{lng}\left(t_k\right) &= -\frac{2}{N_b}\sum_{j=1}^{N_b}\beta_j\left(t_k\right)\sin\psi_j\\ \beta_{lat}\left(t_k\right) &= -\frac{2}{N_b}\sum_{j=1}^{N_b}\beta_j\left(t_k\right)\cos\psi_j\end{aligned} \tag{5.19}$$

where N_b is the number of blades. Provided that the time derivatives of multiblade coefficients can be analytically derived from Eq. (5.19), and letting $\boldsymbol{\beta} = \left(\beta_c, \dot{\beta}_c, \beta_{lng}, \dot{\beta}_{lng}, \beta_{lat}, \dot{\beta}_{lat}\right)^T$, the initial condition for rotor states is defined as

$$\tilde{\boldsymbol{x}}_r\left(t_k\right) = \tilde{\boldsymbol{x}}_{r_0} + \left[\boldsymbol{\beta}\left(t_k\right) - \boldsymbol{\beta}_0\right] \tag{5.20}$$

A second technique is also analysed, based on the hypothesis that only rigid body states $\boldsymbol{x}_B$ of the reference model are truly observable, as it would happen in a real-time application of the algorithm in the form of an actual MPC scheme. This technique will be referred to as partial state initialization in the sequel. In this case the same displacement of fuselage states from their values at trim is assumed for the initial condition at time t_k of the simplified model, as prescribed by Eq. (5.17), whereas inflow and rotor states are not updated from the corresponding values obtained for Model A1 at the end of the previous forward integration interval. In this respect, inflow and rotor states are assumed as not observable and therefore they are initialized with the value achieved at the end of the last inverse simulation run $\tilde{\boldsymbol{x}}_{r/\lambda}(t_k) = \tilde{\boldsymbol{x}}_{r/\lambda}(t_{k-1} + \Delta t)$ for the simplified Model A4.

Note that, when Model B8 is adopted in the IS block, an equivalent definition for its initial conditions at each time t_k is easily derived by dropping inflow states and substituting the ˜ with a ˆ. Also remember that, in this second case, a first–order dynamics is assumed for flapping coefficient, so that, from the definition of $\hat{\boldsymbol{x}}_r = (\hat{a}_0, \hat{a}_1, \hat{b}_1)^T$, only the current values of multiblade coordinates derived from Eqs. (5.19) are necessary, whereas their derivatives are not necessary.

On one side, the choice of selecting rigid body states only as observable states maintains a link to Model Predictive Control procedures. In fact, if a real system replaces the forward simulation model, only some states would be observable. In particular linear and angular velocities as well as attitude variables are usually available from GNC sensors and as a consequence they can be fed to the inverse model in the above mentioned routine, that acts like a controller for the plant. Rotor and inflow states are in general not subject to direct measurement, and therefore no feedback of their actual value from the controlled plant can be provided to the inverse simulation model in a realistic scenario. At the same time, and more importantly in the present off–line inverse simulation framework, partial state initialization seriously challenges the robustness of the MPC-IS algorithm, so it allows one to fully assess the capabilities of the method.

5.3.3 Desired output

When a standard IS scheme is adopted, where the same vehicle model is used for the solution of the inverse problem and for forward propagation of the control action, the fact that the inverse model follows the desired variation of the outputs, $\boldsymbol{y}_{des}(t)$, is sufficient for obtaining a successful inverse solution. This is no longer true for the MPC-IS scheme, where the output variables $\boldsymbol{y}\left(t_k+\Delta t\right)$ for Model A1 achieve different values with respect to those obtained at the same time instant for the simplified model (either A4 or B8) during the solution of the IS step and, as a consequence, they are different from the desired output $\boldsymbol{y}_{des}\left(t_k+\Delta t\right)$.

Several reasons contribute to this difference, as (i) the constraint on the output is exactly enforced during the IS step for the simpler model only, (ii) the control action is propagated for just a fraction of the receding horizon T, so that the actual output is evaluated at a time $t_{k+1} \neq t_k+T$ and, finally, (iii) the output variable increment required over the IS step for the simplified model, $\Delta \boldsymbol{y}^{\star}=\Delta \boldsymbol{y}_{des}+\Delta \boldsymbol{y}_{guid}$, includes the contribution $\Delta \boldsymbol{y}_{guid}$ generated by the guidance term required for limiting the drift between the two models, so that $\Delta \boldsymbol{y}_{des}=\boldsymbol{y}_{des}(t_k+T)-\boldsymbol{y}_{des}(t_k) \neq \Delta \boldsymbol{y}^{\star}$.

Letting the actual increment achieved by Model A4 at time t_F be defined as $\Delta \tilde{\boldsymbol{y}}=\tilde{\boldsymbol{y}}_F-\tilde{\boldsymbol{y}}_I=\tilde{\boldsymbol{g}}(\tilde{\boldsymbol{x}}_F)-\tilde{\boldsymbol{g}}(\tilde{\boldsymbol{x}}_k)=\tilde{\boldsymbol{F}}(\tilde{\boldsymbol{x}}_k,\tilde{\boldsymbol{u}}_k^{\star})-\tilde{\boldsymbol{g}}(\tilde{\boldsymbol{x}}_k)$, the inverse problem can again be stated in terms of a set of algebraic equations in the form

$$\tilde{\boldsymbol{F}}(\tilde{\boldsymbol{x}}_k,\tilde{\boldsymbol{u}}_k^{\star})-\tilde{\boldsymbol{g}}(\tilde{\boldsymbol{x}}_k)=\Delta \boldsymbol{y}^{\star}. \tag{5.21}$$

Note that, as a further variation with respect to a standard IS method, a different definition of the algebraic system is adopted in this work, where, rather than directly enforcing the constraints in terms of actual desired values for the tracked variables at time t_F, their increments over the time interval T between t_I and t_F are required to be equal. The guidance term included in the definition $\Delta \boldsymbol{y}^{\star}$ updates the desired output variables increment by means of a function of the error exhibited by the reference model at the end of the previous forward simulation step, that is, the desired output $\boldsymbol{y}_{des}$ for the following step $t_{k+1}=t_k+\Delta t$ is corrected as a function of the forward simulation output $\boldsymbol{y}\left(t_k+\Delta t\right)$ at the end of the k–th step.

A simple proportional guidance scheme is adopted, where

$$\Delta \boldsymbol{y}_{guid}=K\left[\boldsymbol{y}_{des}(t_I)-\boldsymbol{g}(\boldsymbol{x}_k)\right]$$

such that

$$\Delta \boldsymbol{y}^{\star}=\Delta \boldsymbol{y}_{des}+\Delta \boldsymbol{y}_{guid}=\left[\boldsymbol{y}_{des}(t_F)-\boldsymbol{y}_{des}(t_I)\right]+K\left[\boldsymbol{y}_{des}(t_I)-\boldsymbol{g}(\boldsymbol{x}_k)\right] \tag{5.22}$$

The additional guidance term avoids that the actual solution “drifts away” from the desired path, but it also enforces asymptotic convergence on the tracked variables when they achieve a constant value, during steady–state flight segments (*e.g.* at the end of a manoeuvre).

For both partial and full state initialization techniques, fuselage states for the simplified model are always updated to their actual values achieved by Model A1 at the end of the forward simulation step, Δt. Thus, it is $\tilde{\boldsymbol{g}}(\tilde{\boldsymbol{x}}_k) = \boldsymbol{g}(\boldsymbol{x}_k)$, and it is possible to rearrange Eqs. (5.21) and (5.22) in the form

$$\tilde{\boldsymbol{F}}(\tilde{\boldsymbol{x}}_k, \tilde{\boldsymbol{u}}_k^\star) = \boldsymbol{y}_{des}(t_F) + (K-1)\left[\boldsymbol{y}_{des}(t_I) - \boldsymbol{g}(\boldsymbol{x}_k)\right]$$

This formulation for the IS problem constraints allows one to highlight the following facts. For $K = 0$ the guidance term disappears and one simply requires that the increment of the actual output variables at the end of the whole inverse simulation step $T = t_F - t_I$ equals the increment for the desired variation of $\boldsymbol{y}_{des}$ over the same interval, without taking into account the initial error. In this case the error on the output slowly grows during the manoeuvre. If a value $K = 1$ is used, the second term between square brackets, multiplied by $K-1$, disappears. The lower order model is thus required to exactly follow the desired variation with time of the output, that is, the IS scheme no longer works on the desired output increment. At the same time no information on the error on the tracked variables for the more complex model is available at the beginning of the IS step. This causes the inverse solution to rapidly diverge. An intermediate value between 0 and 1 need to be found which is optimal for the considered application. In the test cases reported in the next Section a value of $K = 0.3$ was adopted throughout.

5.3.4 Test cases

The approach described in the previous Section is demonstrated in this paragraph for a hurdle–hop and a slalom manoeuvres, described in greater details in section 5.2.3. Both manoeuvres, performed at constant speed, show the effectiveness of the MPC–IS approach on aggressive maneuvering tasks.

Trim conditions for Models A1 and A4 (or A1 and B8) are evaluated for initializing the procedure. Then, following the approach described in the previous Section, the inverse solutions based on the simplified models (either A4 or B8) are calculated for the two manoeuvres using inertial velocities as desired output variables, plus an additional constraint introduced to make the IS problem nominal. The condition $\psi = 0$ is enforced for the longitudinal hurdle–hop, that results in a constant nose–pointing during the manoeuvre. A1 constraint on zero lateral acceleration, $a_y = 0$, is introduced for the execution of the slalom manoeuvre by means of coordinated turns.

For each manoeuvre, three solutions are compared. The reference one, based on a standard integration method for the individual blade model (IS Model A1), is represented in the figures by the dashed line. A second solution, represented by means of dotted lines, is obtained for the same problems by inverse simulation of the simplified model (IS Model A4 or B8); finally, a continuous line is used to represent state and control variables obtained from the solution of the same inverse problems by means of the novel MPC–IS approach. In all the figures, commands are scaled with respect to their maximum travel. In particular main rotor collective θ_0 varies between 0 and 1, whereas longitudinal and lateral cyclic pitch and tail rotor collective are scaled between -1 and $+1$.

5.3.5 MPC–IS with IS step based on Model A4

In the first set of solutions discussed, Model A4 is used as the simplified, low order model for the inverse simulation step for the MPC-IS technique. When full state initialization of the inverse problem is adopted, as much information as possible from the complete model is provided to the simplified one at the end of each simulation step, and the results of the MPC–IS scheme perfectly match the inverse solution obtained with an integration method based on Model A1 alone. Only results produced by means of partial state initialization, with update limited to fuselage rigid body states, are presented in the sequel, as this technique challenges the robustness of the new IS scheme.

Figure 5.38 represents the projection on the X–Z inertial plane for the trajectory during a hurdle–hop (lateral displacements in the Y direction are negligible). All the three techniques evaluate a feasible solution that tracks the desired trajectory with great precision for this aggressive manoeuvre. A small delay is barely visible, especially in the final part of the manoeuvre, for the MPC-IS solution. In this case, during the fast descent phase, differences between the Models A1 and A4 used for forward and inverse simulation, respectively, become more significant and the guidance term modifies the desired output of the IS problem for keeping the helicopter on the desired path. This introduces a minor delay in the tracking of the trajectory variables, which, nonetheless, remains satisfactory.

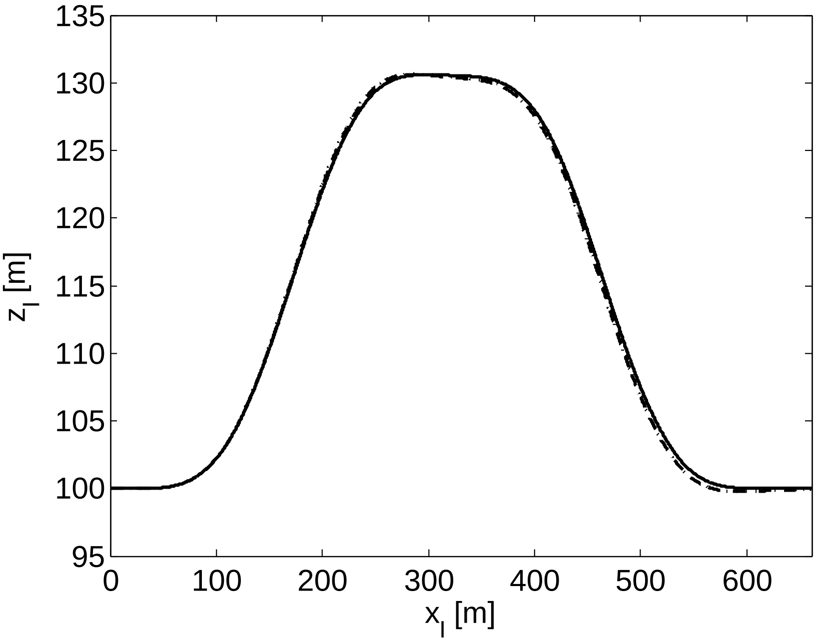

Figure 5.38. Hurdle–hop trajectory (—: MPC-IS; - - - IS for Model A1; ··· IS for Model A4).

In spite of the trajectories being almost identical in the three cases, more significant discrepancies between the solutions are apparent in the time–histories of the control action and the corresponding state variables. These differences are related to both the numerical technique and the effects of the simplifying assumptions at the basis of the simplified model. Figures 5.39 and 5.40 compare the time histories for the controls in terms of absolute position and displacement from trim, respectively. Initial and final differences at trim between the IS for Model A1 and the MPC-IS on one side, and the IS for Model A4 on the other one, are clearly visible in Fig. 5.39. The difference on main rotor collective is related to the fact that Model A4 neglects rotor blade dynamic twist, and a bias in θ_0 is present. Other effects are analysed in more detail in Ref. [97], focused on the effects of helicopter modelling technique on the results obtained from inverse simulation.

This initial bias is removed, when command displacements from trim is considered (Fig. 5.40). In this case the variation of collective pitch is identical in the three cases. The inverse solution of Mod. A4 shows more significant differences on the other command channels, namely A_{1_S}, B_{1_S}, and $\theta_{0_{tr}}$. These differences are again related to the different rotor model employed, especially during the initial and final transient phases, when linear aerodynamics for rotor blades provides a worst approximation for the forces developed by the rotor in ascending and descending flight.

Like command travel, all state variables and required power (not reported in the figures) evaluated by means of the MPC-IS technique remain very close to those obtained from the computationally more demanding solution of the inverse problem by means of the integration method applied to Model A1. Command time histories match almost perfectly those obtained for the IS of Model A1. Minor differences are present only for a short interval at the beginning of the descent phase, when some higher frequency oscillations in longitudinal pitch angle and angular velocity in the IS results for Model A1 are smoothed by the MPC–IS technique. In the latter solution the transition to horizontal flight is slightly more gradual, thanks to the effects of the guidance term generated for tracking the velocity variables in the presence of errors introduced by the use of different models in the forward and inverse simulation steps. A marginally less accurate tracking of the velocity variables thus results into an overall more regular control action.

Figures 5.41 to 5.44 represent the results obtained for the slalom manoeuvre described at the beginning of the Section. Again, as clearly shown in Fig. 5.41, where the projection of the trajectory in the X–Y plane is reported, the solution evaluated by means of the MPC–IS approach provides an inverse solution that correctly tracks the prescribed manoeuvre. Variation of altitude during the manoeuvre is negligible. Also in this second test–case, the conventional integration method provides a feasible solution to the inverse problem that follows the desired trajectory, when applied to both Models A1 and A4, but this time differences in the corresponding command time histories and resulting state variables are more significant.

Differences between controls obtained from the inverse solution of Models A1 and A4, clearly apparent in Fig. 5.42, are related to the type of rotor model implemented in the two cases. As a consequence, the complex coupling of longitudinal and lateral dynamics of a slalom manoeuvre generates significant discrepancies, especially on the cyclic pitch control channels, A_{1_S} and B_{1_S}. In spite of these differences between the two inverse solutions, when Models A1 and A4 are implemented independently in a conventional IS scheme, the use of the inverse solution obtained from Model A4 in the MPC–IS scheme provides an evolution of the control variables that follows the same trend of the inverse solution for Model

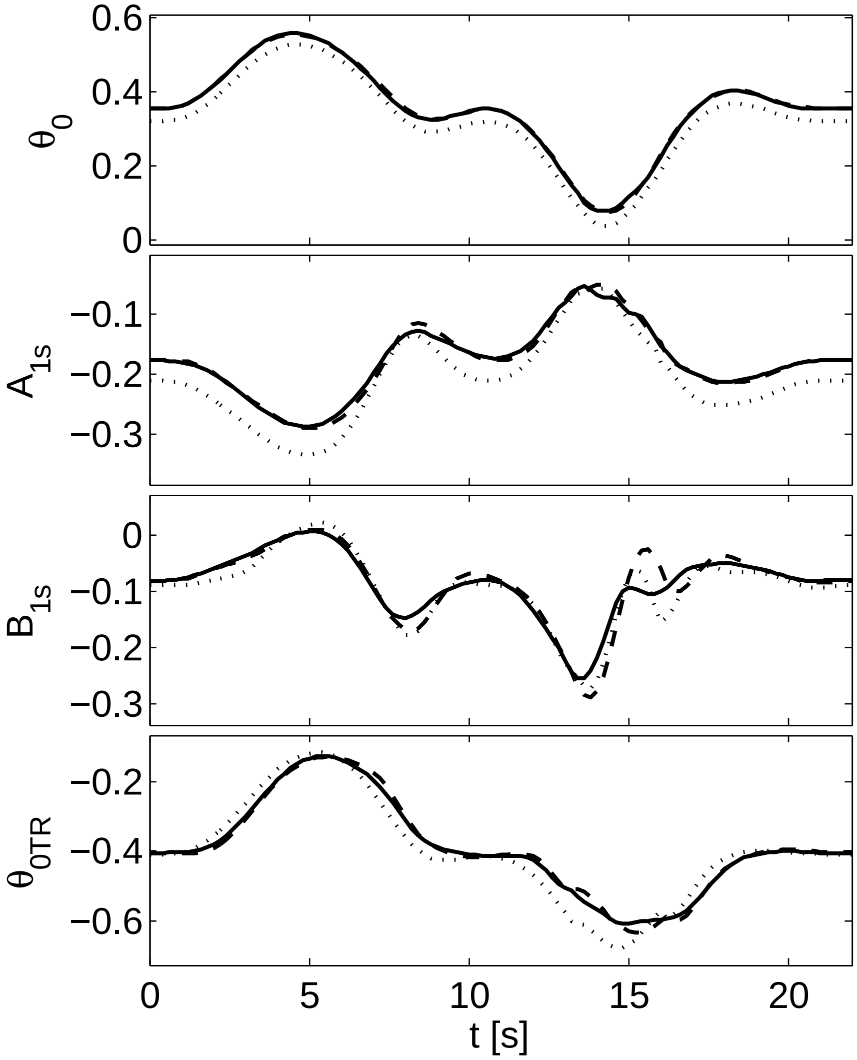

Figure 5.39. Command travel time–histories during a hurdle-hop manoeuvre (—: MPC-IS; - - - IS for Model A1; ··· IS for Model A4).

A1 alone. This means that differences between the models are correctly compensated by the updating process of the initial conditions for rigid–body fuselage states and the guidance term introduced in the definition of the desired output for the IS step. Little differences on maximum command travel are visible, as lower peaks for cyclic pitch and tail rotor collective are present. Discrepancies become smaller when a full–state initialization technique is adopted, but, as a difference with respect to the longitudinal manoeuvre considered previously, they do not disappear. For an aggressive slalom manoeuvre, the smoothing action of the guidance term on the evolution of the tracked variables plays a more significant role, resulting in a reduction of the peaks on command displacement from

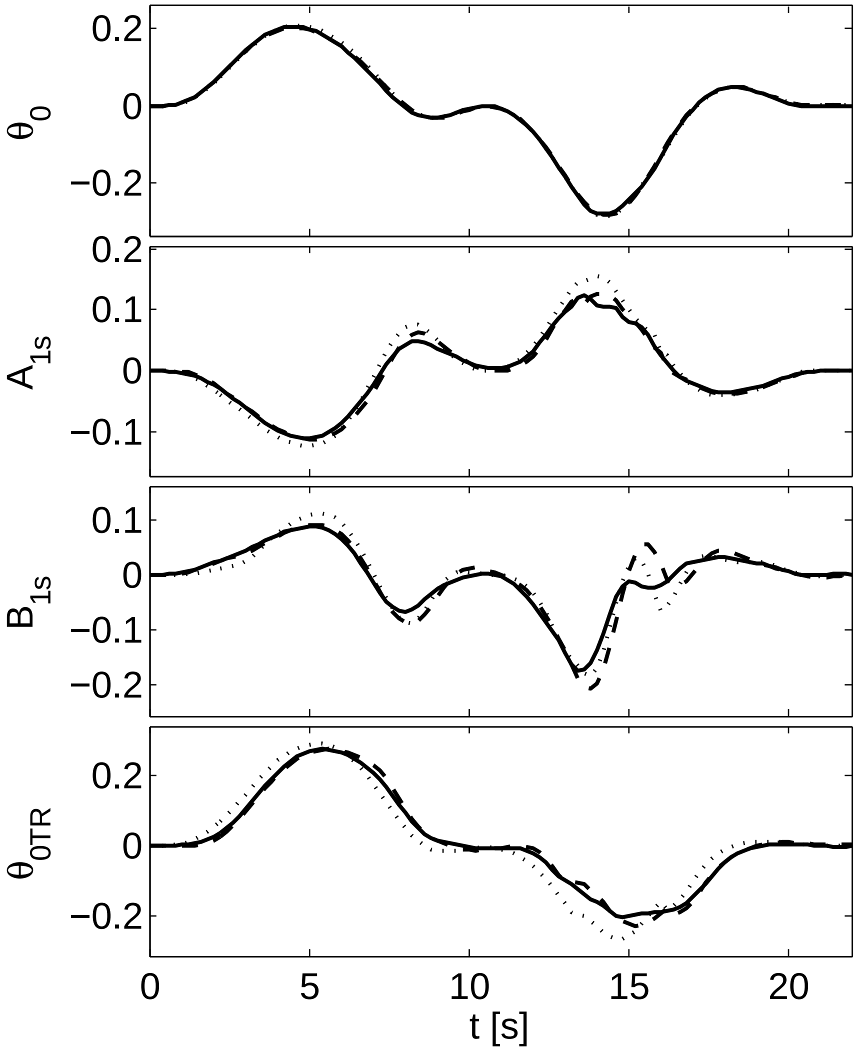

Figure 5.40. Command displacement from trim during a hurdle-hop manoeuvre (—: MPC-IS; - - - IS for Model A1; ··· IS for Model A4).

the initial trim values.

It should be remembered that the guidance logic corrects the drift from the desired trajectory adding a correction term that is determined at the end of the IS time step Δt and acts on the following one. This means that the correction is enforced with a small delay. The effect of this delay, together with the discrepancies between the responses of Models A1 and A4 when partial state initialization is adopted, are at the basis of this small, yet evident discrepancy in the inverse solution. If only fuselage rigid body states for Model A4 are updated to the values achieved by Model A1 at the end of the step, the control action determined during the IS step needs to account for a settling time for those

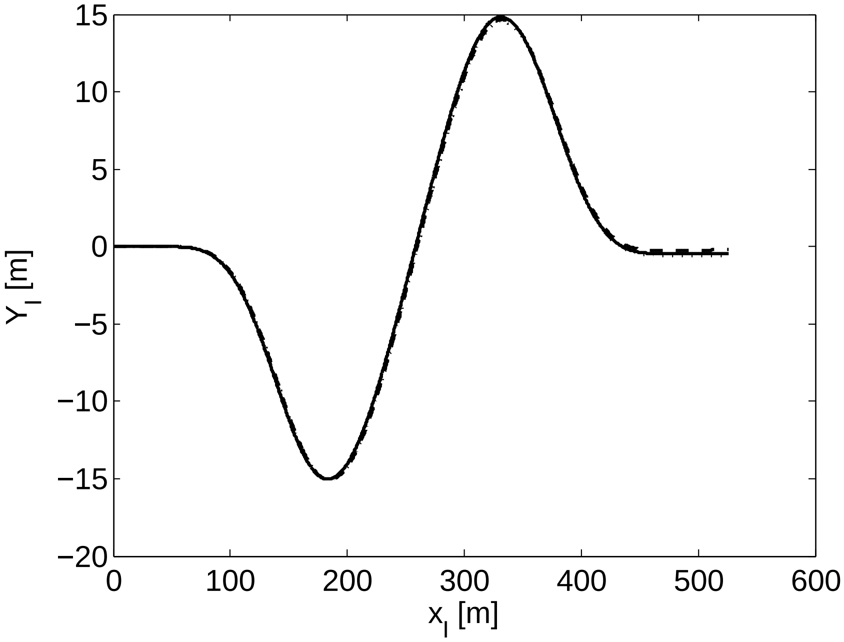

Figure 5.41. Slalom trajectory (—: MPC-IS; - - - IS for Model A1; ··· IS for Model A4).

states (*i.e.* TPP and inflow states) that are not correctly updated.

The selection of the gain in the guidance logic, set to $K = 0.3$ in the present study, represents a tradeoff between numerical robustness in the evaluation of the solution and the need to limit as much as possible deviations from the desired trajectory. When the selected gain is too high, the MPC–IS scheme encounters difficulties in the convergence to the solution and some numerical oscillation may arise. A value $K = 0.3$ allows for a limited drift from the desired solution (barely visible in the trajectory plots) and a reasonable difference in the control action, according to the analysis presented above.

The variation of Euler angles (shown in Fig. 5.43) and that of angular rates (not reported in the figures) are again very similar for all the three solutions, but the MPC–IS approach and the inverse solution of Model A1 by means of a conventional integration method provide an evolution for helicopter attitude where differences smaller than half a degree are present. Roll and yaw angles follow exactly the same patterns. The only visible difference in Fig. 5.43 is on the pitch angle, and mainly for a matter of resolution, given the limited range of the variable. Again, differences on the inverse solution obtained from Model A4 within the IS step of the MPC–IS algorithm are successfully compensated by the initial condition updating scheme and the guidance term adopted.

Inverse simulation schemes can be used to evaluate the feasibility of a given manoeuvre, in terms of command travel and required power. Limiting performance are obtained by challenging the vehicle model on more demanding tasks (*e.g.* increasing the required displacement of the gates from the centerline, for the slalom manoeuvre), until a limit

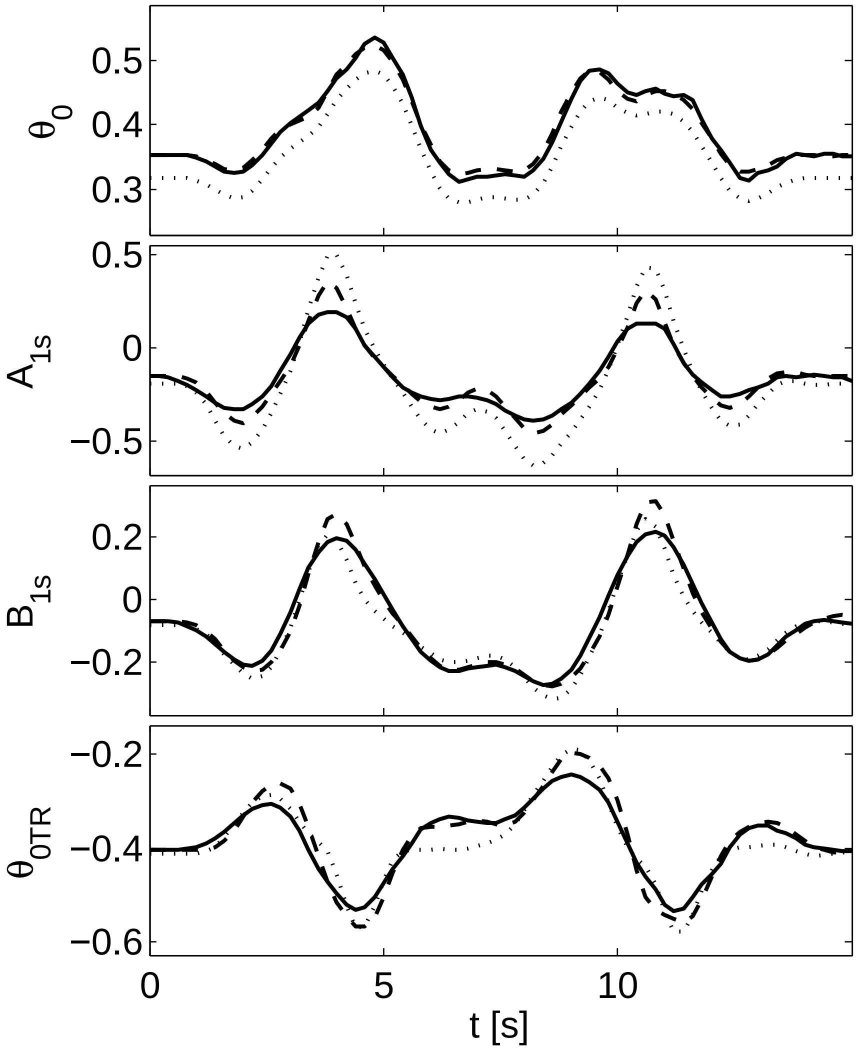

Figure 5.42. Command travel for a slalom manoeuvre (—: MPC-IS; - - - IS for Model A1; ··· IS for Model A4).

on maximum command travel or maximum available power is violated. The feasibility of the control action is readily available from the inverse solution, whereas the constraint on available power requires an estimate of power absorbed by main and tail rotors, taking into account gearbox efficiency and an estimate of on–board system power requirement. More reliable estimate of manoeuvre feasibility or limiting performance are obviously obtained from more accurate models. In this respect, Fig. 5.44 shows that the linear aerodynamics assumed for the main rotor in Model A4 provides a significantly different estimate of required power during the slalom manoeuvre, whereas the estimate of power required based on the MPC–IS solution is similar to the results obtained with the integration

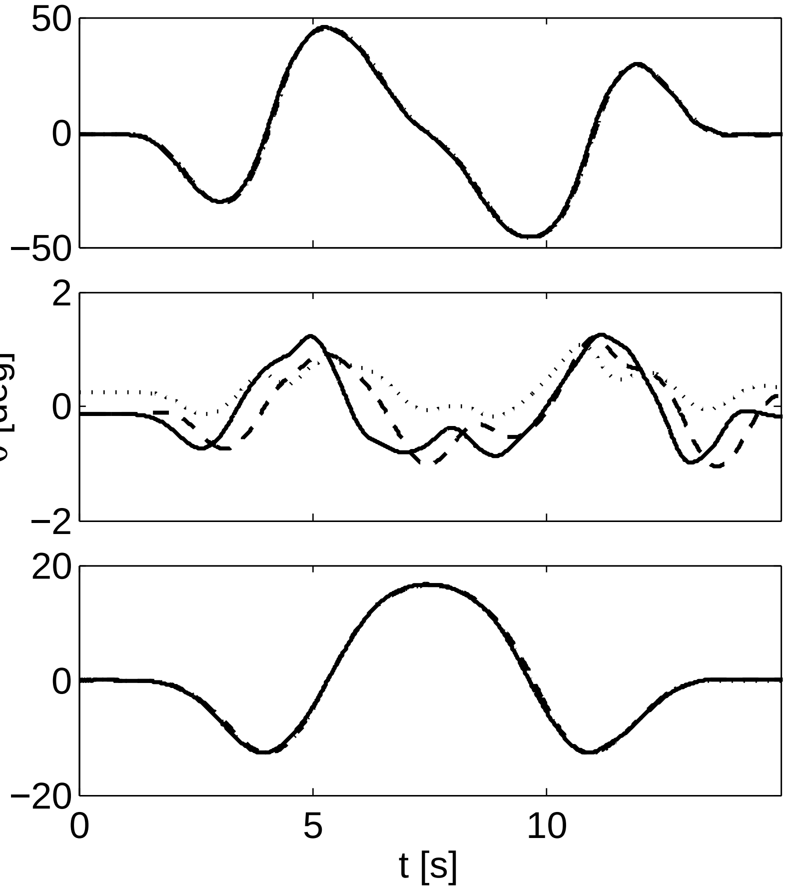

Figure 5.43. Roll, pitch and yaw angles during a slalom manoeuvre (—: MPC-IS; - - - IS for Model A1; · · · IS for Model A4).

method based on Model A1 alone. This means that the two solutions, although obtained by means of different numerical approaches, provide consistent estimate for manoeuvre feasibility and limiting performance for the considered test–case in terms of both command travel and necessary power.

5.3.6 MPC–IS with IS step based on Model B8

As demonstrated above, the MPC–IS approach based on Model A4 represents adequately all the main features of the inverse solution for the considered flight tasks. The approach is then tested using a minimum complexity model (Model B8) for the IS step. Figure 5.45

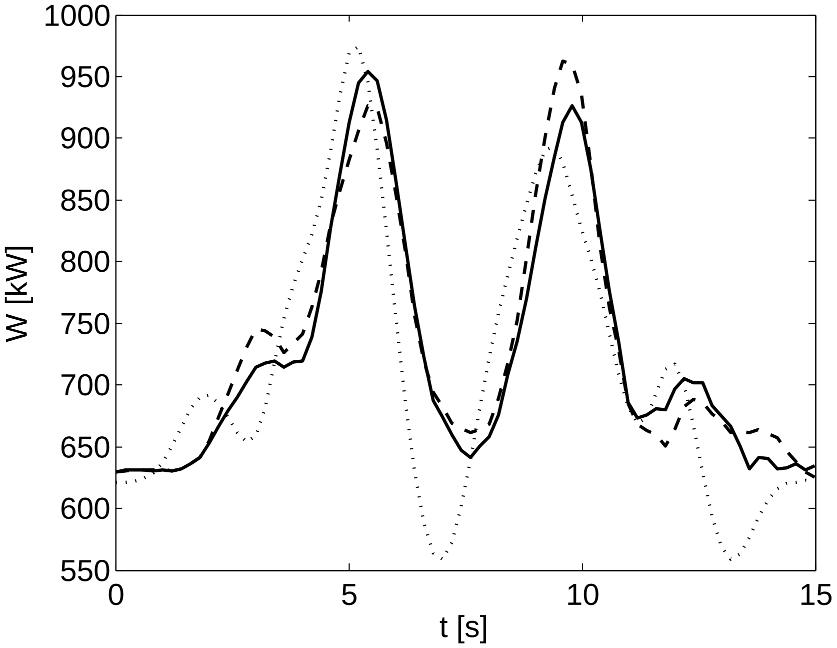

Figure 5.44. Required power during a slalom manoeuvre (—: MPC-IS; - - - IS for Model A1; $\cdots$ IS for Model A4).

presents the control action for the hurdle–hop manoeuvre based on Model B8. The solution of the inverse problem with integration method based on Model B8 presents relevant differences, especially for longitudinal and lateral commands, if compared with the solution for the same task obtained from Model A1 by means of the same IS integration method (indicated by means of dashed and dotted lines in Fig. 5.40, respectively). These differences, due to the simplifying assumptions at the basis of the derivation of of Model B8 listed in the previous Section, are described in detail in Ref. [97].

The MPC–IS approach is again capable of evaluating a feasible command action that tracks well the desired trajectory, also when partial state initialization is adopted, as in the example shown. Similar results are obtained for the slalom manoeuvre. In both cases maximum command travel on all commands and necessary power are precisely estimated and the MPC–IS approach. No difficulties in converging to the inverse solution is encountered, even when very aggressive manoeuvres are dealt with, in spite of the differences between Model B8, used for the IS step, and Model A1, adopted for the forward propagation of the control action.

5.3.7 Computation effort

The computational burden necessary for the solution of an inverse problem depends on the solution scheme and on the complexity of the model. Table 5.6 presents the CPU times (in seconds) for the solution of a hurdle–hop and a slalom manoeuvre, based on

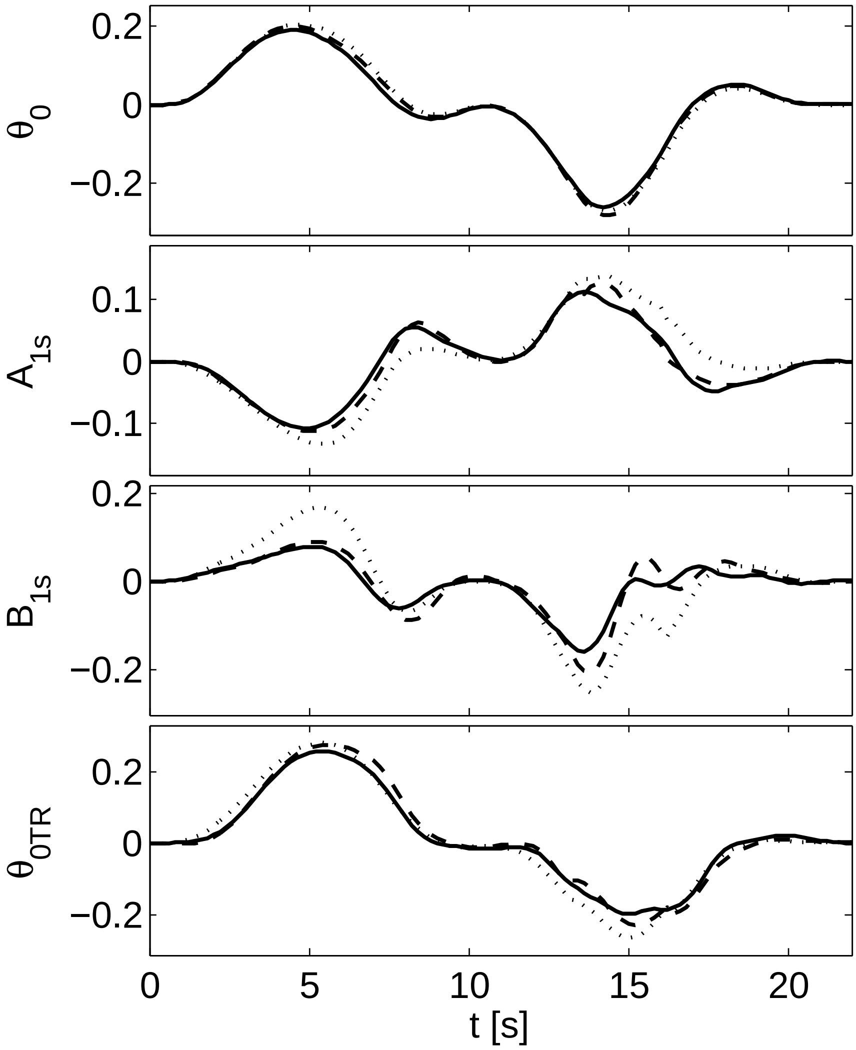

Figure 5.45. Command displacement from trim during a hurdle–hop manoeuvre (—: MPC-IS using Model B8 in the IS step; - - - IS for Model A1; ··· IS for Model B8).

models written in Matlab and running on a 1.6 GHz CPU. Together with total CPU time, also a percentage of a reference CPU time is provided in Table 5.6, using as a reference (100%) the time required for solving the IS problem by means of a conventional integration method applied to Model A1. In all the solutions, a time step $\Delta t = 0.2$ s and a receding horizon equal $T = 0.6$ s are used.

CPU time is quite obviously proportional to the duration of the manoeuvre, 20 s for the hurdle–hop and 13 s for the slalom, but it depends also on the complexity of the control task, where more challenging ones require more iterations for converging during critical flight phases. When comparing the time saved by using the MPC–IS approach, there is a

Table 5.6. Computational time for the solution of the inverse problems (CPU at 1.6 GHz).

		IS A1	IS A4	IS B8	MPC A1+A4	MPC A1+B8
Hurdle–hop	CPU-time (s)	3992	1230	1114	1274	1148
	%	100	30.8	27.9	31.9	28.8
Slalom	CPU-time (s)	2506	876	831	937	857
	%	100	35.0	33.2	37.4	34.2

6% difference between the hurdle–hop and the slalom manoeuvre, where the advantage of using a lower order model is apparently greater for the hurdle–hop. This is due to the fact that the integration method based on Model A1 encounters difficulties in the convergence to an inverse solution during the descending portion of the manoeuvre. In the slalom manoeuvre, Model A1 always converges to the inverse solution in few iterations, and as a consequence the computational time saved by using Models A4 or B8 becomes smaller.

The solution of the IS problem by means of an integration method based on Model A4 is approximately 3 time faster than the solution of the same problem based on Model A1. Using the MPC–IS approach the computational burden is almost identical to the inverse simulation problem based on the simple model, as the forward simulation performed with Model A1 requires a relatively small amount of CPU time, when it remains outside of the iterative process at the basis of the solution of the inverse problem. As a consequence it is possible to evaluate a correct and accurate inverse solution for Model A1, as demonstrated above, at a cost only slightly higher than the (significantly less accurate) inverse solution based on the simplified model only.

Note that, when Model B8 is used, only marginal improvements in terms of computation time are achieved, if compared with the MPC–IS solution based on Model A4, in spite of the reduced number of states (12 instead of 19) and the simpler main rotor and fuselage aerodynamic models. This happens because on one side a computationally expensive iterative process is necessary at every simulation step for evaluating main and tail rotor inflow; at the same time, the computational cost of the integration scheme remains high, in spite of the simplified model dynamics, because more iterations are required for converging to a solution for the IS step, when an initial condition obtained from a different, more complex model is used. In this respect, the use of a minimum complexity helicopter model does not appear to be justified by the modest gain in terms of CPU time.

Chapter 6

Conclusions

The research activity presented in this thesis is characterised by several goals in the framework of studies related to helicopter flight mechanics, with a strong common denominator: the development of low order mathematical models for the evaluation of rotorcraft performance and handling qualities. The identification of a minimum–complexity model suitable for a given analysis task is validated by comparing the results obtained for simplified models with those derived on the basis of more complex and reliable ones.

The analysis includes articulated, teetering and gimballed rotors. Helicopter models featuring these different classes of rotor configuration have been developed using both individual blade dynamics and tip-path-plane dynamics. A technique for the development of low–order models is presented and discussed. An ordering scheme approach was developed, based on a symbolic math–manipulation toolbox, that allows for including in the equations only the most relevant terms, up to a determined order of magnitude.

With this objectives in mind, several models of the same helicopter configuration were tested with different trim techniques in order to evaluate how model complexity and trim approach affect the evaluation of rotorcraft limiting performance in forward, climbing and turning flight. Helicopter models with individual blade dynamics are used as a reference to test simpler models based on TPP dynamics, linear aerodynamics with lower order inflow states and simpler fuselage aerodynamics.

The trim results for a complete individual–blade helicopter model obtained with shooting of the full–order system of dynamic equations and those derived by means of an original nested trim algorithm with averaged rotor loads show a very good agreement in all trim conditions, if not for a small difference in roll angle. This is a minor price to pay in front of the improved numerical efficiency of the nested algorithm, that can thus replace the full–order shooting method in all of the test cases here proposed. Significant savings in computational time, particularly relevant when a complete analysis of the vehicle flight envelope is pursued, are obtained also removing blade lag and twist degrees of freedom. The results in terms of estimation of helicopter performance are hardly affected by this further simplification. Note that a complete set of configuration data (geometry, inertia, airfoil and fuselage aerodynamic data, etc.) is still required, so that the details needed for the study is still considerable, with the only, but significant, exception of the lag damper, that represents a relatively complex element in the model, which is dropped together with the lag degree of freedom.

Models bases on TPP dynamics can provide a good estimate of the helicopter performance in straight flight at a computational cost between one and two orders of magnitude lower than that required for full order models, once the effects of compressibility, retreating blade stall and overall maximum rotor thrust coefficient are properly addresses. In spite of these refinement to the TPP model, the linear formulation for the rotor aerodynamic model does not allow for a precise description of blade behaviour in the complex environment of turning flight, leading to a significant overestimate of limiting performance in terms of expected maximum turn rate. Comparing the results obtained from the various models, a uniform inflow causes a degradation in the evaluation of off-axis behaviour, whereas a simplified description of fuselage aerodynamic forces by means of parasite drag area leads to an overestimate of rotorcraft performance. The results derived from static models at trim, based on separate longitudinal and lateral trim and a very limited set of parameters, are reasonably accurate only for maximum speed and rate of climb. On the converse, the estimation of lateral variables needs to be improved in order to provide reliable indications, even at a preliminary design stage.

Helicopter handling qualities are assessed in terms of both stability and agility potential. The latter is estimated by means if inverse simulation of prescribed manoeuvres. The stability and dynamic behaviour of a novel two–bladed gimballed rotor configuration are analysed first, and compared to a more conventional equivalent teetering rotor. A simplified model of the gimballed rotor is developed in order to highlight the physical mechanisms governing its peculiar behaviour, and, in particular, the sustained wobbling motion exhibited in forward flight. In this respect, one should note that thrust vector direction is constant in spite of wobbling, as blade TPP does not oscillates at steady-state. Use of a fly-bar with aerodynamics paddles is necessary to damp the feathering motion of the hub. At the same time the usual effect of the stability bar, which is expected to improve rotorcraft pitch and roll damping derivatives, is limited when the hub is restrained by elastomeric springs, adopted in order to improve control power when flying at zero-g. Hub stiffness demonstrates a relevant effect on the amplitude of wobbling motion as well, and, in particular, on the steady–state response to commands through the frequency of the feathering motion and the related phase shift. The latter induces a significant reduction of the longitudinal tilt of the blade TPP together with a lateral response to a longitudinal pitch command.

The presence of coning hinges and a high pitch-coning coupling makes the system unstable, when ideal, frictionless hinges are considered. The rotor is stabilized by means of a sufficient amount of dissipation, due to either viscous damping or dry friction in the coning hinges. In this respect, the friction generated in the coning hinges by the high centrifugal load is expected to be largely sufficient to this end in all considered flight conditions. Command and gust response of gimballed and teetering rotors with and without coning hinges have been then compared. The presence of coning degrees of freedom has a marginal effect on both the gimballed and teetering rotors response to commands and steady state behaviour. On the converse, coning hinges provide a significant load alleviation during gust encounters, an effect which is increased when a pitch-coning coupling mechanism is included.

Inverse simulation is used as a tool to analyse the agility potential of rotorcraft. The analysis shows how rotor model, inflow dynamics and fuselage aerodynamic model influence the results obtained from the inverse simulation of a prescribed set of test manoeuvres. The analysis highlights how, in the simplest cases, only minor differences are exhibited by the various models, so that also the simplest ones are expected to provide reliable information on command travel and state evolution during the manoeuvre. Conversely, for more demanding tasks, simpler models may not correctly reproduce relevant phenomena in critical flight regimes, thus harming the validity of the results. In particular, a hurdle-hop longitudinal manoeuvre is well captured by most of the considered models, whereas a more aggressive lateral slalom is not well represented, when an individual blade model is not available. In this respect, one should note that, from the numerical standpoint, individual blade models pose a serious challenge to inverse simulation algorithm, that are required to be carefully tailored in order to properly address issues such as those related to uncontrolled states and non–minimum–phase behaviour. At the same time, fuselage aerodynamic models is shown to play a crucial role in low–speed tasks, such as a lateral repositioning, when a large variation of aerodynamic angles is expected.

A method for the quantitative determination of the accuracy in the definition of the control action for a given series of flight tasks by means of inverse simulation of a certain rotorcraft model is proposed. A technique for deriving an uncertainty interval that captures a reference control action obtained from a more accurate helicopter model is derived, that provides an indication for uncertainty levels on the control action. The results show that the technique adequately measures the capability of each simplified helicopter model in properly capturing (or failing to do so) the characteristics of the control action for a given flight task, within a prescribed level of confidence, defined in terms of percentage of the control action of the reference model for the same task left outside of the assumed uncertainty interval. These figures can be easily adopted in order to provide an estimate of the expected reliability of HQ performance prediction obtained from simple, low-order models, together with an estimate of control uncertainty in the synthesis of robust stability and control augmentation systems. It should be noted that the technique can be easily extended to the comparison of inverse simulation data with experimental flight test data, when available.

Since the solution of inverse problem with individual blade models has a considerable computational cost and poses several numerical difficulties, a novel approach to the solution of inverse simulation problems for helicopter aggressive manoeuvres based on a model predictive control scheme is proposed. The approach significantly reduces the computational burden required by the inverse simulation of a complex nonlinear helicopter model by using a lower–order model in the inverse simulation step. In this framework, the standard integration approach to the solution of the inverse simulation problem is modified introducing an update scheme for the initial conditions of the simplified model at the end of the forward simulation step, performed on the more complex one. A simple guidance law avoids the build-up of errors while tracking the prescribed variation of the output variables.

The approach is tested on two manoeuvres used for the analysis of rotorcraft handling qualities, namely a hurdle–hop and a slalom. The results show that the MPC inverse simulation approach solves the considered inverse problems with good convergence characteristics, generating accurate trajectories that almost overlap the desired one. Time–histories for controls, state variables, and required power are very similar to those generated by a standard integration algorithm applied to the same problem, at a fraction of the computational cost necessary for obtaining the inverse solution directly on the complete helicopter model that, in the MPC-IS scheme, is used only for the forward-integration step. The approach is tested also for a minimum complexity helicopter model. Tracking performance are still adequate, but only a marginal gain in terms of computational time is obtained.

Bibliography

[1] Johnson, W., "Milestones in Rotorcraft Aeromechanics - Alexander A. Nikolsky Honorary Lecture," *Journal of the American Helicopter Society*, Vol. 56, No. 3, 2011, pp. 1–24.

[2] Leishman, J., "Rotorcraft Aeromechanics: Getting through the Dip," *Journal of the American Helicopter Society*, Vol. 55, No. 1, 2010, pp. 1–23.

[3] Peters, D., "How Dynamic Inflow Survives in the Competitive World of Rotorcraft Aerodynamics," *Journal of the American Helicopter Society*, Vol. 54, No. 1, 2009, pp. 1–15.

[4] Hess, R., "A Framework for Robust Rotorcraft Flight Control Design," *Journal of the American Helicopter Society*, Vol. 56, No. 2, 2011, pp. 22004–22011.

[5] Bramwell, A., Done, G., and Balmford, D., *Bramwell's Helicopter Dynamics, 2nd ed.*, Butterworth Heinemann, Oxford, UK, 2001.

[6] Padfield, G., *Helicopter Flight Dynamics: The Theory and Application of Flying Qualities and Simulation Modeling, 2nd ed.*, Blackwell Publishing, Oxford, UK, 2007.

[7] Johnson, W., *Helicopter Theory*, Dover, New York, NY, 1994.

[8] Prouty, R., *Helicopter Performance, Stability, and Control*, Krieger, Malabar, FL, 2001.

[9] Arra, M., *L'Elicottero*, HOEPLI, Milano, Italy, 2001.

[10] Leishman, J., *Principles of Helicopter Aerodynamics, 2nd ed.*, Cambridge University Press, New York, NY, 2006.

[11] Heffley, R. and Mnich, M., "Minimum Complexity Helicopter Simulation Math Model," Tech. rep., NASA Technical Report CR-177476, 1988.

[12] Chen, R., "A Simplified Rotor System Mathematical Model for Piloted Flight Dynamics Simulation," Tech. rep., NASA TM 18575, 1979.

[13] Chen, R., "Effects of Primary Rotor Parameters on Flapping Dynamics," Tech. rep., NASA TP 1431, 1980.

[14] Talbot, P., Tinling, B., Decker, W., and Chen, R., "A Mathematical Model of a Single Main Rotor Helicopter for Piloted Simulation," Tech. rep., NASA TM 84281, 1982.

[15] Howlett, J., "UH-60A 'Black Hawk' Engineering Simulation Program, Volume 1: Mathematical Model," Tech. rep., NASA CR 166309, 1981.

[16] Howlett, J., "UH-60A 'Black Hawk' Engineering Simulation Program, Volume 2: Background Report," Tech. rep., NASA CR 166310, 1981.

[17] Kim, F., *Formulation and validation of high-order mathematical models of helicopter flight dynamics*, Ph.D. thesis, University of Maryland College Park, 1991.

[18] F.J., B., “A Simplified Theoretical Method of Determining the Characteristics of a Lifting Rotor in Forward Flight,” Tech. rep., NACA report No. 716, 1941.

[19] Turnour, S. and Celi, R., “Modelling of Flexible Rotor Blades for Helicopter Flight Dynamics Applications,” *Journal of the American Helicopter Society*, Vol. 41, No. 1, 1996, pp. 52–66.

[20] Yeo, H. and Chopra, I., “Coupled Rotor/Fuselage Vibration Analysis using Detailed 3-D Airframe Models,” *Mathematical and Computer Modelling*, Vol. 33, No. 10-11, 2001, pp. 1035 – 1054.

[21] Neshat, A., *A High Order Simulation Model for the Bell 205 Helicopter*, Master’s thesis, Carleton University - Ottawa, Ontario, August 1995.

[22] Johnson, E. and Schrage, D., “The Georgia Tech Unmanned Aerial Research Vehicle: GTMax,” *AIAA Guidance, Navigation, and Control Conference*, Austin, TX, 11-14 August 2003.

[23] Chaplin, H., “Some Dynamic Properties of a Rigid Two-Bladed Fully Gimballed Tip-Jet Helicopter Rotor with Circulation Control,” Tech. rep., D.W. Taylor Naval Ship Research and Development Center, 1980.

[24] Yen, J., Corrigan, J., Schillings, J., and Hsieh, P., “Comprehensive Analysis Methodology at Bell Helicopter: COPTER,” *American Helicopter Society Aeromechanics Specialists Conference*, San Francisco, CA, 19-21 January 1994.

[25] Peters, D., Kim., B., and Chen, H., “Calculation of Trim Settings for a Helicopter Rotor by an Optimized Automatic Controller,” *Journal of Guidance, Control & Dynamics*, Vol. 7, No. 1, 1984, pp. 85–91.

[26] McVicar, J. and Bradley, R., “Robust and Efficient Trimming Algorithm for Application to Advanced Mathematical Models of Rotorcraft,” *Journal of Aircraft*, Vol. 32, No. 2, 1995, pp. 439–442.

[27] Peters, D. and R.A., O., “Flapping Response Characteristics of Hingeless Rotor Blades by a Generalized Harmonic Balance Method,” Tech. rep., NASA TN D-7856, 1975.

[28] Peters, D. and Barwey, D., “A General Theory of Rotorcraft Trim,” *Mathematical Problems in Engineering*, Vol. 4, No. 2, 1996, pp. 1–34.

[29] Shank, T., *Optimal Aeroelastic Trim for Rotorcraft with Constrained, Non-unique Trim Solution*, Ph.D. thesis, Georgia Institute of Technology, April 2008.

[30] Rutkowski, M., Ruzicka, G., Ormiston, R., Saberi, H., and Jung, Y., “Comprehensive Aeromechanics Analysis of Complex Rotorcraft Using 2GCHAS,” *Journal of the American Helicopter Society*, Vol. 40, No. 4, 1995, pp. 3–17.

[31] Saberi, H., Khoshlahjeh, M., Rutkowski, M., and Ormiston, R., “Overview of RCAS and Application to Advance Rotorcraft Problems.” *American Helicopter 4th Decennial Specialist’s Conference on Aeromechanics*, San Francisco, California, 21-23 January 2004.

[32] Benoit, B., Dequin, A.-M., Kampa, K., Grünhagen, W. v., Basset, P.-M., and Gimonet, B., “HOST, a General Helicopter Simulation Tool for Germany and France.”

56th Annual Forum Proceedings . American Helicopter Society, 56th Annual Forum and Technology Display, 2-4 May 2000.

[33] Bir, G. and Chopra, I., "University of Maryland Advanced Rotorcraft Code (UMARC) Theory Manual." Tech. rep., UM-AERO Report 92-02, 1992.

[34] Bauchau, O., "DYMORE User's Manual." Tech. rep., GeorgiaTech, 2007.

[35] Masarati, P., Morandini, M., Quaranta, G., and Mantegazza, P., "Computational Aspects and Recent Improvements in the Open-source Multibody Analysis Software "'MBDyn"'." *Multibody Dynamics 2005, ECCOMAS Thematic Conference*, Madrid, Spain, 21-24 June 2005.

[36] DuVal, R., "A Real-Time Multi-Body Dynamics Architecture for Rotorcraft Simulation. The Challenge of Realistic Rotorcraft Simulation." *RAeS Conference*, 7-9 November 2001, pp. 9.1 – 9.12.

[37] Quackenbush, T. R., Wachspress, D. A., Boschitsch, A. H., , and Curbishley, T. B., "A Comprehensive Hierarchical Aeromechanics Rotorcraft Model (CHARM) for General Rotor/Surface Interaction." Tech. rep., CDI Report No. 99-03, 1999.

[38] Johnson, W., "Technology Drivers in the Development of CAMRAD II," *AHS Aeromechanics Specialists Conference*, 19-21 January 1994.

[39] Harris, F., "Rotor Performance at High Advance Ratio; Theory versus Test," Tech. rep., NASA CR-2008-215370, 2008.

[40] Johnson, W., "NDARC - NASA Design and Analysis of Rotorcraft Theoretical Basis and Architecture," *Proceedings of the American Helicopter Society Aeromechanics Specialists' Conference*, San Francisco, California, 20-22 January 2010.

[41] Johnson, W., "NDARC - NASA Design and Analysis of Rotorcraft Validation and Demonstration," *Proceedings of the American Helicopter Society Aeromechanics Specialists' Conference*, San Francisco, California, 20-22 January 2010.

[42] Bousman, W. G. and Norman, T., "Assessment of Predictive Capability of Aeromechanics Methods," *Journal of the American Helicopter Society*, Vol. 55, No. 1, 2010, pp. 12001–12001–12.

[43] Thomson, D. and Bradley, R., "Inverse simulation as a tool for flight dynamics research - Principles and applications," *Progress in Aerospace Sciences*, Vol. 42, No. 3, 2006, pp. 174 – 210.

[44] Kato, O. and Sugiura, I., "An Interpretation of Airplane General Motion and Control as Inverse Problem," *Journal of Guidance, Control & Dynamics*, Vol. 9, No. 2, 1986, pp. 198–204.

[45] Thomson, D. and Bradley, R., "Development and Verification of an Algorithm for Helicopter Inverse Simulation," *Vertica*, Vol. 14, No. 2, 1990, pp. 185 – 200.

[46] Hess, R. and Gao, C., "A Generalized Algorithm for Inverse Simulation Applied to Helicopter Maneuvering Flight," *Journal of the American Helicopter Society*, Vol. 38, No. 4, 1993, pp. 3–15.

[47] Avanzini, G., De Matteis, G., and de Socio, L., "Analysis of Aircraft Agility on Maximum Performance Maneuvers," *Journal of Aircraft*, Vol. 35, No. 4, 1998, pp. 529–535.

[48] Thomson, D., "An Analytical Method of Quantifying Helicopter Agility," *12*th *European Rotorcraft Forum ERF 1986*, Garmisch-Partenkirchen, Germany, 22-25

September 1986.

[49] Nannoni, F. and Stabellini, A., "Simplified Inverse Simulation for Preliminary Design Purpose," *15th European Rotorcraft Forum ERF 1989*, Amsterdam, Netherlands, 12-15 September 1989.

[50] Bradley, R., Padfield, G., Murray-Smith, D., and Thomson, D., "Validation of Helicopter Mathematical Models," *Transactions of the Institute of Measurement and Control*, Vol. 12, No. 4, 1990, pp. 186–196.

[51] Bradley, R. and Thomson, D., "Handling Qualities and Performance Aspects of the Simulation of Helicopters Flying Mission Task Elements," *18th European Rotorcraft Forum ERF 1992*, Avignon, France, 15-18 September 1992.

[52] Bagiev, M. and Thomson, D., "Handling Qualities Assessment of an Autogiro," *Journal of the American Helicopter Society*, Vol. 55, No. 3, 2010, pp. 32003–32003–11.

[53] Hess, R., Gao, C., and Wang, S., "Generalized Technique for Inverse Simulation Applied to Aircraft Manoeuvres," *Journal of Guidance, Control & Dynamics*, Vol. 14, No. 5, 1991, pp. 920–926.

[54] De Matteis, G., De Socio, L., and Leonessa, A., "Solution of Aircraft Inverse Problems by Local Optimization," *Journal of Guidance, Control & Dynamics*, Vol. 18, No. 3, 1995, pp. 567–571.

[55] Borri, M., Bottasso, C., and Montelaghi, F., "Numerical Approach to Inverse Flight Dynamics," *Journal of Guidance, Control & Dynamics*, Vol. 20, No. 4, 1997, pp. 742–747.

[56] Celi, R., "Optimization-Based Inverse Simulation of a Helicopter Slalom Maneuver," *Journal of Guidance, Control, and Dynamics*, Vol. 23, No. 2, 2000, pp. 289–297.

[57] Rutherford, S. and Thomson, D., "Helicopter Inverse Simulation Incorporating an Individual Blade Rotor Model," *Journal of Aircraft*, Vol. 34, No. 5, 1997, pp. 627–634.

[58] Avanzini, G. and De Matteis, G., "Two-Timescale Inverse Simulation of a Helicopter Model," *Journal of Guidance, Control & Dynamics*, Vol. 24, No. 2, 2001, pp. 330–339.

[59] Lu, L., *Inverse Modelling and Inverse Simulation for System Engineering and Control Applications*, Ph.D. thesis, University of Glasgow, October 2007.

[60] Bagiev, M., Thomson, D., Anderson, D., and Murray-Smith, D., "Hybrid inverse methods for helicopters in aggressive manoeuvring flight," *17th IFAC Symposium on Automatic Control in Aerospace*, IFAC, Toulouse, France, 25-29 June 2007.

[61] Bottasso, C., Maisano, G., and Scorcelletti, F., "Trajectory Optimization Procedures for Rotorcraft Vehicles, Their Software Implementation, and Applicability to Models of Increasing Complexity," *Journal of the American Helicopter Society*, Vol. 55, No. 3, 2010, pp. 32010–32010–13.

[62] "Handling Qualities Requirements for Military Rotorcraft," Tech. rep., US Army Aviation and Missile Command, ADS-33E-PRF, 2000.

[63] Peters, D. and Hohenemser, K., "Application of the Floquet Transition Matrix to Problems of Lifting Rotor Stability," *Journal of the American Helicopter Society*, Vol. 16, No. 2, 1971, pp. 25–33.

[64] Peters, D., “Fast Floquet Theory and Trim for Multi-Bladed Rotorcraft,” *Journal of the American Helicopter Society*, Vol. 39, No. 4, 1994, pp. 82–89.

[65] McVicar, J. and Bradley, R., “Efficient and Robust Algorithms for Trim and Stability Analysis of Advanced Rotorcraft Simulations,” *The Aeronautical Journal*, Vol. 101, No. 1008, 1997, pp. 375–387.

[66] Peters, D., Lieb, S., and Ahaus, L., “Interpretation of Floquet Eigenvalues and Eigenvectors for Periodic Systems,” *Journal of the American Helicopter Society*, Vol. 56, No. 3, 2011.

[67] Bauchau, O. and Wang, J., “Efficient and Robust Approaches for Rotorcraft Stability Analysis,” *Journal of the American Helicopter Society*, Vol. 55, No. 3, 2010, pp. 32006–32006–9.

[68] G., G., “Effect of Drive Train and Fuel Control Design on Helicopter Handling Qualities,” *Journal of the American Helicopter Society*, Vol. 46, No. 1, 2001, pp. 14–22.

[69] Biggers, J., McCloud, J., and Patterakis, P., “Wind Tunnel Tests of two full Scale helicopter Fuselages,” Tech. rep., NASA TN-D-1548, 1962.

[70] Jenkin, J., Winston, M., and Sweet, G., “Wind-Tunnel Investigation of the Longitudinal Aerodynamic Characteristics of two Full-Scale Helicopter Fuselage Models with Appendages,” Tech. rep., NASA TN D-1364, 1962.

[71] Wilson, J. and Mineck, R., “Wind Tunnel Investigation of Helicopter-Rotor Wake effects oh Three Helicopter Fuselage Models,” Tech. rep., NASA TM-X-3185, 1975.

[72] Renaud, T., O’Brien, D., Smith, M., and Potsdam, M., “Evaluation of Isolated Fuselage and Rotor-Fuselage Interaction Using CFD,” *Proceedings of the 60th Annual Forum of the American Helicopter Society*, Alexandria, VA, 7-10 June 2004, pp. 995–1009.

[73] Takahashi, M., “A Flight-dynamic Helicopter Mathematical Model with a Single Flap-lag-torsion Main Rotor,” Tech. rep., NASA TM 102267, 1990.

[74] Wilcock, T. and Thorpe, C., “Flight Simulation of a Wessex Helicopter A Validation Exercise,” Tech. rep., RAE C.P. 1299, 1974.

[75] Shaughnessy, J., Deaux, T., and Yenni, K., “Development and Validation of a Piloted Simulation of a Helicopter and External Sling Load,” Tech. rep., NASA TP 1285, 1979.

[76] Sturgeon, W. and Phillips, J., “A Mathematical Model of the CH-53 Helicopter,” Tech. rep., NASA TM 81238, 1981.

[77] Hilbert, K., “A Mathematical Model of the UH-60 Helicopter,” Tech. rep., NASA TM-85890, 1984.

[78] Lucertini, F., *Stability and Flying Qualities of a Light Helicopter*, Ph.D. thesis, University of Rome “Sapienza”, Rome, June 2010.

[79] Gavrilets, V., Mettler, B., and Feron, E., “Nonlinear model for a small-size acrobatic helicopter,” *AIAA Guidance, Navigation and Control Conference*, Montreal, Canada, 6-9 August 2001, pp. 1593–1600.

[80] Chen, R., “A Survey of Nonuniform Inflow Models for Rotorcraft Flight Dynamics and Control Applications,” Tech. rep., 1989.

[81] and HaQuang, N., "Dynamic Inflow for Practical Applications," *Journal of the American Helicopter Society*, Vol. 33, 1988, pp. 64–68.

[82] Peters, D., Boyd, D., and He, C., "Finite-State Induced-Flow Model for Rotors in Hover and Forward Flight," *Journal of the American Helicopter Society*, Vol. 34, 1989, pp. 5–17.

[83] Chaplin, H., "Some Dynamic Properties of a Rigid Two–Bladed Fully Gimballed Rotor with Teetering Feedback," Tech. rep., D.W. Taylor Naval Ship Research and Development Center, 1986.

[84] Hohenemser, K., "A Type of Lifting Rotor with Inherent Stability," *Journal of Aeronautical Science*, Vol. 17, 1950, pp. 555–563.

[85] Marks, M., "Comparison of Current Operational Rotor Systems and a Rotor Having Floating Hub and Offset Coning Hinges," *Journal of the American Helicopter Society*, Vol. 5, No. 4, 1960, pp. 13–24.

[86] Robinson, C., *Modeling and Analysis of Helicopter Ground Resonance utilizing Symbolic Processing and Dynamic Simulation Software*, Master's thesis, Naval Postgraduate School - Monterey, California, March 1997.

[87] Avanzini, G., Matteis, G. D., Lucertini, F., and Torasso, A., "Performance Analysis of a Lightweight Helicopter Featuring a Two–Bladed Gimballed Rotor," *37*th *European Rotorcraft Forum ERF 2011*, Gallarate, Italy, 13-15 September 2011.

[88] tevens, B. and Lewis, F., *Aircraft Control and Simulation, 2*nd *ed.*, John Wiley & Sons, Hoboken, N.J., 1992.

[89] Torasso, A., *Simulazione e trim di un modello di elicottero con pale articolate*, Master's thesis, Politecnico di Torino, December 2008.

[90] Yeo, H., Bousman, W., and Johnson, W., "Performance Analysis of a Utility Helicopter with Standard and Advanced Rotors," *Journal of the American Helicopter Society*, Vol. 49, No. 3, 2004.

[91] Bousman, W. and Kufeld, R., "UH-60A Airloads Catalog," Tech. rep., NASA TM-2005-212827, 2005.

[92] Abbot, W., Oliver, R., J.O., B., and R.A., W., "Validation Flight Test of UH-60A for Rotorcraft System Integration Simulator (RSIS)," Tech. rep., USAAEFA PROJECT NO. 79-24, 1982.

[93] EASA - European Aviation Safety Agency, *Certification Specifications for Small Rotorcraft CS-27*, 2003 - last amend 2008.

[94] Biggers, J., "Some Approximations to the Flapping Stability of Helicopter Rotors," *Rotorcraft Dynamics. NASA SP-352, 371 pages, published by NASA, Washington, DC*, 1974.

[95] Guckenheimer, J. and Holmes, P., *Nonlinear Oscillations, Dynamical Systems and Bifurcation of Vector Fields (Applied Mathematical Sciences Vol. 42)*, Springer, New York, N.Y., 2002.

[96] Hansen, R., "Toward a Better Understanding of Helicopter Stability Derivatives," Tech. rep., NASA TM-84277, 1982.

[97] Avanzini, G., Matteis, G. D., and Torasso, A., "Modelling Issues in Helicopter Inverse Simulation," *36*th *European Rotorcraft Forum ERF 2010*, Paris, France, 7-9 September 2010.

[98] Lin, K., Lu, P., and Smith, M., "The Numerical Errors in Inverse Simulation," *AIAA Flight Simulation Technologies Conference*, Monterey, CA, 9-11 August 1993.

[99] Yip, K. and Leng, G., "Stability Analysis for Inverse Simulation of Aircraft," *Aeronautical Journal*, Vol. 102, No. 1016, 1998, pp. 345–351.

[100] Lin, K., "Comment on Generalized Technique for Inverse Simulation Applied to Aircraft Maneuvers," *Journal of Guidance, Control & Dynamics*, Vol. 16, No. 6, 1993, pp. 1196–1197.

[101] Mayne, D., Rawlings, J., Rao, C., and Scokaert, P., "Constrained Model Predictive Control: Stability and Optimality," *Automatica*, Vol. 36, No. 6, 2000, pp. 789 – 814.

Appendix A

Helicopter configuration data

This chapter collects the important configuration data for the rotorcraft used in this study.

A.1 UH-60A

Table A.1 collects the UH–60A configuration data for the individual blade models, while table A.2 collects terms used in lower order model.

Table A.1. UH-60A geometric and mass data [15]. Data between brackets are for the heavier configuration used for envelope, maximum ROC and ROT evaluation.

Fuselage	mass	m	7257.5 (9185.2)	kg
	moments of inertia	I_{xx}	6316.8 (11310)	kg m^2
		I_{yy}	52215.0 (56678)	kg m^2
		I_{zz}	49889.0 (48627)	kg m^2
		I_{xz}	2551.6 (2497.9)	kg m^2
Main rotor	number of blades	N_b	4	
	radius	R	8.18	m
	chord	c	0.53	m
	blade mass	m_b	116.5	kg
	blade first moment	S_b	385.7	kg m
	blade flap moment of inertia	I_b	2050.8	kg m^2
	hinge eccentricity	e	0.38	m
	forward tilt	i_θ	3	deg
	lateral tilt	i_ϕ	0	deg
	blade pitch/flap coupling	δ_3	0	deg
	rotor speed	Ω	27	rad s^{-1}
	position in $\mathcal{F}_B$	$\boldsymbol{r}_S$	[0.3,0, −2.3]	m
Tail rotor	number of blades	$N_{b_{tr}}$	4	
	radius	R_{tr}	1.68	m
	cant angle	Γ	70	deg
	blade pitch/flap coupling	$\delta_{3_{tr}}$	35	deg
	rotor speed	Ω_{tr}	124.6	rad s^{-1}
	position in $\mathcal{F}_B$	$\boldsymbol{r}_{tr}$	[−9.7,0.3, −2.5]	m
Horizontal tail	surface	S_{ht}	4.18	m^2
	position in $\mathcal{F}_B$	$\boldsymbol{r}_{ht}$	[−8.8, 0, −0.46]	m
Vertical tail	surface	S_{vt}	3.00	m^2
	position in $\mathcal{F}_B$	$\boldsymbol{r}_{vt}$	[−8.70 − 1.2]	m

Table A.2. UH-60A simplified model aerodynamic data

Fuselage parasite area	$S_{Fus}C_{D_0}$	3.5	m^2	
Main rotor	solidity	$N_b c/(\pi R)$	0.082	
	airfoil lift slope	C_{L_α}	5.7	rad^{-1}
	rotor drag coefficient	δ	0.013	
Tail rotor	solidity	$N_{b,tr}c_{tr}/(\pi R_{tr})$	0.188	
Horizontal tail	horizontal tail volume ratio	V_{ht}	0.26	
	tail lift slope	$C_{L_{\alpha,ht}}$	3.93	rad^{-1}

A.2 K4A-2H

Table A.3 collects the most important rotor and fuselage configuration parameter for the K4A-2H gimballed rotor.

Table A.3. K4A-2H rotor and fuselage parameters

rotor angular rate	Ω	53	rad/s
rotor radius	R	3.8	m
blade chord	c_b	0.23	m
fly–bar radius	R_2	1.45	m
fly–bar root cut-out	R_1	1.15	m
paddle chord	c_{fb}	0.25	m
blade lift curve slope	C_{L_α}	5.7	
hub stiffness	K	3,610	Nm/rad
pitch hinge stiffness	K_T	150	Nm/rad
primary command ratio	K_H	0.57	
blade inertia	I_b	87.7	kg m^2
blade static moment	S_b	17.7	kg m
blade mass	m_b	10.75 kg	
hub feathering inertia	J_{H_F}	0.088	kg m^2
hub teetering inertia	J_{H_T}	0.195	kg m^2
hub polar inertia	J_{H_P}	0.23	kg m^2
fly–bar inertia	J_{fb}	5.012	kg m^2
fuselage mass	m_f	650	kg
fuselage parasite area	C_{D_f}	5.28	m^2